UCLA-ENG-8604
PPG-930

The Theory of Helium Transport, Clustering and Cavity Evolution in Structural Materials Under Irradiation

Shahram Sharafat

February 1986

This work was supported by the U.S. Department of Energy, Office of Fusion Energy, Grant #DE-FG03-84ER52110, with UCLA.

DISCLAIMER

TABLE OF CONTENTS

FIGURES

CHAPTER I

CHAPTER II

CHAPTER III

CHAPTER IV

CHAPTER V

CHAPTER VI

CHAPTER VII

TABLES

ACKNOWLEDGEMENTS

The author would like to express thanks to his major professor, Dr. N. M. Ghoniem, for guidance, patience, and encouragement during these five years of instruction and research. Particular thanks go to the members on this doctoral committee.

Special mention and thanks must go to Dr. H. Trinkaus and Dr. F. Najmabadi for direction and support. Furthermore this author owes thanks to Dr. P. J. Maziasz who supplied valuable experimental data and shared his findings freely with me.

Finally I wish to express my appreciation to Joan George for her neat and diligent work in typing the manuscript of this thesis.

This work was supported by the U.S. Department of Energy, Grant No. DE-FG03-84ER52110 with UCLA.

ABSTRACT OF THE DISSERTATION

The Theory of Helium Transport, Clustering and
Cavity Evolution in Structural Materials Under Irradiation

by

Shahram Sharafat

Doctor of Philosophy in Nuclear Engineering
University of California, Los Angeles, 1985
Professor Nasr M. Ghoniem, Chair

Metallic alloys exposed to fusion reactor neutron spectra will experience high helium generation rates. The interaction of helium atoms with other neutron-induced radiation damages will inevitably result in a deterioration of bulk material properties. Overwhelming experimental evidence suggests that this could be the second most serious obstacle to commercialization of fusion power.

Because the lifetime of a nuclear reactor is dictated by the integrity of the structural material, extensive efforts have been made over the past decade to understand the effects of helium atoms on bulk material properties.

Despite low solubility, helium atoms will precipitate into bubbles inside structural materials. Little is known about the nucleation and evolution of helium bubbles due to the submicroscopic levels at which these processes occur. Lack of fusion test facilities has encouraged the material research community to use simulation techniques. The main drawback of these experimental techniques is the fact that various radiation damage processes have to be singled out. Thus, the combined effects of all simultaneously occurring radiation phenomena can not be easily tested. The goal of this thesis is to use theoretical approaches to understand the mechanisms of helium transport, interaction with defects, and clustering with vacancies during irradiation.

Helium interaction with metallic alloys during irradiation is first investigated. Helium-defect interaction processes that are helpful in explaining experimental findings are identified in this work. This is then used to determine helium atom transport processes through the matrix. Next we establish nucleation and criticality criteria for the stability of helium-vacancy complexes. All processes are complicated because of the everchanging microstructure caused by neutron interactions with the material. The current efforts include the effects of thermal fluctuations, primary knock-on atoms (PKAs), and self-interstitials on the evolution of the cavity size distribution.

The growth and evolution of helium-filled bubbles are examined by developing and solving a 2-D Fokker-Planck equation describing the evolution phenomena.

Special care was taken in monitoring the boundary conditions of the solution space. The integral finite-difference formulation of the

boundary elements assures conservation of irradiation produced defects, thus minimizing the accumulation and propagation of numerical instabilities.

The 2-D Fokker-Planck equation is solved numerically using a finite differencing scheme. A nodal-line analysis coupled with a trajectory method was used to develop a dynamic mesh-size incrementation method. This method assures high program efficiency. A typical run requires ~ 5 to 7 minutes of Cray computer running time. Such a run will evaluate the cavity size distribution and the helium atom content distribution in stainless steel exposed to up to ~ 14 dpa of total damage in HFIR experiments.

In summary, a unifying model that encompasses all possible processes from an atomistic level of HVCs to measurable helium bubbles is presented in this thesis.

CHAPTER I

INTRODUCTION

At the present time the fusion research community is still faced with major obstacles before a safe fusion power reactor can be realized. The primary requirement for controlled thermonuclear fusion is that of plasma confinement and sustainment for the duration of a burn cycle. Present efforts in plasma physics research coupled with confinement concept studies are setting a timetable of 20 to 30 years before confinement and production of a D-T plasma can be achieved for commercially attractive burn times. Once this primary requirement has been achieved, several other problems will have to be solved in order to make fusion power safe and economical. A major set of problems are the consequences of the interactions between fusion neutrons and the structural materials surrounding the plasma.

Generally, neutron and material interaction leads to radiation-induced deterioration (radiation damage) of the material. Thus radiation damage has been termed the second-most serious obstacle to commercialization of fusion power [1].

Because the lifetime of a nuclear reactor is dictated by the integrity of structural materials, the science of radiation damage originated soon after the first nuclear reactor was built in the early 1940s. It was then that Wigner, for the first time, expressed concern that the effects of fast neutrons and fission products on the microstructure of reactor materials could lead to severe technical problems. Irradiation

induced changes in reactor material microstructure were soon discovered, but it was not until the development of the fast-breeder reactor that the extent of the importance of radiation damage was appreciated and the lifetime-limiting character of radiation damage was understood.

Fast breeder reactors expose structural components to high fluxes of neutrons in the MeV range, which leads to more pronounced radiation damage effects compared to thermal nuclear reactors. Since fusion reactors will produce fluxes with a larger fraction of even higher energy neutrons, it can be assumed that radiation damage will play an even more crucial role in influencing the lifetime of structural materials in a fusion reactor, such as first-wall and blanket components.

Figure 1 compares the integrated neutron flux spectra in a typical fast fission reactor, the Experimental Breeder Reactor (EBR-II), in the first wall of a conceptual fusion reactor with 3 MW m^{-2} wall loading, and in a proposed neutron stripping source (FMIT [2]). The D-T reaction

$$D + T \rightarrow \alpha(3.5\ \text{MeV}) + n(14.1\ \text{MeV}) \quad , \qquad (1)$$

leads to a high portion of 14.1 MeV neutrons.

Microstructural changes are caused by two elementary interactions between lattice atoms and radiation:

1. Particles such as neutrons, ions, and self-ions, transfer recoil energy to the lattice atoms. Depending on the kinetic energy and mass of the bombarding specie and lattice atoms, many collisions take place before the neutron is immobilized

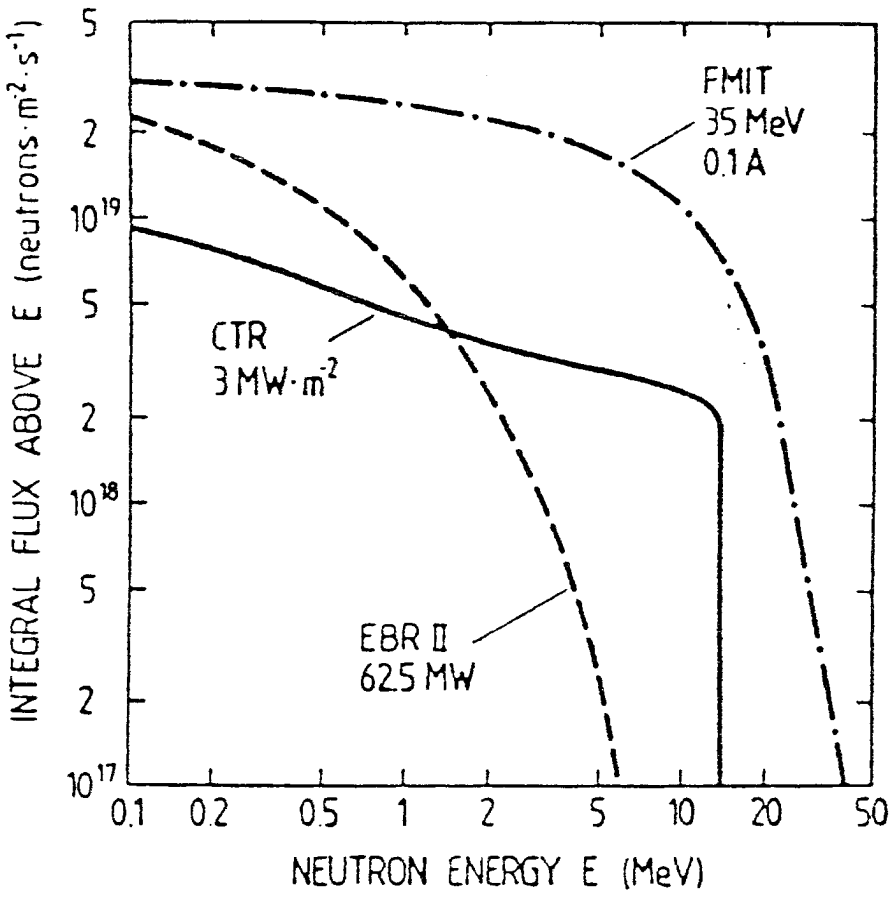

Fig. 1. Integrated neutron flux spectra in (1) the core of the EBR-II fast fission test reactor, (2) the first wall of a conceptual fusion reactor with a 3 MW/m^2 wall loading, and (3) stripping neutron stripping neutron source (FMIT) at maximum flux.

inside the host lattice. If the recoil energy of a collision exceeds the displacement threshold energy (E_{th}) of the host atom [generally $E_{th} \sim A(eV)$ for metals, where A is the atomic number], the host atom is dislodged and embeds itself as a self-interstitial in the matrix. The empty lattice site is called a vacancy. Thus a vacancy-interstitial pair (Frenkel pair, 0-D defect) is created. Once formed under continuous irradiation, vacancies tend to agglomerate into voids (3-D defects) and self-interstitial atoms (SIAs) form dislocation loops (2-D defects) or join existing dislocation lines (1-D defects). These types of radiation effects fall under the category of displacement damage. The displacement damage of future fusion reactors is predicted to be of the same order as that of fast neutron reactors.

2. The second elementary interaction between radiation and the lattice atoms causes nuclear reactions leading to solid or gaseous transmutations. Metals and alloys under fast neutron irradiation produce helium by n,α-reactions. The inert gas helium is highly insoluble inside the matrix and thus stays highly mobile until it is immobilized in lattice defects such as voids and bubbles.

In fission reactors, the production of inert gases in structural materials is relatively low and the major effect of these gases lies in stabilizing displacement damage. However, in fusion reactor environments, the rate of n,α-reactions is considerably higher since the cross

section for these nuclear reactions increases in general with neutron energy. In Chapter III, helium generation in materials will be discussed in more detail. Due to the high helium production rates in fusion environments, helium filled cavities (bubbles) are formed. Their effects on degrading material properties is regarded to be as important as that of displacement damage.

Increased research activities on the behavior of helium in metals can be attributed to the above reason. Figure 2 shows research trends where the number of open-literature publications on helium effects on materials is shown versus years [3].

Besides indicating increased activity in this area, Fig. 2 also provides some overview over the various aspects of different research areas regarding helium effects.

One interesting note is the lack of investigations comparing experimental findings and theoretical research. This thesis is intended to establish such a link, thus allowing more insight into the effects of helium on engineering properties of reactor materials. The reason for the lack of theoretical comparisons to experimental findings lies in the difficulties encountered in measuring fundamental phenomena of helium behavior in metals.

First, as pointed out by Fig. 1, no experimental facilities are yet available experimentally to investigate helium effects on materials under fusion conditions. Furthermore, the combined effects of displacement damage with nuclear reactions on the microstructural evolution do not reach equilibrium conditions, but seem to change continuously until irradiation is turned off. Such a situation complicates understanding

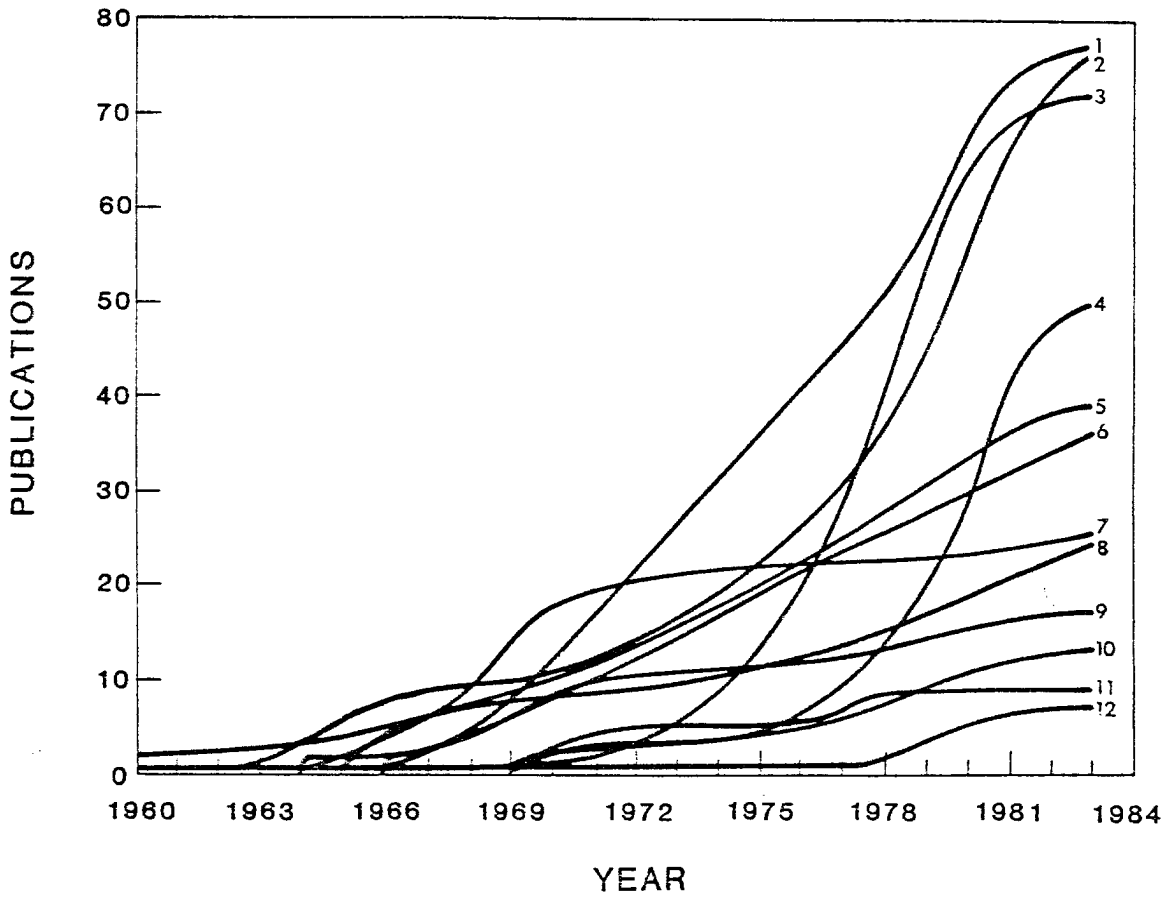

Fig. 2. Cumulative no. of publications in various research areas.

LEGEND

1) Nucleation of gas-filled cavities
2) Cavity growth and swelling
3) Effect of helium on surfaces (blistering and gas release)
4) Effect of helium on microstructure evolution
5) Helium transport and migration
6) Helium effects on embrittlement and creep rupture
7) Noble gases
8) Helium equation of state
9) Bubble mobility
10) Mechanical properties
11) Helium production
12) Helium effects on phase stability and precipitation

of helium effects. First, due to the submicroscopic sizes of fundamental helium vacancy clusters (HVCs), their evolution cannot be monitored experimentally. Second, monitoring the development of microscopic bubbles is only feasible **after** irradiation. These two conditions make most experimental investigations equivalent to taking "snapshots" of an ever-changing microstructure, which do not render themselves readily to extrapolations. The wealth of data on the influence of helium on engineering properties of reactor materials [3] was compiled by performing innovative helium production techniques. These techniques will be reviewed in Chapter III. The shortcomings of these techniques lie in reproducing the simultaneous effects of displacement damage coupled with helium production rates present in fusion environments.

The intent of this thesis is to establish a solid theoretical basis for understanding the evolution of HVCs, and to correlate the results to experimental data. Such a theoretical understanding of the fundamental mechanisms controlling the evolution process is essential to all experimental work on helium effects.

To accomplish this objective, both the submicroscopic or atomistic level of defect formation and the microscopic level of measurable bubble evolution must be dealt with in one comprehensive treatment. The advantages of this approach are numerous. The most important is the self-consistency of the approach, from gas production to the final evolution into microscopic bubbles. If the fundamental atomistic analysis is accurate, then by choosing a set of experimental parameters, the investigation should come close to experimental results. This will mean that we can explain and understand fundamental HVC processes with more

confidence. Furthermore, we will no longer depend on extrapolating between snapshots to understand the development of microstructural evolutions. Being able to monitor the evolution process in its entirety from nucleation to growth will allow us to explain many unresolved microstructural phenomena.

Once the size distribution of bubbles is known, a great deal of information can be extracted to predict the engineering performance of structural materials. The present approach yields this most crucial piece of information: The time-dependent size distribution of HVCs in materials under irradiation.

The importance of this investigative tool being outlined in this thesis will later show itself when variations in input parameters allow the study and explanation of many interesting experimental findings.

Chapter II will outline some basic properties of helium in metals followed by the influence of helium on bulk material properties. Here, some experimental findings on the following will be briefly reviewed:

1. Tensile strength
2. Creep rupture
3. Fatigue
4. Swelling
5. Microstructural and microchemical changes

Chapter II will conclude with a discussion on basic mechanisms of helium effects.

Chapter III starts with an overview of helium generation and retention in fusion materials and helium introduction techniques that

simulate fusion conditions, followed in Chapter IV by an extensive discussion of theoretical treatments up to the present time.

Chapter V is devoted to contributions of the present work to the subject of helium transport, diffusion, and interactions with defects during irradiation.

Chapter VI presents a review of the theory of cavity evolution during irradiation and presents derivations of our approach to the theory of defect clustering.

Chapter VII documents the development of the computational model and its application to a typical HFIR irradiation case.

Finally Chapter VIII presents summary and conclusions of the work.

REFERENCES

[1] G. L.. Kulcincki, in Radiation Effects and Tritium Technology for Fusion Reactors (Proc. Intl. Conf., Gatlinburg, 1975), USERDA Report CONF-750989, Vol. I (1976) 17.

[2] D. L. Johnson et al., J. Nucl. Mater., 85&86 (1979) 467.

[3] N. M. Ghoniem and P. Maziasz, "Helium Effects on Solids: A Reference Manual," Oak Ridge National Lab. Report ORNL-PPG-698 (August 1983).

CHAPTER II

BASIC PROPERTIES OF HELIUM IN METALS

The introduction of helium into structural materials via nuclear reactions during irradiation results in severe deterioration of metal properties. Some macroscopic changes can readily be monitored and measured (e.g., enhanced swelling, intergranular embrittlement, and surface blistering). The cause of these changes can be attributed to the formation of helium bubbles.

In order to understand the formation and development of these helium bubbles, one has to understand the fundamental processes involved. First the atomistic behavior of helium as a single impurity atom inside the host lattice must be investigated. This can be classified as the helium transport phase. Next, the interaction of helium with other defects and small defect clusters must be understood. Here we deal with the nucleation phase of helium bubbles. Finally, the mechanisms of helium and point-defect interaction with bubbles must be known to understand bubble growth under irradiation. These three phases constituting bubble evolution may also be classified according to corresponding size classes, determined by the various experimental techniques and theoretical methods listed in Table I.

1. ATOMISTIC PROPERTIES

The goal of most experimental and theoretical methods listed in Table I is to determine the energetics of helium atoms at various sites. For the first two size classes, the helium-metal and helium-helium

TABLE I [1]

PHASES OF BUBBLE EVOLUTION WITH SIZE RANGES OF THEORETICAL AND EXPERIMENTAL METHODS INDICATED

Kinetics	Transport	Nucleation	Growth	Macroscopic Properties
Typical Sizes	~ 0.2 nm	0.2 nm-1 nm	1 nm-0.1 μm	0.1 μm-1 mm
Number of Defects Involved (He or V)	1-3	3-10	$10-10^7$	
Cluster Type	Defects	Bubble nuclei	Non-ideal gas bubbles	Ideal gas bubbles
Experimental Methods	THDS	TEM, EELS, SAS, NSC		Swelling, creep fatigue, strain test
	FIM	PAS		SEM
Theoretical Methods	Computer simulations	Non-equilibrium statistical mechanics		Micro/macro-mechanics

Abbreviations:
THDS = thermal desorption
TEM = transition electron microscopy
EELS = electron energy loss spectroscopy
SAS = Neutron and x-ray small angle scattering
NSC = Nuclear scattering methods
FIM = Field ion microscopy
SEM = Scanning electron microscopy
He = Helium atoms
V = Vacancies

interaction is important. Figure 1 shows the respective energy levels for some of these interactions in a nickel lattice.

Because of rapid developments in high-speed computing, calculations of defect interaction energetics have been successful. Results of these calculations and comparisons to some experimental results are given in Chapter IV. Important conclusions from theoretical and experimental studies regarding the properties of helium atoms in metals are summarized below.

1. Because of the perfect electronic shell configuration of helium atoms, it does not readily share its electron configuration with the surrounding metal electrons. This causes a high strain field in the vicinity of the helium atom. Thus the heat of solution (E_S^{He}) of an interstitial helium atom (IHA) is very high (2 to 4 eV)[2]. The strain field caused by an interstitial helium atom is almost totally eliminated once it "falls" into a vacant lattice site [and in effect substitutes for a host atom (substitutional helium atom)]. This causes the helium atom to be "bound" to a vacancy by an energy roughly equivalent to E_S^{He}. In the event a self-interstitial atom (SIA) encounters a substitutional helium atom (SHA), the SIA can dislodge the SHA and recombine with the vacancy. (See Fig. 1).

2. The energetically more favorable position of an SHA constitutes a very significant and effective trapping mechanism. Without trapping, helium atoms would simply diffuse to open or closed

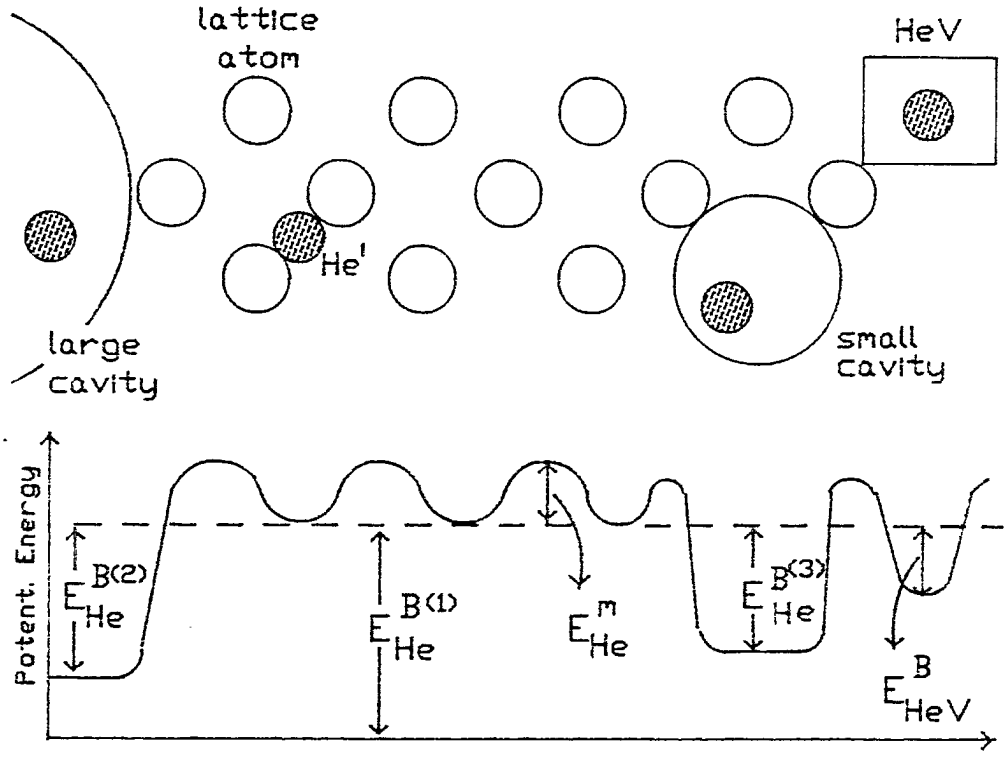

Fig. 1. Energetics of helium in a metal lattice including cavities in nickel.

LEGEND

Heat of solution of helium: $E_{He}^{B(1)} = 3.5$ eV,

Helium binding energy to a large cavity: $E_{He}^{B(2)} = 2.9$ eV,

Helium binding energy to a small cavity: $E_{He}^{B(3)} = 2.5$ eV,

Helium binding energy to a single vacancy: $E_{HeV}^{B} = 2.1$ eV,

Interstitial helium migration energy: $E_{He}^{m} = 0.1$ eV.

surfaces after introduction into the lattice, and the tendency towards helium bubble formation would be difficult. As a consequence, the equilibrium concentration of SHAs is expected to be much larger than that of IHAs.

3. The large heat of solution associated with IHAs is a measure of the low solubility of helium atoms in metals. This low solubility is the main property of helium in metals that causes helium to precipitate into clusters of helium vacancies that later grow to become helium bubbles. These bubbles are the reason for the degradation of structural material engineering properties.

After establishing the fundamental energetics of helium atoms in metals, we can use this information to identify and quantify diffusion mechanisms for helium. Although Chapter V discusses helium diffusion in more detail we outline here some general processes related to helium transport.

1. The first migration process of an introduced IHA is achieved by jumps between interstitial positions caused by thermal agitation until it is "trapped" at a lattice imperfection. Because of the large number of imperfections inside any structural material (such as grain boundaries, thermal vacancies, dislocation lines, and precipitates), the average residence time for a helium atom as an interstitial is very short.

2. The next migration process is of a SHA moving with the vacancy as a helium-vacancy cluster (HVC). For this to occur, a vacancy must be formed next to the HVC. The helium must then interchange with the self-interstitial of the neighboring vacancy. This mechanism can be ignored totally in the absence of irradiation because the thermal-vacancy concentration is small.

   Under irradiation, vacancies and interstitials are produced by displacement damage and both defects are involved in helium transport. The self-interstitial can recombine with the vacancy being occupied by the helium atom, thus in effect detrapping the helium atom. This is called a replacement mechanism.

3. Irradiation can affect the HVC in two other ways. Recoil atoms can dislodge the trapped helium atom if their kinetic energy exceeds the helium-vacancy binding energy (see Fig. 1). The second effect is due to the abundance of single vacancies created by irradiation. With a supersaturation of vacancies larger than one, a single vacancy may encounter a HVC on its migration path. This vacancy will then attach to the HVC thus forming a single helium-divacancy cluster (HV_2). This cluster has a very low migration energy because the helium atom can "rattle" between the two vacancies. Therefore, in effect, one vacancy is always unoccupied which renders the cluster able to do fast-rotational translations.

All of the above mentioned migration mechanisms have been investigated and then included in our overall analysis. We determined effective migration energies and diffusion coefficients for various temperature ranges [3]. For the technologically important temperature range $400°K < T < 800°K$ the helium-effective diffusion coefficient was found to be approximately equal to that of the single-vacancy diffusion coefficient.

As pointed out earlier, the high ionization and potentials of inert gases cause the electrons to remain in atomic orbitals, thus not contributing appreciably to cohesion. This "insolubility" character of helium atoms causes them to precipitate into clusters after a relatively short incubation period which can drastically affect the migration of helium atoms.

The migration of helium atoms to the grain boundary is the key parameter for high temperature embrittlement of structural material [4,5]. Therefore, any phenomena which influences helium migration must be understood in order to predict material performance. This is why nucleation and growth of helium clusters have received much attention.

2. NUCLEATION AND GROWTH

Nucleation and growth of HVCs have been investigated at low ($T \lesssim T_m/3$) and high temperatures ($T \simeq 400°$ to $750°C$).

At low temperatures, HVCs in platelets [6] and spherical shapes [7] have been found to nucleate under high helium production rates. Bubble nucleations can occur spontaneously, i.e., without any thermodynamic

barrier. In the absence of sufficient vacancies, these clusters can nucleate and grow by a loop punching mechanism [7,8] if the pressure in the cluster exceeds the loop punching threshold value P_{LP}:

$$P_{LP} \approx \left(\frac{2\gamma + \mu b}{r}\right) \quad , \tag{1}$$

where γ = surface free energy,

μ = shear modulus of the material,

b = burgers vector,

r = loop radius.

Under conditions relevant to fusion environments, nucleation, and growth of HVCs are subject to thermodynamic barriers. Such thermodynamic barriers determine the stability of nucleating HVCs. Three levels of analyses are generally used to study the degree of stability of HVCs.

The first is an atomistic [9] approach in which HVCs are analyzed using appropriate interatomic potentials. Stable configurations and helium-vacancy ratios, as well as binding and migration energies, are found. Shortcomings of this approach are (1) the method is not applicable to large clusters and (2) the effect of kinetic processes due to irradiation cannot be included.

For the second approach, purely kinetic descriptions are used to derive simplified analytical expressions for the "critical cavity size" for cavity nucleation and growth [10,11]. This approach may ignore important detailed mechanisms.

The third approach investigates nucleation and growth through thermodynamic considerations. Here the energetics and formation of helium bubbles is determined by establishing the free energy of formation [5,12,13]. Although details of this method are discussed in Chapter V, it suffices here to say that the thermodynamic approach has been successful in estimating the order of magnitude of the final bubble density.

A part of this study (Chapter V) is aimed at identifying the stability of HVCs in an irradiation field. Such stability is a complex function of irradiation variables (damage rates, helium production rates, and fluence), as well as material parameters (sink density, temperature, and defect parameters). Consistent with HFIR, EBR-II, and accelerator irradiation conditions, we determine (in Chapter V) respective nucleation regimes based on a nodal line stability analysis for various temperatures and dislocation line densities [14]. We then show how the stability analysis approach is further used in the analysis of helium bubble evolution.

Now that some basic helium properties in structural materials have been mentioned and identified, the next step is to review the influence of helium on bulk material properties.

3. EFFECTS OF HELIUM ON BULK MATERIAL PROPERTIES

The effects of inert gases produced during irradiation in nuclear fuels were studied in the early years of fission reactor development. However, it was not until 1965 that a paper by Barnes [15] appeared which linked high temperature ductility losses [16-18] of irradiated stainless steel to helium bubbles in the grain boundaries. The identification of the role of helium bubbles on deteriorating bulk properties led to numerous investigations of helium effects on Ni-based alloys. With developments in controlled thermonuclear fusion, higher helium contents were expected. This intensified the need to understand and thus investigate helium effects on bulk properties such as tensile strength, creep rupture, fatigue, swelling, and microstructural and microchemical changes. Many experimental proceedures to reproduce fusion reactor conditions have been developed and are used to compile data on helium effects. These methods are reviewed in some detail in the next chapter. Most of the experimental data has been compiled from post-irradiation tensile tests, since in-pile tests are extremely costly and difficult to perform.

In the following sections, a limited review of the most important experimental findings is given. We start with the extent of helium embrittlement, or ductility loss, which is thought to be the most critical of helium effects on structural materials in fusion environments.

3.1. Tensile Strength

Helium bubbles nucleating and growing at grain boundaries lead to premature intergranular failure. Numerous experimental investigations have been carried out under different irradiation and test conditions to determine the extent of ductility loss due to intergranular helium bubbles.

The bulk of the data is compiled from tensile strength tests. Besides the fact that these high strain rate tests are performed as post-irradiation tests, they may not reveal the full extent of the influence of helium bubbles on the tested properties because intergranular helium bubbles have not had enough time to fully develop. However, these tests indicate the severity of helium effects on mechanical properties. As an example, Bloom [19] has compared the temperature dependence of the total elongation of AISI-316 stainless steel under three different conditions: (1) unirradiated, (2) irradiated with a low helium dpa ratio typical of fast reactors, and (3) irradiated under HFIR conditions (i.e., high helium dpa ratio).

Figures 2 and 3 show Bloom's findings for both solution-annealed and 20% cold-worked heats of 316 stainless steel. The helium concentration of the fast reactor irradiated heats of steel after about 50 dpa is only 20 to 25 ppm, while that of corresponding HFIR heats is ~ 4000 ppm. Although 20 to 25 ppm seems to be a small helium concentration, Fig. 4 shows a significant decrease of total elongation for fast reactor irradiated solution-annealed 316 stainless steel. For HFIR irradiated stainless steel, the elongation decreases to even lower values. In fact, above 600°C this material shows zero plastic elongation. Wiffen et al.

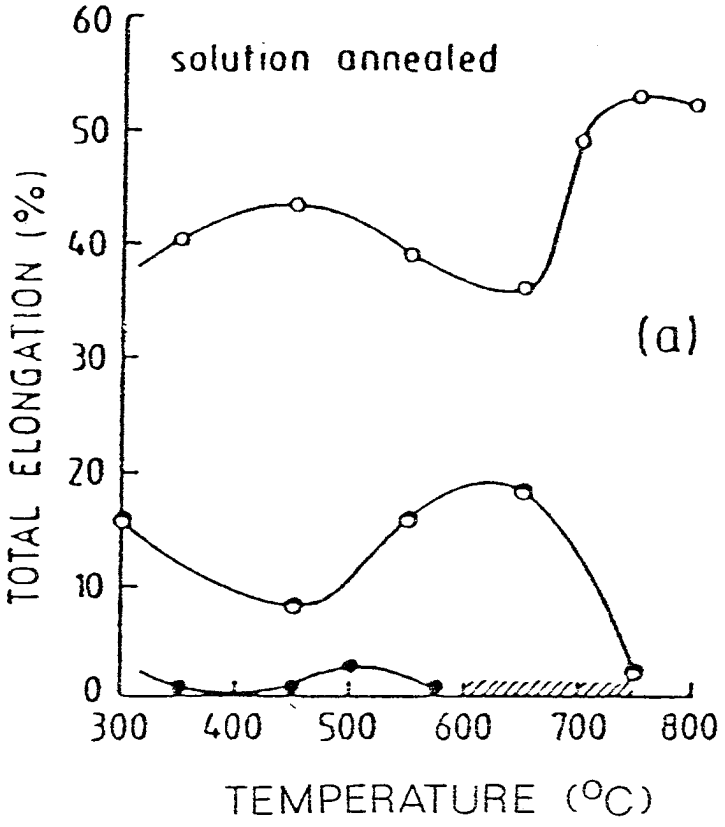

Fig. 2. Tensile testing results of total elongation dependence on temperature for three SA-ANSI-316 stainless steels. (O unirradiated, ◕ irradiated with low He/dpa ratio, ● irradiated with high He/dpa ratio)

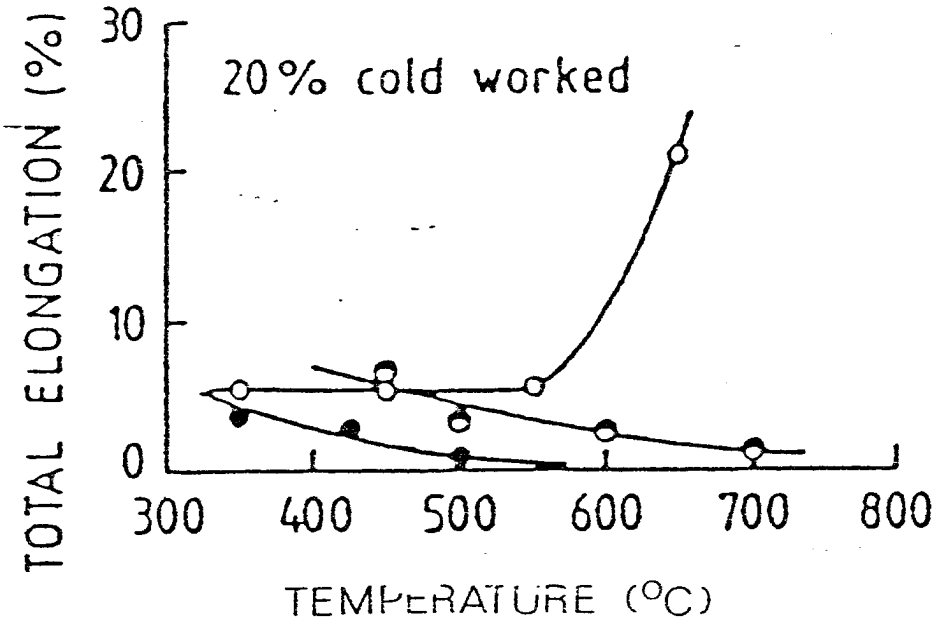

Fig. 3. Total elongation vs temperature for 20% cold-worked AISI-316 stainless steels (O unirradiated, ◐ irradiated with low He/dpa ratio, ● irradiated with high He/dpa ratio)

have obtained similar behavior for the Inconel 600 alloy [20]. Cold-worked stainless steel shows a significant reduction in plastic elongation above 600°C for both 20 and 4000 ppm helium concentration with less pronounced reductions for lower temperatures.

Various experiments scanning different helium dpa ratios and even lower temperatures (25° to 300°C) have been performed on various fcc and bcc alloys [21-29] giving similar results.

In summary both fcc and bcc alloys experience various degrees of high temperature helium embrittlement caused by helium produced nuclear reactions.

3.2. Creep Rupture

Although structural materials which are able to perform below their yield stresses are chosen, the long term accumulation of damage plays an important role in the lifetime of structural components. Thermal creep, which is well known for most materials, is such a process. Under irradiation, thermal creep can be dramatically enhanced and can lead to very short rupture times under otherwise acceptable conditions.

Creep tests, especially for in-pile experiments, are very time consuming, difficult, and expensive. Therefore, an insufficient data base of the effects of helium on creep rupture of stainless steel exists today. Nevertheless, some useful results have been compiled [30-33] which allow us to establish some dependencies of helium embrittlement on various parameters (e.g., stress, temperature, helium content, helium implantation rates, etc.). Some of these dependencies are briefly discussed below. For more detail we refer the reader to a review article

by Ullmaier [34]. Batfalsky et al. [32] gathered data on rupture time t_R and strain to rupture ε_R as a function of helium concentration of annealed AISI-316 stainless steel at 750°C (Figs. 4 and 5). They observed a loss of ductility and lifetime at very low helium concentration (starting at 1 ppm). Furthermore, these reductions did not level out even at helium concentrations above 1000 ppm. This clearly indicates the unreliability of extrapolations of helium effects from fast fission data to fusion conditions.

It should be noted that the results given in Figs. 4 and 5 are obtained from post-irradiation experiments. Various in-pile experiments [35,36] have clearly shown that ductility and rupture times obtained from them have lower stress dependencies in general and are of lower values than those of post-irradiation experiments. This further questions the reliability of the bulk of post-irradiation data available on stainless steel.

One of the most widely used techniques of helium introduction into materials is that of α-implantation (see Chapter III). Investigating the dependence of embrittlement on the helium implantation rate, Batfalsky [32] recorded an interesting result. Figure 6 clearly shows that a reduction in the implantation rate leads to a reduction of rupture times and strain to rupture for a given helium concentration. In other words, the severity of helium embrittlement increases with decreasing helium implantation rates. This finding may imply that fast α-implantation experiments may very well underestimate helium embrittlement rates of fusion environments.

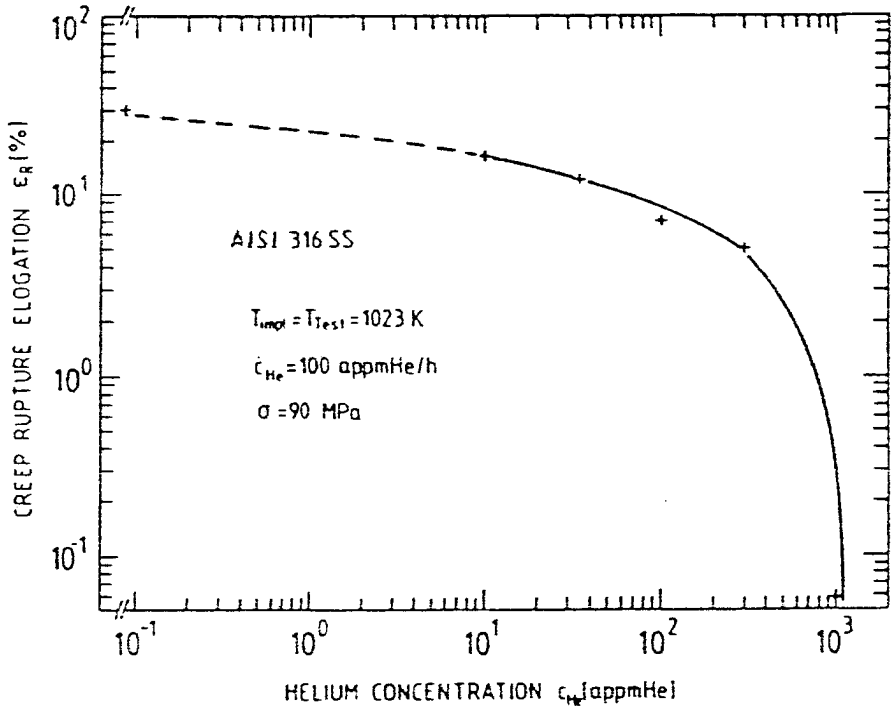

Fig. 4. Creep rupture elongation dependence on helium concentration of annealed AISI-316 stainless steel (after Batfalsky [32].

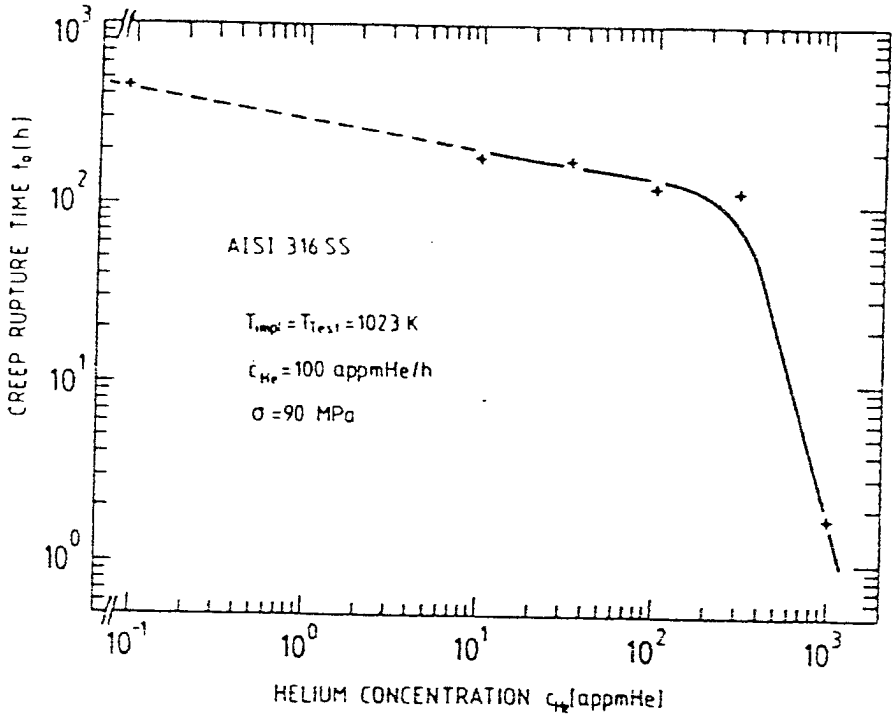

Fig. 5. Rupture time dependence on helium concentration of annealed AISI-316 stainless steel (after Batfalsky [32]).

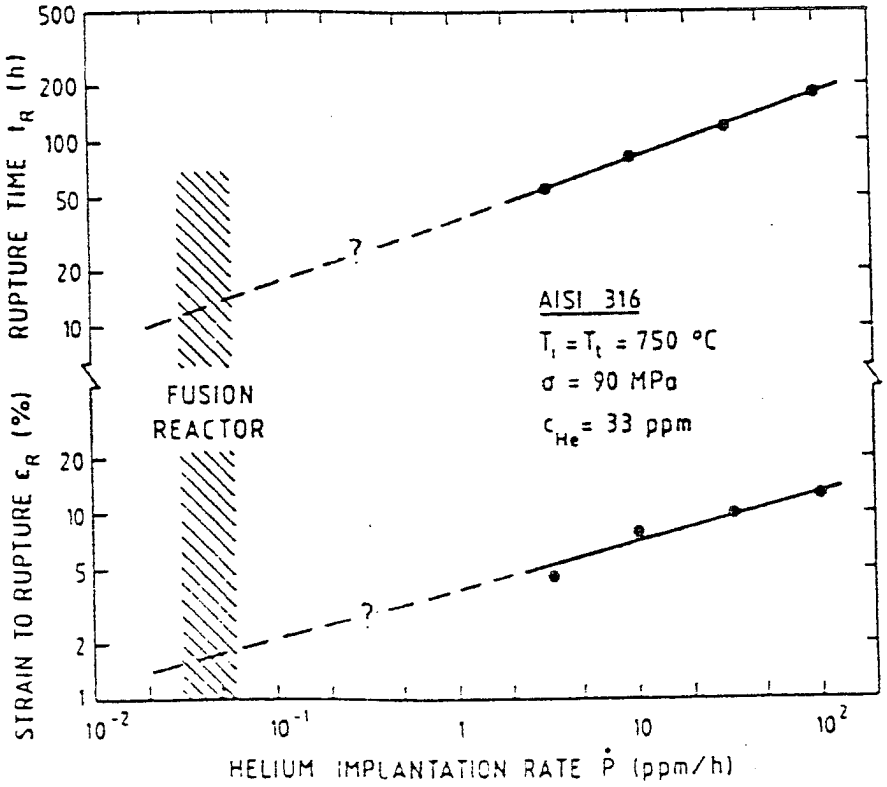

Fig. 6. Strain to rupture ε_R and rupture time t_R dependence on helium implantation rate G in AISI-316 stainless steel (after Batfalsky [32]).

Most experimental results have been carried out to establish the principal features of helium effects on properties. For example, Fig. 7 shows a reduction of rupture time from ~ 1000 hours to ~ 50 hours with a helium concentration of only ~ 8.5 appm at a total damage of ~ 14 dpa as reported by Lovell [37]. This result was obtained at a high temperature of 760°C. Helium embrittlement starts in most materials around 0.4 of the absolute melting temperature T_m [38]. In general this effect increases with increasing temperatures.

Schaaf et al. [39] have investigated the dependence of total elongation on the strain rate of unirradiated and irradiated stainless steel specimens. They have determined that the ductility decreases with decreasing strain rate, consistent with Batfalsky's experiments [32]. This behavior is shown in Fig. 8.

The macroscopic mechanical property changes caused by helium have been identified as microstructural changes. These changes can be measured by TEM, SEM, and other techniques (see Table I). They reveal the location, density, and size distribution of helium bubbles. In general, helium bubbles are found to grow at preferential sites such as grain boundary junctions, precipitate matrix interfaces and, to a somewhat lesser degree, at dislocations. Also, high uniform densities of matrix bubbles have been observed. It has been found that under applied stress, helium bubbles tend to form on grain boundaries that are perpendicular to the applied stress. This could explain the effect of stress on the ductility of the material as mentioned earlier.

Investigations of various alloys with respect to helium embrittlement rates are very scarce. In recent years, Wassilew et al. [40] have

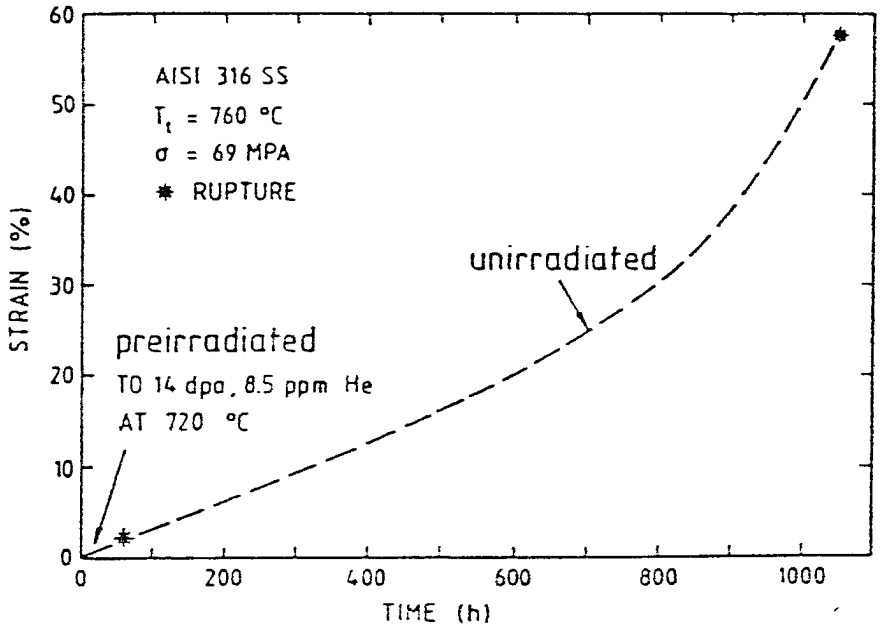

Fig. 7. AISI-stainless steel creep curves for irradiated and unirradiated samples (after Lovell [37]).

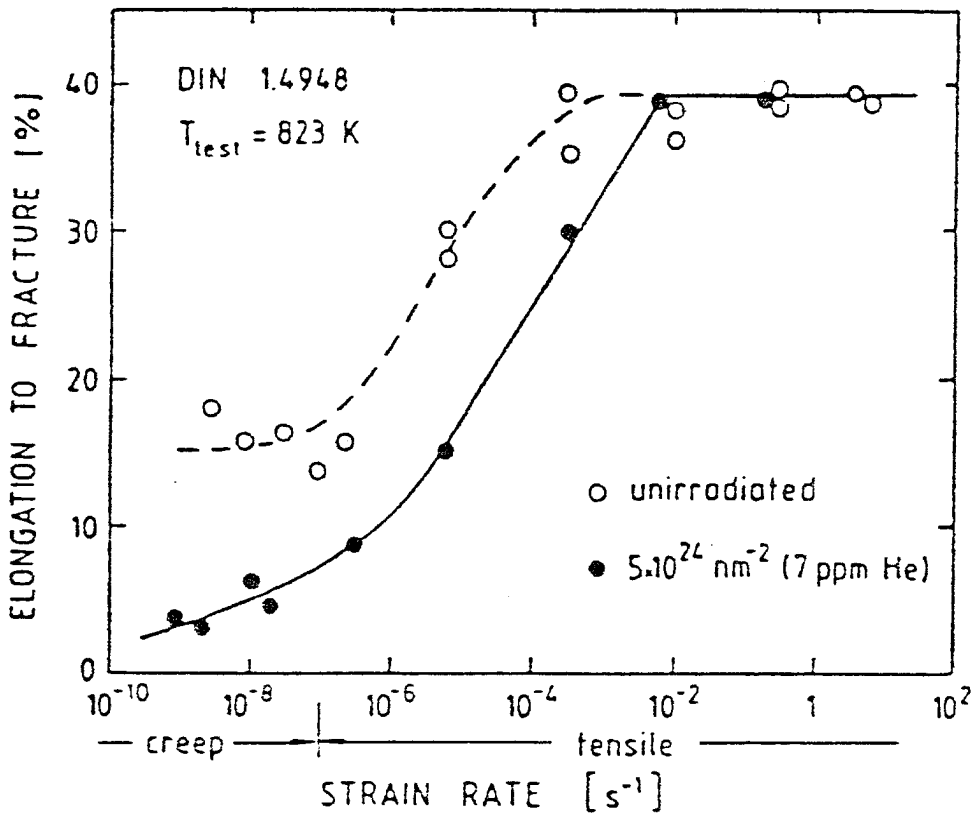

Fig. 8. Rupture elongation as a function of tensile strain rate of irradiated and unirradiated DIN-1.4948 stainless steel (after Schaaf [39]).

compared martensitic steels to austenetic steels in post-irradiation tensile tests at ~ 600°C. They report only small decreases in rupture strains and almost none in rupture times for martensitic stainless steel irradiated to about 8.5 dpa and with a helium content of 70 ppm, produced by n,α-reactions. Since martensitic steels are known to be more swelling resistant than austenetics, this feature when combined with the above indications of better helium embrittlement resistance, makes martensitic steels a good candidate for structural materials in a fusion environment.

3.3. Fatigue

Besides differences in neutron spectrum and flux, the next major difference between fission and fusion is the possible cyclic operation of fusion devices.

Inertia confinement fusion reactors (ICFRs) and tokamaks are examples of fusion devices. The few fatigue experiments on fission reactor materials did not reveal any significant changes in the fatigue-life character of irradiated specimens [41-43]. Recently, fatigue is considered to play an important role in the lifetime of the first wall in cyclic fusion devices. Although the available data are very scarce, some significant effects of helium on the fatigue life and crack growth can be seen. This has already prompted an international effort between the USA, Europe, and Japan to conduct extensive in-pile and post-irradiation experiments of the effects of displacement damage and helium on the fatigue of structural materials [44].

The following is a brief up-to-date summary of what is known about this subject. For further details see Refs. [34] and [45-48].

1. At low temperatures (below ~ 500°C) there do not seem to be any significant changes in the fatigue life even as the helium content is increased to above 90 ppm (Batra et al. [49]).

2. At higher temperatures the number of cycles to failure decreases with

   a. An increase of helium content,
   b. An increase in temperature,
   c. A decrease in loading frequency.

   Figure 9 shows an example of one such high temperature experiment. The figure shows a sudden drop of number of cycles to failure at about 5 Hz. SEM observations show a change of fracture mode from a transgranular at high frequencies, over a mixed fracture mode, to a complete intergranular rupture mode at low frequencies. The ICFR devices will eventually perform at high frequencies but for tokamaks this finding can have significant implications on the lifetime of the first wall which will be exposed to low frequency operation cycles.

3. SEM observations show that cracks initiate within the material and propagate towards the surface when helium is introduced into the material (Batra et al. [49]).

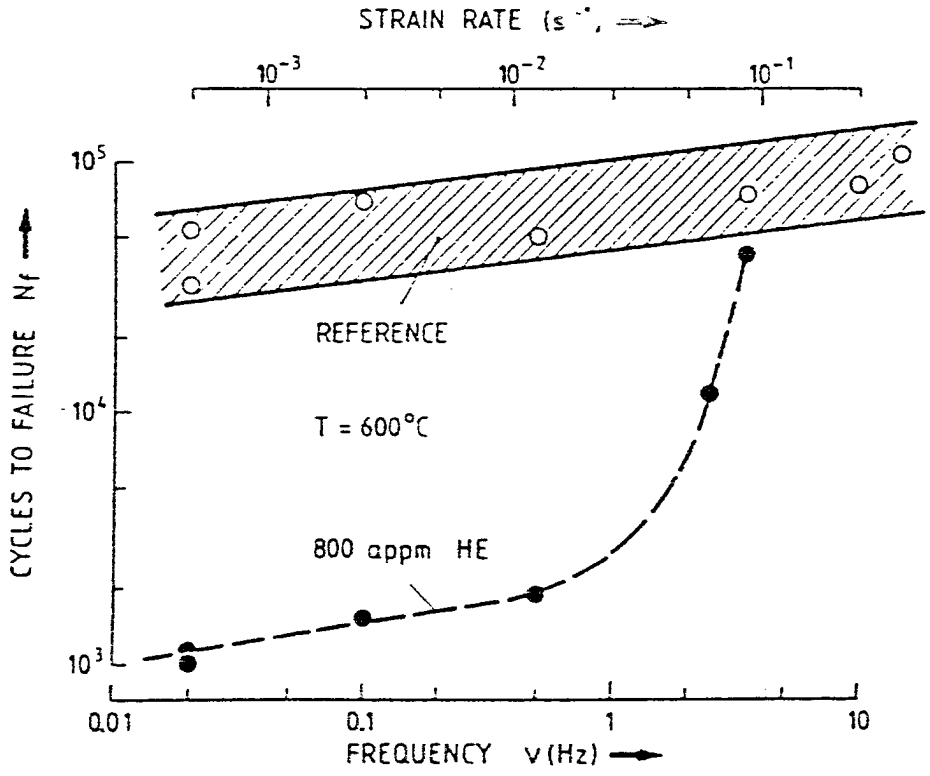

Fig. 9. Dependence of no. of cycles to failure N_f, on fatigue frequency ν for SA-AISI-316 stainless steel with a total strain rate of 1.2% (Ref. sample is helium free) (after Batra [49]).

3.4. Swelling

In fast fission reactors, swelling has been recognized as one of the most severe life-limiting effects of radiation damage on core components. Thus swelling has been extensively studied and is well understood. The primary cause of swelling in structural materials exposed to neutron irradiation is due to voids which form by an agglomeration of vacancies. The simultaneously produced self-interstitials tend to be preferentially attracted by dislocations, thus creating a surplus of free vacancies over free self-interstials. As irradiation continues, self-interstials will cause interstitial loops to grow. The effect is an even greater reduction in self-interstials because their bias towards dislocation lines and void growth is enhanced. These effects change a solid piece of stainless steel into a void-riddled, swiss-cheese-like material. Ghoniem and this author [50] have been successful in developing a new calculational method for the numerical solution of the Fokker-Planck equation describing voids and interstitial loops. Small defect clusters were studied using a detailed rate-theory approach, while large defects were simulated by discretizing a transformed Fokker-Planck equation. Defects containing up to millions of atoms were investigated using this hybrid approach. The numerical results of the model compared well with previous detailed-rate theory calculations, as well as with experimental findings on heavy-ion irradiated 316 stainless steel. The reader is referred to Refs. [50-52] for more details.

Since the mid-1970s, extensive efforts have been put forward to investigate and understand the role of helium on the swelling of structural components under fusion conditions. As pointed out earlier,

simulation of fusion irradiation conditions is not yet practical, therefore various helium implantation techniques are used (see Chapter III). In recent years it has been shown that these experiments produced questionable results. Figure 10 is a very clear example of a comparison of swelling results, compiled by Packan and Farrell [53], of two different methods of helium implantation. Figures 11 and 12, also published by Packan and Farrell, show the effect of the experimental method used on the final results. These figures both point to important findings regarding the effect of helium on swelling. The following is a brief summary of these findings. For more information see Refs. [56-61].

1. Helium atoms stabilize cavity embryos, thus reducing the incubation time for stable cavity nucleation.

2. Figures 11 and 12 show that the presence of helium atoms increases the total concentration of cavities and reduces their sizes. This is due to No. 1, above. The stabilizing effect of helium on otherwise unstable cavities keeps the cavities more finely dispersed in the matrix.

3. The stabilizing character of helium prevents dissolution of cavities at elevated temperature because of the thermal-vacancy emission process.

4. The full effect of helium on swelling can not be readily evaluated because of the need for a more extensive data base to evaluate the effects under different conditions. Theoretical studies will generally help complete the data base and identify

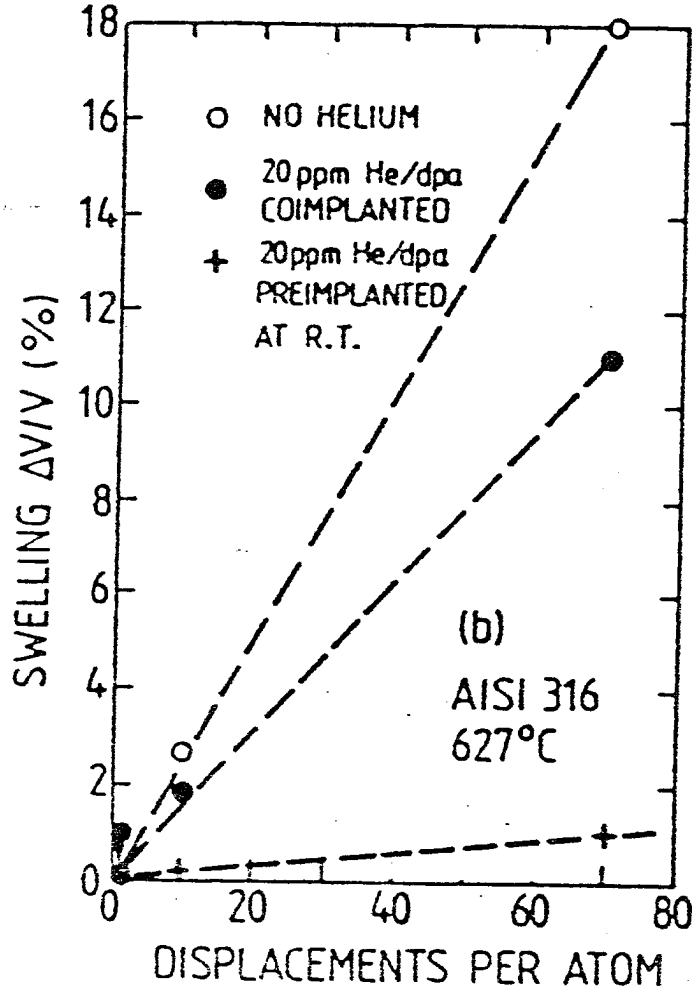

Fig. 10. Swelling as a function of dpa's for various experimental proceedures of AISI-316 stainless steel (after Packan [54].

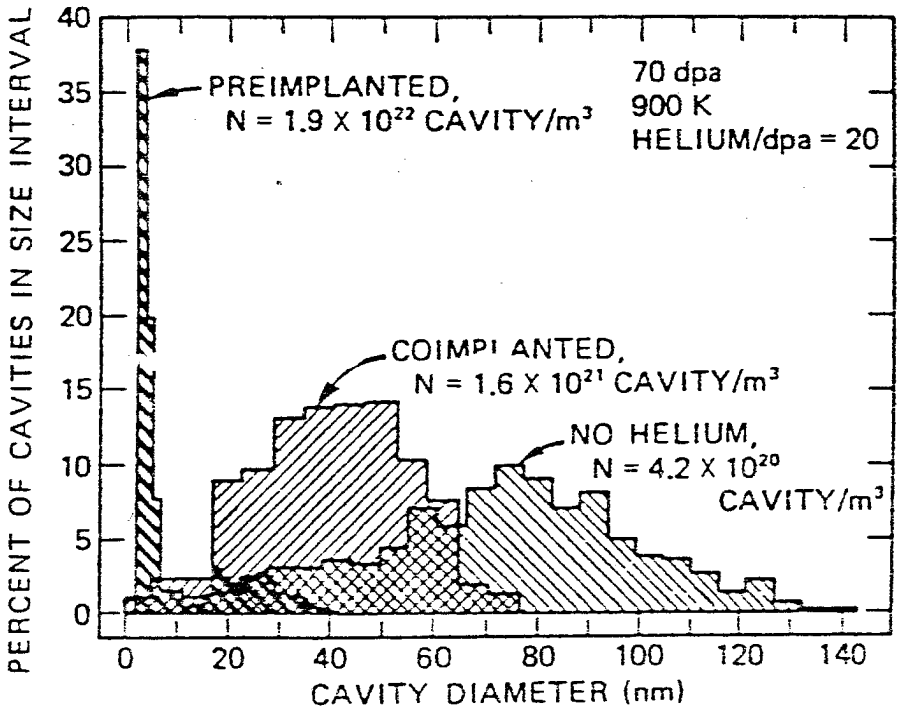

Fig. 11. Effects of choice of helium implantation techniques on the cavity size distribution of high purity austenitic alloy irradiated in a dual-beam facility to 70 dpa and 1400 appm helium concentration (after [54]).

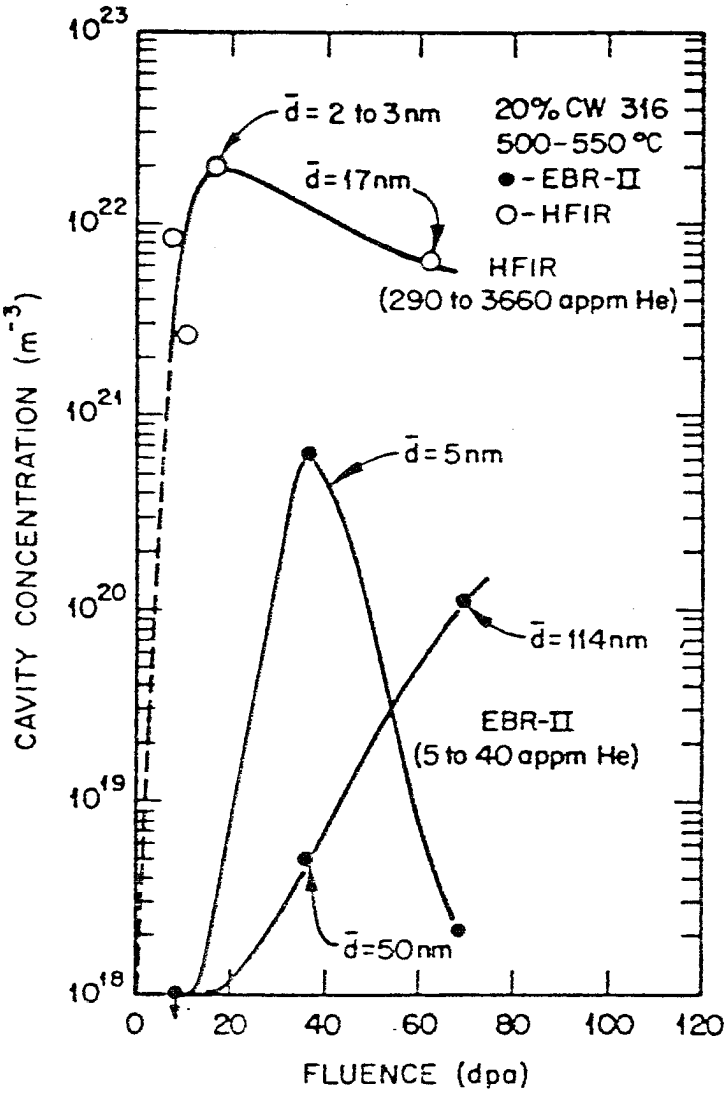

Fig. 12. Comparison of cavity concentrations and sizes for HFIR and EBR-II irradiation experiments as a function of fluence (after [54]).

experimental conditions, where the action of mechanisms are clarified.

3.5. Microchemical Effects

It has been shown that irradiation can have an effect on the microchemistry of alloys. Irradiation enhances the flow and counterflow of solute atoms creating a process known as radiation-induced solute segregation (RISS). Furthermore, irradiation can lead to the formation of various phases not commonly found in alloys [4,62]. The RISS-produced precipitates have been investigated [55-57] using TEM and x-ray electron defraction spectroscopy (EDS) analysis, and various indirect conclusions have been drawn.

1. The higher number of cavities produced under the presence of helium provides more sites for solute segregation and defect recombination which leads to a decrease in the kinetics of solute segregation. The higher number of cavities is expected to suppress RISS.

2. The helium atoms may furthermore get absorbed at various sinks, thereby affecting their bias. Any change in bias can drastically influence point-defect diffusion, which will in turn affect any microchemical or microstructural evolutions.

Because of the paucity of data, these conclusions should not be viewed as decisive evidence of helium effects on microchemistry.

The preceeding brief discussion of the effects of helium on various mechanical properties clearly shows the extent to which helium can influence the lifetime of structural components of any fusion device. Furthermore, it is clear that most of these effects are a direct consequence of the presence of helium bubbles. Thus, one of the most valuable pieces of information is the size distribution of helium-filled cavities as a function of various irradiation parameters. Furthermore, the foregoing descriptions have clearly related high temperature ductility losses to helium bubbles formed on grain boundaries. This may suggest that any theoretical treatment should concentrate on the nucleation and growth processes of grain boundary helium bubbles. The separation of grain boundary bubbles from matrix bubbles is not possible because they directly influence each other. The helium flux to the grain boundary is directly controlled by the helium bubble density inside the grain. This is a direct consequence of changes in sink strengths due to matrix cavitation. The dependence of grain boundary bubbles on matrix bubbles poses one of the biggest obstacles in developing the theory of helium effects on mechanical properties.

Although some theoretical work [62,63] has been successful in determining order of magnitude of bubble concentration, because of the difficulties involved in handling grain boundary bubbles these methods are not yet able to predict bubble size distributions, absolute values of rupture times, and elongation.

This thesis is primarily intended to establish helium bubble size distributions **inside the matrix.** This knowledge is essential in determining the helium flux to the grain boundary. During the course of this

work we have not only developed a new computational tool to evaluate helium bubble size distributions as a function of irradiation parameters, but more importantly we have uncovered fundamental mechanisms which explain various experimental findings [3,14]. However, because of insufficient knowledge of basic properties of helium in metals and lack of understanding of the most fundamental helium transport, clustering, and growth mechanisms, many obstacles have to be overcome to achieve our goal.

Because of the complexity of the problem at this stage, our work considers only homogeneous conditions inside the matrix and excludes grain boundary effects. Furthermore, the cascade nature of defects is not included; therefore pure rate theory is employed. This work will help as an investigative research tool to aid in the development of alloys suitable for long-time fusion applications.

REFERENCES

[1] H. Trinkaus, Radiat. Eff., 78 (1983) 189.

[2] J. E. Ingelsfield and J. B. Pendry, Phil. Mag., 34 (1976) 205

[3] N. M. Ghoniem, S. Sharafat, L. K. Mansur and J. Williams, J. Nucl. Mater., 117 (1983) 96.

[4] N. M. Ghoniem, J. N. Alhajji and D. Kaletta, "The Effect of Helium Clustering on Its Transport to Grain Boundaries," J. Nucl. Mater. (to be pub.).

[5] H. Trinkaus, J. Nucl. Mater., 118 (1983) 39.

[6] H. Ullmaier, Radiat. Eff., 78 (1983) 105.

[7] J. H. Evans, A. Van Veen and L. M. Caspers, Scripta Metall., 15 (1981) 323.

[8] G. W. Greenwood, A. J. E. Foreman and D. E. Rimmer, J. Nucl. Mater., 1 (1959) 305.

[9] W. D. Wilson, C. L. Bisson and M. I. Baskes, "Self-Trapping of Helium in Metals," Phys. Rev. B, 24 (1981) 5616.

[10] L. K. Mansur and W. A. Coghlan, "Mechanisms of Helium Interaction with Radiation Effects in Metals and Alloys," J. Nucl. Mater. (to be pub.).

[11] A. Hishinamu and L. K. Mansur, "Critical Radius for Bias-Driven Swelling," (to be pub.).

[12] H. Trinkaus and H. Ullmaier, J. Nucl. Mater., 85&86 (1979) 823.

[13] H. Trinkaus, Radiat. Eff., 78 (1983) 189.

[14] S. Sharafat and N. M. Ghoniem, J. Nucl. Mater., 122&123 (1984) 531.

[15] R. S. Barnes, Nature (London), 206 (1965) 1307; also Am. Soc. Testing Mater., Richland, WA, 1965, Spec. Tech. Publ. 380, p. 40.

[16] F. C. Robertshaw et al., Am. Soc. Testing Mater., Richland, WA, 1963, Spec. Tech. Publ. 341, p. 372.

[17] N. E. Hinkle, ibid, p. 344.

[18] N. A. Hughes and J. Caley, J. Nucl. Mater., 10 (1963) 60.

[19] E. E. Bloom, ibid, 85&86 (1979) 795.

[20] F. W. Wiffen, in Effects of Radiation on Structural Materials, Am. Soc. Testing Mater., Richland, WA, 1978, Spec. Tech. Publ. 683, p. 88.

[21] F. W. Wiffen and P. J. Maziasz, J. Nucl. Mater., 103&104 (1981) 821.

[22] K. Anderko, ibid, 95 (1980) 31.

[23] R. G. Faulkner and K. Anderko, ibid, 113 (1983) 168.

[24] M. L. Grossbeck and P. J. Maziasz, ibid, 103&104 (1981) 827.

[25] G. R. Caskey, D. E. Rawl and D. A. Mezzanotte, Scripta Metall., 16 (1982) 969.

[26] R. E. Gold and L. Harrod, J. Nucl. Mater., 85& 86, (1979) 805.

[27] M. P. Tanaka, E. E. Bloom and J. A. Horak, ibid, 103&104 (1981) 895.

[28] D. G. Atenridge, A. B. Johnson, Jr., L. A. Charlott, J. F. Remark and R. E. Westerman, in Radiation Effects and Tritium Technology for Fusion Reactors (Proc. Intl. Conf., Gatlinburg, 1975), USERDA Report CONF-750989, Vol. II (1975) 307.

[29] Workshop on Ferritic Steels for Fusion Reactors Applications, 8th ADIP Task Group Meeting, Washington, D.C., July 30-31, 1979.

[30] H. Schroeder and P. Batfalsky, J. Nucl. Mater., 117 (1983) 287.

[31] H. Schroeder and H. Ullmaier, Radiat. Eff., 78 (1983) 297.

[32] P. Batfalsky, H. Schroeder and H. Ullmaier, "The High-Temperature Embrittlement of AISI 316 Stainless Steel by Helium," (to be pub.).

[33] H. Schroeder and P. Batfalsky, J. Nucl. Mater., 85&86 (1979) 839.

[34] H. Ullmaier, Nucl. Fusion, 24 (8) (1984) 1039.

[35] C. Wassilew, K. Anderko and L. Schafer, in Irradiation Behavior of Metallic Materials for Fast Breeder Reactor Core Components (Proc. Int. Conf., Ajaccio, 1979) 420.

[36] J. T. Venard and J. R. Weir, Am. Soc. Testing Mater., Richland, WA, 1965, Spec. Tech. Publ. 380 p. 269.

[37] A. J. Lovell, Nucl. Technol., 16 (1972) 323.

[38] E. E. Bloom and J. O. Stiegler, Am. Soc. Testing Mater., Richland, WA, 1973, Spec. Tech. Publ. 529, p. 60.

[39] B. Van Der Schaaf, M. I. DeVries and J. D. Elen, Radiation Effects in Breeder Reactor Structural Materials , M. L. Bleiberg and J. W. Bennet, Eds. (Proc. Int. Conf., Scottsdale, 1977) (AIME, New York, 1977) p. 307.

[40] C. Wassilew, K. Ehrlich and W. Anderko, in Dimensional Stability and Mechanical Behavior of Irradiated Metals and Alloys (Proc. Conf., Brighton, 1983) (BNES, London, 1984) p. 161.

[41] M. I. DeVries, B. Van Der Schaaf, H. U. Staal and J. D. Elen, Am. Soc. Testing Mater., Richland, WA, 1979, Spec. Tech. Publ. 683, p. 477.

[42] D. J. Michel and G. E. Korth, in Radiation Effects in Breeder Reactor Structural Materials, M. L. Bleiberg and J. W. Bennet, Eds. (Proc. Int. Conf., Scottsdale, 1977) (AIME, New York, 1977) p. 117.

[43] H. H. Smith and D. J. Michel, J. Nucl. Mater., 66 (1977) 125.

[44] J. Darvas and R. J. Verbeek, Am. Soc. Testing Mater., Richland, WA, 1982, Spec. Tech. Publ. 782, p. 1140.

[45] M. L. Grossbeck and K. C. Liu, Nucl. Technol., 58 (1982) 538.

[46] I. S. Batra, H. Ullmaier and K. Sonnenberg, J. Nucl. Mater., 116 (1983) 136.

[47] M. L. Grossbeck and K. C. Liu, ibid, 103&104 (1981) 853.

[48] K. Sonnenberg and H. Ullmaier, ibid., 859.

[49] I. S. Batra, H. Ullmaier and K. Sonnenberg, ibid, 166 (1983) 307

[50] S. Sharafat and N. M. Ghoniem, "Microstructure Evolution in Metals During Irradiation Using a Unified Rate-Theory-Continuum Approach," University of California Los Angeles Report UCLA-ENG-8041 (1980).

[51] N. M. Ghoniem and S. Sharafat, Trans. Am. Nucl. Soc., 33 (1979) 261.

[52] N. M. Ghoniem and S. Sharafat, J. Nucl. Mater., 92 (1980) 121.

[53] N. H. Packan and K. Farrell, ibid, 85&86 (1979) 677.

[54] N. H. Packan and K. Farrell, Nucl. Technol., 3 (1983) 392.

[55] K. Farrell, P. J. Maziasz, E. H. Lee and L. K. Mansur, Radiat.

Eff., 78 (1983) 277.

[56] P. J. Maziasz, J. Nucl. Mater., 108&109 (1982) 359.

[57] H. R. Brager and F. A. Garner, ibid, 117 (1983) 159.

[58] F. A. Cramer and W. G. Wolfer, in Dimensional Stability and Mechanical Behavior of Irradiated Metals and Alloys (Proc. Conf., Brighton, 1983) (BNES, London, 1984) p. 21.

[59] F. A. Garner, in Fusion Reactor Materials (Proc. 3rd Top. Meeting, Alburquerque, 1983), J. Nucl. Mater. (to be pub.).

[60] H. R. Brager and F. A. Garner, J. Nucl. Mater., 108&109 (1982) 347.

[61] L. K. Mansur and W. A. Coghlan, ibid, 119 (1983) 1.

[62] H. Trinkaus, J. Nucl. Mater., 118 (1983) 39.

CHAPTER III

PRODUCTION, RETENTION, AND RELEASE OF HELIUM IN METALLIC ALLOYS

1. INTRODUCTION

There are three helium generation sources in materials employed in fusion devices. The most critical is the n,α-nuclear reaction affecting the bulk of structural materials. The other two sources of helium are surface implantation and tritium decay.

Various components of a fusion reactor face the plasma such as the first wall, divertor plates, and limiters. These components are exposed to high fluxes of α-particles that have escaped confinement. This is the primary source of helium surface implantation. Tritium decay to ^{3}He is a source of helium that has to be considered in solid breeder materials and in tritium recycling components. First, bulk helium production will be discussed followed by a brief description of the latter two processes.

This will be followed by a discussion of anticipated helium generation rates in alloys employed in fusion reactors. To achieve anticipated helium production rates, experimental techniques have been developed and employed to simulate fusion environments. These techniques and their corresponding advantages and disadvantages are summarized and are followed by a discussion of some of the latest experimental results on helium retention and release measurements.

Throughout the radiation damage community, several definitions regarding displacement damage and helium production rates have been adopted. One such definition is displacement per atom (dpa). When a

neutron or ion impacts on a solid it will displace several atoms from their lattice sites before it comes to rest within the matrix. Displacement per atom is thus a measure used to indicate the total dpa sustained by the irradiated material.

As will be explained in the following section, a fast neutron can result in a neutronic reaction with the host atom leading to the formation of a helium atom. To measure the amount of helium produced, the community has adopted the helium atom parts per million (appm) host atoms produced definition. These definitions will be used throughout this thesis.

2. HELIUM GENERATION SOURCES IN FUSION ENVIRONMENTS

2.1. Helium Production by n,α-Reactions

During the development of alloys for fast fission breeder reactors, gas-producing nuclear reactions were investigated [1,2]. A decade later, in the mid-seventies, data regarding cross sections and threshold energies were being compiled. Today there exists a strong enough data base to identify the most significant nuclear reactions that contribute to the production of helium atoms in structural materials exposed to fusion irradiation conditions.

The most important reactions leading to helium production are the high energy neutron-induced n,α-reactions:

$$ {}^{A}_{Z}M + {}^{1}_{0}n^{f} \longrightarrow {}^{A-3}_{Z-2}M' + {}^{4}_{2}He \text{ (several MeV)} \quad , \tag{1} $$

or

$$ {}^{A}_{Z}M + {}^{1}_{0}n^{f} \rightarrow {}^{A-4}_{Z-2}M'' + {}^{1}_{0}n^{th} + {}^{4}_{2}He \quad . \tag{2} $$

Since the D-T plasma reaction [Eq. (1)] leads to a high portion of 14 MeV neutrons, the high energy n,α cross sections have recently been investigated in more detail [3]. Figure 1 shows such cross sections for some typical metals. Note the increase of the n,α cross
energies between 6 and 16 MeV. It is this energy rang
fusion-produced neutrons fall; the 14 MeV n,α-reaction
special attention. Figure 2 shows the cross sections fo
and n,n',α-reactions as a function of target mass numb
figure clearly indicates that helium production cannot be totally eliminated by avoiding certain elements in structural materials. This is probably one of the most significant reasons for the thrust that helium effects research has received: <u>there is simply no way around helium production in materials exposed to a fusion reactor neutron spectrum.</u>

There are also thermal neutron reactions that lead to helium production. These reactions have been studied thoroughly because they provide a powerful simulation technique for achieving high helium production rates.

The first of these reactions has a cross section of 4010 barns (b):

$$ {}^{10}_{5}B + {}^{1}_{0}n^{th} \rightarrow {}^{7}_{3}Li(0.84\ MeV) + {}^{4}_{2}He(1.47\ MeV) \quad . \tag{3} $$

The concentration of ^{10}B is generally in the neighborhood of 10 to 50 appm in stainless steel. Therefore, despite its large cross section,

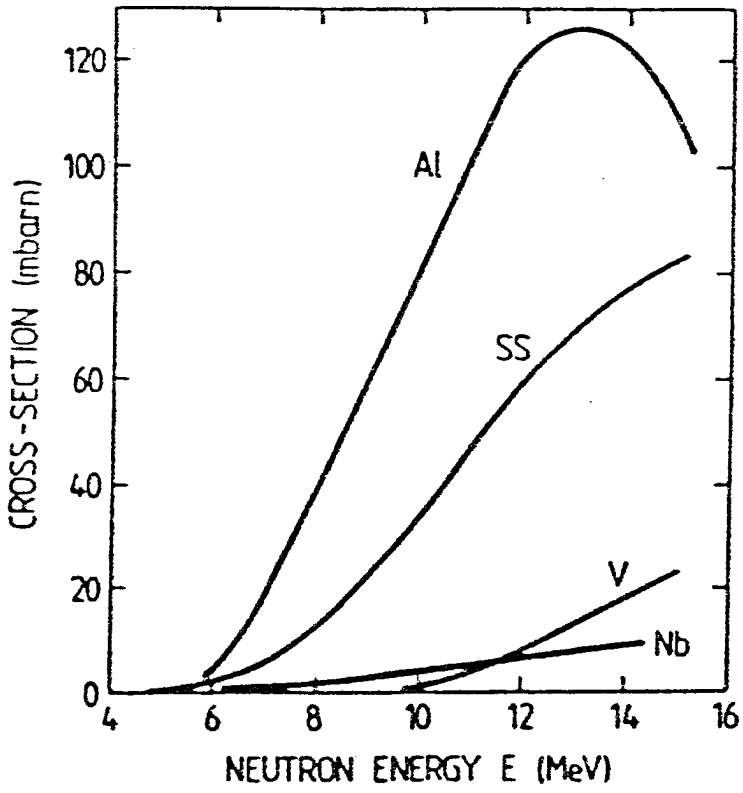

Fig. 1. Cross sections for n,α-reactions for different metals as a function of neutron energy [3].

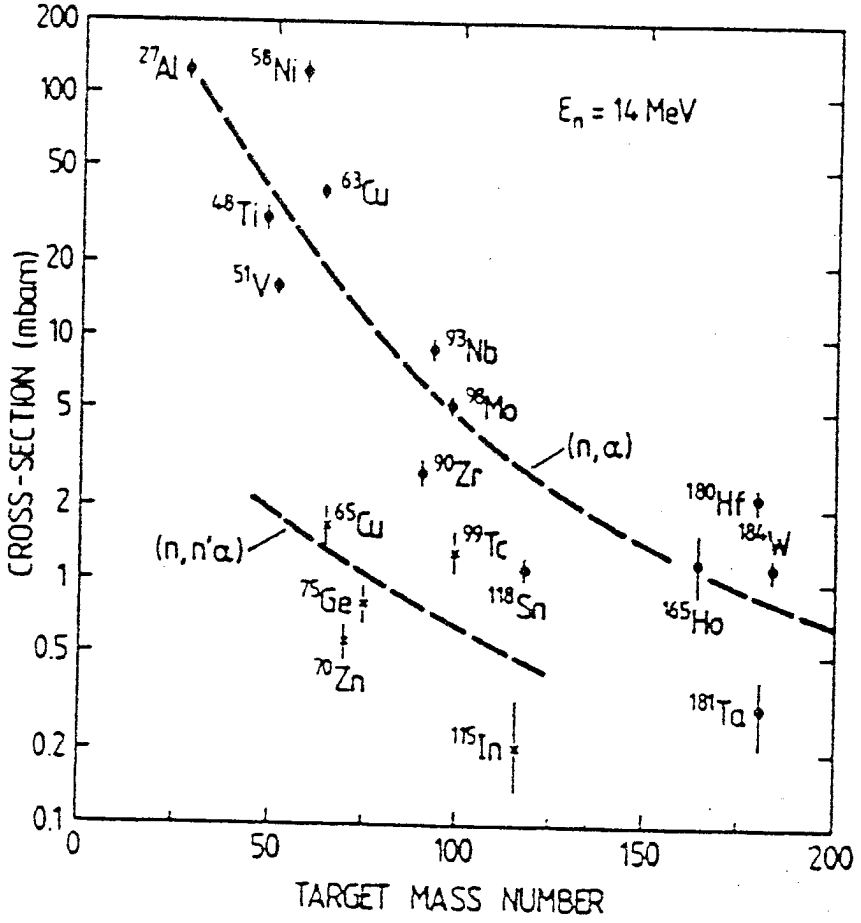

Fig. 2. Cross sections for 14 MeV neutron for n,α- and n,n'α-nuclear reactions as a function of target mass number [4].

its contribution to the helium production is negligible in fusion environments.

The next reaction is a two-step thermal neutron reaction with cross sections of ~ 0.7 and 10 b respectively:

$$\begin{aligned} {}^{58}_{28}\mathrm{Ni} + {}^{1}_{0}\mathrm{n}^{\mathrm{th}} &\longrightarrow {}^{59}_{28}\mathrm{Ni} + \gamma \quad , \\ {}^{59}_{28}\mathrm{Ni} + {}^{1}_{0}\mathrm{n}^{\mathrm{th}} &\longrightarrow {}^{56}_{26}\mathrm{Fe} + {}^{4}_{2}\mathrm{He}(4.76\ \mathrm{MeV}) \quad . \end{aligned} \tag{4}$$

The element Ni is an important constituent of many alloys considered for fusion reactors. In natural form, Ni contains ~ 69% ^{58}Ni. However, here it is the low fraction of thermal neutrons that make the contribution to helium production from Ni negligible. The fast neutrons of a wall loading of 1 MW m^{-2} on a stainless steel wall will produce ~ 269 appm helium, while the thermal reaction of Eq. (4) will produce only ~ 10^{-3} appm helium [69].

2.2. Surface Implantation of Helium

The plasma D-T reaction [Eq. (1) in Chap. I] produces 14 MeV neutrons and 3.5 MeV α-particles. In an Inertial Confinement Fusion Reactor (ICFR) these neutron and α-fluxes will bombard the first wall. With a typical yield of ~ 199 MJ per pellet in a spherical reactor of ~ 7 m radius, about 7 x 10^{16} He at./m^2 will be deposited in a surface layer of the first wall of a thickness of a few microns. The energy carried by the helium atoms constitutes about 7% of the total yield. Besides helium, fuel particles D, T, Si will also bombard the first

wall. The effects of these incident particles on the first wall are: (1) shock waves, (2) extremely high temperatures during a short period of time (e.g., 10^{-6} to 10^{-4} s), and (3) erosion and blistering caused by helium atoms deposited a few microns below the surface [5]. To minimize these effects, various reactor concepts have been proposed aimed at slowing down fuel and pellet debris and absorbing photons [6].

The magnetic confinement reactor concept (e.g., tokamaks, mirrors, stellerator) alleviates some of the problems associated with ICFRs. Here, typically less than 1% of D-T-produced 3.5 MeV α-particles will bombard the first wall by escaping the magnetic field. The confined portion of α-particles will slow down in the plasma and eventually reach the first wall. Thus, helium atoms and other plasma particles (e.g., D and T) arrive at the first wall with an average energy of ~ 100 eV. The primary effect of these low energy particles on the first wall is sputtering. This is the process of physically knocking off surface constituents. Sputtering yields for various plasma particles have been measured for various alloys. Figure 3 depicts such sputtering yields [7]. For typical reactor conditions, estimates of plasma wall interactions produce an α-particle flux of about 10^{18} m^{-2} s^{-1}. This will result in a sputtering yield of about 0.2 at./α-particle, which will correspond to an erosion rate of ~ 0.1 mm/year [7,8]. These erosion rates are expected to be tolerable. However, these values are only estimates and depend on many variables not included in the calculations.

The 3.5 MeV α-particles, contrary to the slow ones, have a range of several microns in considered alloys. With an average flux of 10^{16} m^{-2} s^{-1} they constitute only ~ 1% of the total α-particle flux

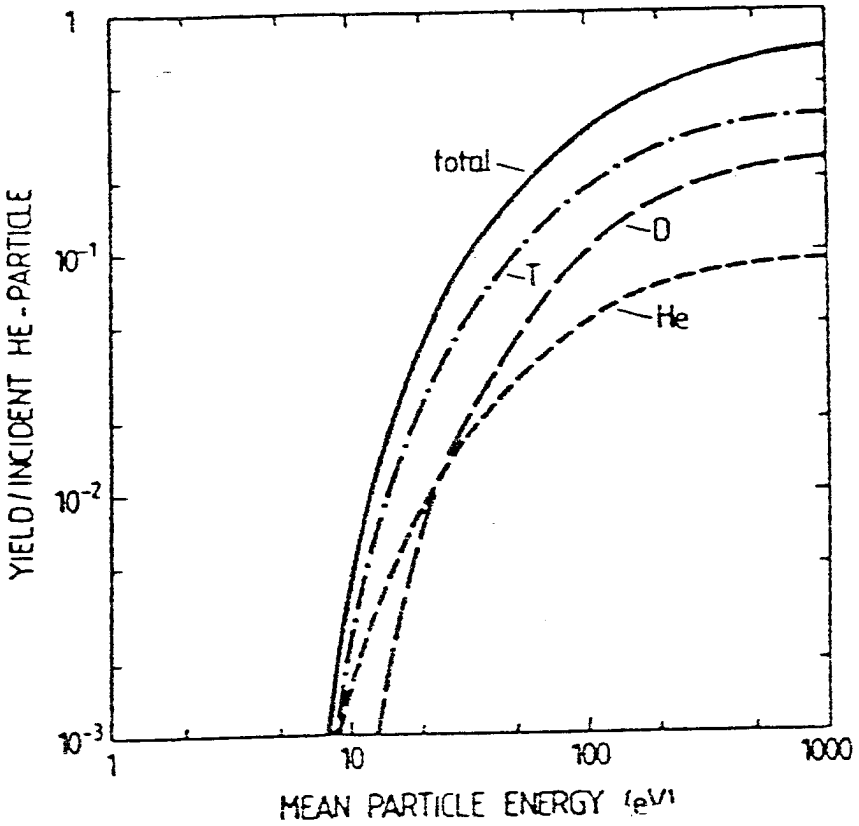

Fig. 3. Sputtering yield per incident particle (He,D,T) of stainless steel as a function of the mean incident particle energy. (The current densities were assumed relative to fractional burnup of D and T of 5% [7].)

incident on the first wall. The range of the fast α-particles has been shown to cause drastic surface modifications such as flaking, blistering, and creating a spongy-type surface layer [9,10]. However at the present time, experiments that combine both 3.5 MeV and 10 to 100 eV α-particle fluxes have not been performed to show the combined effects of sputtering and surface modifications (e.g., blistering, flaking, sponging). It has been shown that blistering will not be a major problem in fusion environments because simultaneous surface erosion by sputtering helps to mitigate blistering.

2.3. Helium Production Through Tritium Decay

The third source of helium atoms in fusion devices is due to tritium decay. Major efforts are now underway to understand the effects of tritium and helium in breeder materials [11-13]. As far as structural alloys are concerned, helium production by decay can reach values comparable to neutron reaction rates if the tritium solubility is very high [14]. This is the case for V-base and Nb-base alloys. However, this problem can be eliminated by coating structural components exposed to tritium with tritium-impermeable films. Nevertheless, tritium decay is a very valuable experimental tool for simulating helium effects in the absence of controlled radiation damage.

3. HELIUM PRODUCTION RATES IN FUSION REACTOR STRUCTURAL MATERIALS

The previous discussions explained the origins of helium atoms produced in fusion reactor components. Ever since conceptual designs of

fusion reactors were proposed in the 1970s, detailed calculations were performed to determine neutron spectra, afterheats, displacement rates $\dot{K}$ and gas production rates $\dot{G}$. These calculations show an insensitivity to changes in magnetic confinement concepts, but depend on the choice of materials used in structural components. In ICFRs, the resulting displacement and helium gas production rates depend very strongly on the first wall protection concept. Table I, compiled from Refs. 6, 15, and 16 clearly demonstrates this point.

TABLE I

ESTIMATED DAMAGE RATES IN FUSION REACTORS [6,15,16]

Concept	Material	$\dot{K}$[dpa·a^{-1}] Displacement Rate	$\dot{G}$[appm·a^{-1}] He-Production Rate	He/dpa [appm/dpa] Ratio
Magnetic confinement	Stainless steel (AISI-316)	11.6	145	12.7
	Vanadium alloy (V20 Ti)	11.7	59	5.0
	Molybdenum	7.5	47	6.3
ICFR	HIBALL Ferritic steel (HT9)			
	Unprotected	10.1	92	9.1
	Protected	1.1	0.14	0.13
	Lithium/ wetted wall stainless steel	10	40	4
	Carbon dry wall Molybdenum	7	31	4.5

Experimental procedures for determining radiation effects on structural materials are very time consuming, complicated, and expensive. Thus irradiation experiments can not keep pace with changing conceptual designs. Furthermore, experimental procedures (see Sect. 4) set certain restrictions on the ranges of displacement and gas production rates that can be investigated. These reasons have prompted the experimental community to establish an anticipated order of magnitude displacement and helium production rates given in Table II. The last row is for comparison.

TABLE II

ANTICIPATED ORDER OF MAGNITUDE FOR DISPLACEMENT AND HELIUM PRODUCTION RATES IN FUSION REACTOR FIRST WALLS [17]

Concept	$\dot{K}$[dpa•s^{-1}] Displacement Rate	$\dot{G}$[appm•s^{-1}] He-Production Rate	He/dpa [appm/dpa] Ratio	NF No. of Power Cycles/Yr
ICFR	10^{-1}	10^{-1}	5	10^{8}
Magnetic confinement (Tokamak)	10^{-6}	10^{-5}	15	10^{5}
Fast-breeder reactor	10^{-6}	10^{-7}	0.2	5-10

At present, the goal is to simulate irradiation conditions listed in Table II for alloy development. The next section examines various experimental techniques that simulate helium introduction into structural materials.

4. EXPERIMENTAL TECHNIQUES FOR SIMULATION OF FUSION REACTOR DAMAGE CONDITIONS

The fusion community has been faced with a challenging problem: the lack of a fusion-simulating test environment for the development of structural fusion materials. Even the next generation of large fusion devices will not achieve fusion's anticipated burn cycles. Thus, they cannot be regarded as immediate future material test facilities. This situation is not expected to change drastically over the next decade. Therefore, non-fusion irradiation sources have to be used to study the effects of anticipated fusion irradiation on materials.

Because the damage rates are comparable in both devices ($\sim 10^{-6}$ dpa/s), Fast Breeder Reactors (FBRs) allow the study of displacement damage expected in fusion. The high helium production, specific to fusion, must also be simulated to achieve damage conditions similar to fusion reactors. Superimposing displacement damage and helium production effects may be the only simulation method which, coupled with theoretical efforts, could lead to the required progress until a fusion reactor prototype has been constructed.

In combining results of various experimental procedures, special caution must be taken in interpreting the results. Helium atoms interact with the fundamental defects affecting their migration, clustering, and growth. Helium atoms interact with both vacancies and interstitials by immobilizing vacancies and competing with self-interstitials for vacancies. Thus helium is expected to affect the microstructural evolution of the material. It is for this reason that different helium introduction techniques will lead to different and

sometimes seemingly contradictory results. Theoretical efforts play an essential role in understanding and interpreting experimental findings and are meant to compliment experimental findings. In the following, we will discuss the advantages and disadvantages of various damage simulation facilities and experimental proceedures.

4.1. Fission Reactors

Because the displacement rates of fission and fusion reactors are similar (see Table II), fission reactors are one of the most important test facilities for fusion materials. The following is a list of some fission test reactors:

- HFIR - High Flux Isotope Reactor (ORNL)
- EBR-II - Experimental Breeder Reactor II (Idaho Falls)
- ORR - Oak Ridge Research Reactor (ORNL)
- BR2 - Belgium Reactor 2 (SCK/CEN Mol)
- PFR - Prototype Fast Reactor (Dounreay)

Gabriel et al. [18] have calculated the irradiation response of materials (Fig. 4) using fission reactor neutron spectra. Figure 4 shows the helium production and displacement damage in Ni-containing austenitic steels in various reactor maximum flux positions. The full dots of Fig. 4 show attainable values after one year of irradiation assuming a 100% plant duty factor. This is a good example of the time involved in performing experiments. Figure 4 also shows displacement and helium production levels for α-implantation and tritium decay experiments

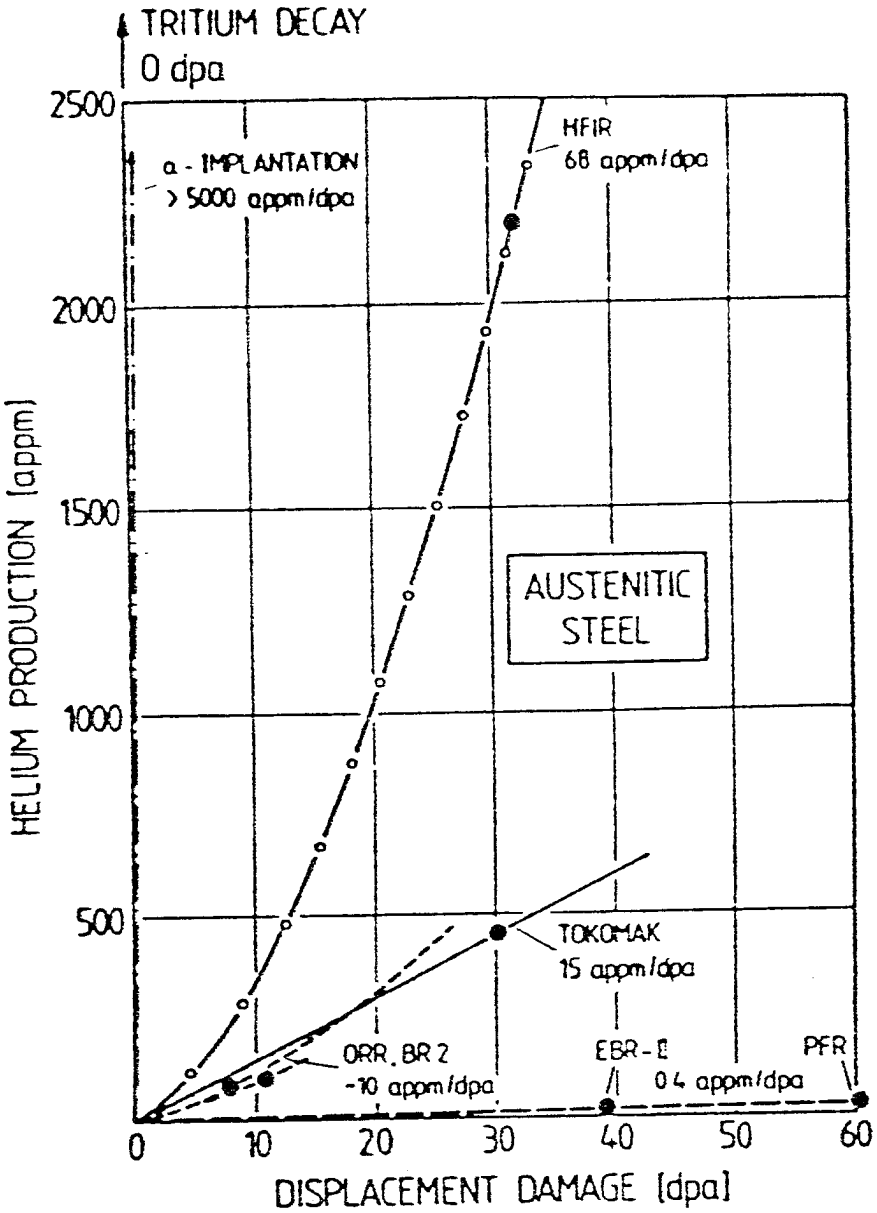

Fig. 4. Helium production in austenitic steel as a function of displacement damage for various fast fission test reactors at the position of maximum flux [18].

(see Sects. 2.2. and 2.3, respectively). Figure 5 shows the same relations for ferritic steels. It is to be noted that while He/dpa ratios typical of fusion reactors are achievable for austenitic steels (e.g., ORR), this is not possible for ferritics because of the lack of nickel.

The following are advantages of fission reactors:

- Ni has a thermal n,α cross section of several b [Eq. (4)]. Therefore in austenitic steels (Ni ≈ 18%) high He/dpa ratios can be achieved for a mixed neutron spectra. (See Figs. 4 and 5.)
- In principle, in-pile tests are possible.
- The large test volume available in most material test reactors allows the study of irradiation effects on bulk specimens in addition to surface and foil experiments.
- During the development of fast breeder materials, extensive experience has been gathered which can be utilized to set up experiments and to perform in-pile and post-irradiation testings.

The following are disadvantages of fission reactors:

- The main drawback in using fission reactors to simulate fusion is the low He/dpa ratio of fission reactors for most materials. Unless Ni is used (see Figs. 4 and 5), the He/dpa ratio of fission devices is generally a factor of 40 to 70 lower than for fusion neutrons.

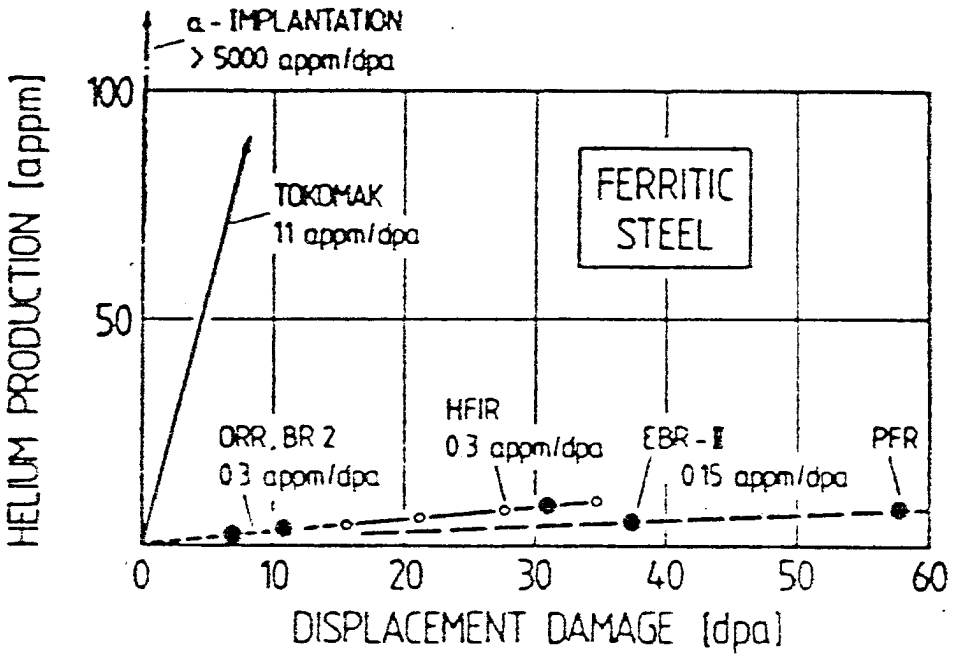

Fig. 5. Helium production in ferritic steel as a function of displacement damage for various fast fission test reactors (Gabriel [18]).

- Some concepts of fusion devices such as ICFRs, and possibly early tokamaks, are pulsed systems (see Table II). This mode of operation cannot be duplicated readily in fission reactors.

- Irradiation experiments in fission reactors are time consuming (see Figs. 4 and 5) and expensive. In-pile experiments are complicated and difficult to perform.

- An additional complication is the high radioactivity of fission reactor irradiated specimens. Post-irradiation experiments are therefore difficult and are performed in hot cells.

4.2. High-Energy α-Implantation

With the use of a cyclotron, α-particles can be introduced into a specimen with energies ranging from several to 100 MeV. Figure 6 shows the dependence of penetration range and number of defects produced as a function of α-particle energy. The number of defects produced is fairly insensitive to the starting energy of the α-particles. But, since the range is energy dependent, a rather uniform He/dpa ratio can be achieved throughout the specimen up to a depth of several 100 μm (Fig. 6). This is very significant for mechanical property measurements [19].

The following are advantages of α-implantation techniques:

- High helium production rates make α implantation via cyclotron a fast experimental procedure. Rates up to 100 appm/hr can be achieved.

- Helium production rates are not test material dependent.

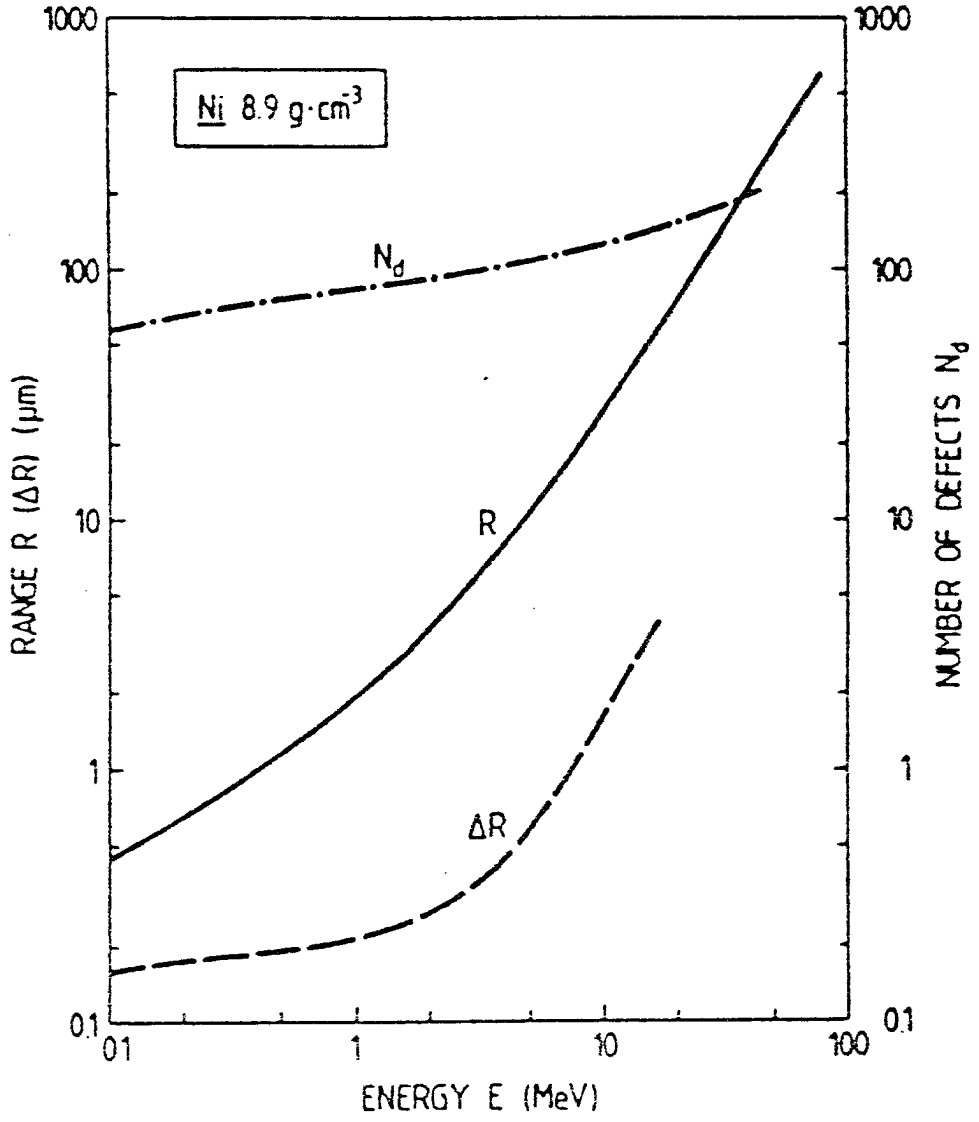

Fig. 6. Number of Frenkel pairs N_d, range R, range width ΔR distribution for α-particles in Ni as a function of energy (Ullmaier [17]).

- A homogeneous helium concentration can be achieved by α-particle energy control.

- In-beam experiments are simple to perform.

- The pulsed nature of some fusion devices can easily be simulated by beam breakers.

- α-implantation induces only small radioactivity therefore hot cells are not required for experiments.

The following are disadvantages of the α-implantation techniques:

- The main drawback of α-implantation facilities is the very large He/dpa ratio compared to fusion (see Figs. 4 and 5; 100 times higher). Thus the combined effects of displacement damage and helium production can not be investigated for fusion regimes of He/dpa ratios.

- The maximum range of implantation is in the neighborhood of a few hundred μm (Fig. 6). This limits the thickness of the specimen being tested. Therefore fracture mechanics experiments cannot be performed.

4.3. High Energy Neutron Sources

The best simulation of fusion environments can be achieved by using high energy (14 MeV) neutrons produced by accelerators. One such neutron source is the Rotating Target Neutron Source (RTNS-II) at Lawrence

Livermore Laboratory. However, the biggest problem is the low peak flux of 1.3×10^{17} n $\cdot$ m^{-2} $\cdot$ s^{-1} of 14 MeV neutrons. (Fusion is typically $\sim 2 \times 10^{18}$ n $\cdot$ m^{-2} $\cdot$ s^{-1} 14 MeV neutron flux). This low flux does not permit production of fusion-relevant damage levels in reasonable times. For this reason new facilities are being designed to increase the intensity of the neutron source. One such design is the stripping neutron source FMIT (Fusion Material Irradiation Test facility [20,21]).

The following are advantages and disadvantages of high energy neutron sources:

- The neutron spectrum can be tailored to produce a He/dpa ratio closely resembling that of fusion at 14 MeV.
- The He/dpa ratio is not heavily dependent on the material.
- Peak neutron fluxes above 10^{19} n $\cdot$ m^{-2} $\cdot$ s^{-1} can be achieved (FMIT [21]).
- In-beam experiments and testings can be performed.
- The capital cost for the construction of FMIT is expected to be in the 150 to 200-million-dollar range. This cost can be prohibitive. Fundamental understanding of radiation effects through modeling and existing facilities may provide an alternative.

4.4. Other Helium Implantation Techniques

4.4.1. Boron doping [22]. The thermal n,α-reaction of boron [Eq. (3)] has a 4010 b cross section. Therefore, by doping a material with boron and then exposing it to thermal neutrons, high helium generation rates can be achieved. The main disadvantage is the low overall defect production in thermal reactors. Furthermore, the final helium concentration is limited by the amount of ^{10}B doping.

Since doping can affect material properties, the doping concentration cannot be increased beyond certain limits. Furthermore, boron tends to segregate into the grain boundaries which makes uniform helium production very difficult.

4.4.2. Tritium trick [23-25]. Tritium has high diffusivity and solubility in metals and alloys. It decays with a half life of 12.3 years. Thus, uniform helium generation rates can be produced in any size specimen in reasonably short time periods. The main disadvantage is, of course, the absence of displacement damage because of the low recoil energy associated with the β-decay of tritium.

4.4.3. Heavy-ion beam simulation [26,27]. The main disadvantage of α-implantation is the low displacement production. This can be alleviated to some degree by using a heavy-ion beam simultaneously with the α-particle beam on the specimen. The main drawback is the relatively short range of heavy ions (< 1 μm).

Therefore, dual-beam irradiations are used mainly to study the effect of helium on swelling. Because of the short range of the heavy ions, other mechanical property changes caused by helium cannot be investigated.

4.4.4. Proton and deuteron damage simulation [28]. Cyclotrons can be used to bombard the specimen with protons or deuterons with energies between 5 and 20 MeV. Reaction rates of p,α or d,α can be controlled by varying the p and d energies and thus fusion-relevant He/dpa ratios can be achieved in many materials. The biggest disadvantage lies in the limited beam intensity. Furthermore, the excessive heat produced during bombardment must be constantly removed; otherwise annealing of radiation effects will distort displacement damage and helium production effects. The low beam intensity would require long-term continuous bombardment periods in order to study accumulating helium and damage-level effects. Cyclotrons can not be operated for long enough periods. Therefore, these experiments are mainly used to study the effects of helium production rates and radiation damage rates.

5. HELIUM RETENTION AND RELEASE

5.1. Experimental Findings on Atomistic Helium Retention and Release

As pointed out in the previous section, helium can be introduced into the lattice by various means, such as cyclotron implantations of α-particles at various energies or by forming metal tritides thus supplying He^3 by the decay of tritium.

After helium has been introduced to desired specifications (concentration, temperature, and uniformity), the diffusion of He^4 or He^3 can be studied at various temperatures by measuring helium release rates. Helium migration has also been studied by using transmission electron microscopy (TEM) on thin films, or by electrical resistivity measurements [29,30]. In the following, we summarize important experimental results on helium retention and release.

Cost et al. [29] used 46 MeV α-particles on film specimens of purified Aℓ (T_m = 660°C, fcc-crystal structure). They irradiated Aℓ at 60°C up to helium concentrations of 50 appm. The experimental observation method used was electric resistivity measurements performed at half-hour isochronal anneals up to 450°C.

Excess resistivity is attributed to atomic helium at temperatures above room temperature because vacancies and interstitials anneal out at low temperatures (< 23°C) in pure aluminum. As temperature was increased, resistivity decreased sharply around 350°C. This would indicate that helium remains atomistic up to ~ 350°C. TEM observations confirmed bubble formation at ~ 350°C.

Bauer et al. [31] also used α-particle bombardment as the helium introduction technique. They used 300 keV (low damage) α-particles at very low implantation temperatures of -180°C (low thermal vacancy concentration) on high purity Ni (T_m = 1455°C, fcc-crystal structure). They used helium release reasurements by mass spectroscopy for 20-min isochronal anneals between 0° to 1250°C and a linear heatup rate of 10°C/min from -180° to 700°C. They found a strong dependence of release rates on helium concentration levels. For helium concentrations up to

~ 1000 appm, they found that increased annealing temperatures are required to achieve release. Beyond 1000 appm, the anneal temperatures dropped with increasing concentrations until about 400,000 appm when release occurs spontaneously at 23°C. For linear heatups, they measured very little helium release for helium concentrations up to ~ 10,000 appm. At 100,000 appm a very substantial release was measured. It could be argued that bubbles account for helium until ~ 10,000 appm, and that beyond 100,000 appm an interconnecting bubble network can cause high release rates.

Barnes [30] and Bauer [31] performed similar experiments on copper (T_m = 1083°C, fcc-crystal structure). Here they used a 38 MeV α-particle beam and irradiated Cu foils at 250°C to helium concentration levels of 1000 appm. They used TEM during annealing with ~ 100 keV electron-beam heating pulses at 700° to 800°C. During the early stages of annealing they found large numbers of small bubbles. TEM allowed them to distinguish between grain boundary and matrix bubbles. With annealing, they found grain boundary bubbles to be larger than matrix bubbles. Furthermore, grain boundary bubbles were surrounded by denuded zones ~ 3000 Å wide which suggested bubble coalescence on grain boundaries. Their measurements showed a conservation of total bubble surface area as coalescence occured. They observed bubble migration in steep temperature gradients, and showed migration velocities to be inversely proportional to bubble size (~ 1000 Å/sec for R ≈ 350 Å bubbles). This velocity was suggestive of a surface diffusion mechanism. Another important observation was the lack of bubble shrinkage. This pointed to the high insolubility of helium in the matrix. Therefore, bubbles do

not grow by absorbing helium atoms dissolved from other bubbles but only by bubble coalescence. Also, bubbles attached to dislocation lines did not shrink. So, bubbles did not lose helium to dislocation lines along which single-helium atom migration can be very fast.

Several authors [32-34] have used metal tritides to study helium retention and release in metals. Bowman [32] used LiT, allowing helium levels of 0 to 66,000 appm via tritium decay at room temperature (23°C). They used nuclear magnetic resonance (NMR) as the observation method at 23°, 75°, and 100°C. They found that at room temperature, practically all helium was retained up to 66,000 appm. They did not observe atomistic helium, but found that all helium was inside clusters. An increase in temperature reduced the amount of helium retained in bubbles. After one year of decay the helium concentration level had reached ~ 83,000 appm resulting in bubbles of r ≈ 50 Å at 23°C and r ≈ 500 Å at 100°C.

Perkins et al. [33] used ScT_2 (scandium-tritium solid solution) and TiT_2 compounds. They allowed helium levels to reach ~ 320,000 appm at room temperature. He^3 release was measured by pressure gauge and mass spectroscopy on ScT_2 and by NMR on TiT_2. In ScT_2, helium release was measured at 23°C; it was found that up to ~ 200,000 appm, all helium was retained. Above this level, it was released at generation rates. In TiT_2, this release occured above ~ 320,000 appm.

Similar experiments performed on UT_3 [32,34] showed a retention saturation at ~ 116,000 appm of helium. These saturation levels may indicate (1) that the produced He^3 could produce its own trapping sites

and (2) that bubble pressures can reach rather high values in order to accommodate the He^3 atoms being produced.

In general, these experiments all point to very high helium retention levels (> 100,000 appm), and that significant release does not occur until ~ 0.45 T/T_m in metals. Beyond ~ 10,000 appm of helium, the release of helium occurs at lower temperatures as the helium concentration increases.

Furthermore, under aging (no continuous defect or helium production) bubbles were found not to shrink; instead they only grew or coalesced [35-38]. Bubbles formed first at grain boundaries and then in the matrix. Grain boundary bubbles were found to be larger [39,40].

5.2. Experimental Findings on Helium Retention in Cavities

Generally, cavities are classified as 3-D defects. They consist of vacancies and gas atoms. We refer to a bubble as a cavity that contains enough gas atoms to be stabilized against thermal shrinkage below temperatures of ~ 0.75 T/T_m. Voids are those cavities that contain a small number of gas atoms (sufficient to stabilize nucleation) and they shrink or grow by vacancy emission or capture, respectively.

Bubbles can exist on grain boundaries, dislocations, precipitates, or in the matrix. Grain boundaries are assumed to be infinite sinks for vacancies and interstitials. This feature of grain boundaries prevents void formation along grain boundaries. This is an important point for experimentalists investigating cavities, since they can immediately distinguish between bubbles and voids along grain boundaries.

One of the most widely used experimental methods to gain information on the cavity size distribution is aging of helium pre-injected alloys. Using a TEM, samples were investigated at certain times or temperature intervals.

The first comprehensive studies of helium bubbles in copper were conducted by Barnes and Masey [30,41] in the early 1960s; Oela and Russell [42,43] followed in the mid-1960s. Barnes and Masey preinjected copper by ion-irradiation; Oela and Russell used neutron-irradiated Cu-B alloys (see Sect. 4.4 for boron characteristics).

More recently Smidt and Preper [44], and Rothaut and Schroeder [45] have used helium pre-injected-and-aged 316 stainless steel to study helium bubble behavior. As an example, Fig. 7 shows the temperature dependence of bubble sizes and concentrations. This figure is from more recent work by Mazey and Francis [46] who used ion-irradiated 316 stainless steel to reach 100 appm of helium before aging the samples. The same experiment was performed at various pre-injected helium levels of 1, 10, 100, and 1000 appm. Bubbles were found starting at 570°C, for helium levels of 10 to 1000 appm. Above 750°C, bubbles were observed at all helium levels.

Figure 7 clearly demonstrates a decrease in bubble concentration and an increase of bubble radius with annealing temperatures, indicating a bubble coalescence mechanism via Brownian motion through the matrix. An interesting observation by Mazey and Francis was that when the amount of pre-injected helium was raised from 100 to 1000 appm, little change in bubble sizes was found, but the bubble concentration increased by a factor of up to ~ 100. Consistent with the Mazey and Francis data,

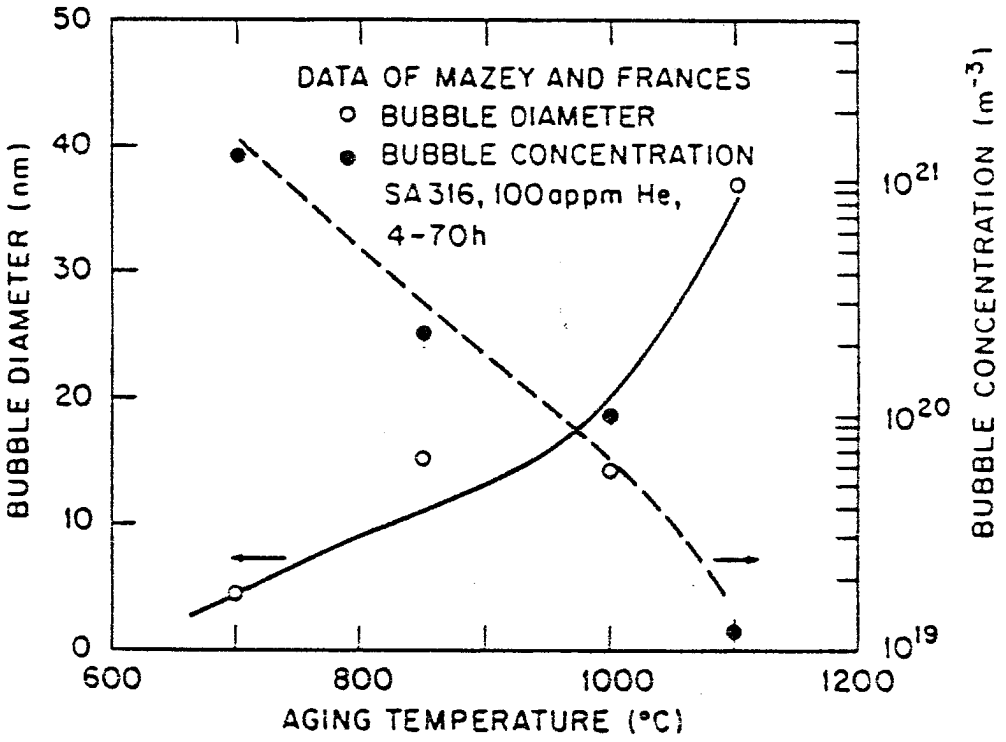

Fig. 7. Bubble sizes and concentrations as a function of annealing temperature (Mazey and Francis [46]).

Maziasz has recently reported similar results for helium pre-injected-and-aged SA-316 stainless steel [56]. This could be explained by the fact that as α-particles come to rest inside the matrix, they produce their own defects (vacancies and interstitials). Therefore, the higher the implantation rate the more trap sites are produced. Thus, at higher helium levels larger bubble concentrations are observed. This clearly suggests that radiation damage plays as crucial a part in bubble size evolution as do the helium levels. Therefore, a separation of these two phenomena can be very misleading. This is one reason why one of the major goals of this thesis it to develop a tool for the analysis of both radiation damage and helium production simultaneously.

Besides helium pre-injection, two techniques to study helium bubble-size evolution commonly used are exposure of alloys to (1) thermal reactors and (2) fast fission reactors. (See Sect. 4.1).

Rowcliffe [47,48] irradiated austenitic stainless steel at 650°C, allowing a helium buildup to ~ 50 appm from ^{10}B reactions. No observable helium bubbles were found prior to post-irradiation annealing experiments performed at higher temperatures. Similar findings were recorded by various other experimentalists (Bloom [49], Brager [50], Robbins [51]). These findings can be explained by the presence of high trap concentrations produced by radiation damage. These traps are able to absorb helium readily and thus disperse the produced helium finely throughout the matrix. Only at higher temperatures will these HVCs either coalesce or become unstable, leading to the growth of stable bubbles.

During the 1970s, the Fast Breeder Reactor (FBR) was extensively used to study voids in the context of swelling behavior of alloys. Nevertheless bubble formation, together with voids, was detected and recorded at temperatures above 625°C in SA-316 stainless steel irradiated in EBR-II by Brager and Straalsund [52]. Post-irradiation anneal experiments of FBR-irradiated stainless steel clearly showed a shrinkage of voids coinciding with the formation of small bubbles [53,55].

Recently Maziasz did an extensive investigation of bubble and void formation in stainless steel using EBR-II and HFIR [56]. Using TEM, he distinguished between voids and bubbles forming in the matrix, on precipitates, or along dislocations. SA-316 stainless steel was irradiated from 500° to 630°C up to doses of 36 dpa. Figure 8 is a summary of void and bubble occurrence as a function of temperature and fluence. Precipitate-associated voids were found at both temperatures and fluences, while matrix voids were found only at higher temperatues. At 625° to 630°C, bubbles were present at low and high fluences; but at lower temperatures of 500° to 525°C, bubbles formed only after high fluences of 31 dpa. It is interesting to note that at ~ 630°C, both bubble and void nucleation seem to stop after about 10 dpa; while at the lower temperatures (~ 500°C) bubble and void nucleation do not saturate.

Maziasz' size distribution analysis for both intermediate and high temperatures revealed even more detail. At intermediate temperatures of 500° to 520°C, a fine, dense, and uniform dispersion of bubbles after 31 dpa was observed (Fig. 9). Previously, bubbles were not observed under these conditions below ~ 600°C [52,57]. The bubbles found at higher temperatures (625° to 630°C) were located initially along

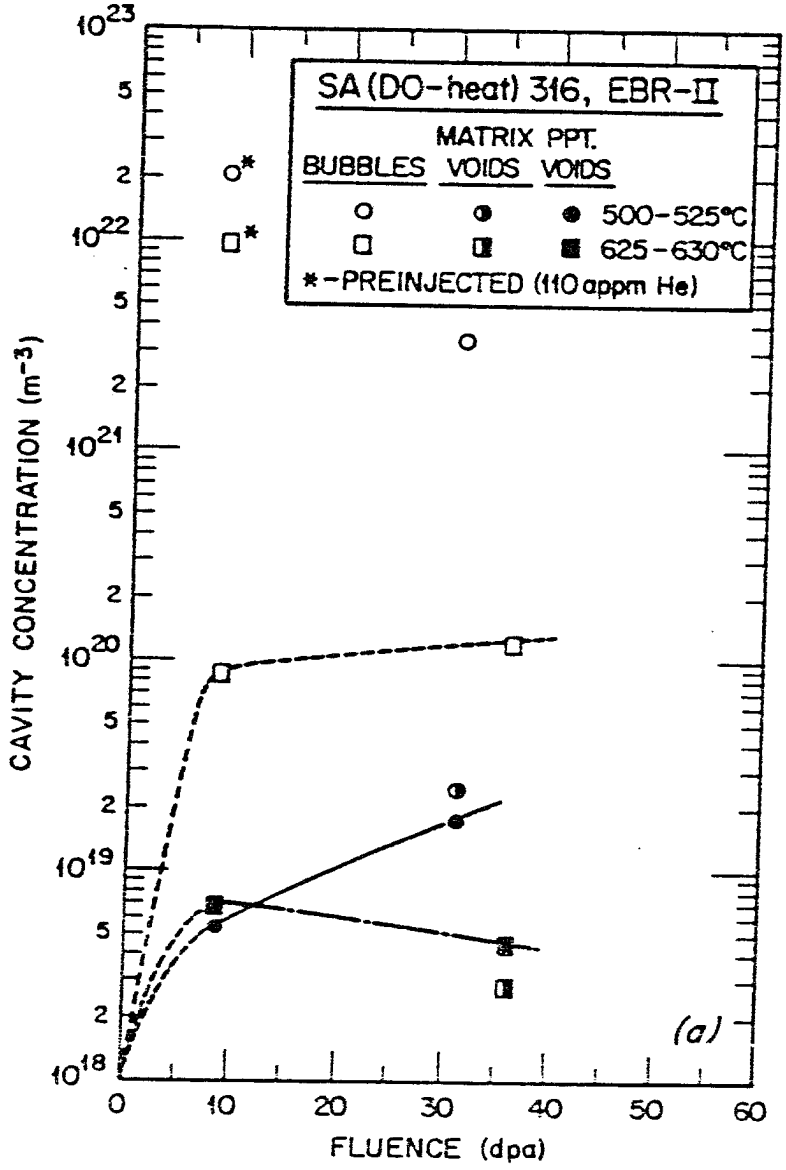

Fig. 8. Cavity microstructural evolution in EBR-II-irradiated SA-316 stainless steel at 500°-630°C showing bubbles, matrix voids, and precipitate-associated void concentrations as a function of fluence (after Maziasz [56]). (8.4 to 36 dpa corresponds to a helium production level of 5 to 22 appm.)

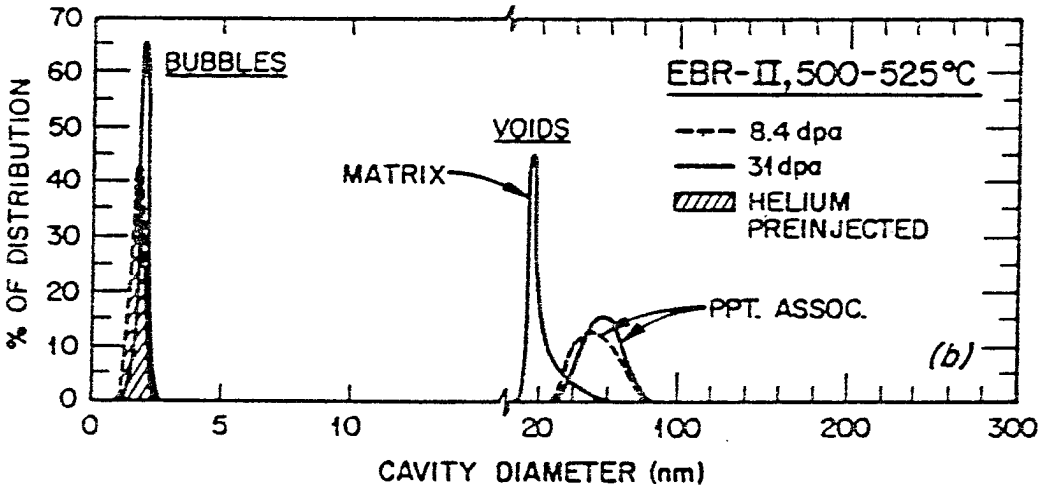

Fig. 9. Size distributions of voids and bubbles at 500°-520°C for EBR-II-irradiated SA (DO-heat) 316 stainless steel (after Maziasz [56]).

dislocation lines for low fluences (8.1 dpa) but as fluence was increased they appeared in the matrix as well (Fig. 10). At higher temperatures another interesting bubble size distribution was observed which was not found at intermediate irradiation temperatures: As the fluence increased the bubble size distribution broadened. This indicates that bubble growth is also accompanied by a small additional nucleation.

Maziasz also investigated the location of various bubbles. He found bubbles in trails near dislocations with a size gradient of the smallest ones nearest to dislocations. It was suggested that bubbles were formed at dislocations and then released as the dislocation moved through the matrix.

In addition to EBR-II, Maziasz also used HIFR to examine bubble and void evolution in SA-316 stainless steel. Because of the nature of void and bubble evolution characteristics, this set of experiments was conducted at different temperature ranges. Also, the HFIR facilities allowed irradiations up to 68.5 dpa. Again, Maziasz distinguished between voids and bubbles forming in the matrix, the grain boundaries, or on precipitates. Figure 11 shows cavity characters plotted as a function of temperature and fluence.

Cavities (voids or bubbles) formed above 425°C. Although voids were only present at 425° to 450°C for fluences < 20 dpa, bubbles were present over the entire range of conditions except for temperatures between 580° and 640°C and fluences between 47 and 64 dpa. At temperatures between 425° and 450°C and low fluences of ~9 to 14 dpa, many fine bubbles were present with an average diameter of ~ 2nm. Under

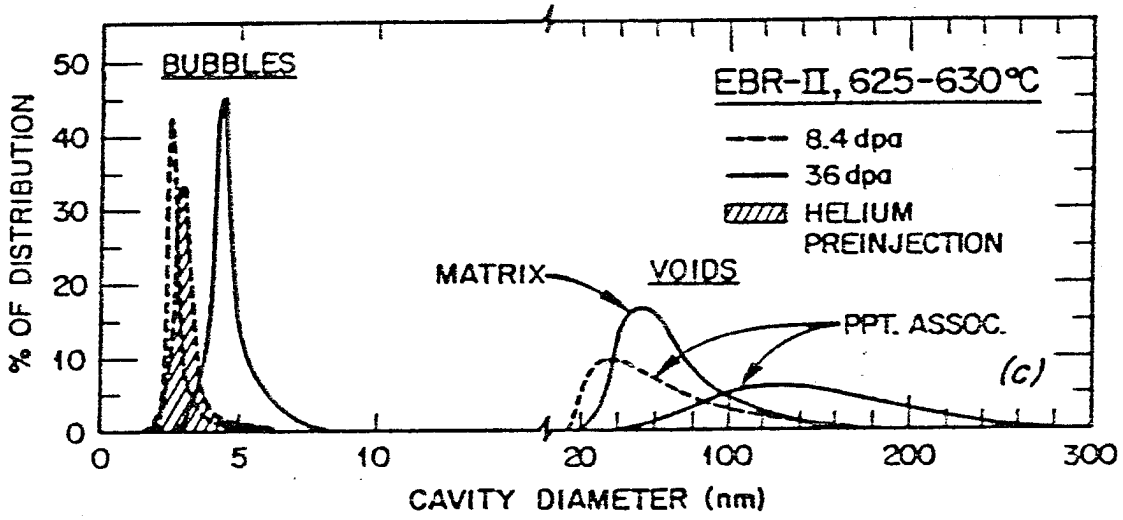

Fig. 10. Size distribution of voids and bubbles at 625°-630°C for EBR-II-irradiated SA (D0-heat) 316 stainless steel (after Maziasz [56]).

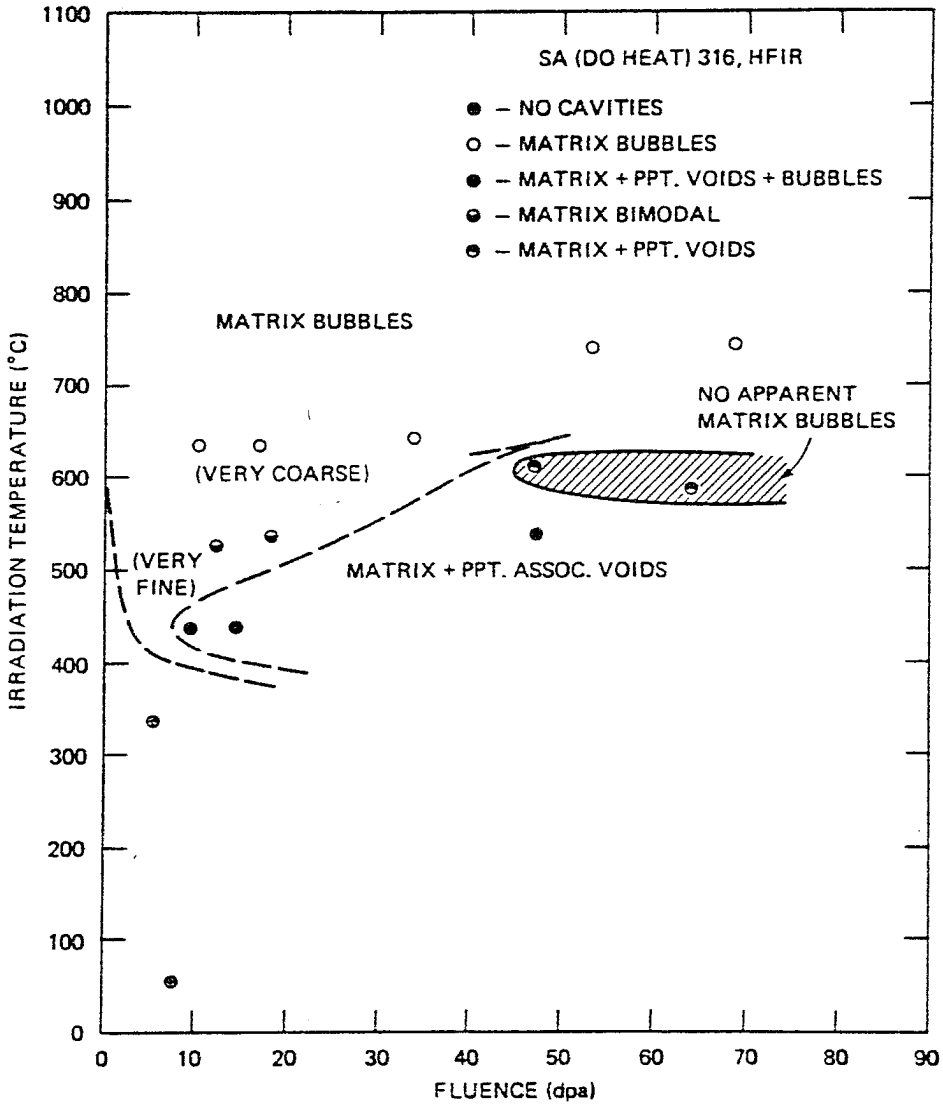

Fig. 11. Cavity character plotted as functions of temperatures and fluence for HFIR-irradiated SA (DO-heat) 316 stainless steel (after Maziasz [56]).

these conditions, swelling peaked as matrix precipitate-associated voids grew [Fig. 12(a)].

At the higher irradiation temperatures of 515° to 640°C, void formation was delayed and the cavities formed were judged to be bubbles. Between 515° and 550°C, a bi-modal bubble distribution developed [Fig. 12(b)]. With increasing fluence, these bi-modals grew and coarsened.

Around 600° to 640°C, bubbles nucleated at an almost single-size population with little growth at low fluences (~ 10 to 18 dpa)[see Fig. 13(a)]. Maziasz pointed out that between 515° and 640°C, all bubbles eventually convert to matrix- and precipitate-associated voids as fluence reached 47 dpa.

However, at 730° to 755°C all cavities reported at high fluences (<53 dpa) were found to be large matrix and grain boundary bubbles [see Fig. 13(b)]. Thus, under these high fluence conditions void swelling had peaked at 500° to 650°C. Figure 14 shows the various cavity characteristics found in HFIR-irradiated SA-316 stainless steel [56].

Figure 15 compares the fluence dependence of cavity concentrations for SA-316 stainless steel irradiated in EBR-II and HFIR at 500° to 550°C. Maziasz pointed out the appearance of dense populations of very fine matrix bubbles (~ 2 nm diam) in both reactors at higher fluences, while at lower fluences such bubbles were not observed. Furthermore there were about 100 times more bubbles than voids in both reactors and about 30 to 40 times more bubbles in HFIR than EBR-II (see Fig. 15). The enhanced bubble nucleation in HFIR versus EBR-II was related to the higher helium production rate in HFIR. It is this early bubble

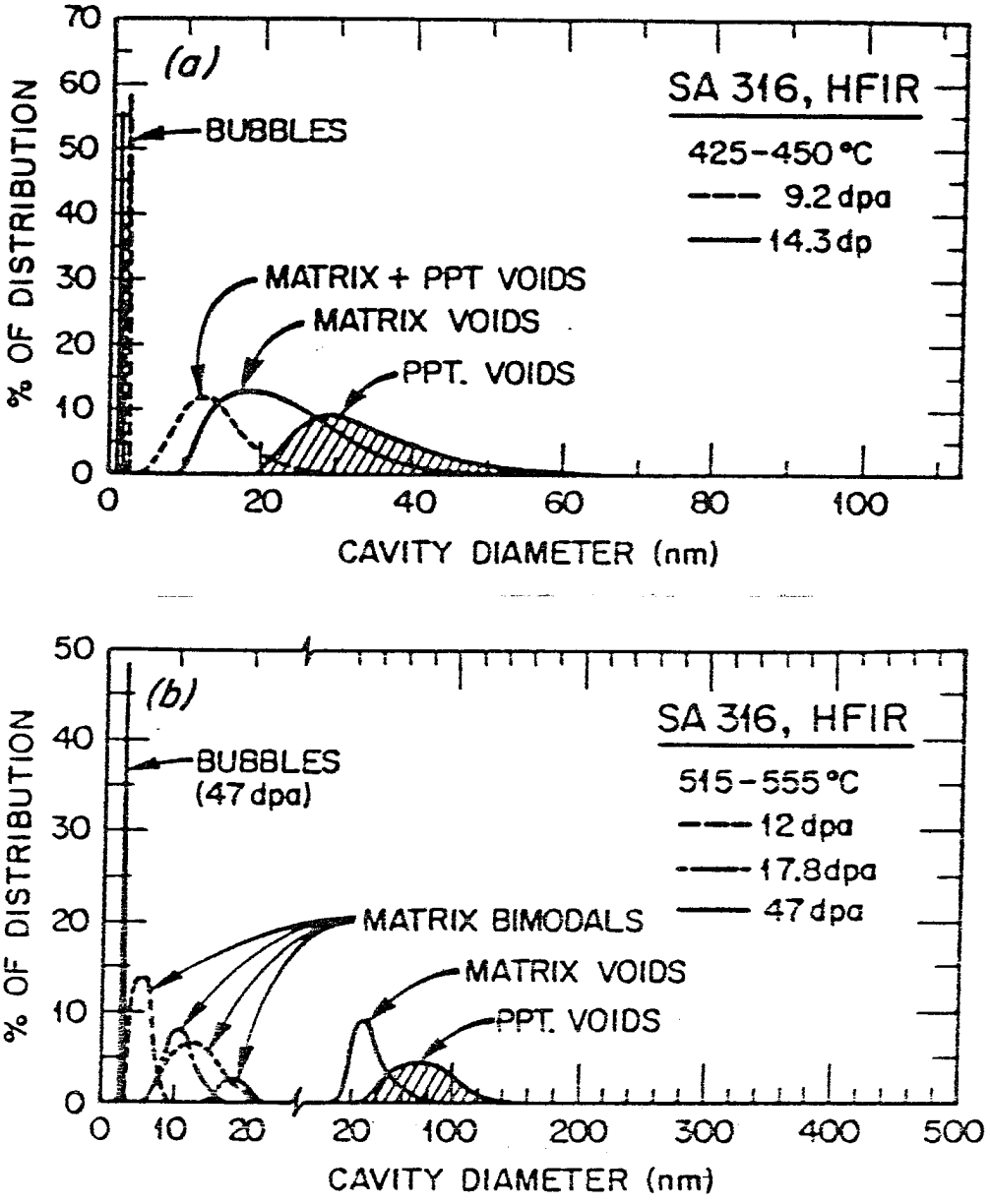

Fig. 12. Cavity size and distribution evolution as a function of fluence for SA (DO-heat) 316 stainless steel in HFIR at (a) 425°-450°C and (b) 515°-555°C (after Maziasz [56]). (A damage of 5.3-68.5 dpa corresponds to a helium production level of 180-4140 appm of He.)

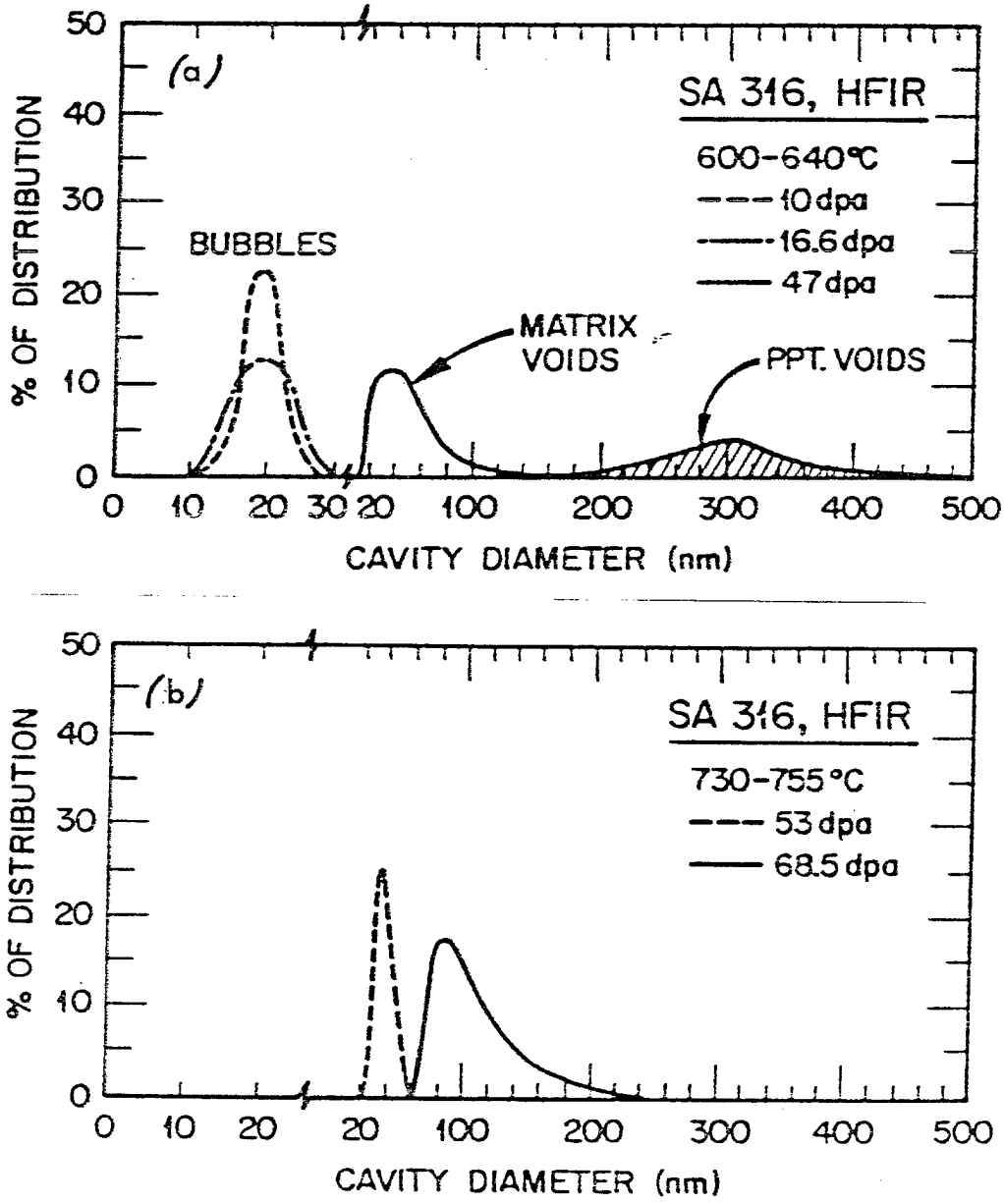

Fig. 13. Cavity size and distribution evolution as a function of fluence for SA (DO-heat) 316 stainless steel in HFIR at (a) 600°-640°C and (b) 730°-755°C (after Maziasz [56]).

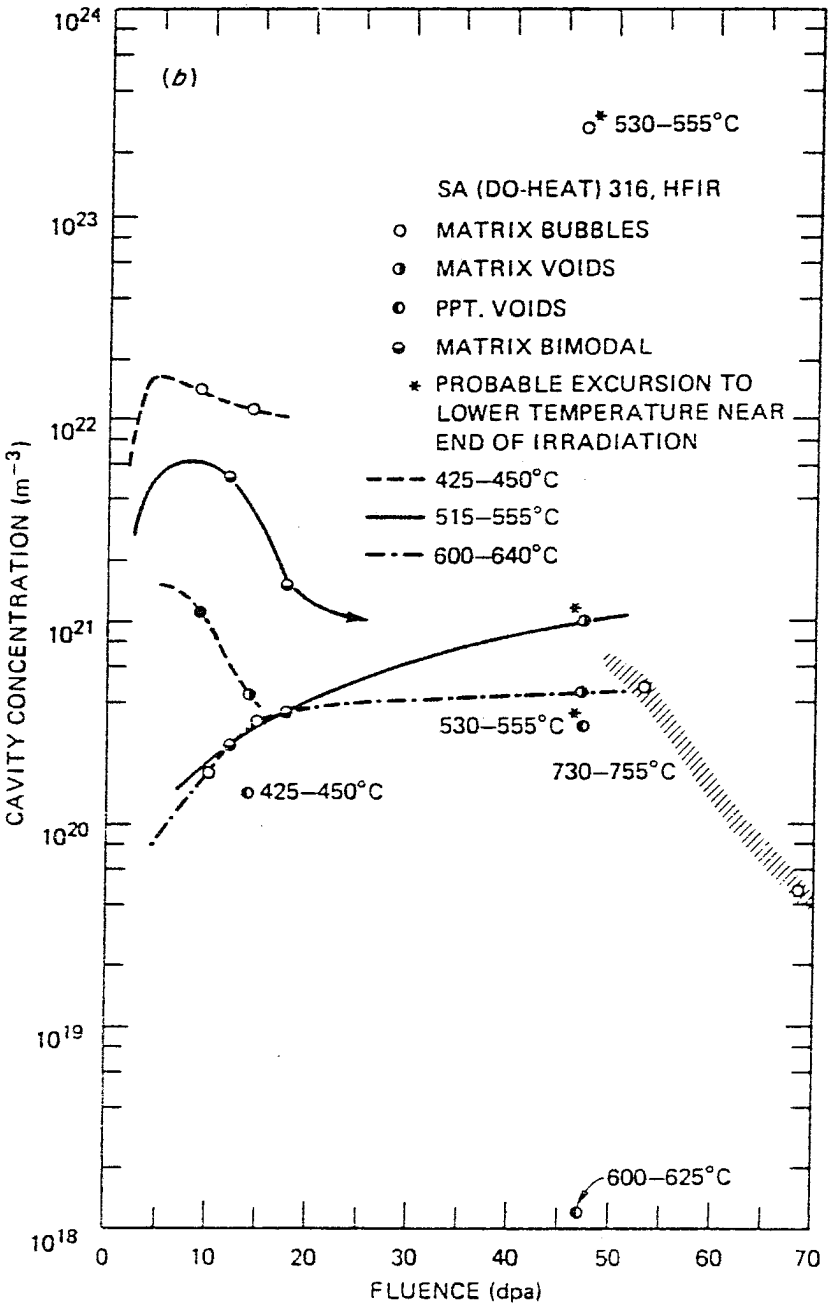

Fig. 14. Plot of concentrations of various cavity components found in HFIR-irradiated SA-316 stainless steel as a function of fluence (after Maziasz [56]).

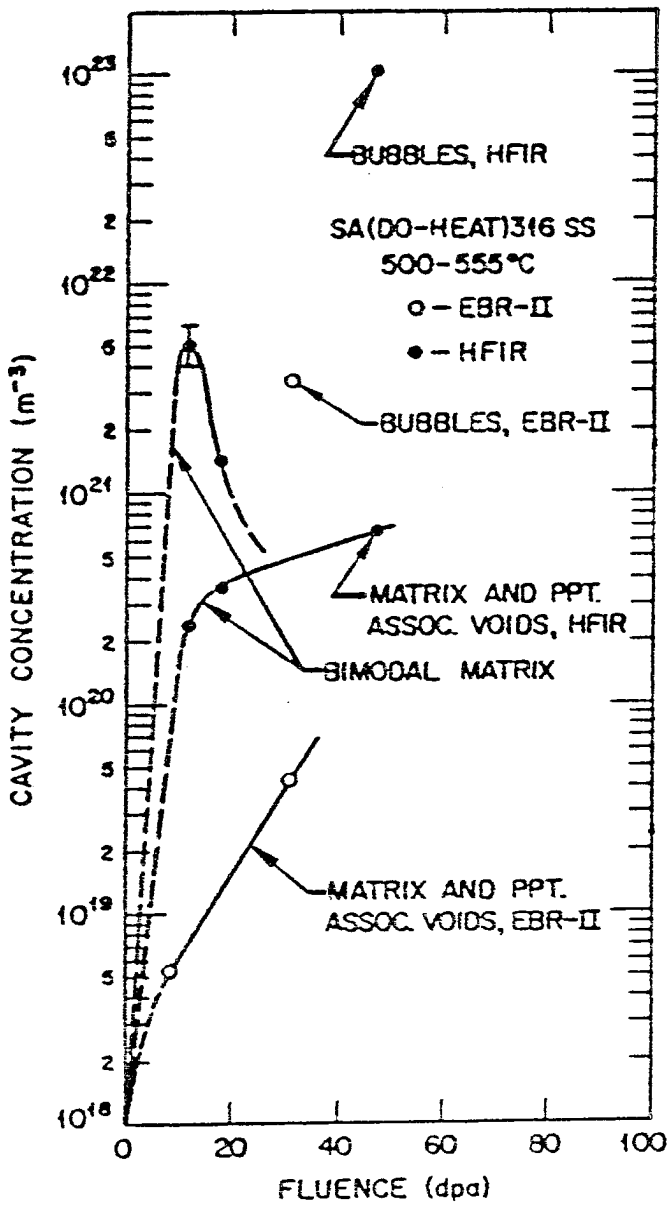

Fig. 15. Comparison of fluence dependence of cavity concentration for SA-316 stainless steel irradiated in HFIR and EBR-II at 500°-550°C (after Maziasz [56]).

nucleation process in HFIR that is suspected to suppress early void formation in HFIR relative to EBR-II. [In EBR-II specimens voids form starting at 31 dpa while in HFIR their formation starts above ~ 47 dpa at 515° to 550°C (see Fig. 12b).]

Another important finding of Maziasz was the lack of precipitate-assisted void formation, despite the many coarse precipitate particles present in the HFIR samples. In HFIR-irradiated samples, bubbles that became unstable converted to matrix voids more readily than in EBR-II samples. Thus, swelling was enhanced in HFIR, while in EBR-II voids increased in size and decreased in concentration with increasing temperatures (see Figs. 9 and 10).

In summary, Maziasz [56] finds that the HFIR data show delayed-followed-by-enhanced void swelling at 500° to 650°C compared to EBR-II experiments. He concludes that the presence of helium changes void swelling behavior because of increased bubble nucleation. The fine distribution of small bubbles affects the balance between dislocation and cavity sink strengths. The net effect is that helium extends cavity swelling to higher temperatures beyond the normal swelling cutoff temperatures present in thermal reactor experiments.

REFERENCES

[1] D. R. Harries, J. Br. Nucl. Energy Soc., 5 (1966) 74.

[2] R. S. Barnes, Nature (London), 206 (1965) 1307.

[3] G. L. Kulcinski, D. G. Coran and M. A. Abdou, in Properties of Reactor Structural Alloys After Neutron and Particle Irradiation, Am. Soc. Test. Mater., Richland, WA, 1975, Spec. Tech. Publ. 570, p. 329.

[4] J. Halil and G. L. Kulcinski, in Radiation Effects and Tritium Technology for Fusion Reactors (Proc. Intl. Conf., Gatlinburg, 1975) USERDA Report CONF-750989, Vol. I (1976) 437.

[5] T. O. Hunter and G. L. Kulcinski, J. Nucl. Mater., 76 (1978) 383.

[6] G. L. Kulcinski, ibid, 85&86 (1979) 87.

[7] R. Behrisch and B. M. U. Scherzer, Radiat. Eff., 78 (1983) 417.

[8] W. Bauer, K. L. Wilson, C. L. Bisson, L. G. Haggmark and R. J. Goldston, J. Nucl. Mater., 76&77 (1978) 396.

[9] B. M. U. Scherzer, in Sputtering by Particle Bombardment II, R. Behrisch, Ed. (Springer-Verlag, Berlin, 1983).

[10] R. Behrisch, M. Risch, J. Roth, and B. M. U. Scherzer in Fusion Technology (Proc. 9th Symp., Padova, 1976) (Pergamon Press, New York, 1976) p. 531.

[11] C. E. Johnson, R. G. Clemmer and G. W. Hollenberg, J. Nucl. Mater., 103&104 (1981) 547.

[12] G. W. Hollenberg, "The TRIO-01 Experiment", Nucl. Technol./Fusion, 4 (1983) 83.

[13] W. Krug with Blanket Group of KfA, in Fusion Technol. (Proc. 12th

Symp., Jülich, 1982), CEC, (Pergamon Press, Oxford, 1983) p. 643.

[14] G. L. Kulcinski, in Radiation Effects and Tritium Technology for Fusion Reactors (Proc. Intl. Conf., Gatlinburg, 1975), USERDA Report CONF-750989, Vol. I (1976) 17.

[15] T. A. Gabriel, B. L. Bishop and F. W. Wiffen, Nucl. Technol., 38 (1978) 427.

[16] M. E. Sawan, G. L. Kulcinski and N. M. Ghoniem, J. Nucl. Mater., 103&104 (1981) 109.

[17] H. Ullmaier, ibid, 24 (8), (1984) 1039.

[18] T. A. Gabriel, B. L. Bishop and F.W. Wiffen, "Calculated Irradiation Response of Materials Using Fission Reactor (HFIR, ORR and CBR-II) Neutron Spectra," Oak Ridge National Laboratory Report TM 6361 (August 1979).

[19] H. Ullmaier, J. Nucl. Mater., 108&109 (1982) 426.

[20] D. L. Johnson, F. M. Mann, J. W. Watson, J. Ullman and W. G. Wyckoff, ibid, 85&86 (1979) 467.

[21] E. W. Pottmeyes, ibid, 463.

[22] T. M. Williams, ibid, 95 (1980) 265.

[23] J. F. Remark, A. B. Johnson, Jr., H. Farrar and D. G. Atteridge, in the Proceedings of the American Nuclear Society meeting, San Francisco, Nov. 1975.

[24] R. G. Hickmann, in Technology of Controlled Nuclear Fusion (Proc. 1st Top. Meeting, San Diego, 1974) U.S. Atomic Energy Commission, CONF-740402 (1974) 535.

[25] H. Andresen and O. K. Harling, J. Nucl. Mater., 85&85 (1979) 485.

[26] M. B. Lewis, N. H. Packan, G. F. Wells and R. A. Buhl, Nucl. Instrum. Methods, 167 (1979) 233.

[27] A. Taylor, J. Wallace, D. I. Potter, D. G. Ryding and B. O. Hall, in Radiation Effects and Tritium Technology for Fusion Reactors (Proc. Intl. Conf., Gatlinburg, 1975) USERDA Report CONF-750989, Vol. I (1976) 158.

[28] H. Ullmaier, Trans. Indian Inst. Metals, 34 (1981) 324; J. Nucl. Mater., 108&109 (1982) 426.

[29] J. R. Cost and D. L. Johnson, J. Nucl. Mater., 36 (1970) 36.

[30] R. S. Barnes and D. J. Mazey, Proc. Roy. Soc. London, Ser. A, 275 (1963) 47.

[31] G. Bauer and W. D. Wilson, Radiation Induced Voids in Metals, (Proc. Intl. Conf., Albany, NY, June 9-11, 1971) AEC Symp. Series No. 26, CONF-710601, p. 230

[32] R. C. Bowman and A. Atalla, Radiation Effects and Tritium Technology For Fusion Reactors (Proc. Intl. Conf., Gatlinburg, 1975) CONF-750989, Vol. II (1976) p. 68.

[33] W. G. Perkins, W. J. Kass and L. C. Beavis, ibid., Vol. IV, p. 83.

[34] M. E. Malinowski and P. R. Coronado, ibid., p. 53.

[35] A. F. Rowcliffe, J. Nucl. Mater., 18 (1966) 60.

[36] P. J. Goodhew and S. K. Tyler, Proc. Roy. Soc. London, Ser. A, 377 (1981) 151.

[37] J. O. Smith and B. Russell, J. Nucl. Mater., 35 (1970) 137.

[38] G. K. Walker, ibid, 103&104 (1981) 1023.

[39] D. N. Braski, H. Schroeder and H. Ullmaier, ibid, 83 (1979) 265.

[40] K. Shiraishi and T. Murata, J. Nucl. Sci. Technol., 3 (1966) 466.

[41] R. S. Baines and D. J. Mazey, Philos. Mag., 5 (1960) 1247.

[42] P. Vela and B. Russell, J. Nucl. Mater., 19 (1966) 321.

[43] Ibid, p. 327.

[44] F. A. Smidt and A. G. Preper, in Properties of Reactor Structural Alloys After Neutron or Particle Irradiation, Am. Soc. Testing Mater., Richland, WA, 1971, ASTM-STP-570, p. 352.

[45] J. Rothaut and H. Schroeder, J. Nucl. Mater., 103&104 (1981) 1023.

[46] D. J. Mazey and S. Francis, in Consultant Symp. The Physics of Irradiation Produced Voids, AERE Harwell Report AERE-R-7934 (January 1975) 257.

[47] A. F. Rowcliffe, J. Nucl. Mater., 18 (1966) 60.

[48] A. F. Rowcliffe, G. J. C. Carpenter, H. F. Merrick and R. B. Nicholson, in Effects of Radiation on Structural Materials, Am. Soc. Testing Mater., Richland, WA, 1978, ASTM-STP-483, p. 161.

[49] E. E. Bloom, W. R. Martin, J. O. Stregler and J. R. Weir, J. Nucl. Mater., 22 (1967) 68.

[50] H. R. Brager and R. E. Robbins, Trans. Met. Soc. AIME, 242 (1968) 2010.

[51] H. R. Brager and J. L. Straalsund, J. Nucl. Mater., 46 (1973) 134.

[52] R. E. Robbins, ibid, 33 (1969) 101.

[53] J. J. Holmes, R. E. Robbins, J. L. Brimhall and B. Mastel, Acta Metall., 16 (1968) 955.

[54] D. I. Norris, Radiat. Eff., 14 (1972) 1.

[55] J. O. Stregler and E. E. Bloom, J. Nucl. Mater., 33 (1969) 173.

[56] P. J. Maziasz, "Effects of Helium Content on Microstructural Development in Type 316 Stainless Steel Under Neutron Irradiation," Ph.D. thesis, University of Tennessee, Knoxville (December 1984).

[57] P. J. Barton, B. L. Eyre and D. A. Stow, J. Nucl. Mater., 67 (1977) 181.

CHAPTER IV

REVIEW OF THEORETICAL TREATMENTS ON HELIUM CLUSTERING IN IRRADIATED MATERIALS

1. INTRODUCTION

The energy of solution of helium atoms in metals has been shown to be highly negative [1], indicating insolubility no matter how small the concentration. As a result, it is energetically favorable for the helium atom to become substitutional (by residing in a vacant lattice site), and for more helium atoms to precipitate out in the form of over-pressurized bubbles.

The phenomena of cavity formation in fast breeder reactor cladding and ducts, and the associated swelling and loss of dimensional stability are now well known. Typically, cavity densities of some 10^{15} cm^{-3} produce swelling of several per cent to tens of percent over the $\approx 3 \times 10^{23}$ n/cm^2 fast neutron fluences ($\sim$ 130 dpa) to which fast reactor claddings are subjected. The swelling occurs mostly in the temperature range between about 0.3 and 0.6 of the absolute melting point.

Cavities form by the agglomeration of irradiation-induced vacancies which remain after preferential absorption of self-interstitials at dislocation lines. Helium which is formed by (n,α)-transmutations, and in simulation studies may be ion implanted, often plays an important but puzzling role. In some materials, very few cavities form in the absence of helium, even after intense irradiation. In many other materials cavities form readily under a variety of irradiation conditions, even in

the absence of helium. Why some materials require helium to stabilize cavities, typically in the 10^{-6} apa (atom per atom) range, and others do not, and the reason for that particular level, can be understood by studying detailed nucleation and growth mechanisms.

Summaries of experimental observations of cavities in metals have been presented by Bement [2] and by Norris [3]. In addition, the papers in two conferences devoted to cavities [4,5] contain much detailed information pertinent to the experimental and theoretical status of the subject. Emphasis is placed on cavities formed in neutron-irradiated stainless steel. In addition to fast-neutron irradiation, cavities may be formed by bombarding metals with heavy ions (e.g., protons, carbon, and self-ions) or with electrons. The bulk of the experimental information on cavity formation in metals has been obtained by transmission electron microscopy (TEM). Most theoretical treatments, however, only predict the average cavity size, assuming that the cavity density is a specified number rather than the complete cavity distribution function.

2. CLASSICAL NUCLEATION

Cavity formation theories usually divide the overall process into distinct nucleation and growth phases. At high temperature, the cavity distribution functions tend to be very broad and to contain some very large cavities and a small proportion of small ones. This type of distribution suggests that nucleation has ceased and a constant density of cavities is in the process of growing.

Nucleation of cavities refers to the rate at which small embryos of these defect clusters appear in the solid. Once nucleated, the embryos

tend to grow and are safe from destruction. Supersaturation of the solid with point defects is a prerequisite to both nucleation and growth, but a higher supersaturation is required to force nucleation than to continue growth of existing embryos.

The most common example of nucleation is the condensation of water vapor in air. If the partial pressure of water in dust-free air is slowly increased beyond the equilibrium vapor pressure, nothing happens until the supersaturation (i.e., ratio of the partial pressure to vapor pressure) attains a value of about 5 to 6. At this point a fog, which corresponds to nucleation of small liquid droplets, appears. The supersaturation of the gas phase falls abruptly at the onset of nucleation, and the newly born droplets consume the remaining excess water vapor at a purely diffusion-limited rate until the equilibrium vapor pressure in the gas phase is attained.

Formation of cavities in solids may not be as clearly divisible into nucleation and growth phases because, in this case, generation of point defects acts to maintain the supersaturation. Nucleation of new cavities may proceed in parallel with the growth of existing ones.

Nonetheless, nucleation and growth processes have been analyzed as individual phenomena, the rates of which are functions of the point-defect supersaturations, the helium content of the solid, and the temperature.

As with the condensation of water, nucleation of cavities in metals can be classified as either homogeneous or heterogeneous. Homogeneous nucleation refers to the buildup of small clusters by chance encounters of individual point defects executing random walks in the solid. The

stability of these clusters relative to the individual point defects of which they are composed (i.e., cavities contain vacancies and helium atoms) is the driving force for nucleation.

Heterogeneous nucleation refers to the appearance of cavities on distinct structural features of the solid. In water condensation, for example, dust particles provide heterogeneous nucleation sites. In metals the heterogeneities that may accelerate cavity nucleation include existing gas-atom clusters, incoherent precipitate particles, and dislocations.

The details of the processes by which helium affects cavity nucleation were not precisely known until recently. The mechanism was simply speculated as a matter of stabilizing embryo cavities that have nucleated without the aid of gas atoms. However, it will be shown that helium is intimately involved in the nucleation process by precipitating simultaneously with vacancies to form embryo cavities that are partially gas filled. Although cavity nucleation probably occurs by a mixture of homogeneous and heterogeneous processes, each assisted by helium, only homogeneous nucleation has been treated quantitatively. Classical homogeneous nucleation of cavities in metals is not simply a matter of applying classical nucleation theory to a new system.

Classical theory, which was developed to explain liquid-droplet formation from supersaturated vapor of condensible gases, has been applied to many precipitation processes occurring in solids. However, in all nucleation problems that have been treated by classical theory, growth or shrinkage of small clusters occurs by exchange of a single species between embryos and supersaturated medium. Cavity nucleation,

however, involves the exchange of at least two species (the vacancy and its antiparticle the self-interstitial) between the cluster and the lattice. Moreover, if helium is involved in the nucleation process, three species which contribute to homogeneous nucleation must be considered in the shrinkage and enlargement processes.

The physics of cavity nucleation, particularly the role of helium, have been the subject of several theoretical papers [6-12]. The earliest theories [10,11] were for cavity nucleation by co-precipitation of vacancies and self-interstitials. Simple rate equations were derived, which of course could not reflect the influence of helium.

These early theories for cavity nucleation in a solid supersaturated with vacancies and self-interstitials were based on the assumption of high mobility of point defects between the cavity and the bulk solid. Katz and Wiedersich [8] and Russell [9] later extended the cavity nucleation theory to account for helium in the metal. They assumed that helium was immobile once it was introduced into the solid and furthermore, that any release of helium atoms from any cluster, cavity, or trap was very difficult.

So, in effect, they regarded the helium atoms as immobile nucleation sites to which vacancies and interstitials can migrate to form clusters. Consequently, nucleation in the presence of helium need not involve the simultaneous equilibration of all three species (vacancies, self-interstitials, and helium atoms). In addition to the heterogeneous nucleation paths provided by helium clusters in the metal, they [8,9] kept the homogeneous nucleation mechanism [6,7] to derive a combined

nucleation rate for cavities. All nucleation processes were assumed to be driven by the prevailing vacancy and interstitial supersaturations.

A gas-free cavity cluster can grow by capturing vacancies or emitting interstitials. Thus, the nucleation current is the difference between the rate at which clusters pass from size m to size m+1 plus the rate at which clusters of size m+1 are reduced to size m.

$$I(m \longrightarrow m+1) = \beta_v(m)N(m) - \alpha_v(m+1)N(m+1) - \beta_i(m+1)N(m+1) \quad , \tag{1}$$

where $I(m \longrightarrow m+1)$ = nucleation rate of size m+1 clusters of vacancies,

$N(m)$ = cavity number density for non-equilibrium but steady state,

$\beta_v(m)$ = rate of vacancy capture by size m cluster,

$\alpha_v(m)$ = rate of vacancy emission by size m cluster,

$\beta_i(m)$ = rate of interstitial capture by size m cluster.

Generally α_v is eliminated from Eq. (1) by the use of the principle of detailed balance or constrained equilibrium. This principle states that equilibrium is attained if the rate at which clusters of m vacancies capturing single vacancies is equal to the rate at which clusters of size m+1 emit vacancies, or

$$\beta_v(m)N^{eq}(m) = \alpha_v(m+1)N^{eq}(m+1) \quad . \tag{2}$$

Here $N^{eq}(m)$ is the equilibrium cluster distribution function of size m.

Katz and Wiedersich [8] and Russell [9] extended the homogeneous nucleation current [Eq. (1)] by accounting for the stabilizing effect of helium. They evaluated the reversible work to form a cavity embryo of m vacancies and n gas atoms [13].

Since helium is nearly insoluble in the metal, it has a natural tendency to escape from the solid to the gas space of the cavity. Therefore, we expect that work can be recovered by reversibly transferring helium from the solid to the cavity, or that this step reduces the work required for cavity formation and consequently enhances nucleation. Isothermal reversible expansion of n helium atoms of an ideal gas from pressure P_{eq} to pressure P provides a release of free energy of the amount of W:

$$W = nkT \ln\left(\frac{P_{eq}}{P}\right) \quad . \tag{3}$$

Assuming an ideal gas law and using statistical thermodynamic, P_{eq} is determined (Katz and Wiedersich [8] and Russell [9]). Thus they were able to determine the free energy of cavity formation as a function of the number of vacancies and number of gas atoms. This information allowed them to determine the heterogeneous nucleation rate which, combined with the homogeneous rate, gave the total cavity nucleation rate in the presence of helium atoms.

To include the effects of mobile inert gas and continuous helium production, a unified treatment of the nucleation process was developed by Russell [14]. The theory begins by considering cavities as characterized in a 2-D phase space (Fig. 1), where a cavity is fully

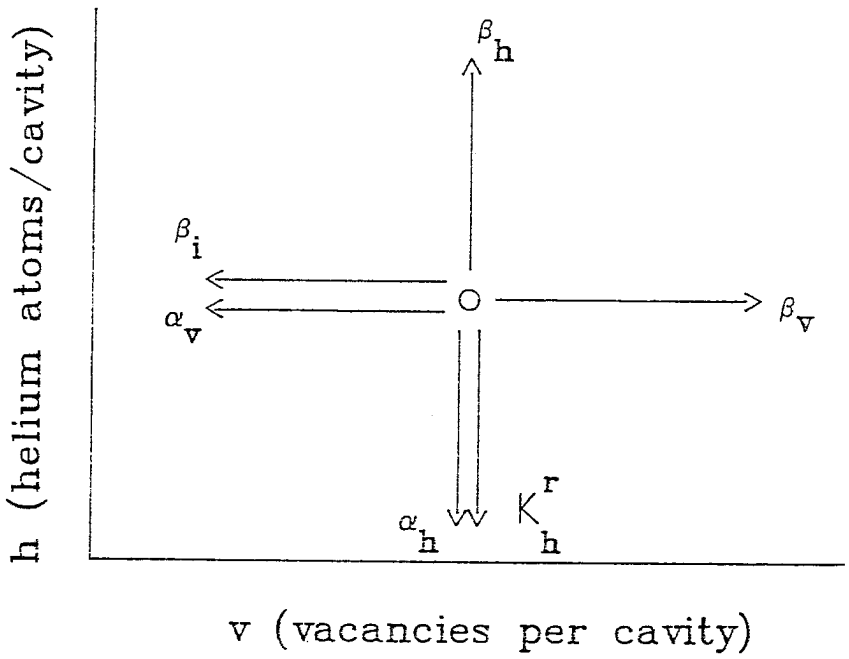

Fig. 1. Phase space for cavity nucleation, showing movements of a cavity following point-defect capture (β_v,β_i,β_h) or loss (α_v,α_i,K_h^r)(after Russell [14]).

characterized by the number of vacancies v and the number of helium atoms h that it contains. Each coordinate in the vacancy-helium phase space can be assigned a phase velocity.

The cavity may move in the positive v direction by capturing a vacancy and may move in the negative v direction by either emission of a vacancy or capture of an interstitial. Movement in the h direction can occur by capture or emission of a helium atom, or by radiation re-solution. Radiation re-solution is the process by which a gas atom is knocked back into the bulk by a primary knock-on atom. The rate of vacancy capture β_v, vacancy emission α_v, interstitial capture β_i, gas capture β_h, gas emission α_n, and gas re-solution rate K_h^r, define average velocities in this helium-vacancy phase space given by

$$\frac{dv}{dt} = \dot{v} = \beta_v v^{1/3} - \alpha_v - \beta_i v^{1/3} \quad , \tag{4}$$

$$\frac{dh}{dt} = \dot{h} = \beta_h v^{1/3} - \alpha_h - hK_h^r \quad , \tag{5}$$

where the factor $v^{1/3}[v\Omega = (4/3)\pi r^3]$ accounts for the dependence of the capture rates upon cavity size, and K_h^r is the rate per gas atom of radiation re-solution.

The emission rates are solved in terms of arrival rates by using the constrained equilibrium principle [see Eq. (2)] and by using the Gibbs free energy of formation of a cavity containing v vacancies and h helium atoms as derived earlier by Katz and Wiedersich [8] and Russell [9]:

$$\alpha_v = \beta_v v^{1/3} \exp\left(\frac{1}{kT} \frac{\partial G}{\partial v}\right) \quad , \tag{6}$$

where $\beta_v v^{1/3}$ is the arrival rate of vacancies to a cluster size v and the exponential term is a mathematical expression for the probability of emission. This is sometimes also expressed in terms of binding energies E_V^B:

$$\text{Probability of emission} = \exp\left(- E_V^B/kT\right) \quad , \tag{7}$$

where kT is the Boltzman factor; G, the free energy of formation includes the stabilizing effect of helium on the cavity. It consists of the vacancy formation energy E_v^F, the surface energy E_v^S, and the work required to compress the gas W^C:

$$\Delta G = E_v^F + E_v^S + W^C \quad , \tag{8}$$

where

$$E_v^F = -vkT \ln S_V \quad , \tag{9}$$

and

$$S_v = \frac{C_v}{C_v^{eq}} \quad . \tag{10}$$

C_v is the total vacancy concentration and C_v^{eq} is the termal vacancy equilibrium concentration. S_v is called the supersaturation of vacancies. Equation (9) is based on the principle of chemical equilibrium.

$$E_v^S = (36\ \pi\Omega^2)^{1/3}\ v^{2/3}\gamma \quad , \tag{11}$$

$$\Omega \simeq a_o^3/4 \quad , \tag{12}$$

where a_o is the lattice constant, Ω is the atomic volume, and γ is the surface tension of the solid (~ 500 ergs/cm^2 for stainless steel).

The work done in compressing the gas is given by,

$$W^e \simeq hkT \ln(h/h_{eq}) - hkT \quad , \tag{13}$$

where h_{eq} is the cavity gas content which would be in equilibrium with gas in the matrix.

Equations (4) and (5) are two first-order differential equations which lend themselves to Nodal Line analysis. This analysis emphasizes the loci of points where $\dot{v}$ and $\dot{h}$ are zero (nodal lines) and points of intersection where $\dot{v} = \dot{h} = 0$ (critical point). Thus by setting $\dot{v}$ and $\dot{h}$ equal to zero and by plotting the nodal lines, Russell determined three nucleation mechanisms (spontaneous, homogeneous, and gas-assisted) which are visualized in Figs. 2 and 3. A mechanism is established according to helium generation rates, temperature, and sink density. Two types of cavity nucleation paths, spontaneous and homogeneous, are shown in Fig. 2. Solid lines denote steady growth and the dashed line is growth by fluctuation. Spontaneous growth takes place for any cluster whose coordinates lie above the $\dot{v} = 0$ and below the $\dot{h}$ nodal line, because only these are guaranteed stability against thermal dissociation or radiation defects causing shrinkage. When the two nodal lines do not cross (Fig. 2), any cluster forming between them is stable.

Homogeneous cavity nucleation occurs only when vacancies are collected. While nucleation and growth rates take place at the average

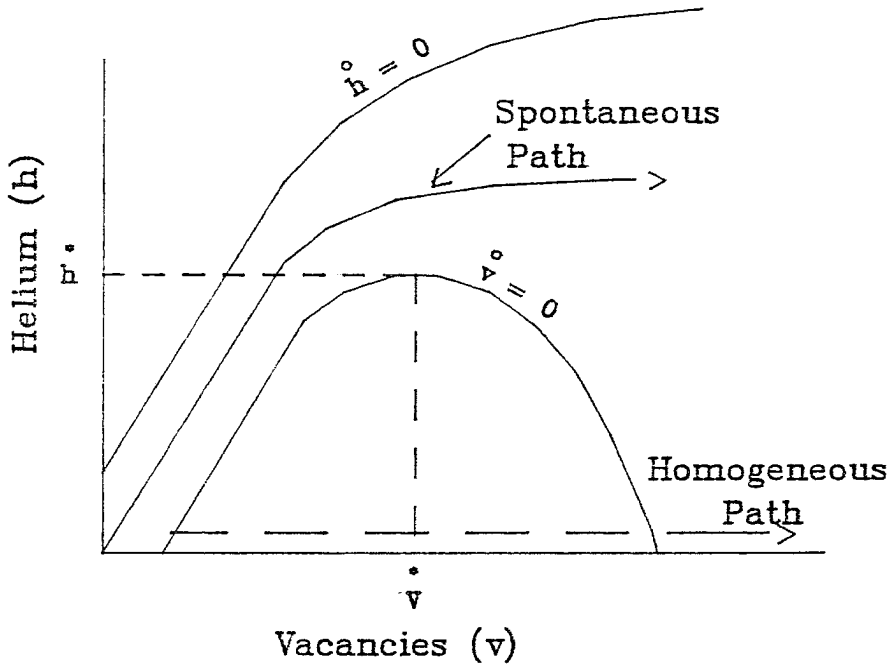

Fig. 2. Schematic of spontaneous and homogeneous nucleation paths, shown on a nodal line plot (after Parker and Russell [17]).

velocities given by Eqs. (4) and (5), the homogeneous nucleation is not a kinetic process governed by these equations. A void (cavity with no helium) can only survive dissociation by some statistical probability, where enough vacancies cluster together simultaneously to achieve a cluster size larger the v^*. Any cavity containing less than v^* vacancies will dissociate.

The third nucleation path, defined as "gas-assisted" by Russell [14], occurs when nodal lines cross (see Fig. 3). Nucleation occurs when an equilibrium bubble undergoes a fluctuation in which it collects several vacancies and reaches the rapid growth region of the helium-vacancy phase space. Both the spontaneous and gas-assisted growth regions are characterized as a rapid phase by vacancy acceptance alone. At the critical point v^*,h^* (see Fig. 3), equilibrium bubbles have zero velocity and all of the unstable cavities in its vicinity will dissociate to the combination of vacancies and helium atoms of the critical points. Thus, it is the largest possible gas-assisted nucleation site.

In Chapter V, we will outline our contributions to the nodal line analysis [15]. In particular, we used it to explain various bi-modal cavity distributions found in HFIR-irradiated samples. Figures 4 through 6 show some of Russell's results using the nodal line analysis compared to measured cavity distribution from Ref. [51]. The figures show that the theory has a temperature dependence which is too strong for the cavity number density. Although the calculated mean size is only about a factor of 2 to 4 too large, it does not produce very symmetric bell-shaped curves for the size distribution.

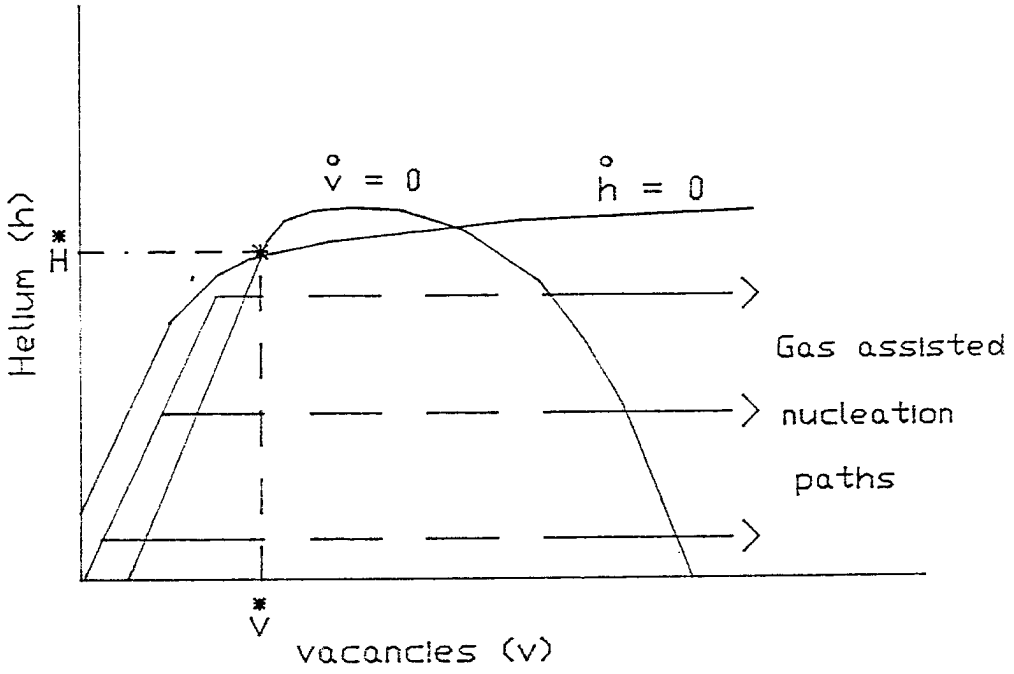

Fig. 3. Schematic of nucleation paths for gas-assisted nucleation on a nodal line plot (after Parker and Russell [17]).

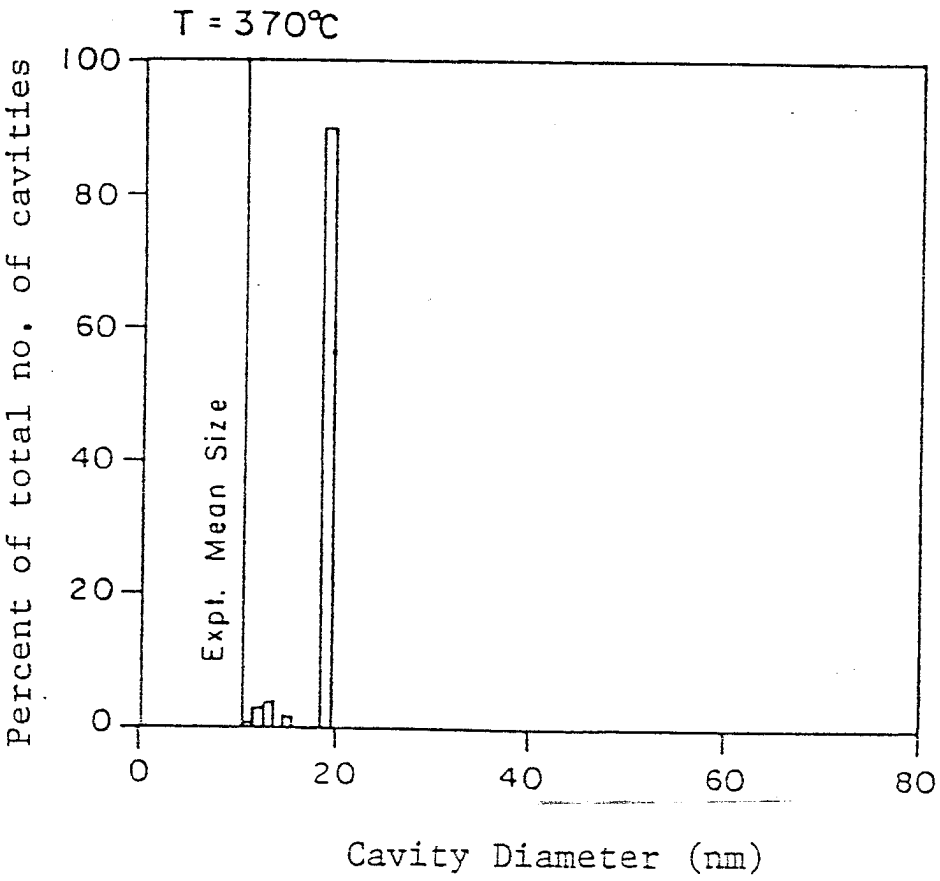

Fig. 4. Calculated cavity distribution for simulated EBR-II irradiation at T=370°C (after Parker and Russell [17]).

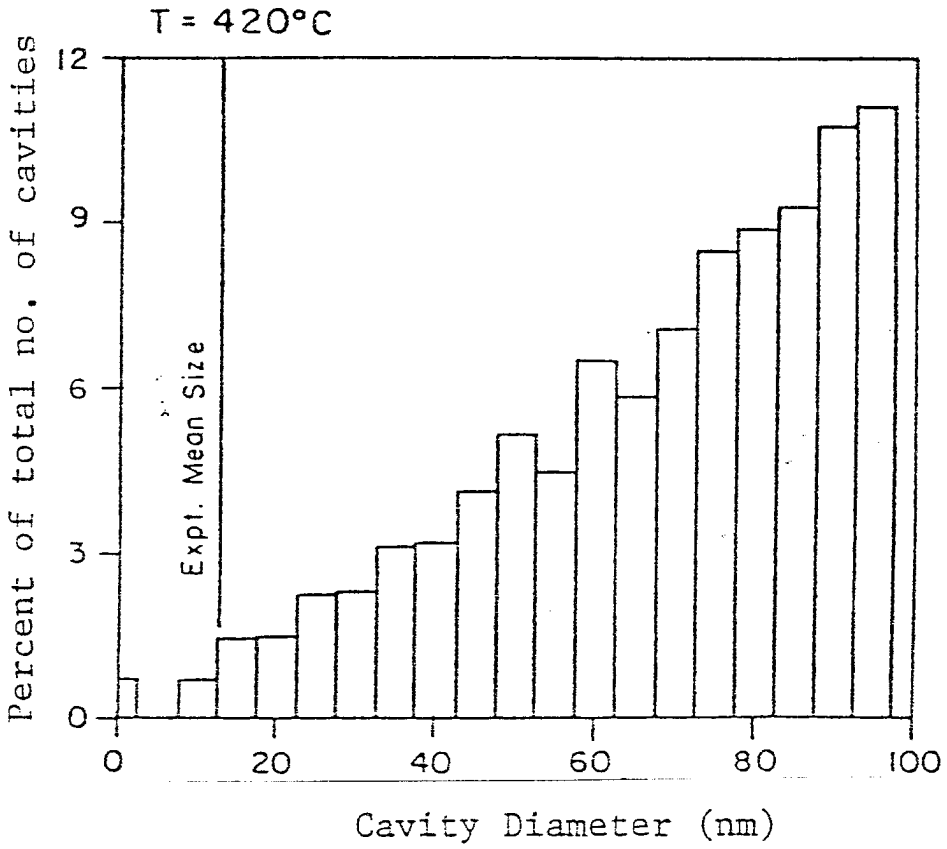

Fig. 5. Calculated cavity distribution for simulated EBR-II irradiation at T=420°C (after Parker and Russell [17]).

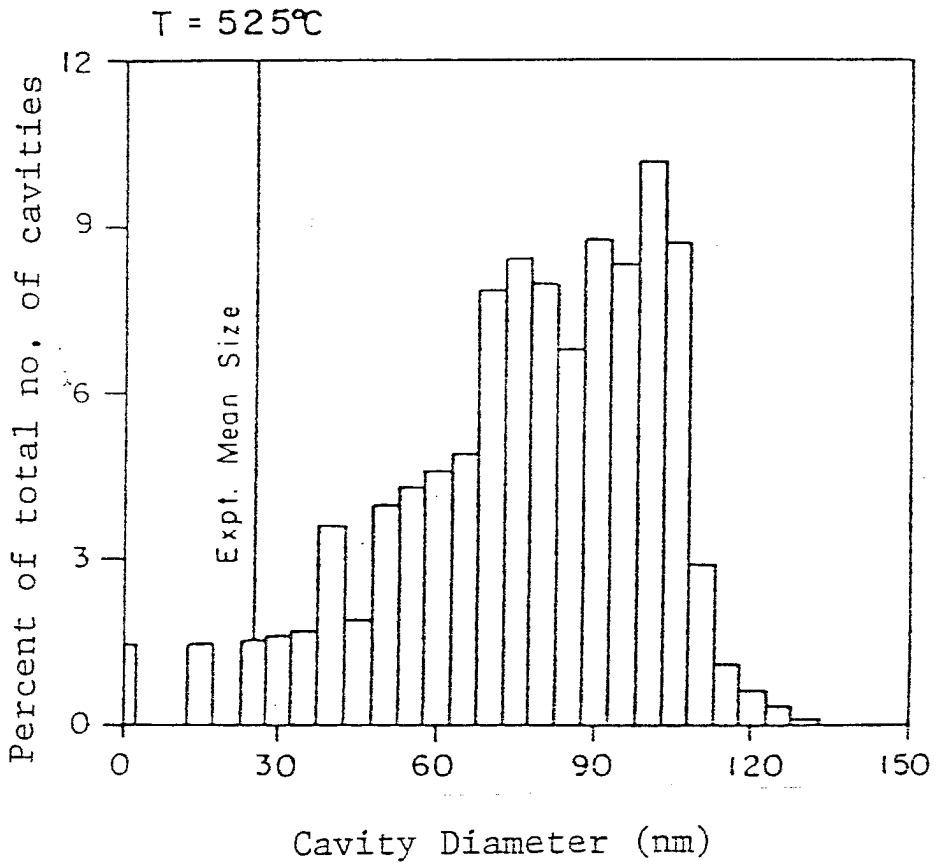

Fig. 6. Calculated cavity distribution for simulated EBR-II irradiation at T=525°C (after Parker and Russell [17]).

Despite some recent improvements [17], quantitative predictions cannot be made using the model, because of approximations made in the model and uncertainties in the physical parameters.

Wiedersich, Burton and Katz [12] also contributed to the theory of nucleation with constant helium generation rates. Single helium atoms were found to increase the cavity nucleation rate only modestly, whereas clusters of helium atoms give substantial enhancements. However, the assumption of immobile helium is not consistent with the need for some mobility to form clusters.

Wiedersich et al. [12] also based their theory of cavity nucleation on the processes shown in Fig. 1 and, in addition, allowed for displacement of a helium atom by capture of a self-interstitial. They derived a system of simultaneous equations for the concentrations of cavities of various sizes and gas content and then solved the system numerically under steady-state conditions.

To assist subsequent discussions, we present a simple derivation of concentrations of vacancies and of mobile gas atoms. Detailed derivations can be found in Refs. [18-20]. The calculations which follow are only valid in the central portion of the temperature range of the cavity swelling, where dislocations are the primary point defect sink, and where thermal production of vacancies is relatively unimportant. The steady-state vacancy concentration C_v (in atomic fraction) is then dictated by the balance between the atomic displacement rate K and the annihilation at dislocation sinks. Thus,

$$\dot{C}_v = 0 = K - C_v D_v Z_v \rho_d \quad , \tag{14}$$

where D_v = vacancy diffusivity in cm^2/sec,

Z_v = dislocation bias factor for vacancies ≈ 1,

ρ_d = dislocation density in cm/cm^3,

K = displacement rate,

then

$$C_v = \frac{K}{D_v Z_v \rho_d} \quad , \tag{15}$$

and vacancy supersaturation is

$$S_v \equiv \frac{C_v}{C_v^e} = \frac{K}{D Z_v \rho_d} \quad , \tag{16}$$

where C_v^e = thermal equilibrium vacancy concentration,

$D \equiv D_v C_v^e$ = vacancy self-diffusion coefficient.

A similar calculation may be performed for interstitials, to give the ratio of the arrival rates of the two defects as

$$\frac{D_i C_i}{D_v C_v} = \frac{Z_v}{Z_i} \quad , \tag{17}$$

where Z_i = biasing factor for self interstitials. The ratio Z_v/Z_i is between about 0.9 and 0.99.

The same arguments hold for helium:

$$\dot{C}_h = 0 = K_T^h C_h^T - C_h D_h \left(k_h^2 - \frac{C_h^T}{a^2}\right) \quad , \tag{18}$$

where K_T^h = rate of detrapping of helium from sinks,

D_h = diffusivity of intestitial helium,

C_h^T = trapped helium concentration,

C_h = mobile helium concentration,

k_h^2 = sink strength [Eq. (21).

The helium flux is

$$J_h = \frac{C_h D_h}{a^2} \quad , \tag{19}$$

where a = lattice parameter

$$J_h(C_{T,max} - C_h^T) = \text{FLOW-IN of He atoms} \quad , \tag{20}$$

and

$$k_h^2 \equiv \frac{C_{T,max}}{a^2} \quad . \tag{21}$$

The trapped and untrapped helium concentrations are related by

$$C_h^o = C_h + C_h^T \quad , \tag{22}$$

where C_h^o = total helium concentration.

In cases where sinks are far from saturated, Brailsford and Bullough [19] use the following arguments to derive an equation for the mobile helium (untrapped) concentration given by a balance between trapping and detrapping.

First, the total helium concentration C_h^o is much less than the total trap concentration $C_{T,max}$:

$$C_h^o << C_{T,max} \quad . \tag{23}$$

Using the definition for the sink strength we get

$$C_{T,max} = k_h^2 a^2 \quad . \tag{24}$$

Since all helium introduced into the system is immediately trapped, the total helium concentration can be approximated by

$$C_h^o \simeq C_h^T \quad . \tag{25}$$

So Eq. (18) becomes

$$C_h^o = 0 = K_T^h C_h^o - C_h D_h \left(k_h^2 - \frac{C_h^o}{a^2}\right) \quad . \tag{26}$$

But from Eqs. (23) and (24) we have

$$C_h^o << k_h^2 a^2 \quad , \tag{27}$$

or

$$\frac{C_h^o}{a^2} << k_h^2 \quad . \tag{28}$$

So Eq. (26) combined with Eq. (28) gives

$$C_h^o = 0 = K_T^h C_h^o - C_h D_h k_h^2 \quad , \tag{29}$$

which can now be solved for the mobile helium concentration

$$C_h = \frac{C_h^o \, K_T^h}{D_h \, k_h^2} \quad . \tag{30}$$

Bullough and Brailsford [19] were thus able to find the free helium concentration as a kinetic balance between trapping and detrapping. Wiedersich [12] used an expression equivalent to Eq. (18) in solving for C_h. A study of their equations shows, however, that instead of solving directly for the mobile gas concentration, they solved for C_h^T by a series expansion and obtained C_h by difference. They found for C_h

$$C_h = \frac{(C_h^o)^2}{(C_h^o + k_h^2 a^2)} \quad . \tag{31}$$

Thus instead of the free gas concentration being given by the balance between trapping and detrapping [Eq. (30)] the kinetic factors do not enter at all in Eq. (31).

For $C_h^o = 10^{-6}$ apa, $a^2 = 10^{-15}$ cm^2 and $k_h^2 = 10^{11}$/cm^2, Eq. (31) gives

$$C_h \simeq 10^{-2} \, C_h^o \quad , \tag{32}$$

whereas the same conditions used in Eq. (30) give

$$C_h \simeq 10^{-13} \, C_h^o \quad , \tag{33}$$

if we use a typical value for $K_T^h \simeq 10^{-3}$ dpa/sec and $D_h \simeq 0.1$ cm^2/s. Equation (31) thus overestimates C_h by a factor of about 10^{11}.

Calculations based on this equation are thus unlikely to predict either absolute values or trends in the cavity nucleation rate.

This brief review of Refs. [12] and [19] clearly points out the discrepancies between various theoretical approaches which are expected in view of the inconsistent approximations made.

3. CLASSICAL GROWTH THEORY

Having nucleated, the cavity embryos are now driven to grow in the presence of displacement damage. Point-defect balances provide the means of computing the vacancy and interstitial supersaturations (S_v and S_i, or equivalently, C_v and C_i) which drive both the nucleation and growth processes.

The concentrations of vacancies and interstitials in the irradiated solid are determined by equating the rate of production of point defects to the rate of removal by all mechanisms. The analytical treatments are performed quasi-stationary because the time derivatives dC_v/dt and dC_i/dt are neglected. This approximation is justified on the grounds that changes in the sink strengths due to the evolution of the microstructure during irradiation, and hence the rates of point-defect removal, are very slow compared with the time required for the point-defect population to respond to such changes.

The spatial gradients in point-defect population are also neglected because both the rates of production and removal are assumed to be uniform throughout the metal. Therefore, the calculations are of the infinite-medium type. Very strong concentration gradients which are responsible for point-defect absorption do exist in the immediate

vicinity of the microstructural features of the solid. This complication is removed from the point-defect balances by homogenizing the sinks. That is, the discrete sinks in the solid are replaced by spatially uniform absorbers of point defects. The strength of the homogenized sinks, however, must be determined by solving the point-defect diffusion equations in the immediate vicinity of the discrete sinks.

Point-defect balance equations have been developed by Wiedersich [18], Brailsford and Bullough [19], and Harkness, Tesk and Li [21]. These three analyses are equivalent in approach but differ in detail.

The theoretical description of irradiation damage (Harkness and Li [21]) entails analysis of the migration of intrinsic point defects to a spatial distribution of sinks. The latter are almost invariably distributed at random and only rarely is any long-range order observed. Thus spatial disorder in the dispersal of sinks is a prime characteristic. This complexity on the microscale may be contrasted with macroscopic quantities such as electrical resistivity, creep rates, etc. Such macroscopic properties will be largely insensitive to the finer details of the sink distribution, much as the properties of a gas are independent of the detailed kinetics of its constituent molecules. Thus, in the same fashion as averages suffice for the description of properties of a gas, one expects some averaging method to work in the description of defect problems.

This philosophy, in fact, underlies the majority of theories known to us in this field.

3.1. Point-Defect Concentrations

The concentrations of vacancies and interstitials must be known in order to determine nucleation and growth of clusters. These are determined from the rate theory commonly used in point-defect problems. We follow Ref. [19] in describing the rate theory.

The rate theory is derived from the basic continuity equations for vacancies and self-interstitials which are:

$$\partial C_v/\partial t + \text{div } \vec{j}_v = K - \alpha C_v C_i \quad , \tag{34}$$

$$\partial C_i/\partial t + \text{div } \vec{j}_i = K - \alpha C_i C_v \quad , \tag{35}$$

where C_v and C_i are the atomic fractions of the defects, and $\vec{j}_v$ and $\vec{j}_i$ denote the respective fluxes. The quantity K is the defect production rate in displacements per atom per second (dpa s^{-1}), and α is the intrinsic recombination coefficient. For simplicity, higher order cluster production is ignored.

In the derivation of rate theory it is assumed that the sinks form some type of a periodic array. Thus we can divide space into a set of primitive cells (unit cells). The normal component of point-defect fluxes vanishes on the cell boundaries. Brailsford and Bullough [19] take the first moments of Eqs. (34) and (35). These are obtained by integrating over the cell volume. The result from Eq. (34) is:

$$\int_{V_M} \frac{\partial C_v}{\partial t}\, dV + \sum_L \vec{J}_L^V = KV_M - \alpha \int_{V_M} C_i C_v \, dV \quad , \tag{36}$$

where $\vec{J}_L^V$ is the integral of $\vec{j}_L^V$ over the sink surface, V_M is the volume of matrix within the cell, and L denotes sink type. The corresponding self-interstitial equation can be obtained by interchanging the labels i and v. As a reminder, there is no point-defect loss across the outer boundary by construction. The main issue concerns the $\vec{J}_L^V$ and the corresponding quantities for self-interstitials. Brailsford [19] defines each flux in terms of a sink strength $k^2_{L,V}$ and a thermal emission rate $K_{L,v}$, by the following relation:

$$\vec{J}_L^V = D_V \, k^2_{LV} \int_{V_M} c_v \, dV - K_{L,V} \, V_M \quad , \tag{37}$$

with a corresponding definition for interstitial quantities. In Eq. (24), D_v is the vacancy diffusivity.

Introducing the notation:

$$\langle C \rangle = v_M^{-1} \int_{V_M} C \, dV \quad , \tag{38}$$

Brailsford and Bullough derive the two rate equations:

$$\frac{d\langle C_V \rangle}{dt} + \sum_L \left(D_V \, k^2_{LV} \langle C_V \rangle - K_{LV} \right) - K + \alpha \langle C_i \rangle \langle C_V \rangle = 0 \quad , \tag{39}$$

and

$$\frac{d\langle C_i \rangle}{dt} + \sum_L \left(D_i \, k^2_{Li} \langle C_i \rangle - K_{Li} \right) - K + \alpha \langle C_i \rangle \langle C_V \rangle = 0 \quad . \tag{40}$$

These equations are to be solved to obtain the $\langle C_V \rangle$ and $\langle C_i \rangle$ as functions of time for some prescribed initial conditions. In principle, such a procedure is straightforward, if the sink strength k_L^2 and the thermal emission rate K_L are known for each defect and each sink type.

Thus, the subsequent procedure is: One must solve the continuity equations within each cell to compute $\vec{J}_L^V$ and hence derive $k_{L,V}^2$ and K_{LV}. The same must be done for self-interstitials.

3.2. Methodology for Sink-Strength Calculations

First, the concept of so-called quasi-steady-state growth is invoked. Because the relaxation times for changes in the concentrations are generally much shorter than characteristic times for changes in reaction rate constants, all characteristic dimensions entering the sink strengths are to be treated as time independent.

Subject to this simplification, if the production rate is independent of time, the time derivatives in the rate equations are of no importance except for deriving initial transients or treating pulsed irradiation conditions [19]. The rate equations are then simply algebraic relations which can be solved for the concentrations, with the sink strengths and emission rates entering as parameters (Wiederich 1970 [7], Brailsford and Bullough 1972 [19], Harkness and Li 1971 [20]). Results of Ghoniem and Gurol [22] are given below:

$$C_{V,i} \simeq \left(\frac{1}{2\alpha\ \tau_{i,V}}\right)\left[(1 + 4\alpha\ K\ \tau_V \tau_i)^{1/2} - 1\right] \quad , \tag{41}$$

$$\tau_{i,V} = \left(\frac{1}{D_{i,V}\ Z_{i,V}\ \rho}\right) \quad , \tag{42}$$

where $\tau_{i,V}$ is the mean time it takes a self-interstitial or a vacancy to diffuse to a sink, respectively, and $Z_{i,V}$, are the notations used henceforth for sink strengths.

3.3. Sink Strengths and Sink Efficiencies

The sink strength is essential in determining the loss rate of a point defect to a sink type. The loss rate is simply the product of the bulk point-defect concentration C, with the point-defect diffusion coefficient D, and the sink strength S. A complete treatment is given in Refs. [23] and [24], where other work is also mentioned. We follow here the notations used in Ref. [24] for the derivation of sink strength for the cavity. Results for other sink types are also quoted.

Assume an isolated cavity in an infinite medium with smeared-out sinks of strength S. Furthermore neglect recombination and thermal-vacancy generation by sinks other than cavities. Thus in spherical coordinates we can write for either defect type:

$$\frac{D}{r^2}\frac{d}{dr}r^2\frac{dC}{dr} - DS_C + G = 0 \quad , \tag{43}$$

and the boundary condition at the cavity surface is given by,

$$D\left.\frac{dc}{dr}\right|_{r=r_c} = w[C(r_c) - C^e(r_c)] \quad . \tag{44}$$

Here r is the distance from the cavity center, w is the point-defect transfer velocity at the cavity surface, G is the defect production rate, and $C^e(r_c)$ is the thermal equilibrium bulk concentration given by:

$$C^e(r_c) = C_v^e \exp\left[\left(\frac{2\gamma}{r_c} - P\right)\frac{\Omega}{k_B T}\right] \quad , \tag{45}$$

where T is the temperature, γ the specific surface free energy, Ω the atomic volume, k_B the Boltzmann's constant, and P the pressure due to any enclosed gas.

The solution to Eq. (43) is

$$C = C_\infty - \frac{[C_\infty - C^e(r_c)]wr_c/D}{1 + S^{1/2} r_c + wr_c/D} \frac{r_c}{r} \exp[-S^{1/2}(r - r_c)] \quad , \tag{46}$$

where C_∞ is the bulk concentration.

The current of point defects to the cavity is:

$$4\pi r^2 D \left.\frac{dC}{dr}\right|_{r=r_c} = \frac{4\pi[C_\infty - C^e(r_c)]\ wr_c^2(1 + S^{1/2} r_c)}{1 + S^{1/2} r_c + wr_c D} \quad . \tag{47}$$

By the definition of sink strength, the sink strength of a cavity is given by:

$$S^c = 4\pi r_c(1 + S^{1/2} r_c)\frac{wr_c/D}{(1 + S^{1/2} r_c + wr_c D)} \quad . \tag{48}$$

Equation (48) consists of three parts. The first part, $4\pi r_c$ is a simple geometric term; the second part, $1 + S^{1/2} r_c$, is designated as a multiple sink correction term; and the third part is the sink capture efficiency designated as Z^c. The latter measures how good an absorber the sink is. Alternatively, Mansur et al. [25] have lumped the second and third terms together as a generalization of capture efficiency.

An equivalent definition of capture efficiency is [26]:

$$Z^c = \frac{C - C(r_c)}{C - C^e(r_c)} \quad . \tag{49}$$

The sink strengths of straight dislocations, dislocation loops, grain boundaries, free surfaces and precipitates have all been derived by analogous methods [27-28]. For example, the sink strength for straight dislocations is given by:

$$S^d = Z^d \rho \quad , \tag{50}$$

where

$$Z^d = 2\pi/\ell n(r_L/r_d) \quad . \tag{38}$$

Here ρ is the dislocation density, $r_L = (\pi L)^{-1/2}$ is a measure of dislocation spacing, and r_d is the dislocation capture radius for a point defect. The capture radius depends on the type of defect. Generally $Z_i^d > Z_v^d$ because $r_d^i > r_d^v$.

4. MODERN APPROACHES TO MICROSTRUCTURE EVOLUTION

The previously mentioned treatments have not been found to be completely satisfactory for describing the development of microstructural components under irradiation. This stems primarily from two reasons:

1. In many instances, nucleation is a continuous process that cannot be easily separated from growth. Cavity evolution is therefore dependent on both nucleation and growth acting simultaneously.

2. Details of the size distribution cannot be obtained through analysis based on the previous theories. In fact, using previous methods, Hayns [29] has failed to produce even qualitative agreements with experimental observations.

In the mid-1970s, Brown, Kelly and Mayer [30] carried out calculations for interstitial clustering in graphite. They considered heterogeneous nucleation to occur when one unbound interstitial encounters another interstitial atom already bound to a trapping site such as boron impurities. Using di-interstitials as the smallest size loops, they concluded that heterogeneous nucleation can be taken into account in the reaction rate theory by reducing the velocity of interstitial by an amount which corresponds to the time they spend bound to an impurity. Recently Kiritani [31] used a model similar to Brown et al. to explain high voltage emission microscopy (HVEM) experimental results on interstitial loop formation. Vacancy mobility and the existence of di-vacancies have been included in his analysis.

Hayns [32] studied the nucleation and early stages of growth of interstitial dislocation loops in irradiated materials. A hierarchy of rate equations was solved to simulate the homogeneous nucleation of interstitial dislocation loops. The assumption that di-interstitial atom pairs are stable against thermal dissociation was examined and it was concluded to be appropriate. Lam [33] developed a time- and space-dependent model to study the radiation-induced defect buildup and radiation-enhanced diffusion in a foil under irradiation. The distribution of interstitials, monovacancies, and vacancy aggregates (containing

two to six vacancies) in a silver foil under irradiation was calculated as a function of both distance from the surface of the foil and irradiation time, by numerically solving the rate equations for various temperatures and internal sink concentrations. In an investigation of interstitial cluster nucleation at the onset of irradiation, Johnson [34] developed rate equations for the concentrations of single and small clusters of vacancies and interstitials. The effects of irradiation, temperature, and displacement rate were investigated, and it was found that the cluster concentrations are sensitive to cluster binding energies. Hall and Potter [35] included interstitial-impurity trapping in a time-dependent nucleation and growth model that is used to calculate both vacancy and interstitial cluster densities and size distributions during irradiation. Calculations were performed for nickel alloys with interstitial-solute binding energies between 0 and 1 eV. Recently, Ghoniem and Cho [36] developed a rate-theory model for the simultaneous clustering of point defects during irradiation. Size-dependent bias factors and self-consistent reaction rate constants were used to evaluate the feedback effects between the vacancy cluster and interstitial loop populations. An atom conservation principle was used to determine the number of necessary rate equations as a function of irradiation time. It was found that the concurrent presence of vacancy clusters depletes the matrix vacancy population and thereby reduces mutual point-defect recombination. This was concluded to enhance interstitial loop formation, increasing loop concentration, nucleation rate, average size, and growth speed of the average size.

The basic limitation to the rate-theory approach (or equivalently, the Master Equations formulation) lies in the one-to-one relationship between the number of simultaneous differential equations and the number of species in a cluster. Although the previously mentioned methods have been detailed enough to analyze fundamental point-defect kinetics and to describe the effects of various irradiation and material parameters, the computations become prohibitively expensive for large defect clusters.

Correlating the results of the computations with experimental data can be very useful in theory development and for guiding well thought-out experiments. The need for the correspondence of theory and experiment has prompted the development of approximate computational methods for the kinetics of defect clustering. Kiritani [37] has developed a scheme for the nucleation and growth of clusters in which clusters within a range of sizes are grouped together, and he has applied the method to vacancy clustering after quenching. Hayns [38] has applied the Kiritani grouping scheme to study the nucleation and growth of interstitial loops during irradiation, and he has shown that objections to the method by Koiwa [39] can be surmounted. Hayns [40] also reported calculations using the grouping scheme to study nucleation and growth of interstitial loops under fast reactor and simulation conditions.

A different approach for studying the nucleation and growth of defect clusters has considered solving continuum equations rather than rate equations. Sprague et al. [41] were able to describe vacancy clusters containing up to 3920 vacancies by descretizing a diffusion-type equation with variable diffusivity. Recently Wolfer et al. [42] followed similar lines to demonstrate that the rate equations describing

clustering kinetics can be condensed into one Fokker-Planck continuum equation. The latter was interpreted as a diffusion equation with drift terms. They showed that cavity nucleation and growth can be both incorporated into such a unified formalism. No attempts were made to investigate the numerical solutions of these equations, however. Hall [43] investigated point-defect clustering, considering a different form of the continuum description. Only the cluster concentrations were expanded in a Taylor series and the resulting set of rate equations were shown to be condensed into one partial differential equation.

Either because of the high computational penalties in rate-theory methods or because of the restrictive approximations in grouping methods, the majority of the approaches mentioned above have not been able to accurately describe the long-term behavior of defect clusters. We developed a novel calculational method for the solution of the Fokker-Planck equation describing cavities and interstitial loops [36]. The strength of that method lies in its hybrid nature. Small clusters were treated using separate rate equations including all possible details. On the other hand, a continuum approach was used for larger clusters by descretizing a transformed Fokker-Planck equation. Defects containing up to millions of atoms were investigated using this hybrid approach. The numerical results of the method compared well with experimental findings on heavy-ion irradiated 316 stainless steel.

All approaches mentioned above are directed at understanding the nucleation and growth processes of irradiation produced cavities. One of the general results of research in radiation effects is that the type and severity of radiation damage are found to be highly dependent on

alloy composition. An impurity mostly singled out (first, because of its extreme potency and second, because of its unavoidable production in transmutation reactions during neutron irradiation) is the insoluble gas, helium. The modern approaches mentioned so far have all excluded the effects of helium on cavity nucleation and growth. Various nucleation and growth mechanisms for helium inclusions in cavities have been suggested. We will briefly mention the basic ideas of some of these.

Critical Cavity Radius

Because of differences in capture efficiencies, unequal partitioning of point defects to sinks leads to biases which results in a larger flux of vacancies to cavities and of interstitials to dislocations. However, the thermal emission rate of vacancies from cavities follows $e^{1/r}$ dependency. Therefore, at a given temperature there is a critical radius above which the bias-induced vacancy influx is larger than the thermal-vacancy outflux. A similar critical radius concept was developed earlier in calculations of gas bubble growth in fissile materials [44]. Brailsford and Bullough [45] have introduced the related concept of a critical stress for stress-driven breakaway swelling. For a given stress this can be translated to a critical radius. There it arises because the cavity absorbs a net vacancy flux provided by sources, such as dislocations and grain boundaries, that emit enhanced vacancy fluxes under stress. Many other workers in the field have also used the concept of a critical radius (e.g., Ref. [46-48]).

Lately, Hishinuma and Mansur [46] gave a simple explicit expression for both the ideal and the Van der Waal's gas law, with accurate dose

rate and temperature dependences. The solution of this equation was used to develop a cavity stability map and to discuss the occurrence of bi-modal cavity distributions in experiments where helium is present during irradiation.

The related concept of a critical number of contained gas atoms has also been developed and applied by Mansur and Coghlan [47] to develop predictions of interest. For example, the temperature shifts of cavity growth with dose rate and microstructure was derived by Mansur, using the critical cavity-radius concept [48].

Wolfer and Glasglow [49] on the other hand, state that cavity growth in the presence of helium is not bias driven but pressure driven because small clusters of helium atoms and vacancies have a significant interaction with self-interstitials. They suggest three growth mechanisms: self-interstitial ejection, dislocation loop punching, and stress-assisted thermal vacancy absorption. Under the assumption that the overpressure in the helium cluster is the driving force for all three mechanisms, it is shown that the interstitial ejection is the dominant mechanism for the growth of bubbles with radii less than 5 to 10 Burgers vectors, while loop punching becomes dominant for larger radii. Finally, they show that thermal-vacancy absorption becomes important at still larger radii and temperatures $\lesssim$ 700°K. Above 800°K and helium production rates of 10^{-4} appm/s however, they show the thermal-vacancy absorption to be the dominant growth mechanism at all bubble radii.

REFERENCES

[1] J. E. Inglesfield and J. B. Pendry, Philos. Mag., 34 (1976) 205.

[2] A. L. Bement, Advan. Nucl. Sci. Technol., 7 (1973) 28.

[3] D. I. Norris, Radiat. Eff.., 14 (1972) 151.

[4] J. W. Corbett and L. C. Ianniello, Eds., Radiation Induced Voids in Metals, (Proc. Intl. Conf., Albany, NY, June 9-11, 1971) AEC Symp. Series No. 26, CONF-710601 (1972).

[5] Voids Formed by Irradiation of Reactor Materials, (Proc. Conf.,) Reading, England 1971) BNES.

[6] K. C. Russell, Acta Metall., 19 (1971) 753.

[7] J. L. Katz and H. Wiedersich, J. Chem. Phys., 55 (1971) 1414.

[8] J. L. Katz and H. Wiedersich, J. Nucl. Mater., 46, (1973) 43; also in Proc. Conf. on Defects and Defect Clusters in B.C.C. Metals and their Alloys, R. J. Ansenault, Ed., National Bureau of Standards, Gathersburg, MD, August 1973, p. 530.

[9] K. C. Russell, Acta Metall., 20 (1972) 899.

[10] B. T. M. Loh, ibid, 1305.

[11] K. C. Russell, Scripta Metall., 7 (1973) 755.

[12] H. Wiedersich, J. J. Burton and J. L. Katz, J. Nucl. Mater., 51 (1974) 287.

[13] D. R. Olander, Fundamental Aspects of Nuclear Reactor Fuel Elements, NTIS TID-26711-P1 (Nat. Tech. Info. Serv., Springfield, VA, 1976).

[14] K. C. Russell, Acta Metall., 26 (1978) 1615.

[15] S. Sharafat and N. M. Ghoniem, J. Nucl. Mater., 122 (1984) 531.

[16] J. R. Brager, J. L. Straalsund, J. J. Holmes and J. F. Bates, Report No. WHAN-FR-16, 1970.

[17] C. A. Parker and K. C. Russell, Effects of Radiation on Materials: Eleventh Conference, H. R. Brager and J. S. Perrin, Eds., Am. Soc. Testing Mater., 1982, ASTM-STP-782, pp. 1042-1053.

[18] H. Wiedersich, Radiat. Eff., 12 (1972) 111.

[19] A. D. Brailsford and R. Bullough, J. Nucl. Mater. 44 (1972) 1212.

[20] P. T. Heald and M. V. Speight, Acta Metall., 23 (1975) 1389.

[21] S. D. Harkness and C. Y. Li, Metall. Trans., 2 (1971) 1457.

[22] N. M. Ghoniem and H. Gurol, Radiat. Eff. 55 (1981) 209.

[23] A. D. Brailsford and R. Bullough, Philos. Trans. R. Soc. (London), 302 (1981) 87.

[24] L. K. Mansur, "Defect Agglomeration in Metals ...," Kinetics of Nonhomogenous Processes, G. R. Freeman, Ed., (Wiley-Interscience, New York, to be pub.)

[25] L. K. Mansur, A. D. Brailsford and W. G. Wolfer, J. Nucl. Mater., 105 (1982) 36.

[26] L. K. Mansur, Nucl. Tech., 40 (1978) 5.

[27] W. A. Coghlan and M. H. Yoo, ibid, p. 152.

[26] R. Bullough, M. R. Hayns and C. H. Woo, J. Nucl. Mater., 84 (1979) 93.

[28] A. D. Brailsford and L. K. Mansur, J. Nucl. Mater., 103&104 (1981) 1403.

[30] L. M. Brown, A. Kelly and R. M. Mayer, Philos. Mag., 19 (1969) 721.

[31] M. Kiritani, Proc. Conf. on Fundamental Aspects of Radiation Damage in Metals, M. T. Robinson and F. W. Young, Eds., CONF-751006-P2 (Nat. Tech. Info. Serv., Springfield, VA, 1975) p. 775.

[32] M. R. Hayns, J. Nucl. Mater., 56 (1975) 267.

[33] N. Q. Lam, ibid, 125.

[34] R. A. Johnson, J. Nucl. Mater., 75 (1978) 77.

[35] B. O. Hall and D. I. Potter, in Proc. 9th Intl. Symp. on Effects of Radiation on Structural Materials, Am. Soc. Testing, Mater., Richland, WA, July 11-13, 1978, ASTM-STP-683, p. 789.

[36] N. M. Ghoniem and D. D. Cho, Phys. Status Solidi A, 54 (1979) 171.

[37] M. Kiritani, J. Phys. Soc. Jpn. 35 (1973) 95.

[38] M. R. Hayns, J. Nucl. Mater., 59 (1976) 175.

[39] M. Koiwa, J. Phys. Soc. Jpn., 37 (1974) 1532.

[40] M. R. Hayns, in Proc. Harwell Consultants Symp. Inert Gases in Metals and Tonic Solics, AERE-R9733, v. II (March 1980) p. 409.

[41] J. A. Sprague, K. C. Russell and Y. H. Choi, ibid, p. 1181.

[42] W. G. Wolfer, L. K. Mansur and J. A. Sprague, Radiation Effects in Breeder Reactor Structural Materials, M. L. Bleiberg and J. W. Bennet, Eds., (Proc. Intl. Conf., Scottsdale, AZ, 1977) (AIME, NY, 1977) p. 841.

[43] B. O. Hall, submitted to J. Nucl. Mater.

[44] G. W. Greenwood, et al., ibid, 4 (1959) 305.

[45] A. D. Brailsford and R. Bullough, ibid, 48 (1973) 87.

[46] A. Hishinuma and L. K. Mansur, "Critical Radius for Bias-Driven Swelling ...," ibid (in press).

[47] L. K. Mansur and W. A. Coghlan, "Mechanisms of Helium Interaction with Radiation Effects in Metals and Alloys," ibid (to be pub.).

[48] L. K. Mansur, ibid, 78 (1978) 156.

[49] W. G. Wolfer and B. B. Glasglow, "Growth Mechanisms for Helium Inclusions and Bubbles," to be published.

CHAPTER V

HELIUM TRANSPORT AND INTERACTIONS WITH DEFECTS DURING IRRADIATION

1. INTRODUCTION

The physical situation of interest is the transport of helium atoms in alloys undergoing simultaneous radiation damage. The radiation-produced helium atoms interact with radiation-produced defects and with the microstructure of the material. During the course of irradiation, the microstructure of the irradiated material changes, which in turn affects the diffusion behavior of the helium atoms. Because of the complexity of the mechanisms involved in helium transport during irradiation, simple experiments designed to measure activation energies of motion for helium through the material of interest may be difficult to interpret. Therefore, in order to answer the question of how helium migrates or diffuses through the lattice, several mechanisms must be investigated.

In this chapter, we will first determine in Sect. 1.1 how a highly insoluble inert gas atom like helium resides in metals. In Sect. 2 we will discuss an investigation of helium transport and migration mechanisms through the metal during irradiation. In Sect. 3 we will introduce the concept of trajectories to investigate the stability and average size development of HVCs under irradiation.

1.1. Helium Residence in Metals

Helium permeation through metals was first studied shortly after helium was isolated as an element, in about 1897. In order to explain

the solution of an inert gas in metal, researchers postulated compound formation between the metal and the helium. In 1957 Rimmer and Cottrell [1] suggested a defect configuration between inert gas atoms and vacancies which pointed to a strong trapping of helium to a vacancy.

A helium atom can reside in the lattice either as an interstial atom or as a substitutional inside a vacant lattice site. In simple defect configurations, helium can also occupy more complex defects such as divacancies or several helium atoms and several vacancies forming a helium vacancy cluster (HVC). In order to study the defect nature of helium, detailed theoretical atomistic calculations are performed [2]. By calculating interatomic potentials for the host atom interaction and studying the atomic relaxation of a few hundred atoms in the vicinity of the defect, the energetically most favorable positions of host atoms can be determined. These calculations also determine the most favorable migration jumps with the associated activation energies.

Bauer and Wilson [3] used interatomic potentials for He-Fe, He-Pd, and He-Cu to investigate helium interstitial and substitutional positions in bcc and fcc metals. Figures 1 and 2 show the symmetrical interstitial positions for helium atoms in fcc and bcc metals, respectively.

It can be seen from Figs. 1 and 2 that an interstitially lodged helium atom can jump from one possible interstitial site to a neighboring one, provided enough energy is available to overcome the potential barrier. The activation energies for the jumps are generally in the 0.1 to 0.7 eV range, depending on the metal and lattice crystal structure [3]. Bauer and Wilson found the activation energy for interstitial

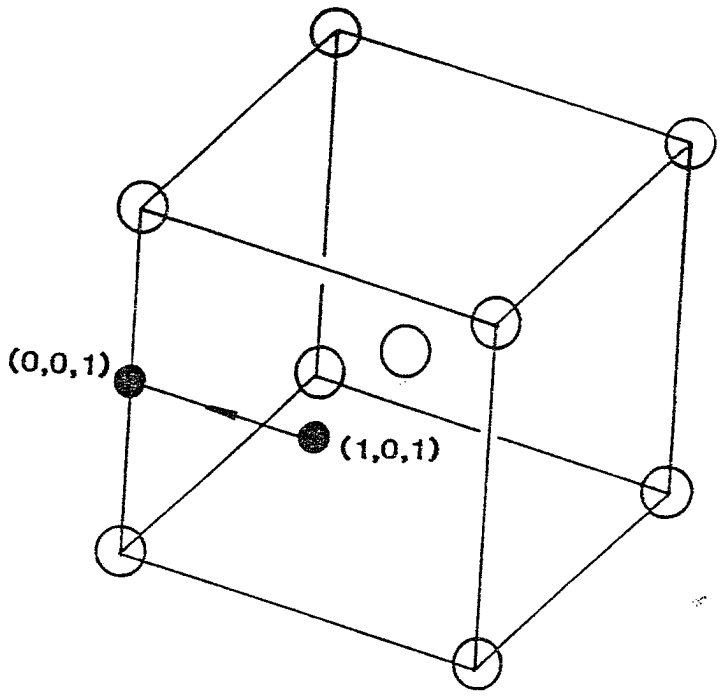

Fig. 1. Interstitial positions of helium atoms in a bcc metal lattice.

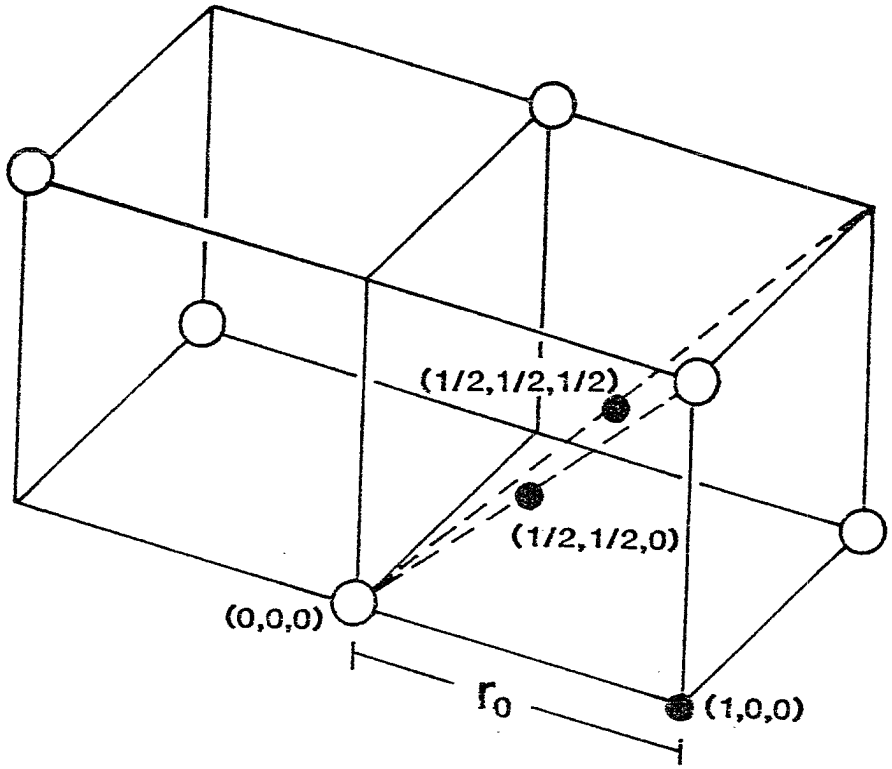

Fig. 2. Interstitial positions of helium atoms in an fcc metal lattice.

helium motion to vary little (0.45 to 0.71 eV), depending on the choice of potentials used in Cu [3]. In bcc metals such as V, Fe, Mo, Ta, and W, the interstitial activation energies were in the $\lesssim$ 0.25 eV range, which is about half that of Cu. The results of Bauer and Wilson are shown in Table I [3].

TABLE I
CALCULATED ACTIVATION ENERGIES OF MOTION FOR HELIUM (eV) [3]

Metal	Interstitial	Substitutional	Pop-Out
Cu	0.57	2.15	1.88
Pd	1.74	—	3.16
Ag	0.86	—	1.53
Fe	0.17	3.98	3.75
V	0.13	3.20	2.96
W	0.24	4.75	4.42
Ta	0	3.44	3.30
Mo	0.23	4.19	3.87

Interstitial formation energies are about a factor of two greater in bcc(s) than in fcc(s). The strain energy for an interstitial helium in Cu is 1.74 to 3.22 eV while the strain energy for helium in a vacancy is 0 to 0.13 eV. Furthermore, the strain energy to place a helium atom into a bcc vacancy is an order of magnitude greater than into an fcc vacancy. Once lodged inside a vacant lattice site, the helium atom has two means of migration: (1) To move as a whole in its simple defect configuration, and (2) to acquire enough energy to pop out of its substitutional site. Both mechanisms were considered by Bauer and Wilson. Table I includes their results for both mechanisms [3]. Figures 3 and 4 depict the paths of helium atoms during the

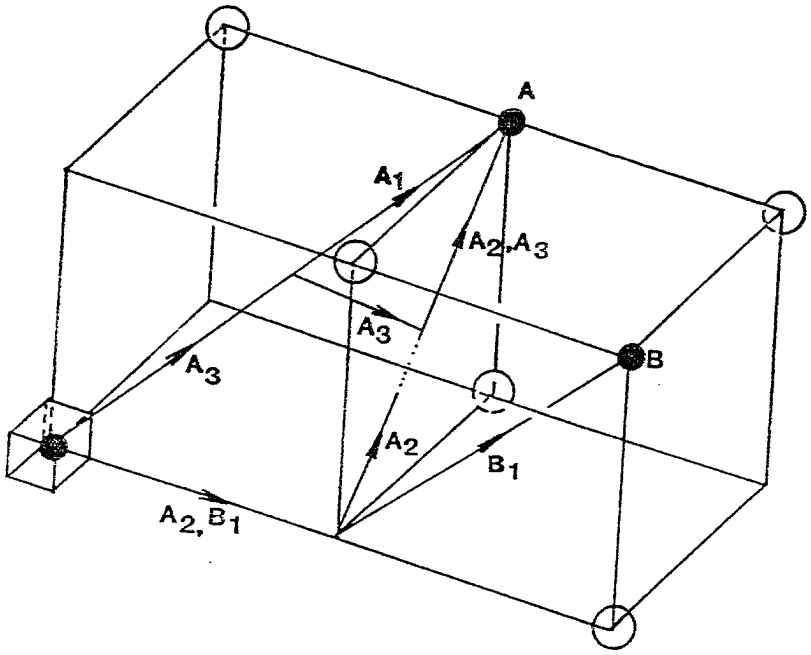

Fig. 3. Various migration paths for substitutional detrapping of a helium gas atom (pop-out) in an fcc metal lattice.

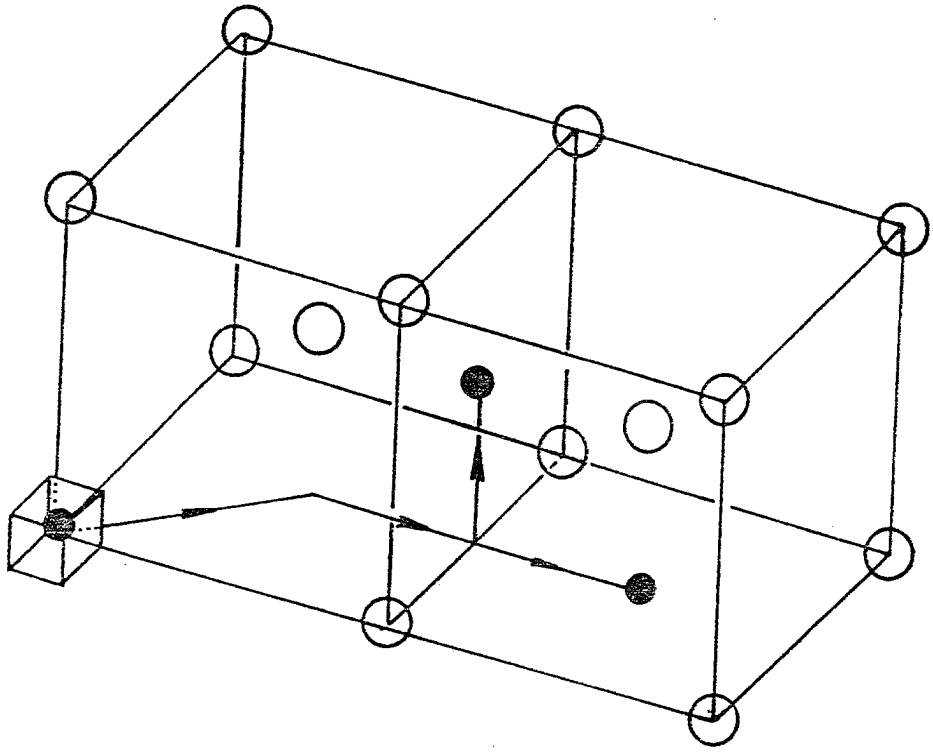

Fig. 4. Migration paths for a substitutional detrapping of a helium gas atom in a bcc metal lattice.

substitutional de-trapping or pop-out process. Because a higher energy barrier has to be overcome, the substitutional pop-out energy is considerably larger than the interstitial motion energy but slightly less than the substitutional defect migration energy. Because of these high activation energies (1.5 to 4.2 eV), the rate-limiting step for substitutional motion is the initial jumping of a helium atom from a substitutional site to an adjacent interstitial site. It occurs only at high temperatures, above 500°K/eV. Although the contribution of this migration mechanism seems to be negligible, we will later discuss the effects of a radiation environment on the pop-out rates.

Besides studying simple defect configurations, extensive research has been done on determining properties of multiple gas atoms and vacancy clusters. Experimental observations of the migration of helium in metals provided some guidance to the theoretical study of the properties of small clusters of helium and vacancies.

The experimental method widely used in studying the behavior of helium migration is the technique of thermal evolution spectrometry [4]. Gas ions are implanted into the target metal at energies from a few eV to a few MeV. A careful choice of the implant energy, dose, temperature, and the target pre-damage allows one to make deductions about the nature of the helium gas diffusion. In a post-bombardment annealing schedule, the target is heated, usually linearly, at rates of from a few deg/s up to 40°K/s. During these anneal schedules, the rate of release of the implanted species is monitored. In general, the release occurs in a number of stages, each corresponding to an evolution rate maximum. The temperature of the evolution rate maximum can be related to

the activation energy of the mechanism responsible for the release. For example, in cases where the implanted gas resides within a few layers of the surface, a single jump mechanism can be responsible for the release (see Ref. [4]). In cases where the implanted species lie deeply embedded in the bulk of the target, a multi-step diffusion system has been adopted [5,6]. However, the release of implanted gas observed is rarely by a simple mechanism. The many unresolved release-rate maxima suggest release mechanisms that are a result of other than the simple combination of a gas atom and a vacancy or simple interstitial diffusion. This led to the investigation of clustering effects. More complex configurations such a single helium residing in a divacancy or two or more helium atoms clustering with or without one or more vacancies had to be studied.

Wilson and Bisson [7] investigated helium in a copper divacancy and found the minimum energy configuration of a helium atom in a divacancy to be 0.13 eV, which is the same as that for a single vacancy they had reported earlier [8]. Their findings on the divacancy migration energy have been significant. When containing a helium atom, a divacancy migration energy was found to be 0.74 eV compared with 0.47 eV when empty, which agrees reasonably with experimental values reported by Wright and Evans [9].

Next, clusters of the form He_nV for n up to 4 were independently studied by Wilson et al. [2] and Caspers et al. [10]. These studies dealt specifically with the interpretation of thermal evolution data in a tungsten single crystal. The data was the result of work undertaken by Kornelson [11,12]. Two stable configurations of three helium atoms

in a vacancy in tungsten as calculated by Caspers [10] are shown in Fig. 5. Table II gives a comparison of experimental findings and theoretical results of Wilson and Casper of the binding energy of the last helium atom to the He_nV cluster.

TABLE II
COMPARISON OF EXPERIMENTAL AND THEORETICAL LAST HELIUM BINDING ENERGIES TO A He_nV CLUSTER IN TUNGSTEN (eV)

	Kornelson [11]	Wilson [8]	Caspers [10]
HeV	4.05	4.39	5.07
He_2V	3.14	2.89	3.43
He_3V	2.88	2.52	3.02
He_4V	2.41	2.50	2.94

The next clusters examined were He_nV_m clusters for n and m up to 3. Instead of listing the details of these findings, some interesting trends that develop in the higher order clusters will be noted. For both divacancy and trivacancy clusters, the addition of more helium tends to immobilize the cluster and inhibit vacancy loss. The binding energy of one of several helium atoms to the larger clusters tends to be a constant high value. So, for in clusters of the He_nV_m type, there is less possibility of helium migration or vacancy loss. In tungsten, it seems [10] that the cluster He_3V_2 is most stable (except HeV), with a migration energy of 4.0 eV, a vacancy dissociation (binding) energy of 4.83 eV, and a helium dissociation (binding) energy of 4.34 eV.

Wilson et al. [8] also investigated properties of helium clustering for copper. They have investigated the binding energy of the nth helium atom in a cluster of n interstitial helium atoms and the binding of the

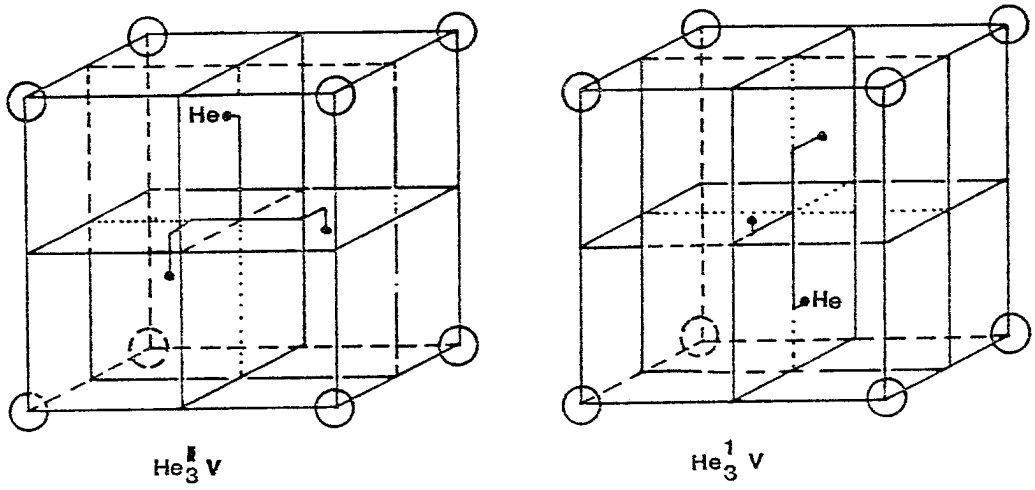

Fig. 5. Two stable configurations of three helium atoms in a single vacancy (He_3V) in tungsten.

nth helium and the mth vacancy in a cluster He_nV_m. Their findings are summarized in Table III.

TABLE III
THE nth-HELIUM BINDING ENERGY (eV)
TO A He_nV_m-CLUSTER IN COPPER [2]

No. of Vacancies	No. of Helium Atoms in the Cluster									
	1	2	3	4	5	6	7	8	9	10
0	--	0.08	0.18	0.08	0.18	0.02	--	--	--	--
1	1.84	0.79	0.57	0.66	0.60	0.86	0.25	0.24	0.20	0.20
2	1.84	1.84	1.09	0.60	0.85	0.90	0.75	0.85	0.67	0.85
3	1.84	1.84	1.84	1.25	0.89	0.99	0.69	0.78	0.98	0.70
4	1.97	1.84	1.73	1.93	1.25	1.13	1.12	1.10	0.65	0.82

The binding energy of the nth helium atom in an interstitial cluster was found to be small (see Table III) with the sixth atom not bound at all. The presence of a vacancy increases the binding energy of the nth helium atom. The binding energy of a vacancy, on the other hand, tended to increase with helium content.

A radically different approach to evaluating the binding energies of helium atoms or vacancies to He_nV_m clusters was used by Russell [13]. He used a thermodynamic approach to calculate the free energy change in forming a cluster of He_nV_m type. He found a steady increase in the free energy with increasing n and m until a saddle point was reached at n=6 and m=11. Beyond this combination the free energies decreased with increasing n and m. Russell also investigated the stability of clusters and concluded that the most stable would be around He_6V_{11} beyond which the cluster can grow freely by vacancy and/or gas

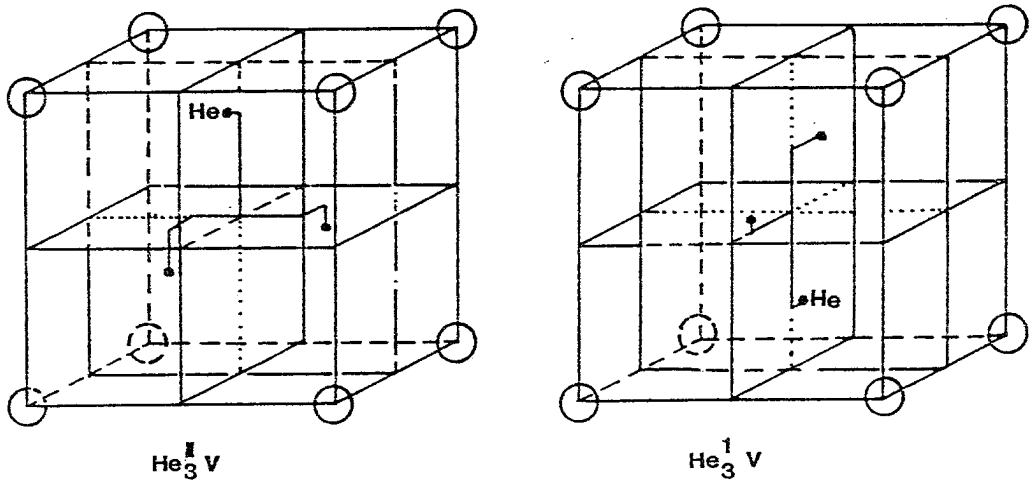

Fig. 5. Two stable configurations of three helium atoms in a single vacancy (He_3V) in tungsten.

nth helium and the mth vacancy in a cluster He_nV_m. Their findings are summarized in Table III.

TABLE III
THE nth-HELIUM BINDING ENERGY (eV)
TO A He_nV_m-CLUSTER IN COPPER [2]

No. of Vacancies	No. of Helium Atoms in the Cluster									
	1	2	3	4	5	6	7	8	9	10
0	--	0.08	0.18	0.08	0.18	0.02	--	--	--	--
1	1.84	0.79	0.57	0.66	0.60	0.86	0.25	0.24	0.20	0.20
2	1.84	1.84	1.09	0.60	0.85	0.90	0.75	0.85	0.67	0.85
3	1.84	1.84	1.84	1.25	0.89	0.99	0.69	0.78	0.98	0.70
4	1.97	1.84	1.73	1.93	1.25	1.13	1.12	1.10	0.65	0.82

The binding energy of the nth helium atom in an interstitial cluster was found to be small (see Table III) with the sixth atom not bound at all. The presence of a vacancy increases the binding energy of the nth helium atom. The binding energy of a vacancy, on the other hand, tended to increase with helium content.

A radically different approach to evaluating the binding energies of helium atoms or vacancies to He_nV_m clusters was used by Russell [13]. He used a thermodynamic approach to calculate the free energy change in forming a cluster of He_nV_m type. He found a steady increase in the free energy with increasing n and m until a saddle point was reached at n=6 and m=11. Beyond this combination the free energies decreased with increasing n and m. Russell also investigated the stability of clusters and concluded that the most stable would be around He_6V_{11} beyond which the cluster can grow freely by vacancy and/or gas

atom acquisition. A similar trend was suggested by atomistic calculations where a critical combination of a few vacancies and helium atoms (He_3V_2), if exceeded, gave rise to a stable cluster [2].

In summary, we can see that helium will agglomerate in defects that will minimize the lattice strain, such as mono-, di-, tri-, or multivacancies. The lowest motion activation energy is for helium to move interstitially. This migration energy increases by a factor of about 4 (see Table I) if helium is trapped inside a vacancy. The presence of helium will also reduce the mobility of the entrapping vacancy. Once entrapped, the pop-out or dissociation energy decreases as the number of helium atoms inside that cluster increases.

Both theoretical approaches predict a stable He_nV_m cluster beyond which growth is ensured by acquiring vacancies or helium atoms. However, it is important to note that direct application of these atomistic or thermodynamic results to the nucleation and growth problem of the He_nV_m clusters does not readily follow, since the effect of irradiation can not be included.

Recently the interaction of a free self-interstitial with a single occupied vacancy has been considered as a helium replacement mechanism during irradiation [14,15]. Wilson et al. [14] have concluded that a first neighbor self-interstitial was able to displace substitutional helium in copper. This re-solution mechanism is energetically possible because the required detrapping energy is smaller than the energy produced by the interstitial-vacancy recombination. Table IV shows the detrapping and recombination energies for various metals [14].

TABLE IV
HELIUM DETRAPPING AND
INTERSTITIAL-VACANCY RECOMBINATION ENERGIES

	E_{He}^{de-tr}	E_{v-i}^{rec}
Cu	1.88	3.81
Ni	3.16	4.81
Ag	1.53	4.15

De Hosson et al. [16] have examined a much neglected helium trapping site, the edge dislocation. They used an atomistic approach to study molybdenum (Mo) and tungsten (W). In both Mo and W, the dissociation energy of a helium roughly doubles from ~ 1.95 eV from an edge dislocation to ~ 4.2 eV from a vacancy in Mo. In other words, the helium atom is bound nearly twice as strongly in a vacancy than it is on an edge dislocation. In addition de Hosson, et al. [16] have also calculated the migration energy of helium (0.3 to 0.4 eV) along an edge dislocation to be in the same range as interstitial helium migration through the bulk (0.4 eV for Mo and W). This suggests the possibility of pipe diffusion along edge dislocation until a jog is encountered.

1.2. A Continuum Approach to Calculations of Helium-Vacancy Binding Energies

As discussed in Sect. 1.1, atomistic calculations by Wilson et al. [2,3,7,8,14] have provided binding energies for small HVCs up to ~ 20 constituents. However, because of computational limitations, these calculations can not be extended to investigate larger HVCs. Since this thesis is aimed at investigating the development of HVCs from embryo to bubbles, we need helium-vacancy binding energies that span the whole

size range. While extrapolation of these atomistic results to larger size HVCs is not feasible, the use of ideal gas laws describing helium gas thermodynamics inside cavities has been shown to be erroneous, especially for small cavities. Wolfer et al. [17] have estimated helium pressures to reach 10^6 to 10^9 atm. for small cavities which are close to liquid helium pressures.

In order to determine the binding energies of helium atoms and vacancies to larger HVCs, we have resorted to a continuum approach. This approach immediately points to the question of a valid equation of state (EOS) for helium which takes into account the high pressures caused by a large number of helium atoms to of vacancy ratios in HVCs. Such a numerical equation has been formulated by Wolfer et al. [17] using interatomic He-He and He-metal potentials. We have utilized Wolfer's numerical EOS to determine vacancy and helium binding energies to HVCs [18] by estimating the compressibility factor as a function of temperature and helium density. A description of our work is given below.

The work done in compressing residing helium atoms when a vacancy is emitted from a cluster is calculated by

$$W = - \int_{V_1}^{V_2} P \, dV \quad , \tag{1}$$

where W = reversible work done in compressing helium,

V = volume of bubble,

P = pressure.

Expressing the pressure in terms of virial coefficients we have

$$\frac{PV}{kT} = z = 1 + \frac{B}{V} + \frac{C}{V^2} + \cdots \quad , \tag{2}$$

and substituting Eq. (2) into Eq. (1) we obtain, using up to three virial coefficients, the following expression for the work

$$W = -kT\left[\ell n\left(\frac{V_2}{V}\right) - B\left(\frac{1}{V_2} - \frac{1}{V_1}\right) - \frac{C}{2}\left(\frac{1}{V_2^2} - \frac{1}{V_1^2}\right)\right] \quad . \tag{3}$$

The virial coefficients, B and C, are obtained by fitting Eq. (2) to Wolfer's numerical EOS over a limited pressure range. Knowing the work done in compressing helium atoms, we now estimate the binding energy E_V^B of the last vacancy to a HVC by adding to it the energy gained from the change in surface area ΔE_S, and the vacancy formation energy E_V^F:

$$E_V^B \sim E_V^F + \Delta E_S + W \quad , \tag{4}$$

$$E_v^S = (36\ \pi\Omega^2)^{1/3}\ v^{2/3}\gamma \quad , \tag{5}$$

$$\Omega \simeq a_o^3/4 \quad , \tag{6}$$

where a_o is the lattice constant, Ω is the atomic volume, and γ is the surface tension of the solid ($\sim$ 500 ergs/cm^2 for stainless steel). The derivation of Eq. (4) is based on the classical drop model [19] which will be elaborated on in Sect. 2.3. Using the above approach, we are now able to evaluate the vacancy binding energy as a function of the number of vacancies, the number of helium atoms per HVC, and

temperature. The results of such calculations for Ni parameters for the binding energy of the last vacancy are shown in Fig. 6.

As physically expected, Fig. 6 shows that for small helium-vacancy ratios of large clusters, the vacancy binding energy approaches the vacancy formation energy. This is due to the fact that at low helium-vacancy ratios, the work done in compressing helium atoms is negligible and with increasing size, the change in surface energy decreases also.

For large helium-vacancy ratios the compression work becomes quite large, approaching few electron volts. This means that a vacancy is practically undetachable for large helium-vacancy ratios. Figure 6 shows correct trends of our approach for helium-vacancy binding energies to large sized HVCs. However, to compare our continuum model to atomistic results of small HVCs, we produced a series of 2-D plots comparing our results of binding energies to those of Wilson et al. [2]. Figure 7 demonstrates such comparisons for the helium binding energies E_H^B. Agreement between atomistic and continuum calculation increases as the size of the HVC increases.

In evaluating the helium binding energy, we use a straight line approximation for evaluating the change in energy content of the HVC when a helium atom is emitted. Thus Eq. (1) is approximated by

$$W = -(P_2 + P_1)(V_2 - V_1) \quad . \tag{7}$$

The straight line approach was chosen because we no longer have a thermodynamic system of constant mass when a helium atom is emitted. By reducing the helium content of the HVC by one atom, we effectively

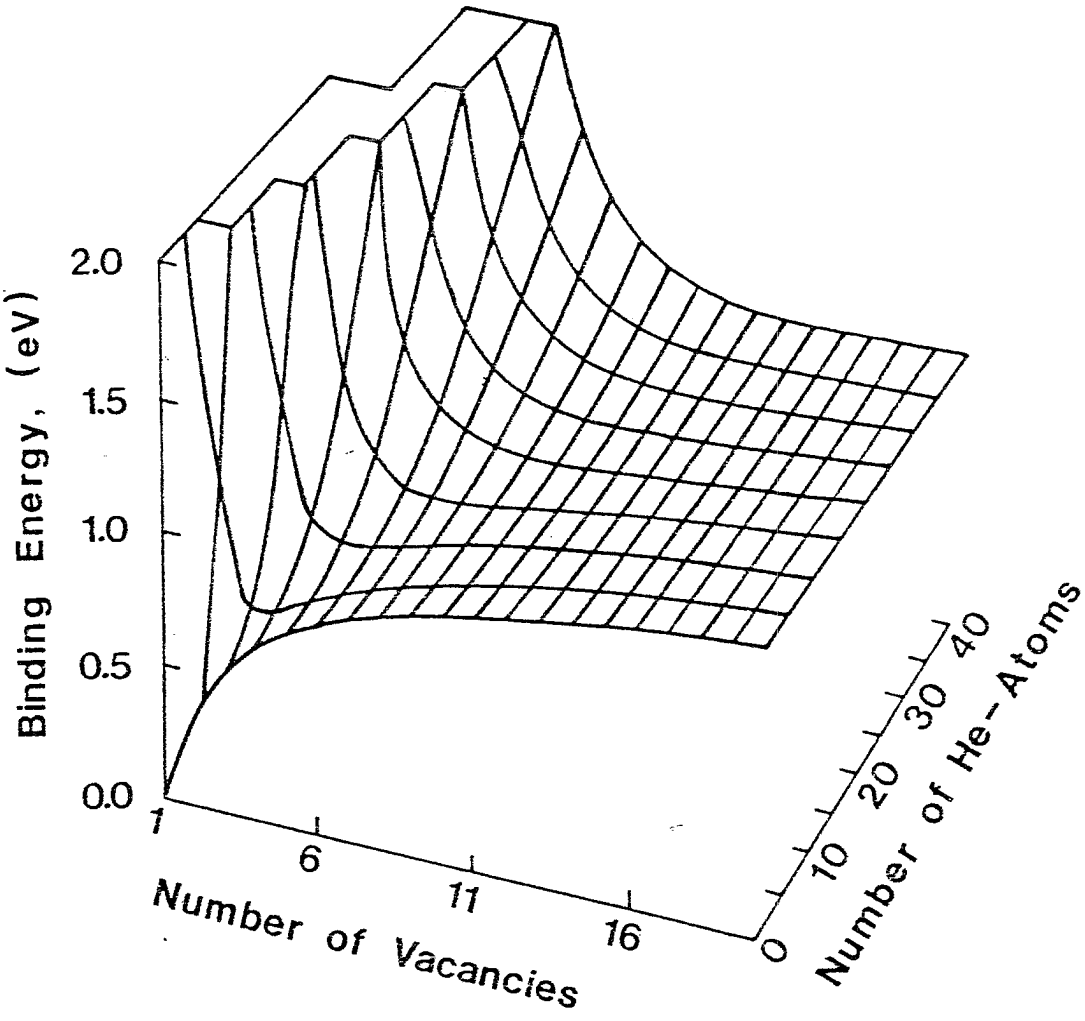

Fig. 6. Binding energy of the last vacancy to a HVC as a function of number of vacancies and helium at./HVC, using a continuum approach in stainless steel at T=500°C [18].

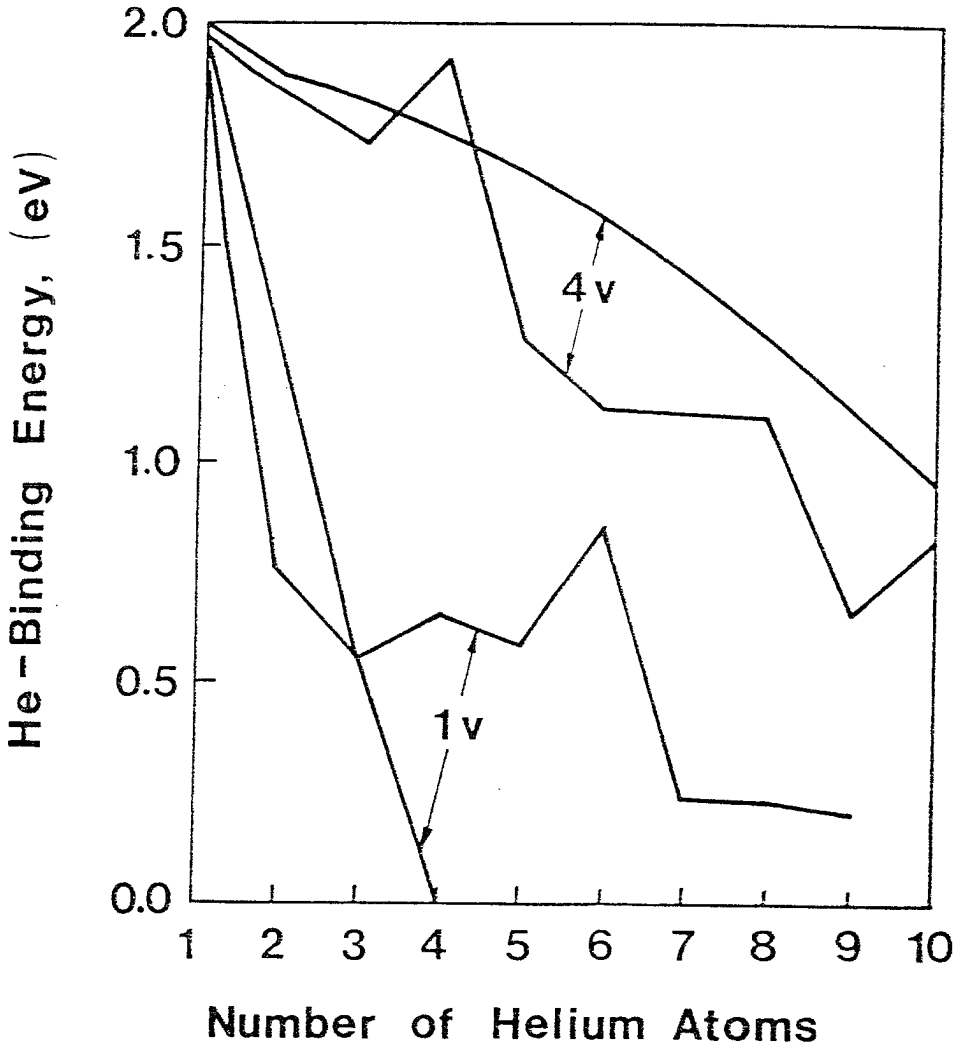

Fig. 7. Comparison of atomistic [2] to continuum helium binding energies [18] to a single-, and to a low-vacancy cluster (continuum--smooth curve).

evaluate the energy gained in allowing n-1 helium atoms to expand to a new low pressure.

The helium binding energy is evaluated by adding the energy of the "heat of solution" (E_H^S) of helium to the expansion work.

$$E_H^B = E_H^S + W \quad . \tag{8}$$

Ingelsfield and Pendry [20] concluded that it takes at least 2.07 eV to keep a helium atom dissolved in a molybdenum matrix. We have used $E_H^S \sim 3.5$ eV because no precise value is yet available for Ni or stainless steel. Furthermore, Fig. 7 shows that with $E_H^S \sim 3.5$ eV we get the best agreement with atomistic E_{He}^B for Ni parameters.

From these comparisons (Fig. 7), it can be seen that our continuum approach to evaluating helium and vacancy binding energies is applicable for large and small HVCs containing as little as two or three vacancies.

2. HELIUM TRANSPORT AND MIGRATION MECHANISMS THROUGH METALS DURING IRRADIATION

In order to model helium bubble nucleation and growth successfully, a sound understanding of helium transport and migration mechanisms has to be acquired.

Prior to this work, the only information regarding helium transport through metals was based upon a very few experimental results. Theoretically, very few attempts were made to describe helium transport under irradiation [21]. This is due to the complexity of helium migration paths through metals. Therefore, our analytical and numerical

approaches to this problem constitute a pioneering effort in this field. The results of our findings were published in 1983 (see Ref. [22]). Most of the experimental information regarding helium migration and clustering has been obtained from thermal desorption measurements [23,24].

Helium is introduced first by implantation into a solid. Then the material is heated at a constant rate under ultra-high vacuum. The desorbed helium is monitored by a quadropole mass spectrometer and the helium release rate is determined. The release rate peaks are then correlated with various vacancy helium reactions. For a review of experimental methods, see Ref. [23]. Although a controlled amount of damage is sometimes introduced in the sample before irradiation [23,24], the simultaneous interaction of helium and displacement damage has not yet been experimentally studied.

Through constant heating rate experiments on helium pre-implanted polycristaline nickel samples [23], an activation energy for helium migration at elevated temperatures was deduced. Similar experiments were performed on gold and copper [22]. At temperatures above two-thirds of the melting point, thermal vacancies dominate as helium traps. However, for these experiments to give useful information on helium-vacancy trapping, the matrix helium concentration had to be kept below 0.1 ppm [23]. This effectively ensured no precipitation of helium into cavities with consequent small release. Philips and co-workers [24] concluded that the effective helium diffusion coefficient in nickel D^{eff}, between 800° and 1250°C, can be expressed by

$$D_{He}^{eff} = 10^{-2.2\pm0.3} \exp\left(-\frac{0.81 \pm 0.04}{kT}\right)\left(\frac{cm^2}{s}\right) \quad , \tag{9}$$

where k is the Boeltzmann's constant and T is the temperature in °K.

The effective activation energy (0.81 eV) was interpreted as the difference between the dissociation energy of a helium atom in a substitutional site and the vacancy formation energy. Their calculated pre-exponential factor D_o is in agreement with Zener's [25] estimate. That is, for interstitial atom diffusion,

$$D_o \, a_o^2 \, \nu \approx 10^{-3} \frac{cm^2}{s} \quad , \tag{10}$$

where a_o is the lattice parameter and ν is the vibrational frequency of the interstitially diffusing atom.

More recently, Philips and Sonnenberg [24] measured helium interstitial diffusion in nickel. Due to the strong interaction of helium atoms with vacancies, vacancy generation during implantation was avoided. Using a low energy ion gun (~ 100 eV), they measured a helium interstitial migration energy E_{He}^M of 0.14 ± 0.03 eV.

Under irradiation conditions, where helium atoms are introduced concurrently with displacement damage, three more features complicate the understanding of helium transport. The first is the competition between self-interstitials and helium atoms to react with vacancies. Second, helium atoms tend to agglomerate with available vacancies, which effectively immobilizes helium. And third, displacement collision cascades can supply enough energy to remove helium "bound" in deep traps. In the following section, we present a comprehensive model for

the transport and clustering of helium in structural materials under irradiation. The theory is presented in Sect. 2.1, including possible reactions influencing helium migration during irradiation.

To understand and interpret the numerical results of the theory, an analytical model is presented in Sect. 2.2. While the numerical computations are essential, the analytical model is intended to guide the parameters of the theory and give exact values of the effective diffusion coefficient in limiting cases. In Sect. 2.3, results of our investigations are summarized and discussed.

2.1. Theory of Helium Transport

A major problem in formulating a theoretical model for helium migration lies in the complicated possibilities of helium interaction with point defects. During irradiation, helium reactions include:

1. Trapping and thermal detrapping of helium in single vacancies, divacancies, and higher order clusters,
2. Helium trapping at dislocations and grain boundaries,
3. Replacement of helium bound to single vacancies by self-interstitials,
4. Helium clustering into HVCs,
5. Displacement of trapped helium atoms by irradiation,
6. Migration of helium as an interstitial atom or in a divacancy.

Ignoring the majority of the above possibilities, Reed [21] developed a simple model for helium diffusion in irradiated materials. In this model, helium is assumed to be thermally detrapped from irradiation produced vacancies. The effective helium diffusion coefficient is expressed as:

$$D_{He}^{eff} = \nu_h \frac{\lambda^2}{6} C_V^{-2/3} \exp - \frac{E_{He}^D}{kT} \quad . \tag{11}$$

In this study, we include all of the possibilities outlined before. The basic assumption in our analysis is that helium point-defect interactions is homogeneous in time and space. As such, the discontinuous defect production nature due to the generation of collision cascades is not treated [26]. Reaction rate constants derived from spatial diffusion calculations were shown to be reproducible by Monte Carlo simulation of atomistic jumps [27]. In the present model, reaction rate constants are derived by extending Chandrasekhar's earlier treatment of coagulation [28]. In a previous paper [29], a simplified rate theory was developed for the analysis of the effects of helium on swelling. The focus of the present work is twofold:

1. Determination of the helium effective diffusion coefficient.

2. Calculation of the time-dependent nucleation rates for small HVCs.

2.2. Rate Equations

The effect of mobile helium on cavity nucleation during irradiation has been considered by Loh [30], Russell and Hall [31], Wiedersich et al. [19], and Wiedersich and Hall [32]. The basic approach has been to solve a set of algebraic equations that define "constrained equilibrium" cluster concentrations. An effective free-energy surface is then established, from which a nucleation rate is calculated. Helium was included in the classical nucleation analysis by effectively reducing the energy required to create the cavity surface, and hence was found to help increase cavity nucleation rates. Various assumptions had to be made regarding helium mobility, and its role in stabilizing cavities.

The approach used in our work has a different basis. Chemical reaction rate theory is used to describe clustering events between randomly migrating species. This method has been first used to calculate nucleation rates of fission gas bubbles in nuclear fuels [33]. More recently, Hall [34] used chemical reaction rate theory to analyze point-defect clustering in the presence of mobile helium. In order to calculate nucleation rates of HVCs, however, the mobility and binding energies must be included in the calculations. The detailed description of the time-dependent concentrations of HVCs is therefore essential. The influence of helium migration on clustering and vice versa is the major difference between our approach and previous attempts [30-32].

The following set of equations describe the time-dependent concentrations of various helium point-defect clusters (see Nomenclature for symbols):

Unoccupied Vacancies

$$\frac{dC_{10}}{dt} = (1-\varepsilon)G + Z_v^d D_v \rho_d (C_v^e - C_{10}) + gGC_{11}$$

$$+ (R_{I,20}C_{20} - R_{I,10}C_{10})C_I + \sum_{i=0}^{M}\sum_{j=0}^{N} (E_{ij}^v - R_{10,ij}C_{10})C_{ij} \quad . \qquad (12)$$

Self Interstitials

$$\frac{dC_I}{dt} = G - \sum_{i=1}^{M}\sum_{j=0}^{N} R_{I,ij}C_{ij}C_I - Z_I^d \rho_d D_I C_I - 2R_{I,I}C_I^2 \quad . \qquad (13)$$

Interstitial Helium

$$\frac{dC_{01}}{dt} = G_{He} - (Z_{He}^d D_{He} \rho_d + R_{10,01}C_{10})C_{01} + R_{I,11}C_I C_{11}$$

$$+ Z_{He}^d D_{He} \rho_d C_{01}^e + \sum_{i=1}^{M}\sum_{j=1}^{N} (E_{ij}^{He} + jgG - R_{01,ij}C_{01})C_{ijk} \quad . \qquad (14)$$

Divacancies

$$\frac{dC_{20}}{dt} = 0.5(\varepsilon G + R_{10,10}C_{10}^2) - (\sum_{i=0}^{M}\sum_{j=0}^{N} R_{ij,20}C_{ij} + Z^d{}_{20} D_{20} \rho_d$$

$$+ R_{I,20}C_I + E_{20}^v)C_{20} + (E_{30}^v + R_{I,30}C_I)C_{30} + E_{21}^{He}C_{21} \quad . \qquad (15)$$

Complexes Containing m Vacancies and n Helium Atoms

$$\frac{dC_{mn}}{dt} = E^{He}_{m,n+1}C_{m,n+1} - \Big(\sum_{i=0}^{M}\sum_{j=0}^{N} R_{ij,mn}C_{ij} + Z^{d}_{mn}D_{mn}\rho_d + ngG + R_{I,mn}C_I + E^{He}_{mn} + E^{v}_{mn}\Big)C_{mn} + \big(E^{v}_{m+1,n} + R_{I,m+1,n}C_I\big)C_{m+1,n} + \sum_{\substack{i+k=m \\ j+l=n}} R_{ijkl}C_{ij}C_{kl} \quad , \qquad (16)$$

Equations (12)-(16) are not amenable to analytical solutions in the present form. The Gear [35] implicit multi-step numerical integration methods are therefore used for the solution of this set of stiff equations. A brief outline of the calculational method for the reaction rates of the previous set of equations is given below. It is important to note that in Eqs. (12)-(14), reactions in the double sum over i and j should be implemented only once. Rates similar to $R_{oo,mn}C_{mn}C_{oo}$ are meaningless, and therefore are not included. Also, reactions involving diffusivities of immobile species will naturally be set to zero.

2.3. Reaction Rates

2.3.1. Impingement Rates. Gosele [39] studied the ways by which defect clusters react, and classified the calculational methods for their rate constants into the jump method for surface reactions and the diffusion method for diffusion-limited reactions. In the jump method, which is more suitable for small clusters [37], the reaction rate constant for the impingement is given by:

$$R_{\alpha,mn} = K^{\alpha}_{mn}\Gamma_{\alpha} \quad , \qquad (17)$$

where

$$K_{mn}^{\alpha} = \text{effective surface area/area per atom} \quad ,$$

$$= \text{combinatorial number for the interaction of mobile defect } \alpha \text{ with an m-n complex} \quad ,$$

$$\Gamma_{\alpha} = \text{jump frequency of defect } \alpha \quad ,$$

$$= \nu_{\alpha} \exp(- E_{\alpha}^{M}/kT) \quad . \tag{18}$$

The effective surface area can be written in terms of an effective trapping radius R_{tr} and the area per atom,

$$K_{mn}^{\alpha} = \frac{4\pi R_{tr}^{2}}{\lambda^{2}} \quad . \tag{19}$$

The combinatorial number K_{mn}^{α} can be dependent on a number of variables. It has been recently shown by Fastenau [27] that this number is dependent on both sink concentration and temperature. Their conclusions are based on Monte Carlo studies of helium-vacancy interactions.

In order to determine the combinatorial numbers, we consider two groups of cavities. In the first group, $m > n$ (number of vacancies is larger than the number of helium atoms per cluster), and in the second group $m \leq n$. For the case $m > n$, the cavity will behave like a void, and the trapping radii of these clusters for mobile species can be determined from the bias calculations of Wolfer et al. [38]. The effective trapping radius R_{tr} is related to the bias factor Z by

$$R_{tr}^{eff} = R(m)Z(m) \quad , \tag{20}$$

where R(m) is the physical radius of the cluster containing m vacancies. The bias factor Z(m) is calculated directly from Ref. [38]. When $m \leq n$, cavities will contain more helium than vacancies. The approach taken by Wolfer et al. [14] will no longer be applicable because of the difference in the strain field around the cluster. Based upon thermal desorption measurements, Kornelson et al. [39] proposed an empirical equation for the effective trapping radius of the cluster. This is expressed as

$$R_{tr}(n) = R_o[1 + 0.25(1+n)] \quad 1 \leq n \leq 10 \quad , \tag{21}$$

where R_o is the physical radius of the cluster. The results of this combinatorial analysis are shown in Table V. The results are shown only for vacancies and interstitial atoms. However, the other mobile species are approximated by either a vacancy or an interstitial for the calculation of their respective combinatorial numbers. It is to be noted that the values in Table V are in general agreement with the Monte Carlo calculations of Fastenau et al. [27].

Vibrational frequencies ν_α of the mobile species are not well known. If the average vibrational frequency of an interstitial atom is taken as 5×10^{13} sec^{-1}, the following values are simply estimated:

single vacancy	$- \nu_V = 5 \times 10^{12}$ sec^{-1}
divacancy	$- \nu_{V_2} = 1 \times 10^{12}$ sec^{-1}
interstitial helium	$- \nu_{He} = 5 \times 10^{13}$ sec^{-1}
self-interstitial	$- \nu_i = 5 \times 10^{13}$ sec^{-1}
single helium divacancy	$- \nu_{Hev_2} = 5 \times 10^{12}$ sec^{-1}

TABLE V
COMBINATORIAL NUMBERS FOR SOME HVCs

	Complex	K^{v}_{mn}	K^{i}_{mn}
m>n			
	HeV	11.84	45.49
	He_2V_2	16.09	53.53
	He_3V_3	19.50	59.54
	HeV_2	16.09	53.54
	HeV_3	19.50	59.59
m<n			
	He_2V	20.0	20.72
	He_3V_2	35.46	35.46

2.3.2. Emission Rates. Two different approaches have been usually used to determine the emission rates E^{v}_{mn} and E^{He}_{mn}. The first method as proposed by Wiedersich et al. [19] uses the idea of detailed balance on a hypothetical equilibrium Boltzmann-distribution of voids. This approach is sometimes referred to as the classical drop model. The emission rate is given by

$$E^{v}_{mn} = K^{v}_{mn}\ \nu_v\ \exp\left(-\ E^{v}_{M}/kT\right) C^{eq}_{01}\ \exp(-\ \Delta F/kT) \quad , \tag{22}$$

where ΔF is the free energy change in the emission process. The free energy is calculated using the Wiedersich-Hall model [32], where ΔF depends on the surface energy and the work done on the helium gas. When the cluster size is small, this approach may not be valid. The concepts

of surface energy and of gas pressure are suspect when there are only few gas atoms and vacancies in a cluster.

Small HVCs are treated by a different method in our analysis. The emission rate of a vacancy is given by

$$E^{V}_{mn} = (\text{no. of sites for emission}) \times (\text{vib freq}) \times (\text{probability of dissociation})$$

$$= K^{V}_{mn}\ \nu_{V}\ \exp\left[-\left(E^{V}_{B} + E^{V}_{M}\right)/kT\right] \quad . \tag{23}$$

Comparing Eqs. (22) and (23), the energy needed for the binding of the last vacancy to a cluster containing m vacancies and n helium atoms is therefore given by

$$E^{V}_{B} = \Delta F + E^{V}_{F} \quad . \tag{24}$$

The binding energy E^{V}_{B} is shown in Fig. 7 as a function of the number of vacancies in a cluster. The solid line is obtained by using the classical drop model, and the discrete points are computer simulations or deduced from measurements, as in Table VI.

The thermal emission rates of helium atoms are calculated using the method described. Values, calculated, are in basic agreement with Refs. [40,41] and [43-46].

TABLE VI
DEFECT PARAMETERS FOR NICKEL AND COPPER

Defect, α	Migration Energy, E_M^α (eV)	Vacancy Binding Energy, E_B^v (eV)	Helium Atom Binding Energy, E_B^{He} (eV)
v	1.4 [40]		
i	0.2 [44]		
2v	0.9 [45]	0.25 [40]	
He	0.08 [27], 0.17 [42]		
He_s	3.26 [43]	2.15 [41]	2.15 [41]
He_2V_2		1.27* [6]	1.84* [41]
He_3V_3		1.20* [6]	1.84* [41]
He_2V		3.87* [6]	0.79 [41]
HeV_2	1.35 [43]	0.47 [40]	1.84 [41]
He_3V_2		1.79* [6]	1.09* [41]
He_2V_3		0.45* [41]	1.84* [41]

*Values for pure copper.

Finally, the coefficients for the migration of mobile species to dislocations are calculated from their jump frequencies Γ, using the relationship

$$D_\alpha = f_\alpha \lambda_\alpha^2 \Gamma_\alpha \quad , \tag{25}$$

where f_α is a numerical factor of order unity and λ_α is the jump distance for defect α.

2.4. Analytical Model for Helium Transport

While the set of equations [Eqs. (12-16)] describes the basic features of helium and point-defect interactions, it must be numerically integrated under any given conditions. This can be computationally tedious if the most important underlying physics is not clearly brought out. In an attempt to guide the numerical model of Sect. 2.1, and to find exact expressions for the helium effective diffusion coefficient, we present a simplified analytical model in this section. The basic assumptions of the present model are:

1. The system is considered to contain the following defects: interstitial helium atoms, substitutional helium atoms, vacancies, self-interstitials, dislocations, and a cavity size distribution.

2. This system is in quasi-equilibrium (steady state).

3. Nucleation and clustering are ignored; existing cavities are only in a state of growth.

4. The divacancy population is negligible.

2.4.1. Simplified Steady-State Rate Equations.

Unoccupied Vacancies

$$G + G_T + E_{11}^{He} C_{11} + gGC_{11}$$

$$- R_{I,10} C_{10} C_I - R_{01,10} C_{01} C_{10} - K_{10} C_{10} = 0 \quad , \tag{26}$$

where

G_T = thermal vacancy rate

$$= D_v C_v^e \{ Z_v^d \rho_d + Z_v^c \int dr_c 4\pi r_c N(r_c) \exp\left[\left(\frac{2\gamma}{r_c} - P_g \right) \frac{\Omega}{kT} \right] \} \quad , \tag{27}$$

$$K_{10} = D_v \left[Z_v^d \rho_d + Z_v^c \int 4\pi r_c N(r_c) dr_c \right] \quad . \tag{28}$$

Self-Interstitials

$$G - R_{I,10} C_{10} C_I - R_{I,11} C_{11} C_I - K_I C_I = 0 \quad , \tag{29}$$

where

$$K_I = D_i \left[Z_i^d \rho_c + Z_i^c \int 4\pi r_c N(r_c) dr_c \right] \quad . \tag{30}$$

Interstitial Helium

$$G_{He} + E_{11}C_{11}^{He} + R_{I,11}C_I C_{11} + D_{He}Z_{He}^{d}\rho_d\left(C_{01}^{eq} - C_{01}\right)$$

$$+ \int \{[E^{He}(r_c) + jgG - R_{01,r_c}C_{01}]\}4\pi r_c N(r_c)dr_c$$

$$- R_{01,10}C_{01}C_{10} = 0 \quad . \tag{31}$$

Substitutional Helium

$$R_{01,10}C_{01}C_{10} - E_{11}^{He}C_{11} - gGC_{11} - R_{I,11}C_{11}C_I = 0 \quad . \tag{32}$$

Equations (26), (29), (31), and (32) are equivalent to Eqs. (12), (13), (14), and (16), respectively.

Understanding helium clustering and transport under irradiation can be acomplished by the simultaneous solution of the set of Eqs. (12-16). When clustering is neglected, the solution of Eqs. (26-32) provides a simplified insight into the problem of helium transport at steady state. An effective helium diffusion coefficient for helium migration is defined as

$$D_{He}^{eff} \sum_{m=0}^{M} \sum_{n=0}^{N} C_{mn} = \sum_{m=0}^{M} \sum_{n=0}^{N} D_{mn}C_{mn} \quad , \tag{33}$$

where the sums in Eq. (33) are only for mobile species. In the special case where helium is transported only as an interstitial or a substitutional atom, Eq. (33) simplifies to

$$D_{He}^{eff} (C_{11} + C_{01}) = D_{01}C_{01} + D_{11}C_{11} \quad . \tag{34}$$

Since $D_{11} \ll D_{01}$, Eq. (34) gives

$$D_{He}^{eff} \simeq \frac{D_{01}C_{01}}{C_{11} + C_{01}} \quad . \tag{35}$$

Solving Eq. (32) for C_{01}, and substituting back in (35)

$$D_{He}^{eff} \simeq \frac{D_{01}\left(E_{11}^{He} + gG + R_{I,11}C_I\right)}{\left(R_{01,10}C_{10} + E_{11}^{He} + gG + R_{I,11}C_I\right)} \quad . \tag{36}$$

Equation (36) gives the effective diffusion coefficient of helium in terms of the following quantities: the interstitial helium diffusion coefficient, the helium-vacancy binding energy, capture radii for point-defect reactions, the helium radiation displacement rate, and the vacancy and interstitial and diffusion coefficients concentrations . In the following, we will analyze limiting cases for the solution of Eq. (36).

2.4.2. Helium Effective Diffusion Coefficient in Limiting Cases.

2.4.2.1. Domination by thermal detrapping. In this case, the thermal dissociation rate of substitutional helium is greater than the interstitial replacement rate and the radiation displacement rate. Equation (36) therefore becomes:

$$D_{He}^{eff} = \frac{D_{01} E_{11}^{He}}{R_{01,10} C_{10} + E_{11}^{He}} \quad , \tag{37}$$

substituting for E_{11}^{He} [Eq. (23)], $R_{01,10}$ [Eq. (17)], and setting C_{10} = thermal equilibrium vacancy concentration, we obtain

$$D_{He}^{eff} = \frac{\alpha \exp\left[-\left(E_{Hev}^{B} + E_{He}^{M} - E_{v}^{f}\right)/kT\right]}{1 + \beta \exp\left[-\left(E_{Hev}^{B} - E_{v}^{f}\right)/kT\right]} \quad , \tag{38}$$

where,

$$\beta = \frac{K_{11}^{v}}{K_{01}^{10} \exp(S_{v}^{F}/k)} \quad , \tag{39}$$

and

$$\alpha = \beta D_{He}^{o} \quad . \tag{40}$$

This equation reverts to the expression derived by Philips and co-workers [42] for $E_{Hev}^{B} > E_{v}^{f}$.

2.4.2.2. Domination by replacement reaction. When the irradiation temperature is low enough for thermal detrapping to be negligible, substitutional helium can only be detrapped by the effect of irradiation. This may be direct by irradiation displacement or indirect by self-interstitials replacing helium in the substitutional sites. We will now derive an approximate expression for the latter case. In this case, Eq. (36) becomes

$$D_{He}^{eff} = \frac{D_{01} R_{I,11} C_{I}}{R_{01,10} C_{10} + R_{I,11} C_{I}} \quad , \tag{41}$$

and substituting for $R_{I,11}$, $R_{01,10}$, and D_{01} we obtain

$$D_{He}^{eff} = \frac{\nu_{He}\lambda^2 e^{-E_{He}^M/kT} K_{11}^I \nu_I e^{-E_I^M/kT} C_I}{K_{11}^I \nu_I e^{-E_I^M/kT} C_I + K_{01}^{10} \nu_{He} e^{-E_{He}^M/kT} C_{10}} \quad . \tag{42}$$

However, at steady state

$$\overline{Z}_I D_I C_I = \overline{Z}_v D_v (C_{10} - \overline{C_{10}^e}) \quad , \tag{43}$$

where $\overline{C_{10}^e}$ is the average thermal-vacancy concentration and the Z's are weighted averages of the sink capture efficiencies. When several not too stringent conditions are satisfied, the effective helium-diffusion coefficient takes a much simpler form. Under the following conditions

$$C_{10} >> \overline{C_{10}^e} \quad , \tag{44}$$

$$E_{He}^M << E_v^M \quad , \tag{45}$$

$$\overline{Z}_v \simeq \overline{Z}_i \quad , \tag{46}$$

the effective helium-diffusion coefficient simplifies to

$$D_{He}^{eff} = \eta D_v \quad , \tag{47}$$

where $D_v \equiv D_{10}$ = vacancy-diffusion coefficient, and η is a factor of order unity given by

$$\eta = K_I^{11}/K_{01}^{10} \quad . \tag{48}$$

2.4.3. Domination by Displacement Reaction. The rate of displacement of helium from vacancies is greater than both the thermal-dissociation and the self-interstitial replacement rates. Under these conditions, Eq. (36) becomes

$$D_{He}^{eff} = \frac{D_{01} gG}{R_{01,10} C_{10} + gG} \quad . \tag{49}$$

Using Eqs. (17) and (18) for $R_{01,10}$, the effective helium-diffusion coefficient is

$$D_{He}^{eff} = \frac{D_{01} gG}{K_{01}^{10} \nu_{01} \exp(-D_{He}^{M}/kT) C_{10} + gG} \quad . \tag{50}$$

In order to simplify Eq. (49), an appropriate expression for C_{10} must be substituted. This depends on whether point-defect concentrations are controlled by either mutual recombination or by diffusion to sinks. For mutual recombination to dominate, the following condition must be satisfied [46]

$$R >> 1 \quad , \tag{51}$$

where

$$R = \frac{4K_{01}^{I} G \exp(E_{v}^{M}/kT)}{S_I S_v \nu_v \lambda^4} \quad . \tag{52}$$

If $R >> 1$ (recombination-dominated regime), the vacancy concentration C_{10} is given by [46]:

$$C_{10} \approx \left(\frac{\lambda^2 G\ S_I}{K_{01}^I\ S_v}\right)^{1/2} D_v^{-1/2} \quad . \tag{53}$$

Substituting in Eq. (50) and rearranging, we obtain

$$D_{He}^{eff} = \phi(G\ D_v)^{1/2} \quad , \tag{54}$$

where

$$\phi = \frac{g}{\lambda K_{01}^{10}}\left(\frac{K_{01}^I\ S_v}{S_I}\right)^{1/2} \quad . \tag{55}$$

In deriving Eq. (54), the second term gG in the denominator of Eq. (50) is much smaller than the first term, for any reasonable combination of parameters.

On the other hand, when point-defect diffusion to sinks is more dominant ($R \ll 1$), the vacancy concentration becomes

$$C_{10} \approx \frac{G}{D_v\ S_v} \quad , \tag{56}$$

and the effective helium-diffusion coefficient in Eq. (50) takes the form

$$D_{He}^{eff} = \Psi\ D_v \quad , \tag{57}$$

where

$$\Psi = g\lambda^2\ S_v/K_{01} \quad . \tag{58}$$

2.4.4. Conditions for the Validity of Approximations. In this section, we will derive formulas representing the conditions under which the previous approximate treatments of D_{He}^{eff} are valid.

2.4.4.1. Domination by thermal detrapping. In this case the thermal emission rate must be large:

$$K_{11}^{He} \nu_{He} \exp[-(E_{He}^{M} + E_{Hev}^{B})/kT] >> \frac{gG}{(K_{11}/\lambda^2)D_I C_I} . \qquad (59)$$

This is satsified when

$$n\ G << 1 \quad , \qquad (60)$$

where

$$n = \frac{g \exp[(E_{He}^{M} + E_{He}^{B})/kT]}{K_{11}^{He} \nu_{He}} . \qquad (61)$$

Also, the following conditions must be satisfied

$$\varepsilon\ G << 1 \quad , \qquad (62)$$

$$\varepsilon = \frac{K_{11}^{I} \exp[(E_{Hev}^{B} + E_{He}^{M})/kT]}{K_{11}^{01} \lambda^2 \nu_{He} S_I} \quad , \qquad (63)$$

for diffusion-limited point-defect kinetics, and,

$$\xi\, G \ll 1 \quad , \tag{64}$$

$$\xi = \left(\frac{K_{11}^{I}}{K_{11}^{OI}}\right)^{2} \frac{\nu_v \exp\{2[E_{He}^{M} + E_{Hev}^{B} - (E_v^M/2)]/kT\}}{\nu_{He}^{2} K_{VI}} \quad , \tag{65}$$

for recombination-limited point-defect kinetics.

2.4.4.2. Domination by replacement reaction.

$$R_{I,11} C_I \gg \frac{gG}{K_{11}^{v} \nu_{He} \exp[-(E_{He} + E_{Hev})/kT]} \quad . \tag{66}$$

This is satisfied when both

$$\ell \gg 1$$

and $$\varepsilon\, G \gg 1 \quad , \tag{67}$$

for sink-controlled point-defect concentrations where

$$\ell = K_{11}^{I}/\lambda^2\, g\, S_I \quad . \tag{68}$$

For the case of recombination-limited point-defect kinetics, the following must be satisfied:

$$m\, G^{-1/2} \gg 1$$

and $$\xi\, G \gg 1 \quad , \tag{69}$$

where

$$m = \frac{K_{11}^{I} \nu_v}{g}^{1/2} \exp - \frac{E_v^M}{2kT} \quad . \tag{70}$$

The results of Eqs. (67) and (69) are straightforward substitutions in Eq. (66).

2.4.4.3. Domination by radiation displacement.

$$gG >> \frac{R_{I,11} C_I}{K_{11}^{v} \nu_{He} \exp[-(E_{He}^{M} + E_{HeV}^{B})/kT]} \quad . \tag{71}$$

Equation (71) is satisfied when both

$$\ell << 1$$

and , (72)

$$nG >> 1$$

for diffusion-limited point-defect kinetics. For the case of recombination-limited kinetics, the following conditions must be satisfied:

$$mG^{-1/2} << 1$$

and . (73)

$$nG >> 1$$

2.5. Helium Transport Results

It is computationally prohibitive to solve the previous set of numerical equations for the entire range of material and irradiation conditions possible. Moreover, dominant reaction mechanisms are not

immediately clear. Therefore, we will first discuss the results of the analytical formulation, and then proceed to compare it to the more exact numerical computations.

Figure 8 shows the dominant detrapping mechanisms at any given combination of damage rate and irradiation temperature of well annealed nickel ($S_v \sim 10^9$ cm/cm^3). Recombination determines the kinetics of point defects for any combination of G and T above the line R=1. The effective helium-diffusion coefficient is determined therefore by thermal detrapping below the line $\xi G=1$. Immediately above this line, self-interstitial replacement of trapped helium becomes the dominant mechanism. It is interesting to note that the higher the damage rate, the higher the dividing temperature between interstitial replacement and thermal displacement as detrapping mechanisms. This is effectively a temperature shift because of the higher displacement damage rate. Above this temperature, the effective helium migration energy is the difference between the dissociation energy of bound helium and the vacancy formation energy. Below this temperature the effective helium migration energy is roughly the vacancy migration energy. At still lower temperatures, radiation displacement takes over as a dominant detrapping mechanism. For example, the irradiation temperature has to be below 350°K for radiation displacement to be dominant under reactor conditions ($G \simeq 10^{-6}$ dpa/s) and below 400°K under typical accelerator conditions ($G \simeq 10^{-3}$ dpa/s). At higher effective sink densities, point-defect concentrations are controlled by diffusion to sinks, except at very low temperatures. The dividing line for the temperature between

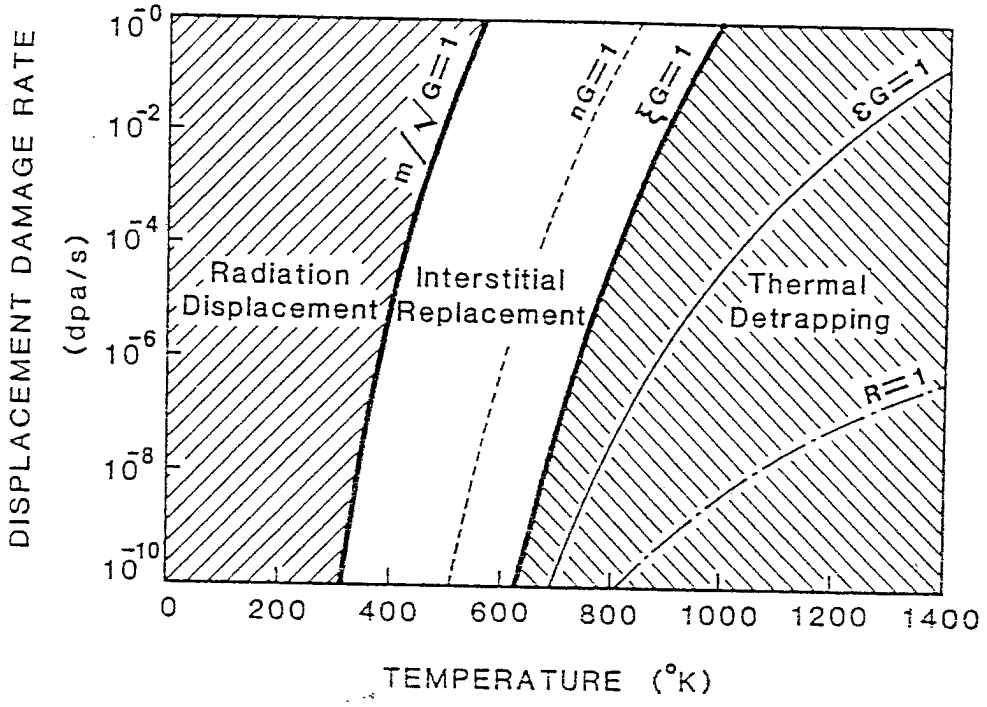

Fig. 8. Dominant detrapping mechanisms for given combinations of displacement damage rate and temperature at $S_v=10^9$ cm/cm^3 [22].

self-interstitial replacement and thermal detrapping is therefore $\xi G = 1$ above the line R=1, and $\xi G = 1$ below the line R=1, as shown in Fig. 9.

The validity of the analytical approximations is dependent on the attainment of conditions satisfying the basic assumptions. Many of the equations have been simplified by the assumption that the overall self-interstitial current to sinks is equal to the overall vacancy current to sinks. This is expressed as $\overline{Z}_I D_I C_I = \overline{Z}_v D_v (C_v - C_v^e)$; the bias factors $\overline{Z}_{I,v}$ being averaged over all sinks. This can be violated under two conditions: (1) when the time interval is less than a few vacancy mean lifetimes; and (2) when a fraction of the produced vacancies are retained in clusters that have a different mobility (divacancies), or immobile higher order clusters. Figure 10 shows the ratio of the interstitial to vacancy flux, as previously defined, for typical reactor irradiation conditions ($G = 10^{-6}$ dpa/s and $\rho_d = 10^{11} cm/cm^3$) allowing for clustering and divacancy formation. It is shown that at higher temperatures (> 800°K), divacancy and multiple vacancy cluster formation is very weak and the flux ratio reaches approximately unity within seconds. However, at lower temperatures, the ratio is much larger than unity at the start of irradiation and then gradually decreases to a steady-state value that is still larger than unity. The basic reason for this is the formation of vacancy clusters that change the balance between vacancies and self-interstitials. In order to have numerical computations that are based on the same analytical model, the calculations were again performed without allowing for divacancy or vacancy cluster formation, and the results are shown in Fig. 11. It is clear that the assumptions of the analytical approach are valid for times greater than few vacancy

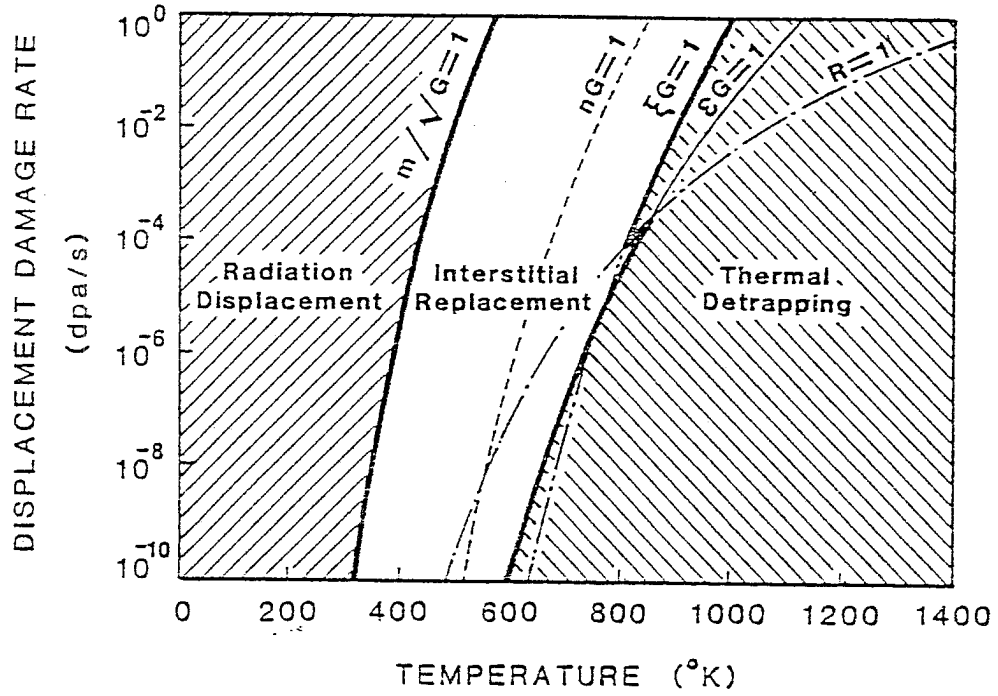

Fig. 9. Dominant detrapping mechanisms for given combinations of displacement damage rate and temperature at $S_v=10^{12}cm/cm^3$ [22].

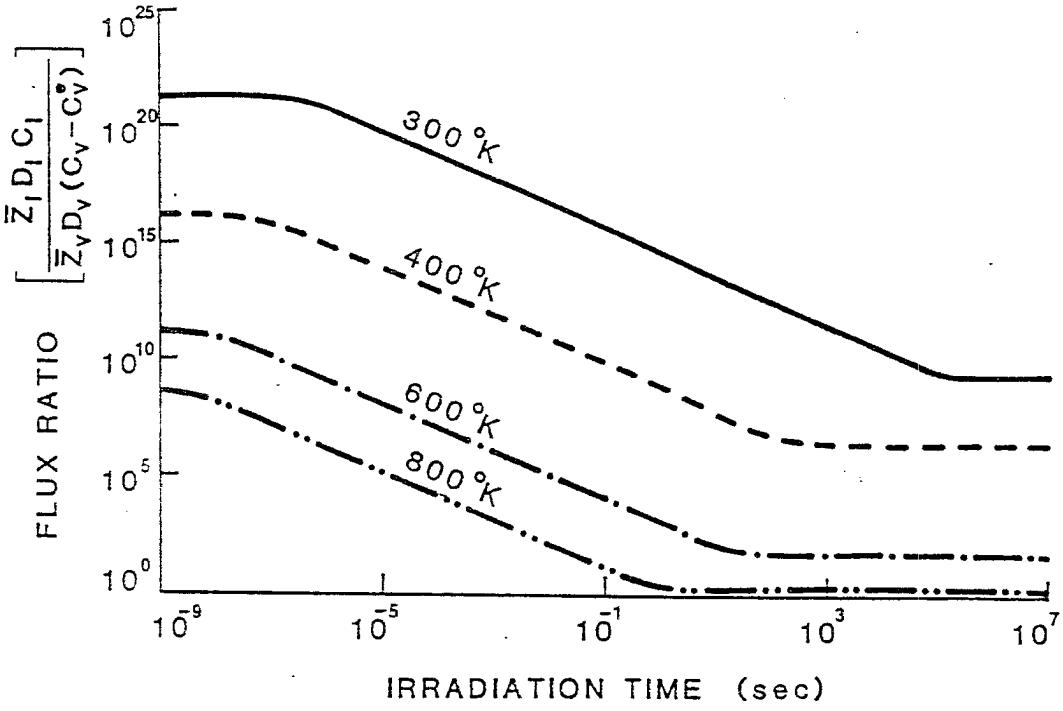

Fig. 10. The ratio of interstitial to vacancy flux for typical reactor conditions ($G=10^{6}$ dpa/s and $\rho_d=10^{11}$ cm/cm^3), allowing for clustering and divacancy formation [22].

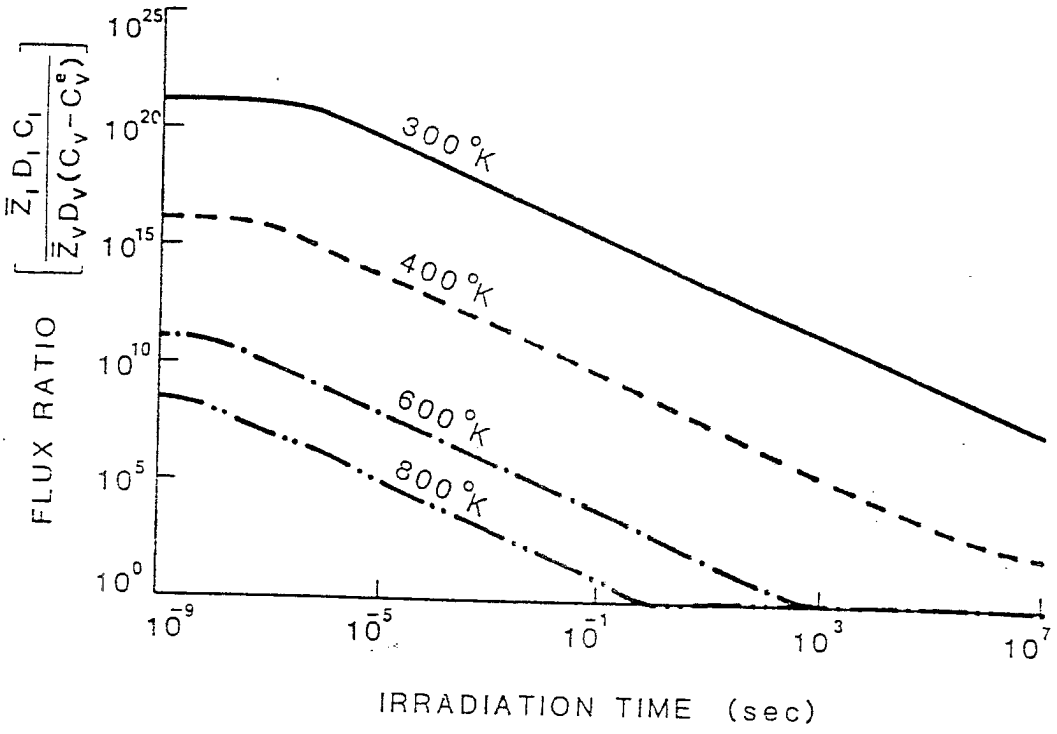

Fig. 11. Ratio of interstitial to vacancy flux for typical reactor conditions ($G=10^6$ dpa/s and $\rho_d=10^{11}$ cm/cm^3), without allowing for clustering and divacancy formation [22].

mean lifetimes. However, this can be very long at low temperatures as shown in Fig. 11. The mobile self-interstitial flux is orders of magnitude greater than the vacancy flux at temperatures lower than 450°K and irradiation times less than roughly one year.

A comparison between the numerical calculations and the analytical approximation for the effective helium diffusion coefficient is shown in Fig. 12. While the comparison is not meaningful at low temperatures because the point-defect concentrations are still building up, it shows that the analytical solution can be used as a first order estimate of D_{He}^{eff}. The agreement is almost perfect at very high temperature where thermal detrapping is the only operating mechanism for helium release from traps. At intermediate temperatures, the combination of detrapping mechanisms makes the numerically evaluated D_{He}^{eff} higher than the analytical approximation.

Further comparisons between the two methods are shown in Figs. 13 and 14. The effective helium migration energy during reactor irradiation for nickel is taken as the slope of D_{He}^{eff} vs 1/T as in Fig. 12. Allowing for vacancy clustering and divacancy formation in the numerical model, the effective migration energy is given in Fig. 13 as a function of temperature. Figure 14 shows similar results when clustering and divacancies are suppressed in the numerical model. The agreement is reasonable in Fig. 14, especially at the high temperature limit, and in that intermediate temperature regime. It is to be emphasized, however, that the analytical solutions are not intended to duplicate the more extensive numerical ones. Analytical estimates are used to explore

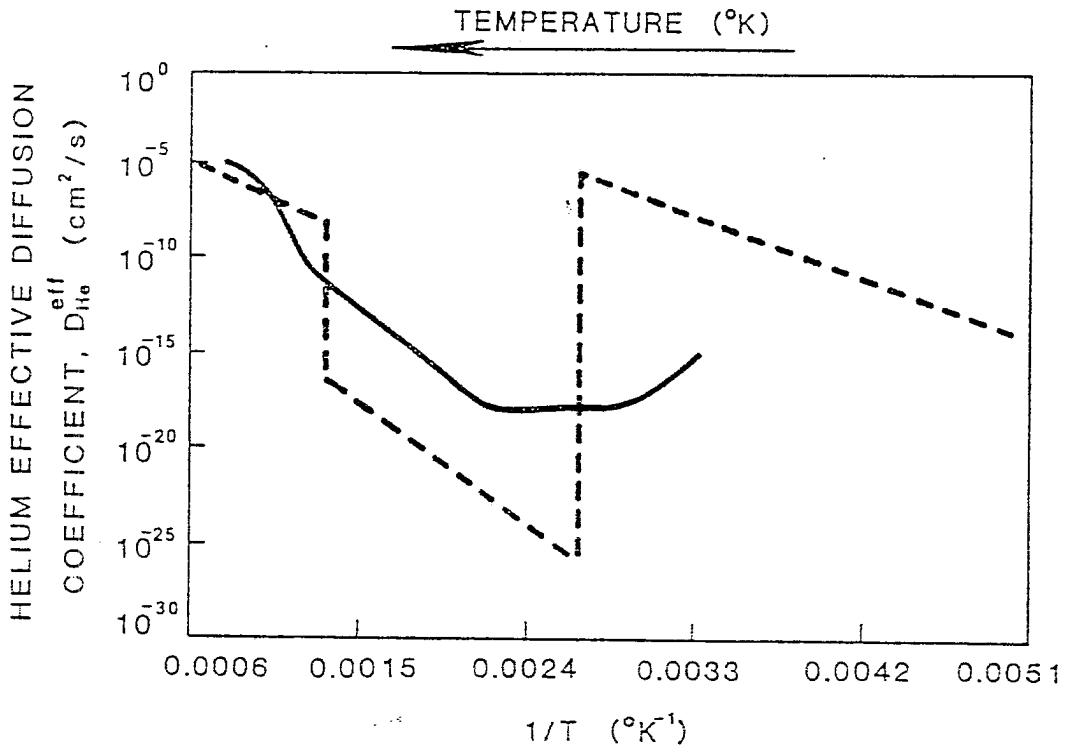

Fig. 12. Effective helium diffusion coefficient in nickel with no divacancies and no clustering [22]. (Dashed line is the analytical solution; solid line represents the numerical results.)

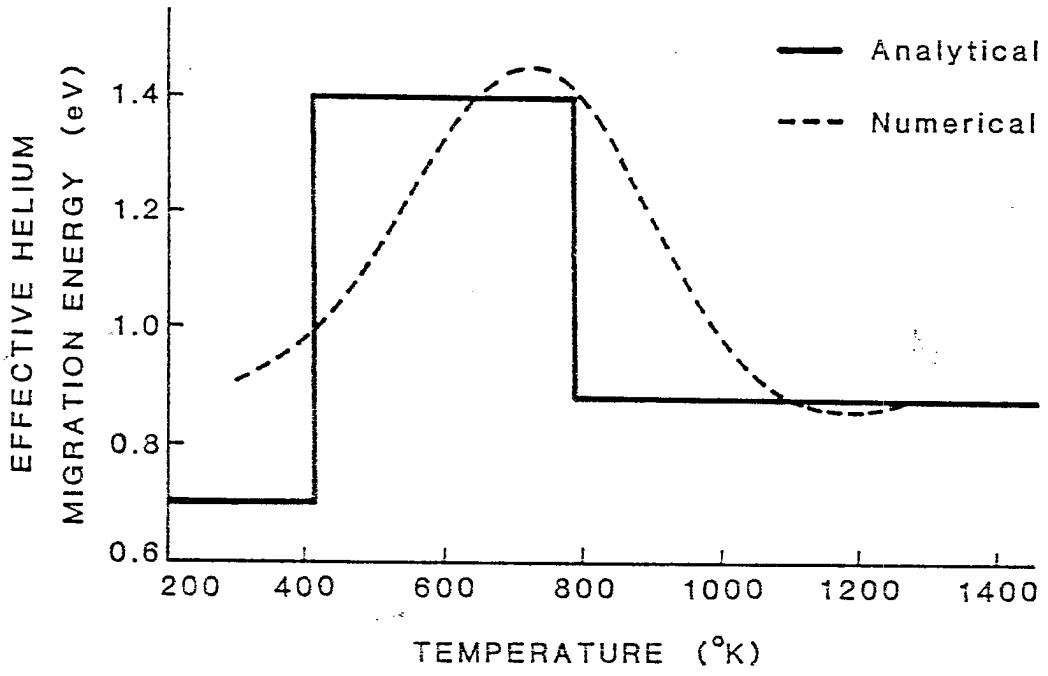

Fig. 13. Effective helium migration energy as a function of irradiation temperature for nickel at typical reactor conditions [22].

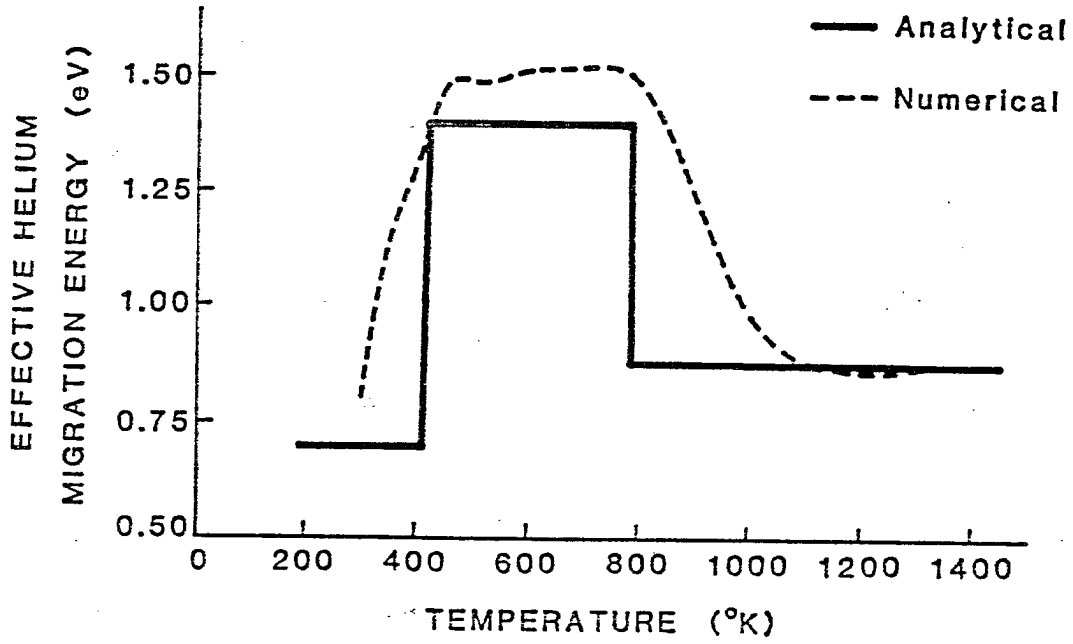

Fig. 14. Effective helium migration energy as a function of irradiation temperature for nickel in typical reactor conditions when divacancies and HVCs are not allowed to form [22].

mechanisms and to give a first order approximation to the exact value of D_{He}^{eff} under irradiation.

2.6. Conclusions of Helium Migration Theory

The problem of helium migration during the production of radiation damage is a critical one. Without understanding migration mechanism and diffusion rates, it is hopeless to account for the fate of helium atoms injected or produced by irradiation in structural alloys. This study provides two parallel and complementing approaches to the problem. An analytical formulation is developed which is valid roughly above 350°K for reasonable reactor irradiation times (~ years). Below this temperature, the slow transient buildup in point-defect concentration necessitates a time-dependent numerical solution. Under reactor irradiation conditions, the analytical model gives the following approximate values for helium-effective migration energy in nickel:

1. $E_{He}^{eff} \simeq 0.83$ eV; $\left(E_{He}^{eff} \simeq E_{He}^{B} + E_{He}^{M} - E_{v}^{F}\right)$; $T \geq 800^0$K,

2. $E_{He}^{eff} \simeq 1.4$ eV; $\left(E_{He}^{eff} \simeq E_{v}^{M}\right)$; $400^0\text{K} \leq T \leq 800^0$K,

3. $E_{He}^{eff} = 0.65$ eV; $T \leq 400^0$K.

The numerical model gives values of the effective migration energy that are functions of material and irradiation parameters as well as time. It is found that, at temperatures between 400° and 600°K in nickel irradiated in typical reactor conditions, the mobility of helium

is enhanced over the analytically predicted results by migration in divacancy single-helium complexes. Also, above ~ 800°K, helium mobility is less than the analytical value because of increased trapping at irradiation-produced vacancies. The influence of such irradiation-produced vacancies is totally negligible by ~ 1100°K.

3. THE "TRAJECTORY" METHOD FOR THE AVERAGE SIZE CAVITY DEVELOPMENT

The objective of the previous sections was to find an expression for the effective helium- diffusion coefficient. This is useful in understanding microstructural phenomena that depend upon the overall helium flux to a specific zone in the irradiated material (e.g., matrix cavities, grain boundaries, dislocations, and precipitates). The arrival of the helium flux to grain boundaries, dislocations, and precipitates generally does not affect their characteristics (i.e., size distributions, concentrations, and densities. However, helium arrival to cavities has a determining effect on their physical characteristics. This will in turn influence the effective diffusion coefficient of helium.

This interdependence between cavity evolution and various defect fluxes (helium vacancies, and self-interstitials) constitutes the major complication in any cavity evolution model. Furthermore, conditions such as temperature, helium to dpa ratio, displacement damage, and material choice will all affect cavity evolution.

3.1. Stability of HVCs During Irradiation

One of the major uncertainties in understanding cavity nucleation and growth is the degree of stability of HVCs under given irradiation conditions. Such stability is a complex function of irradiation variables (damage rates, helium production rates, and fluence), as well as material parameters (sink density, temperature, and defect parameters).

Stability studies generally aim at establishing a critical HVC size. This is defined such that larger clusters are ensured to grow under the current irradiation conditions.

The nodal line analysis has been developed for stability studies of kinetic systems [47]. Recently, Russell [48,49] used the same approach to analyze phase stability under irradiation.

We will follow here a similar method for the linear stability analysis of helium-vacancy clustering. An important aspect of our work is that we use vacancy and helium binding energies instead of changes in free energy to describe various HVC growth and shrinkage processes under irradiation. The model we have developed to determine helium and vacancy binding energies as a function of the number of vacancies and helium atoms/HVC has been described in Sect. 2.

Furthermore, we are able to include two more irradiation reactions in our extended nodal line analysis. These reactions are helium replacement by self-interstitial impingement on HVCs and radiation resolution of helium atoms from HVCs into the lattice.

By considering HVCs as characterized in a 2-D phase space, various kinetic processes can be represented schematically as shown in Fig. 1 in Chapter IV. An HVC can grow by capturing a vacancy or helium atom

($R^c_{v,h}$) or by emitting a SIA (R^e_i). Also it may shrink by thermal emission of either vacancy or helium atom ($R^e_{v,h}$), by capture of SIAs (R^c_i), by a gas replacement mechanism (R^{gr}_i), or because of PKAs (R^r_h). The summation of these rates results in corresponding component velocities in phase space, given by:

$$\dot{v} = R^c_v - R^e_v - R^c_i \quad , \tag{74}$$

$$\dot{h} = R^c_h - R^e_h - R^{gr}_i - R^r_h \quad . \tag{75}$$

The rates in Eqs. (74) and (75) are calculated by using quasi-steady-state values for C_v, C_i, and C_{He}. In the present analysis we ignore SIA emission.

Ghoniem and Gurol [46] showed approximations for vacancy and SIA concentrations. With the knowledge of an effective helium diffusion coefficient [18] as a function of C_v and C_i, we are able to estimate a quasi-steady-state helium concentration.

Setting $\dot{v} = 0$ and $\dot{h} = 0$ and plotting the loci of points which satisfy this condition in the helium-vacancy phase space, we find the helium and vacancy nodal lines. Now if we investigate the trajectories in the vicinity of these nodal lines, regions of growth or shrinkage of HVCs in this phase space can be determined, as shown in Fig. 15. We find that:

- In region I, HVCs grow in vacancy but shrink in helium atom content.

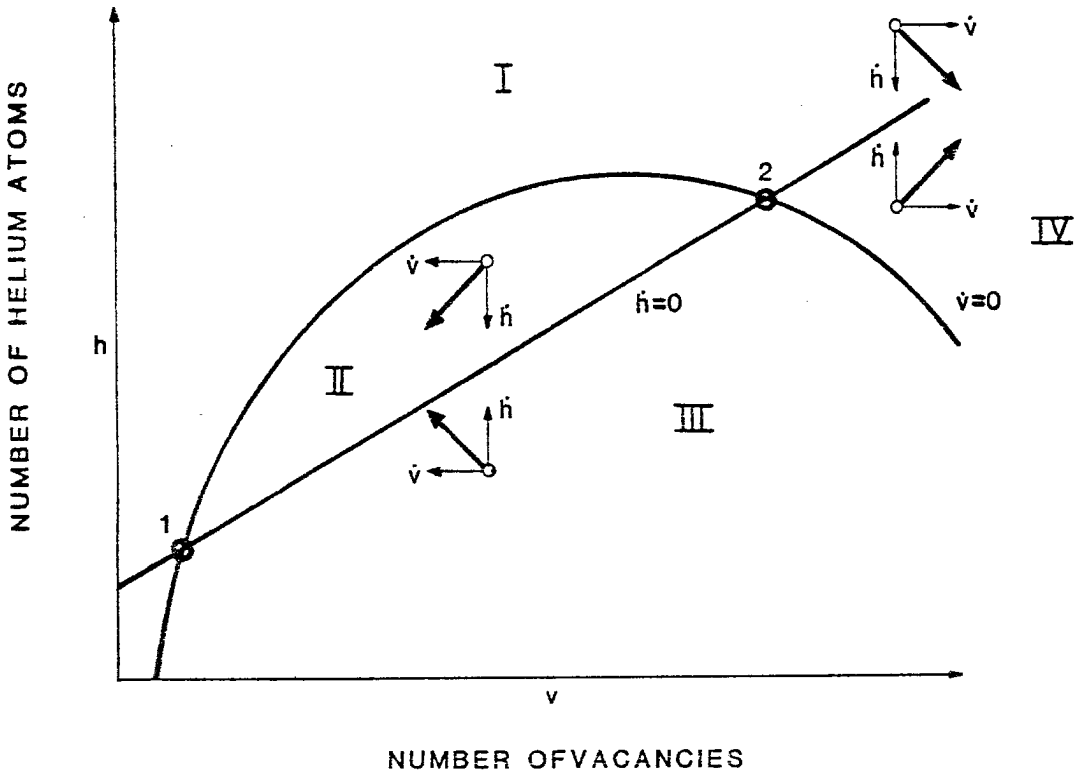

Fig. 15. Nodal lines showing regions of growth and shrinkage of HVCs in a helium vacancy phase space.

- In region II, HVCs shrink in both number of vacancies and helium atoms.

- Region III lets HVCs grow in helium content but they shrink by a net loss of vacancies.

- Only in region IV do all HVCs experience growth in both number of vacancies and number of helium atoms.

Thus, region IV can be termed the "region of stability" which will ensure growth of HVCs. The boundary of this growth region thus separates the stable from unstable HVCs. We can therefore view the HVCs residing on the boundaries of region IV as "critical" HVCs.

We have found, using the nodal line analysis/clustering method, that there are two general nucleation modes. In the first one, helium precipitation into bubbles occurs **spontaneously** (see Fig. 16a). Very small nucleation barriers exist in this case, and nucleation proceeds homogeneously in the matrix. This occurs under irradiation conditions of high helium generation rates, low temperature, and low sink density. The high helium generation rates tip the competition for vacancies between SIAs and helium atoms in favor of helium atoms. This reduces vacancy annihilation rates by SIAs, and the chance for survival of fundamental HVCs is enhanced.

Stochastic nucleation is the second mode. Here, cavity formation proceeds with substantial nucleation barriers (i.e., regions I, II, or III in Fig. 16b), which must be overcome by subcritical HVC embryos in order to reach stable configurations. This case is best achieved at

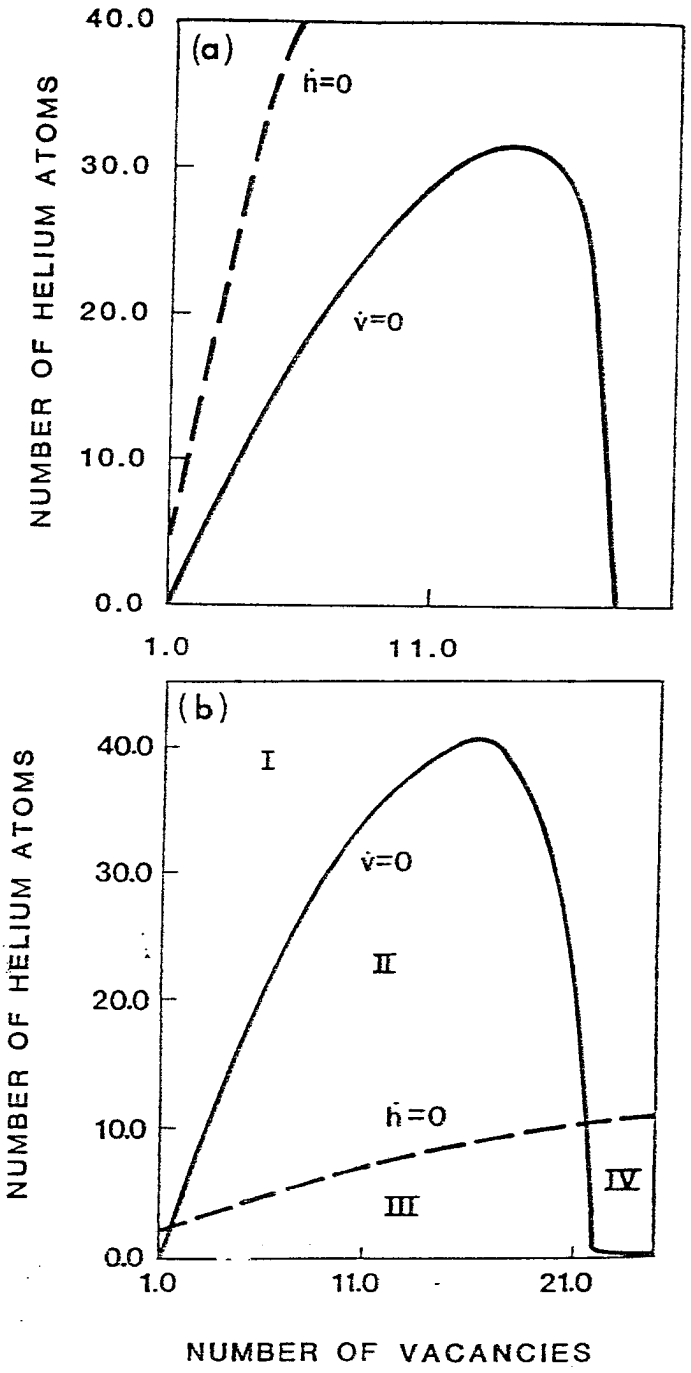

Fig. 16. Stability analysis for HVCs showing (a) spontaneous and (b) stochastic nucleation (T=500°C, $\rho_d=10^{10}$ cm^{-2}).

high temperatures, high dislocation sink density, and low helium generation rates. The combination of high temperature and high sink density renders short defect mean-life times. These, coupled with low helium generation rates, increase the chances of SIAs of competing against helium for vacancies. These effects (nucleation barriers) suppress the production of stable HVC embryos. Therefore, stable HVCs must be produced by some mechanism, such as a stochastic one, able to overcome the nucleation barriers.

3.2. Spontaneous and Stochastic Nucleation Regimes

To simulate fusion irradiation environments with existing facilities, extensive use has been made of the HFIR, the EBR-II, and accelerators. These facilities differ mainly in their helium dpa ratios. In HFIR, the helium dpa ratio is 57 while in EBR-II it is 0.1 at 10^{-6} dpa/s of damage production.

The basic experimental findings [50] concerning cavities in the temperature range of 300° to 650°C are as follows: (1) in HFIR, cavities appear to be bubbles rather than voids, (2) they are about 10 times smaller, and (3) they are 20 to 50 times more numerous in HFIR than voids are in EBR-II-irradiated steels.

Scanning a temperature range between 300° and 650°C with other irradiation conditions (helium dpa ratio, dislocation sink density, and dpa) fixed, we were able to trace the loci of points which separate regions of spontaneous from delayed nucleation as a function of temperature and helium dpa ratios (see Fig. 17 and 18).

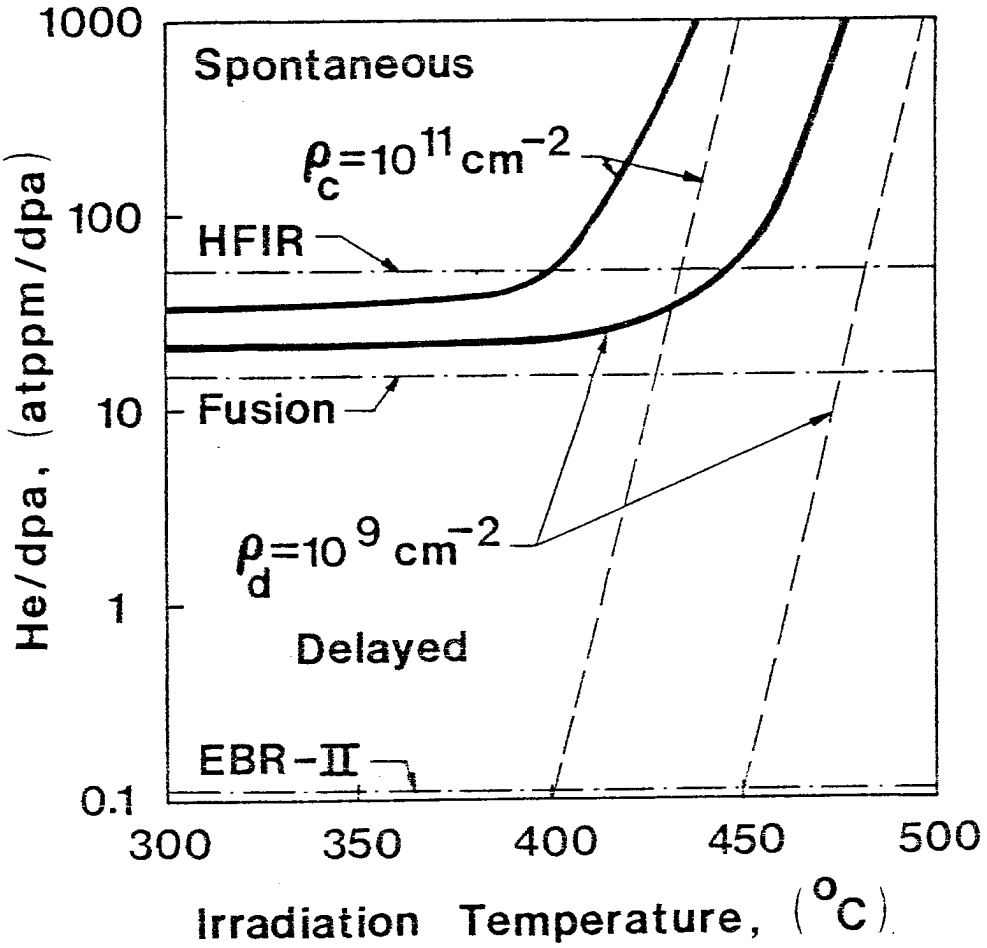

Fig. 17. Nucleation regime analysis for reactor conditions showing spontaneous and delayed regions [18].
(dotted line: re-solution parameter=0)

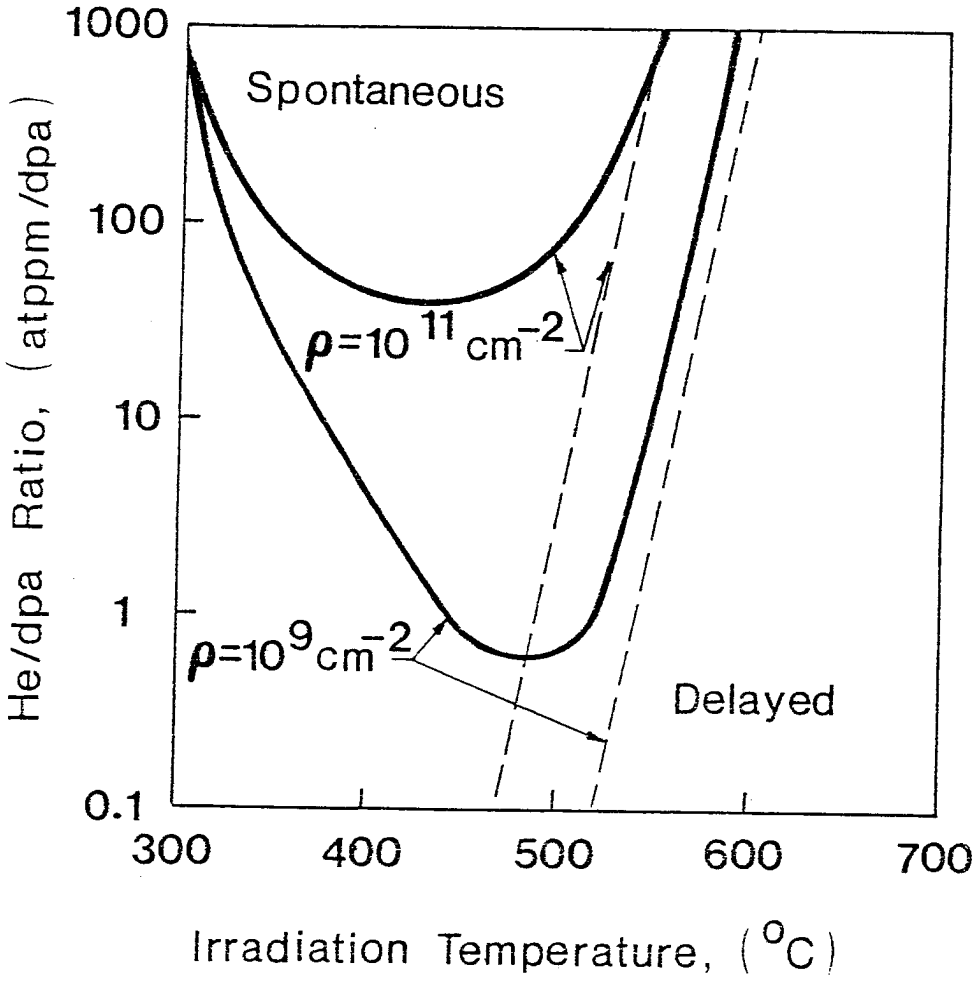

Fig. 18. Nucleation regime analysis for accelerator conditions showing spontaneous and delayed regions [18].
(dotted line: resolution parameter=0)

For EBR-II irradiation, we find that all cavity nucleations proceed as stochastic (Fig. 17). Nodal line analysis for EBR-II conditions show strong nucleation barriers, such as shown by region II in Fig. 16(b). Nucleation of critical HVCs is delayed because any size HVC outside of region IV disassociates to subcritical clusters. When the helium dpa ratio is increased, the nucleation barrier (region II [Fig. 16(b)]) is reduced until it vanishes completely. These conditions are met in HFIR experiments where small cavities with a high number density are found.

Decreasing the dislocation line density shifts the spontaneous nucleation region to higher temperatures and lower helium dpa ratios (Figs. 17 and 18).

Similar spontaneous and delayed nucleation regimes can be identified by investigating accelerator conditions ($\sim 10^{-3}$ dpa/s) (Fig. 18). When compared with reactor conditions ($\sim 10^{-6}$ dpa/s), the basic difference can be seen in the low temperature region. Here we see the reappearance of a nucleation barrier after a minimum between 400° and 500°C. The growth of the nucleation barrier shifts the nucleation mode back into the delayed one. This can be explained by the high helium re-solution taking place in accelerator environments. As the temperature is increased from 300° to 400°C, the re-solution becomes less significant because helium capture rates increase with increasing temperature. By further increasing the temperature beyond 500°C, the helium emission rates take over and the nucleation barriers become stronger.

This high temperature behavior of HVC number densities in accelerator environments has been established experimentally [51] as a function of temperature and helium dpa ratios.

3.3. The Trajectory Method to Determine Average Cavity Sizes

As pointed out in Sect. 3.1, we used the nodal line analysis to determine regions of stability for HVCs under various irradiation conditions. We have identified regimes of spontaneous and stochastic (delayed) nucleation as functions of temperature, helium dpa ratios, dislocation densities, and re-solution parameters for both reactor and accelerator conditions. Although this information is very valuable in understanding cavity evolution, it is not sufficient for determining HVC size evolutions. The nodal line analysis determines the irradiation conditions under which stable HVCs will nucleate and it gives some indications as to the regions of possible ultimate growth.

However, we need to establish regions in the helium-vacancy phase space that will ensure HVC evolution. Since our model depends on numerical solutions of coupled rate equations (see Chapter VI), analytical guidance is needed to investigate the correct regions for the evolution of the cavity size. Knowledge of the regions of the most probable HVC combinations not only reduces the numbers of equations to be solved, but will also increase confidence in later numerical results.

For this purpose we use the method of growth trajectories which was recently developed by Trinkaus [52]. He developed an analytical formulation to predict the average helium-vacancy ratio in helium-vacancy phase space for constant helium and vacancy fluxes. This approach is used to evaluate the evolution of the average HVC size and helium-vacancy ratio, for varying helium and vacancy fluxes.

We start here with the growth equations for vacancies and helium atoms in a HVC. For vacancies, the HVC growth equation is represented by the difference between the vacancy and self-interstitial fluxes:

$$\frac{dR}{dt} = \frac{1}{R}\left[D_v C_v - D_i C_i - D_v C_v^e \left\{ \exp\left[\frac{\Omega}{kT} \left(\frac{2\gamma}{R} - P \right) \right] - 1 \right\} \right] , \qquad (76)$$

where $D_v C_v$ = vacancy flux,

$D_i C_i$ = interstitial flux,

and the last term in Eq. (76) is the vacancy emission rate which is a function of:

P = pressure due to helium gas,

γ = surface tension of the bubble,

T = temperature.

(Please see Nomenclature at the end of this chapter for the remaining symbols.)

In the analytical work of Trinkaus [52], the assumption is made that helium atoms do not return to the matrix once captured. Thus the helium growth equation is simply the capture rate of helium (h):

$$\frac{dh}{dt} = 4\pi R\, D_{He} C_{He} / \Omega \quad . \qquad (77)$$

Equation (77) depends on the helium flux $D_{He} C_{He}$, which can vary during irradiation. A simpler growth equation states that all helium produced is distributed equally among all bubbles. Thus,

$$dh/dt = P_{He}/C_B\Omega \quad , \tag{78}$$

where P_{He} is the helium production rate and C_B is the bubble concentration. Equation (78) also assumes no loss of helium to other sinks (such as grain boundaries and precipitates). It is also to be noted that these growth equations assume that nucleation of HVCs has stopped and growth is the only mechanism under investigation. Equation (76), the vacancy growth equation, can also be expressed in terms of v, the number of vacancies:

$$\frac{dv}{dt} = 4\pi R\, D_v C_v^e \left(\frac{1}{kT}\right)\left[\frac{kT}{\Omega}\left(\frac{C_v}{C_v^e} - \frac{D_i C_i}{D_v C_v^e}\right) + P - \frac{2\gamma}{R}\right] \quad , \tag{79}$$

where we have linearized the exponential $e^x \sim 1 + x + x^2/2 \ldots$ and kept only the first two terms.

By defining:

$$D = D_v C_v^e \quad , \tag{80}$$

$$\sigma = kT/\Omega(C_v/C_v^e - D_i C_i/D_v C_v^e) \quad , \tag{81}$$

$$dv/dt = \dot{v} \quad , \tag{82}$$

we obtain the growth equation used by Trinkaus:

$$\dot{v} = 4\pi RD\left(\frac{1}{kT}\right)\left(P + \sigma - \frac{2\gamma}{R}\right) \quad . \tag{83}$$

The symbol σ was chosen because this term reflects the effects of the hydrostatic stress on vacancy emission or capture at HVCs.

The following section gives a brief analytical solution to the previous growth equations as developed by Trinkaus [52].

3.4. Analytical approach to growth trajectories

Starting with the growth equations [Eqs. (77), (78), and (83)] we can determine several dimensionless quantities.

$$r = r^* x \quad , \tag{84}$$

$$N = N^* y \quad , \tag{85}$$

$$t = t_o \tau \quad . \tag{86}$$

From Eq. (83) and

$$\frac{dv}{dt} = \frac{4\pi r^2}{\Omega} \frac{dr}{dt} \quad , \tag{87}$$

we get

$$\dot{r} = \left(\frac{D\Omega}{kT}\right) \frac{1}{r} \left(P + \sigma - \frac{2\gamma}{r}\right) \quad . \tag{88}$$

The dimensionless quantities r^* and N^* can be determined from the condition of:

$$\dot{r} = d\dot{r}/dr = 0 \quad . \tag{89}$$

To illustrate the meaning of r^* and N^* we refer to Fig. 19. The rate of change of radius of a HVC containing N helium atoms can behave differently as a function of N. The symbols r^* and N^* stand for the values of size and of the helium content of the critical HVCs.

Helium atoms stabilize clusters of vacancies from disintegration. When the helium content is not enough to do so, $N < N^*$, a cluster with a size smaller than r^*, will shrink to a size of r_1 (see Fig. 19). When the cluster reaches a size r_2, growth is ensured. When a cluster

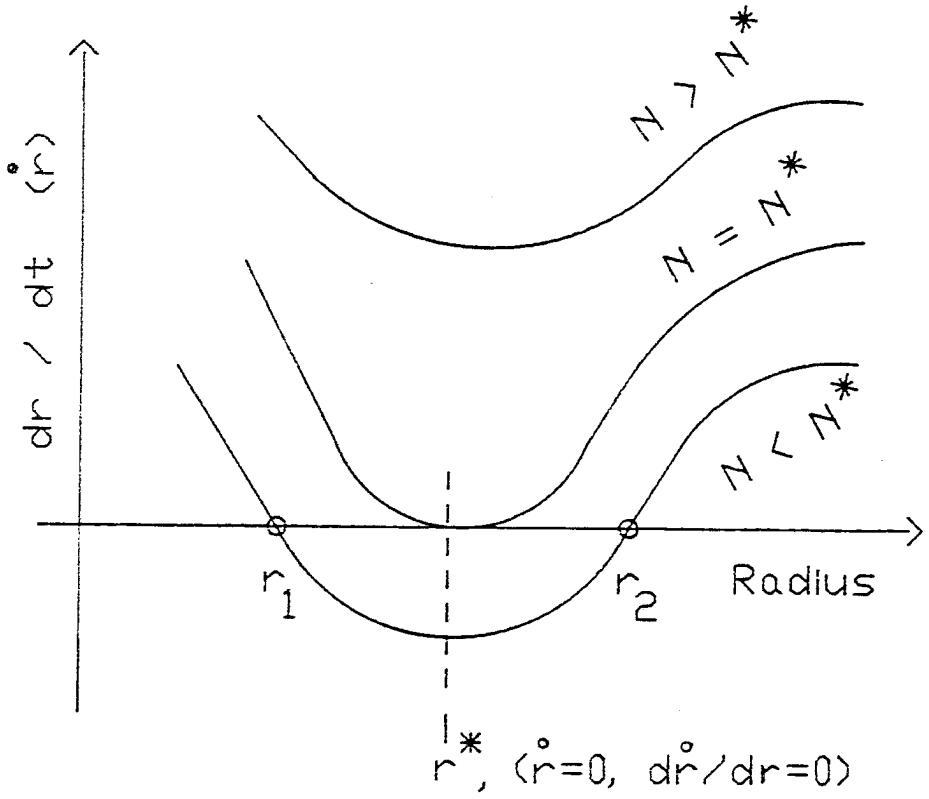

Fig. 19. Schematic relating r* and N*, the critical radius and critical helium content, respectively.

contains N* helium atoms, it is assured gorwth no matter what its original size. The same holds true for clusters containing N > N* helium atoms. N* is determined from the curve when both $\dot{r}$ and $d\dot{r}/dr$ are zero. Mansur [53] has recently used an approach similar to the one described here in order to determine the critical size. From Eq. (88) we have

$$\frac{d\dot{r}}{dr} = \left(\frac{\Omega D}{kT}\right) \frac{1}{r^2} \left(-\frac{3NkT}{r^3\pi} - \sigma + \frac{4\gamma}{r}\right) \quad , \tag{90}$$

$$\frac{d\dot{r}}{dr} = 0 \text{ gives } N = \frac{\pi}{3kT} \left(4\gamma r^2 - \sigma r^3\right) \quad , \tag{91}$$

and

$$\dot{r} = 0 \text{ gives } N = \frac{4\pi}{3kT} \left(\frac{2\gamma}{r} - \sigma\right) \quad , \tag{92}$$

or solving for r* and N*, and using Eqs. (91) and (92) we obtain

$$r^* = \frac{4\gamma}{3\sigma} \quad , \tag{93}$$

$$N^* = \frac{128\ \pi\gamma^3}{81\ kT\ \sigma^2} \quad . \tag{94}$$

Now we can use r* and N* to express the growth equations in terms of dimensionless quantities x and y. From

$$r = r^* x \quad , \tag{95}$$

and

$$\frac{dr}{dt} = r^* \frac{dx}{dt} \quad , \tag{96}$$

coupled with Eq. (88), we get

$$r^* \frac{dx}{dt} = \frac{\Omega D}{kT} \frac{1}{r^* x} \left[\frac{N^* y \; kT}{(4/3)\pi (r^* x)^3} + \sigma - \frac{2\gamma}{r^* x} \right] \quad , \tag{97}$$

where $y = N/N^*$.

Using for N^* [Eq. (94)] we get upon rearranging

$$x \frac{dx}{dt} = \frac{\Omega D}{kT} \frac{4r}{3r^{*3}} \left(\frac{y}{2x^3} + 1 - \frac{3}{2x} \right) \quad . \tag{98}$$

And using r^* [Eq. (93)] and defining

$$t_o = \frac{r^{*2} \; kT}{2D \; \sigma\Omega} \quad , \tag{99}$$

we get for the dimensionless vacancy growth quation

$$2x\dot{x} = \frac{1}{2} \frac{y}{x^3} + 1 - \frac{3}{2x} \quad . \tag{100}$$

We can now derive the following two-dimensionless growth equation for y, corresponding to Eqs. (77) and (78), respectively,

$$\dot{y} = \alpha x \quad , \tag{101}$$

where

$$\alpha = 2\pi \; D_{He} C_{He} \; r^{*3} kT/(D\sigma\Omega^2) \quad , \tag{102}$$

and

$$\dot{y} = \beta \quad , \tag{103}$$

where

$$\beta = P_{He}\, r^{*2} kT/(2D\, C_b \sigma \Omega^2) \quad . \tag{104}$$

The new system of growth equations is thus:

(a) For vacancies

$$2x\dot{x} = \frac{1}{2}\frac{y}{x^3} + 1 - \frac{3}{2x} \quad . \tag{105}$$

(b) For the given helium flux (case 1)

$$\dot{y} = \alpha x \quad , \tag{106}$$

(c) For total helium absorption in clusters, this is given by (case 2)

$$\dot{y} = \beta \quad . \tag{107}$$

By taking the ratio of $\dot{x}/\dot{y}$, we can eliminate the time dependance. For case 1 we get:

$$\frac{dy}{dx} = \frac{2\alpha x^2}{(1/2)(y/x^3) + 1 - (3/2x)} \quad , \tag{108}$$

and for case 2 we obtain

$$\frac{dy}{dx} = \frac{4\beta x^4}{y + 2x^3 - 3x^2} \quad . \tag{109}$$

Solving Eqs. (108) or (109), the distinct relationship between y and x or number of helium atoms to number of vacancies can be determined for the average size in the distribution. The loci of these points, the **trajectory**, thus represents the average helium and vacancy contents of HVCs during their evolution.

Trinkaus was able to develop an analytical solution for the trajectory of case 2, but case 1 did not seem to have a simple analytical solution.

By defining $y = 1 + \eta$, Eq. (109) is transformed to

$$\frac{d\eta}{dx} \simeq \frac{4\beta x^4}{(x-1)^2(2x+1)} \quad , \tag{110}$$

which can be solved for η

$$\eta = \frac{4}{3}\beta\left[-\frac{1}{x-1} + \frac{10}{3}\ln(x-1) + \frac{1}{24}(2x+1)\right.$$

$$\left. + \frac{9}{4}x + \frac{3}{4}x^2\right] + 3\left(\frac{\pi}{2}\beta\right)^{2/3} \quad . \tag{111}$$

Thus for the assumption of a uniform dispersion of helium among bubbles, and ideal gas law, Eq. (111) coupled with Eqs. (94) and (85) can predict the average HVC during evolution.

3.5. A Numerical Approach to Determine Average Cavity Sizes

As pointed out in the previous section, we [18] have established similar growth equations as used by Trinkaus. These are given by

$$\frac{dv}{dt} = \frac{4\pi R}{\Omega}\left(D_v C_v - D_i C_i - D_v C_v^e\left\{\exp\left[\frac{\Omega}{kT}\left(\frac{2\gamma}{R} - P\right)\right] - 1\right\}\right) \quad , \tag{112}$$

for vacancies, while for helium we have

$$\frac{dN}{dt} = \frac{4\pi R}{\Omega}\left(D_{He}C_{He}\right) - Nb \quad , \tag{113}$$

where b is the re-solution parameter and N is the number of helium atoms per HVC.

In our approach, we do not need to make restrictive assumptions and simplifications in order to achieve an analytical solution. The Van der Waal's Equation Of State (EOS) for helium is used in our analysis. Thus pressure given by

$$P = \frac{NkT}{(4/3)\pi R^3 - NB} \quad . \tag{114}$$

For high gas pressures at small radii, a virial expansion is used for greater accuracy:

$$P = \frac{NkT}{v\Omega}\left[1 + \left(\frac{NB}{v\Omega}\right) + \left(\frac{NB}{v\Omega}\right)^2 + \left(\frac{NB}{v\Omega}\right)^3 + \left(\frac{NB}{v\Omega}\right)^4\right] \quad , \tag{115}$$

where $v\Omega$ is the volume occupied by v number of vacancies per HVC. In our analysis, the exponential term in Eq. (112) is not linearized. More important is the fact that our solution is no longer restricted to the simple helium dispersion equation [Eq. (78)]. Also, case 1 is chosen, where the arrival rate of helium atoms rather than the production rate of helium determines the growth. Furthermore, we can include the effects of helium atom re-solution due to primary knock-on atoms (PKAs).

Using Eqs. (112) and (113) we establish the trajectory by numerical integration of the equation:

$$\frac{dv}{dN} = f(v,h) \quad , \tag{116}$$

where f(v,h) is the ratio of the right-hand sides of Eqs. (112) and (113). Equation (116) depends on the various defect fluxes (i.e., vacancy, interstitial, and helium fluxes). The solution of a small set of coupled rate equations provides the necessary information. In Sect. 2, we have described the methods used to determine these fluxes.

Examples of the solution of Eq. (116) are shown in Fig. 20 for various irridiation facilities. HFIR and EBR-II have similar displacement damage rates of $\sim 10^{-6}$ dpa/s but differ in the helium dpa ratios [i.e., HFIR: helium/dpa ~ 57.1 (appm/dpa); EBR-II: helium/dpa ~ 0.1 (appm/dpa)]. Accelerators generally deliver a displacement rate on the order of $\sim 10^{-3}$ dpa/s with high helium dpa ratios of ≈ 100 (appm/dpa). Besides the trajectories depicted in Fig. 20, the helium-vacancy contents for cavities in mechanical equilibrium is also shown. The pressure is simply in equilibrium with the surface tension force.

Figure 20 shows the effect of the helium dpa ratio on the helium content of bubbles. The effect of the ideal gas law on the trajectories is also investigated in Fig. 21. Figure 21 shows the trajectory for EBR-II irradiation conditions using Van der Waal's EOS and the ideal gas law. It can be seen that, as the size of the HVCs increase, the ideal gas law trajectory approaches that of the Van der Waal EOS trajectory.

The effect of the re-solution parameter b was studied. Figure 22 compares the effects of b=0 and b=1 on the trajectory behavior of EBR-II irradiation conditions at 500°C. Even though the effect of re-solution

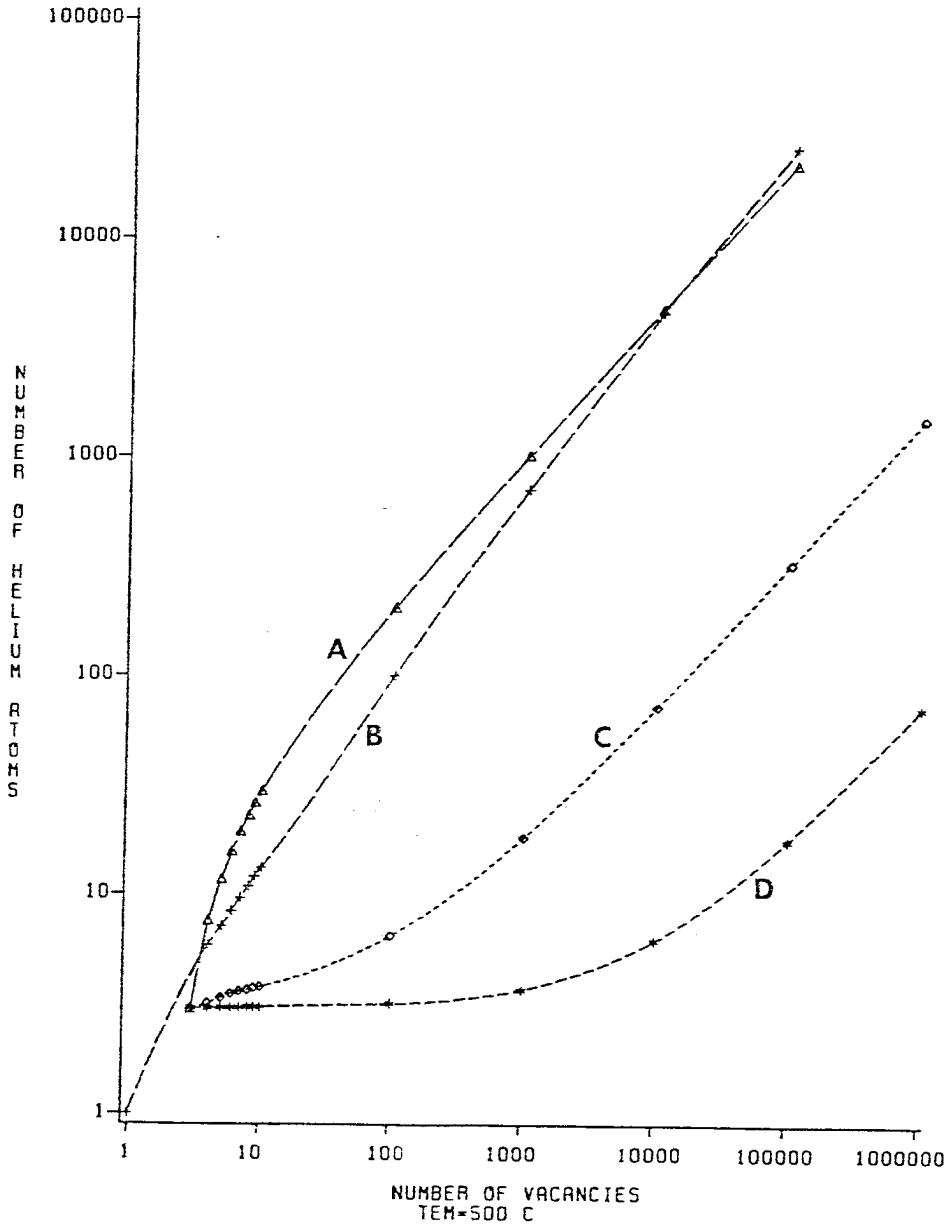

Fig. 20. Growth trajectories for accelerator, HFIR, and EBR-II irradiation conditions at 500°C. (A: accelerator; B: equilibrium bubbles; C: HIFR; D: EBR-II)

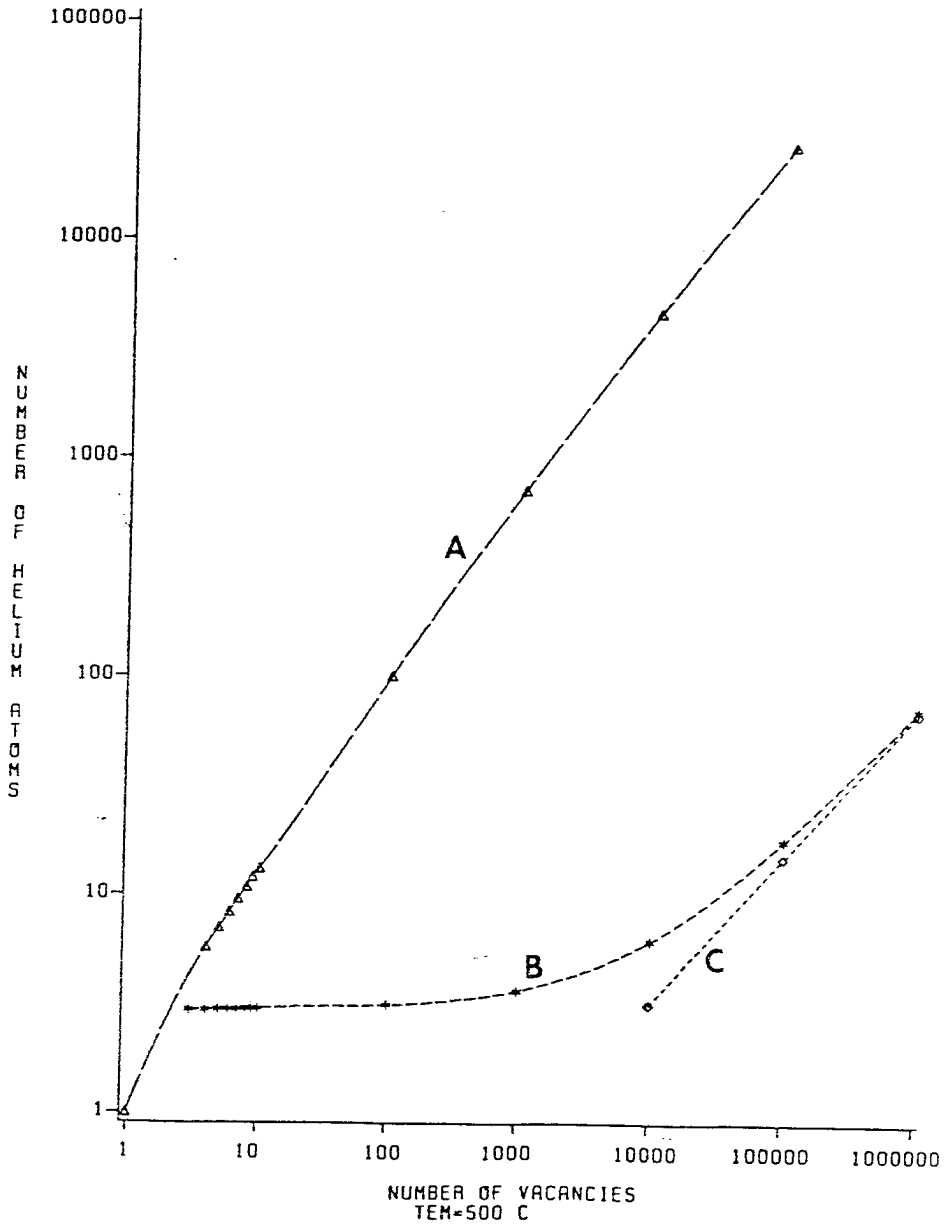

Fig. 21. Growth trajectories for EBR-II irradiation conditions using Van der Waal's EOS and ideal gas law to describe the pressure inside HVCs. (A: equilibrium bubbles; B Van der Waal's EOS; C: ideal gas law)

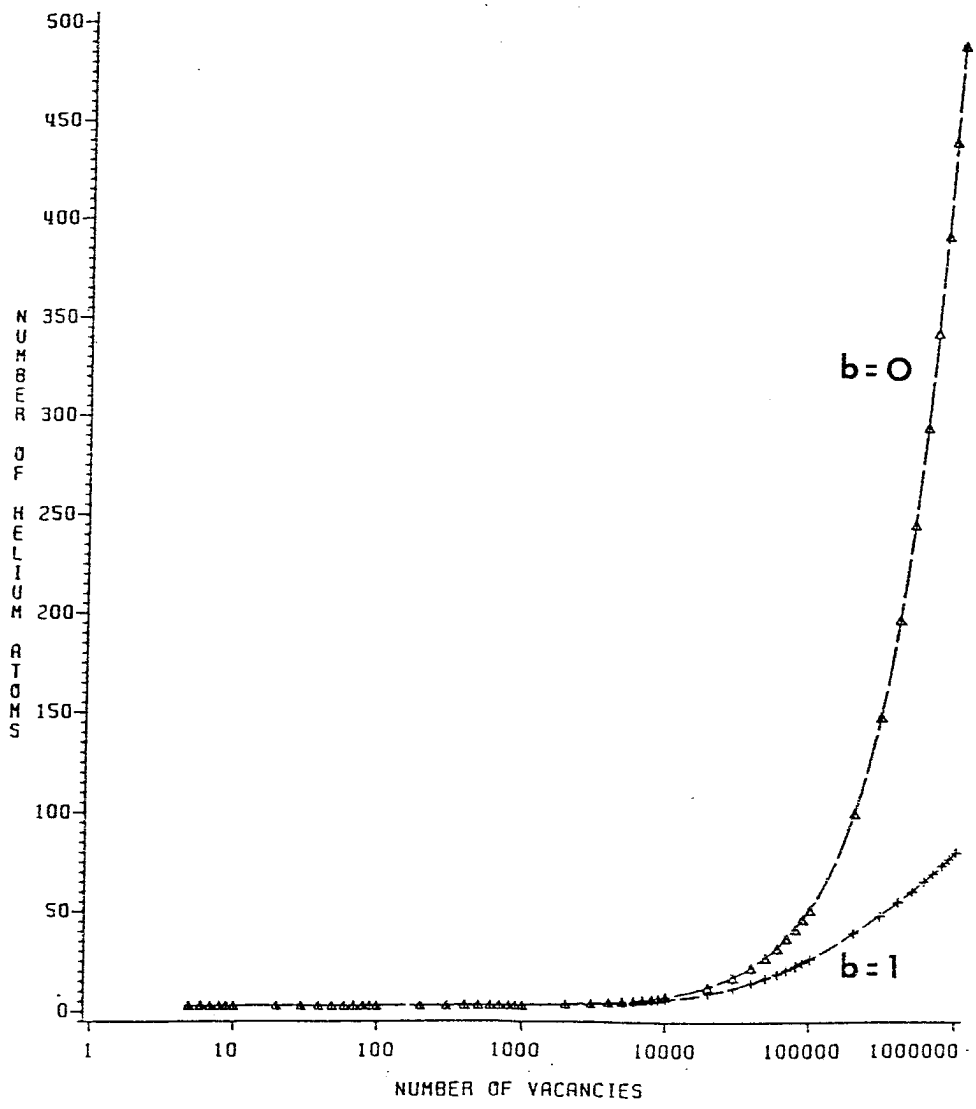

Fig. 22. Growth trajectories for EBR-II irradiation conditions for $b=\phi\cdot\phi$ and b=1 re-solution parameters.

is negligible on small HVCs containing less than 10^4 vacancies, it becomes an important parameter in determining the helium content of larger bubbles.

Finally there is one more question that needs to be addressed regarding our numerical approach to finding the growth trajectories. Our integration scheme requires a starting point or critical HVC size. If the method used here is sound, then regardless of the starting HVC size, the trajectory should always lead to the same final trajectory. Four starting points near the four corners of a square of 10 He x 10 v in a helium-vacancy space are chosen to represent initial nucleation conditions. Figure 23 shows such an example for HFIR conditions, where it is clear that, regardless of the starting point, the four trajectories converge to one trajectory at larger sizes.

3.6. Determination of an Equivalent "Finite" Solution Space for Numerical Analysis

Any attempted numerical solution to a time-dependent, 2-D partial differential equation of the Fokker-Planck type is expected to be computer intensive. Since the mathematical solution space is the infinite, positive helium-vacancy phase space, it is important to make appropriate approximations for the numerical solution. Also, boundary conditions must be clearly specified for the equivalent "finite" solution space. In this section, we develop a method for the determination of this space, and for prescribing the appropriate boundary conditions.

The numerical solution of the trajectory, as described in Sect. 3, leads to an approximate determination of the position of the average

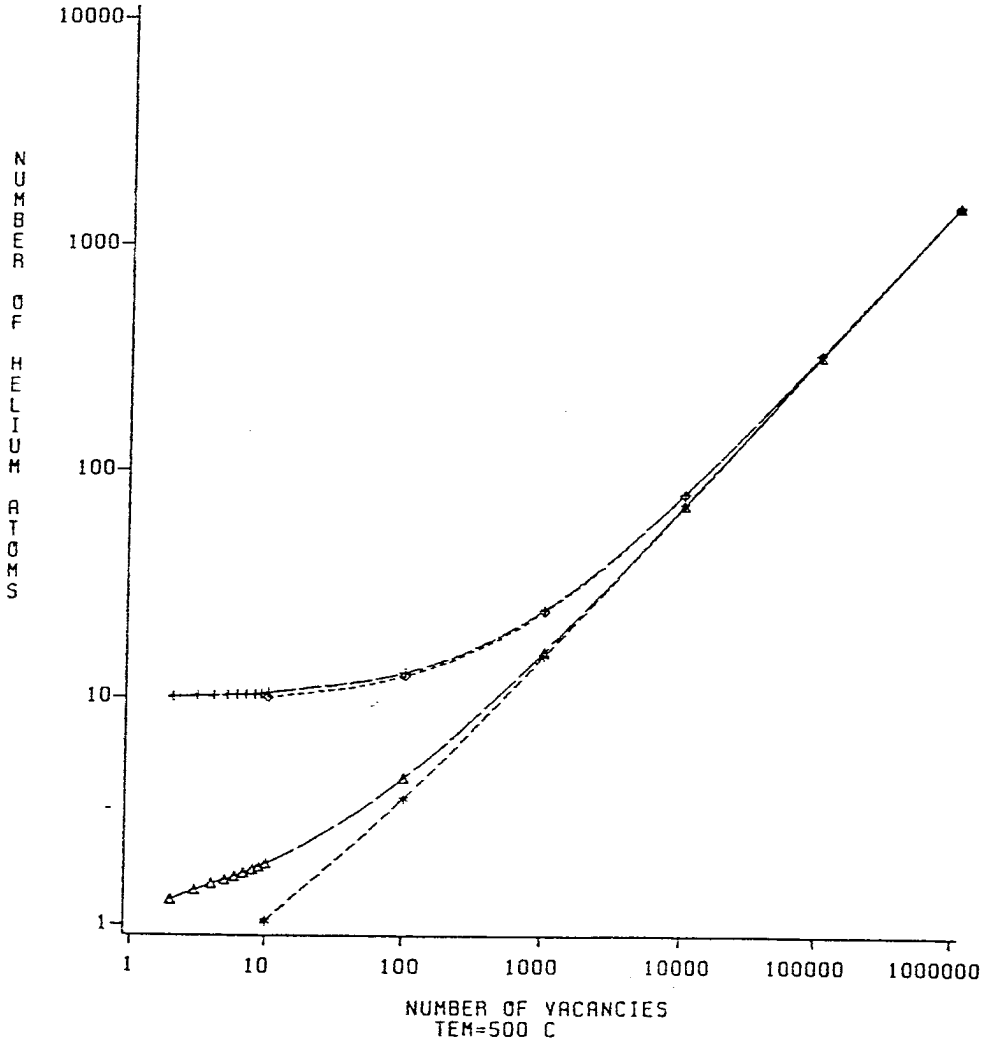

Fig. 23. Growth trajectories for HFIR irradiation conditions using four different starting conditions.

size in the helium-vacancy phase space. It can be shown that the trajectory solution is equivalent to an approximate solution for the first moment of the distribution function described by the Fokker-Planck equation.

Our approach is to conserve the zeroth moment of the distribution, by invoking zero-current boundary conditions on a prescribed contour in the helium-vacancy phase space. This contour should contain, at all times, the first moment of the solution. It is therefore necessary to define the zero-current contour around the trajectory. The extent of the chosen solution space should be determined by higher moments of the distribution function. A reasonable choice is based on the second moment, which is described below.

Starting with growth equations $\dot{v}$ and $\dot{h}$, Eqs. (74) and (75), we can quantify a diffusional spread in the vacancy and in the helium directions as follows:

$$\langle \Delta V \rangle^2 \equiv 4D^v \tau \quad , \tag{117}$$

$$\langle \Delta h \rangle^2 \equiv 4D^h \tau \quad , \tag{118}$$

where D^v and D^h are determined from the corresponding growth equations:

$$D^v = \frac{1}{2} \frac{4\pi R}{\Omega} \left(D_v C_v + D_i C_i + D_v C_v^e \left\{ \exp\left[\frac{\Omega}{kT} \left(\frac{2\gamma}{R} - P \right) \right] - 1 \right\} \right) , \tag{119}$$

$$D^h = \frac{1}{2} \left[\frac{4\pi R}{\Omega} \left(D_{He} C_{He} \right) + Nb \right] \quad . \tag{120}$$

A numerical approach must be used to calculate the time τ, corresponding to every vacancy-helium combination on the trajectory. This can be given by

$$\tau = \int_0^{\tau} dt' = \int_{v^*}^{V} \frac{dv'}{f(v';h)} = \int_{h^*}^{H} \frac{dh'}{f(v,h')} \quad , \tag{121}$$

where the integration is a line integral along the trajectory, from either v* or h* to V or H that correspond to τ.

Now that diffusional spreads have been determined we will use these results in the evaluation of approximate values of the standard deviation in the vacancy and helium directions. As a conservative estimate for diffusion spreading, we use a multiple of the standard deviation. A factor between 5 and 10 is a reasonable estimate. Figure 24 shows the results of calculations, where we have used a multiplication factor of 5. Note that the diffusional spreads of helium and vacancies trace different loci. This is due to the diffusional terms which are sensitive to irradiation conditions. As a rule, we choose the larger of the two boundaries. In case of HFIR irradiation conditions the boundaries are determined by the helium spread (see Fig. 24). Later, we will demonstrate that the choice of a multiplication factor between 5 and 10 has minor effects on the distribution function. Thus the loci determined by diffusional spreads around the growth trajectories constitute the boundaries of a system across which no cavity evolution currents flow. We thus have a closed boundary system, provided we establish a maximum possible HVC size. This, as will be shown later, is an important ingredient in evaluating cavity evolution.

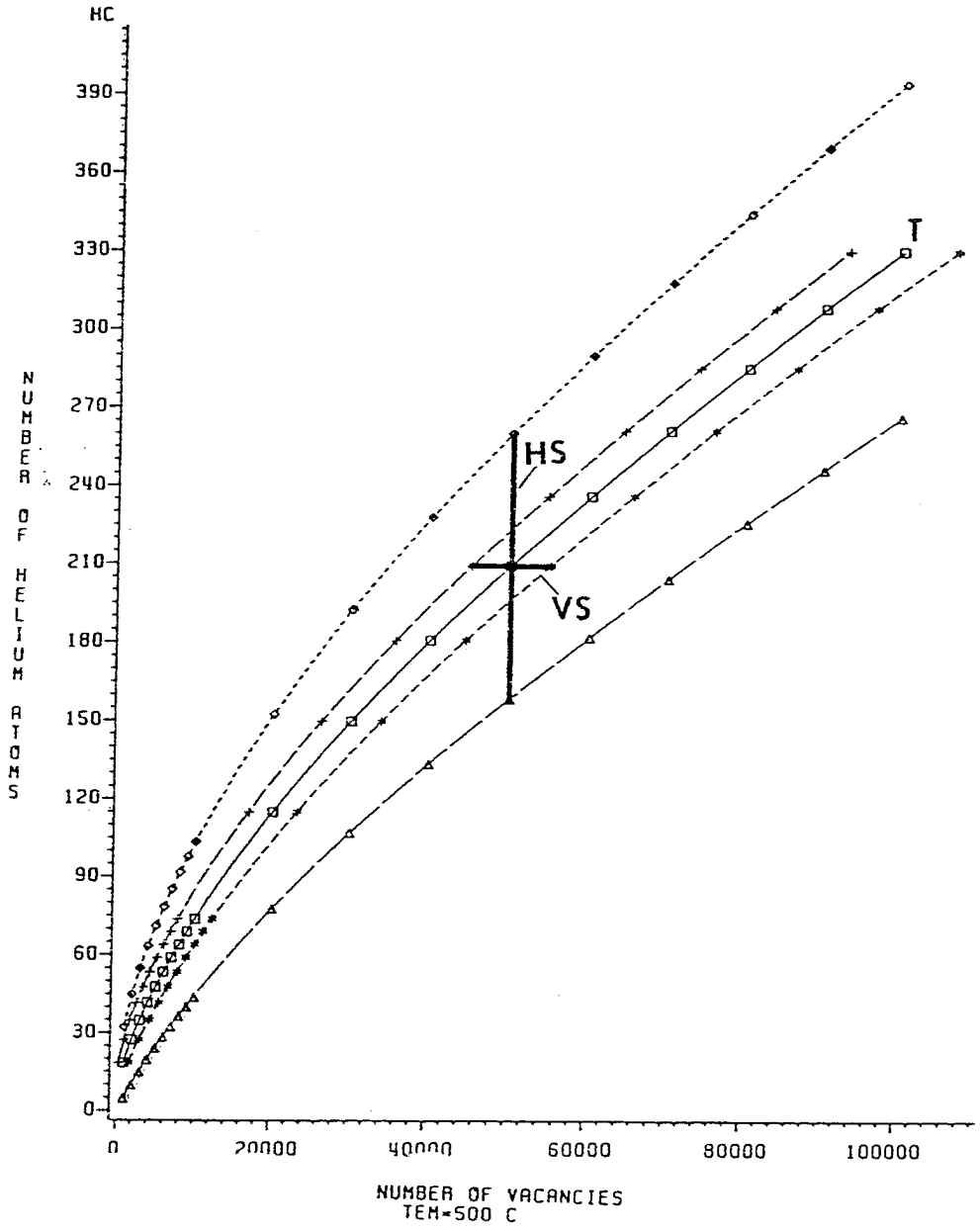

Fig. 24. Growth trajectory with estimated helium and vacancy diffusional spreads multiplied by a factor of 5 for HFIR irradiation conditions at T=500°C. (T: trajectory; HS: diffusional spread in the helium direction; VS: diffusional spread in the vacancy direction)

NOMENCLATURE

Symbol	Description	Units
a	Lattice parameter	(cm)
B	Van der Waal's constant	
C_v^e	Thermal equilibrium vacancy concentration	(at./at.)
C_I	Self-interstitial concentration	(at./at.)
C_{ij}	Concentration of complex containing i vacancies and j He atoms	(at./at.)
D_α	Diffusion coefficient of defect α	(cm^2/s)
D_α^0	Diffusion coefficient pre-exponential for defect α	(cm^2/s)
E_{ij}^v	Emission rate constant of a vacancy from an ij complex	(s^{-1})
E_{ij}^{He}	Emission rate constant of a helium atom from an ij complex	(s^{-1})
E_α^M	Migration energy of defect α	(eV)
E_α^B	Binding energy of defect α	(eV)
E_α^F	Formation energy of defect α	(eV)
E_{He}^D	He detrapping energy from a substitutional site	(eV)
G	Frenkel-pair generation rate	(dpa/s)
G_H	He atom generation rate	(at./at./s)
G_T	Thermal vacancy generation rate	(dpa/s)
g	Re-solution parameter	1 - 10
i	No. of vacancies in a cavity	
j	No. of He atoms in a cavity	

k	Boltzmann's constant	$eV \cdot {}^{\circ}K^{-1}$
K_{ij}^{α}	Combinatorial no. for defect α impinging on an ij complex	
M	Maximum no. of vacancies in the ij complex	
N	Maximum no. of He atoms in the ij complex	
$N(r_c)$	Cavity No. density per unit size	(cm^{-4})
P_g	Gas pressure inside a cavity	(eV/cm^3)
r_c	Critical growth radius	(cm)
R_{tr}	Trapping radius	(cm)
$R_{I,mn}$	Reaction rate between a self-interstitial and an mn complex	(s^{-1})
$R_{ij,mn}$	Reaction rate between an ij complex and an mn complex	(s^{-1})
R_{ij,r_c}	Reaction rate between an ij complex and a cavity with radius r_c	(s^{-1})
S_I	Self-interstitial sink strength	(cm^{-3})
S_v	Vacancy sink strength	(cm^{-3})
s_v^F	Entropy of vacancy formation	
t	Time	(s)
T	Temperature	(°K)
Z_{α}^{c}	Cavity bias factor for defect α	
Z_{α}^{d}	Line dislocation bias factor for defect α	
ΔF	Free energy change due to an emission process	(eV)
ε	Fraction of vacancies produced directly as divacancies by irradiation	
Γ_{α}	Jump frequency of specie α	(s^{-1})
γ	Surface tension	(eV/cm^2)
λ_{α}	Jump distance for defect α	(cm)

ν_α	Vibration frequency of specie α	(s^{-1})
Ω	Atomic volume	(cm^3)
ρ_d	Line dislocation density	(cm/cm^3)

REFERENCES

[1] D. E. Rimmer and A. H. Cottrell, Philos. Mag., 2 (1957) 1345.

[2] W. D. Wilson, M. J. Baskes and C. L. Bisson, Phys. Rev. B (1976) 1572.

[3] G. Bauer and W. D. Wilson, in Radiation Induced Voids in Metals (Proc. Intl. Conf., Albany, NY, June 9-11, 1971) AEC Symp. Series No. 26, CONF-710601 (1972) p. 230.

[4] G. Carter, Vacuum, 12 (1962) 245.

[5] G. Farrell and G. Carter, ibid, 17 (1967) 15.

[6] R. Kelly and E. Ruedl, J. Nucl. Mater., 20 (1975) 197.

[7] W. D. Wilson and C. L. Bisson, Radiat. Eff., 25 (1975) 197

[8] W. D. Wilson and C. L. Bisson, ibid, 19 (1973) 53.

[9] P. Wright and J. H. Evans, Philos. Mag., 13 (1966) 521.

[10] L. M. Caspers, H. Van Dam, and A. Van Veen, DAFS Progress Report Series A, 1 (1974) 39.

[11] E. V. Kornelson, Can. J. Phys., 48 (1970) 2813.

[12] E. V. Kornelson, Radiat. Eff., 13 (1972) 227.

[13] K. C. Russell, Acta Metall., 20 (1972) 889.

[14] W. D. Wilson and C. L. Bisson, Bull. Am. Phys. Soc., 19 (1974) 372.

[15] M. W. Guinan and R. M. Stuart, Am. Nucl. Soc. Trans., 21 (1975) 164.

[16] J. Th. M. de Hosson, A. W. Sleeswyk, L. M. Caspers, W. Van Hengten and A. Van Veen, Solid State Commun., 18 (1976) 479.

[17] W. G. Wolfer, in Proc. 10th Conf. on Effects of Radiation on Materials, Am. Soc. Testing Mater., Savannah, GA, June 3-5, 1980, ASTM-STP-725, D. Kramer, H. R. Brager and J. S. Perrin, Eds. (1981) p. 201.

[18] S. Sharafat and N. M. Ghoniem, J. Nucl. Mater., 122 (1984) 531.

[19] H. Wiedersich, J. J. Burton and J. L. Katz, J. Nucl. Mater., 51 (1974) 287.

[20] J. E. Inglesfield and J. B. Pendry, Philos. Mag., 34 (1976) 205.

[21] D. J. Reed, Radiat. Eff., 31 (1977) 129.

[22] N. M. Ghoniem, S. Sharafat, J. M. Williams and L. K. Mansur, J. Nucl. Mater., 117 (1983) 96.

[23] E. V. Kornelsen and A. A. van Gorkinn, ibid, 92 (1980) 79.

[24] C. Zener, Imperfection in Nearly Perfect Crystals, W. Shockley, Ed., (Wiley, New York, 1952) p. 289.

[25] V. Philips and K. Sonnenberg, J. Nucl. Mater. (to be pub.).

[26] L. K. Mansur, W. A. Coghlan and A. D. Brailsford, J. Nucl. Mater., 85&86 (1979) 591.

[27] R. J. J. Fastenau, "Diffusion Limited Reactions in Crystalline Solids, Theory and Computer Simulations," Ph.D. thesis, Delft University, 1982.

[28] S. Chandrasekhar, Rev. Mod. Phys., 15 (1) (1943) 1.

[29] N. M. Ghoniem and M. L. Takata, J. Nucl. Mater., 105 (2&3) (1982) 276.

[30] B. T. M. Loh, Acta Metall., 20 (1972) 1305.

[31] K. C. Russell and D. H. Hall, Nucl. Metall., 105 (1973) 545.

[32] H. Wiedersich and B. O. Hall, J. Nucl. Mater., 66 (1977) 187.

[33] B. L. Eyre and R. Bullough, J. Nucl. Mater., 26 (1968) 249; also see D. Olander, Fundamental Aspects of Nuclear Reactor Fuel Elements, NTIS TID-26711-P1 (Nat. Tech. Info. Serv. Springfield, VA, 1976) Ch. 13.

[34] B. O. Hall, in Proc. 10th Conf. on Effects of Radiation on Materials, Savannah, GA, June 3-5, 1980, ASTM-STP-725, D. Kramer, H. R. Brager and J. S. Perrin, Eds., (1981) p. 512-527.

[35] A. C. Hindmarch, June 17, 1980 Version of LSODE, Lawrence Livermore Lab. Report UCID-3001 (1974).

[36] U. Gosele, J. Nucl. Mater., 78 (1978) 83.

[37] N. M. Ghoniem and D. D. Cho, Phys. Status Solidi A, 54 (1979) 171.

[38] W. G. Wolfer and M. Ashkin, J. Appl. Phys., 46 (1975) 547.

[39] E. V. Kornelsen and A. A. Van Gorkum, J. Nucl. Mater., 92 (1980) 79.

[40] M. I. Baskes, C. L. Bisson and W. D. Wilson, Sandia Lab. Report SAND-78-8836 (June 1979).

[41] W. D. Wilson, M. I. Baskes and C. L. Bisson, Phys. Rev. B, 13 (1976) 2470.

[42] V. Philips, K. Sonnenberg and J. M. Williams, "Diffusion of Helium in Nickel," J. Nucl. Mater. (to be pub.).

[43] C. F. Melius, W. D. Wilson and C. L. Bisson, in Proc. Harwell Consultants Symp. on Inert Gases in Metals and Tonic Solids, AERE-R9733, v. I (March 1980) p. 14.

[44] N. M. Ghoniem and G. L. Kulcinski, Radiat. Eff., 39 (1978) 47.

[45] A. C. Damask and G. J. Dienes, Phys. Rev., 120 (1), (1960) 99.

[46] N. M. Ghoniem and H. Gurol, Radiat. Eff., 55 (1981) 209.

[47] W. D. Wilson and R. A. Johnson, Interaction Potentials and the Simulation of Lattice Defects, C. Gehlen, R. J. Beeler and R. I. Jaffee, Eds. (Plenum, NY, 1972) p. 375.

[48] K. C. Russel, Acta Metall., 26 (1978) 1615.

[49] S. I. Maydet and K. C. Russel, J. Nucl. Mater., 82 (1979) 271.

[50] P. J. Maszias and M. L. Grossbeck, ibid, 103&104 (1981) 987.

[51] M. Snykes and E. Ruedl, ibid, p. 1075.

[52] H. Trinkaus, private discussions.

[53] L. K. Mansur and W. A. Coghlan, J. Nucl. Mater. (in press).

CHAPTER VI

THEORY OF CAVITY EVOLUTION DURING IRRADIATION

The goal of experimental and theoretical investigations of bubble formation during irradiation in structural materials is to determine and understand the cavity size distribution. As pointed out in Chapters I and II it is the cavity size distribution that will ultimately decide the level of structural material property degradation.

Of all the stages of cavity evolution, the cavity-size distribution has proven to be the most challenging one to model, because of the stochasticity effects on atomic clustering.

Stochastic effects can be divided into two groups; external and inherent. External stochastic effects are due to the nature of defect and nucleation sources. Both are random functions of space and time. On the other hand, inherent stochastic effects associated with atomic clustering is due to the atomic discreteness of absorption and emission processes for individual atoms or vacancies.

If the nucleation process produced bubbles of the same size, all bubbles would grow at the same rate provided that the only processes operating on the bubbles are addition or removal of one gas atom at a time. Markworth and Baroody [1] have determined the shape of such a bubble distribution. They showed that the variance of the distribution at time t is the product of the variance of the initial distribution and a decay time [2] exp(-bt), where b is the microscopic re-solution parameter. Thus an initially non-uniform distribution becomes narrower

because of re-solution, but an initially uniform distribution (i.e., zero variance) remains uniform during growth.

Hayns and Wood [3] investigated the void-size distribution functions using a numerical procedure and void growth laws. It was found that diffusion controlled void growth invariably leads to tightening of the void size distribution due to the faster growth of smaller cavities. The expected broadening of the distribution due to thermal emission effects was found to be small, and confined to low doses, but more appreciable for surface-reaction controlled growth. However, they caution that their numerical results are only intended for illustration, and that at higher doses, or for high void concentrations, one would expect coalescence amongst the population, which would lead to a broadening of the distribution regardless of growth kinetics [4].

In their model [3], Hayns et al. assumed that the void density remains constant with increasing dose. Furthermore, to utilize their numerical model they had to assume an initial distribution of void sizes which is representative of the end of the nucleation period.

Experimental findings on cavity size distributions [5], clearly indicate that the size distribution broadens as dose is increased. It is easy to show that coalesence events are rare, and do not generally contribute to such broadening. The theoretical work of Markworth and Baroody [1] and Hayns et al. [3] are not therefore consistent.

In the following section, a brief discription of stochasticity effects will be given, and of how such stochastic effects have been modeled by appropriate rate constants for various processes. The next section also describes the use of chemical reaction rate equations which

enable us to model, in detail, the fundamental kinetic processes resulting in defect fluxes and initial critical HVC concentrations.

Stable complexes resulting from these discrete rate equations will then be considered as the nucleii for larger cavities. These cavities will now be examined in the final section by using a continuum approach that leads to the derivation of the Fokker-Planck equation.

I. SOURCES OF STOCHASTICITY IN ATOMIC CLUSTERING

Radiation damage and radiation effects can be distinguished by their characteristic time scales; the primary events produced by nuclear irradiation are over in less than $\sim 10^{-11}$ seconds after the bombarding particle has interacted with the solid. Subsequent processes require much longer times; the diffusion of radiation-produced point defects to sinks in the solid can take milliseconds to months. The time scale for the nucleation and growth of cavities in metals by agglomeration of radiation-produced vacancies is of the order of months to years.

The energy transferred to a stationary lattice atom in a collision with a high-energy bombarding particle is on the order of tens to hundreds of kiloelectron volts, which is much higher than the displacement damage energy ($\sim$ 25 eV). The lattice atom first struck and displaced by the bombarding particle is called the primary knock-on atom (PKA). Because a PKA possesses substantial energy, it becomes an energetic particle, which is able to create additional lattice displacements. These subsequent generations of displaced lattice atoms are

known as higher order knock-ons, or recoil atoms. The ensemble of point defects created by a single PKA is known as a displacement cascade.

The earliest theory of radiation damage treated the cascade as a collection of isolated vacancies and interstitials and gave no consideration to the spatial or time distribution of point defects. In the simplest approximation the number of displaced atoms is computed by approximating the collision partners as hard spheres. Hard-sphere scattering can be represented by energy-transfer cross sections based on realistic interatomic potentials. Many improvements on these simple collision models have been made, but the idea of a cascade consisiting of isolated point defects was retained until recently.

When the distance between successive collisions of a recoil atom and the stationary lattice atoms approaches the interatomic spacing of the crystal structure, a dense cluster of point defects called a displacement spike is formed. These displacement spikes are random functions of space and time. It was hypothesized that the nature of these displacement spikes would have a profound influence on nucleation and growth of defect clusters under irradiation. Although still under investigation, it has been shown that previous estimates of average defect concentrations are good approximations [6]. In particular, it has been established by Chou and Ghoniem [6] that the variance of cascade spikes decreases for higher energy PKAs, typical of fusion conditions.

The production of point defects in displacement cascades is an example of external sources of stochasticity. Others are the distribution of sinks within the medium, and the random nature of sink-cavity

pairs. Previous work in this area [6] has indicated that such external sources of stochasticity may have a small effect on cavity evolution, especially during the growth period. We will therefore not include such effects in our analysis. The theme of this thesis is to analyse the effects of inherent stochasticity on the evolution of the size distributions.

The inherent sources of stochasticity for atomic clustering are absorption and emission processes, since they occur at a discrete atomic level. Here clusters can absorb or emit atomic constituents, with the rates being dependent on different atomic sizes. If such rates were to depend on only one size, no size distribution would occur. This simple origin of the evolution of the size distribution will be demonstrated in the following section.

2. RATE EQUATIONS FOR HVCs

As pointed out in Chapter III, the problem of nucleation and growth of defect clusters during irradiation has been a challenging one. Defect clustering is a complex combination of kinetic processes, such as diffusion of point defects and migration of clusters, and time independent processes such as absorption and emission which depend on concentrations and geometrical factors.

A successful approach to study the nucleation and growth of defect clusters has been the use of chemical reaction rate theory [7]-[13].

Hayns [9] studied the nucleation and early stages of growth of interstitial dislocation loops in irradiated materials. A hierarchy of rate equations was solved to simulate the homogeneous nucleation of

interstitial dislocation loops. The assumption that di-interstitial atom pairs are stable against thermal dissociation was examined and it was concluded to be appropriate. Lam [10] developed a time- and space-dependent model to study the radiation-induced defect buildup and radiation-enhanced diffusion in a foil under irradiation. The distribution of interstitials, monovacancies, and vacancy aggregates containing two to six vacancies in a silver foil under irradiation was calculated as a function of both distance from the surface of the foil and irradiation time by numerically solving the rate equations for various temperatures and internal sink concentrations. In an investigation of interstitial cluster nucleation at the onset of irradiation, Johnson [11] developed rate equations for the concentrations of single and small clusters of vacancies and interstitials. The effects of irradiation temperature and displacement rate were investigated, and it was found that the cluster concentrations are sensitive to cluster binding energies. Hall and Potter [12] included interstitial-impurity trapping in a time-dependent nucleation and growth model that is used to calculated both vacancy and interstitial cluster densities and size distributions during irradiation. Recently, Ghoniem and Cho [13] developed a rate theory model for the simultaneous clustering of point defects during irradiation. Size-dependent bias factors and self-consistent reaction rate constants were used to evaluate the feedback effects between the vacancy cluster and interstitial loop populations. An atom conservation principle was used to determine the number of necessary rate equations as a function of irradiation time.

The underlying principle of rate equations is to represent production and removal rates of a particular defect size in a species balance equation.

For the sake of self-consistency, we will briefly discuss the rate equations approach as described in Chapter IV, Sect. 2.2.

Discrete Rate Equations

The kinetic processes involved in the nucleation of stable HVCs require far more detailed analysis as compared to growth mechanisms. It is therefore essential to include in our model of cavity evolution a detailed description of the time-dependent concentrations of small HVCs.

In order to calculate nucleation rates of stable HVCs, the mobility and binding energies must be included in the calculations. This will allow a study of the influence of helium migration on clustering and vice versa.

The major problem in formulating a theoretical model for HVC formation lies in the complicated possibilities by which helium interacts with point defects. During irradiation, helium can be trapped and thermally detrapped from single vacancies, divacancies, and higher order clusters. Also, helium can be trapped at dislocations and grain boundaries. Helium bound to single vacancies can be replaced by self-interstitials or it can be displaced by irradiation produced PKAs. Combined with the many possibilities for helium-defect reactions, special attention must also be given to vacancy and self-interstitial reactions with each other and with external sinks such as dislocation networks and grain boundaries.

The chemical rate theory can be used to describe clustering events between randomly migrating species

In our model, we include all possible reactions of mobile and immobile HVCs. We consider mobile species to be

1. Single vacancies,
2. Self-interstitials,
3. Interstitial helium atoms,
4. Divacancies,
5. Divacancies single helium clusters.

Representing the number of vacancies per HVC by m, and the number of helium atoms per HVC by n, we have derived a generalized rate equation for any combinations of m and n. Thus, a set of rate equations can be written to span the helium-vacancy phase space up to any desired combination of m vacancies and n helium atoms. For a description of the rate equations, the reader is referred to Chapter IV, Sect. 2.2.

The number of rate equations necessary to describe cavity evolution is prohibitively too large, if not impractical to solve numerically. Thus, we will use this system of discrete rate equations only to determine quasi-steady-state values of point-defect fluxes and of nucleation currents for the critical HVCs.

The results of calculations for HFIR irradiation conditions are shown in Fig. 1, using discrete rate equations. Note that we have excluded the following clusters from our description: di-helium cluster, tri-helium cluster, trivacancy cluster, and trivacancy

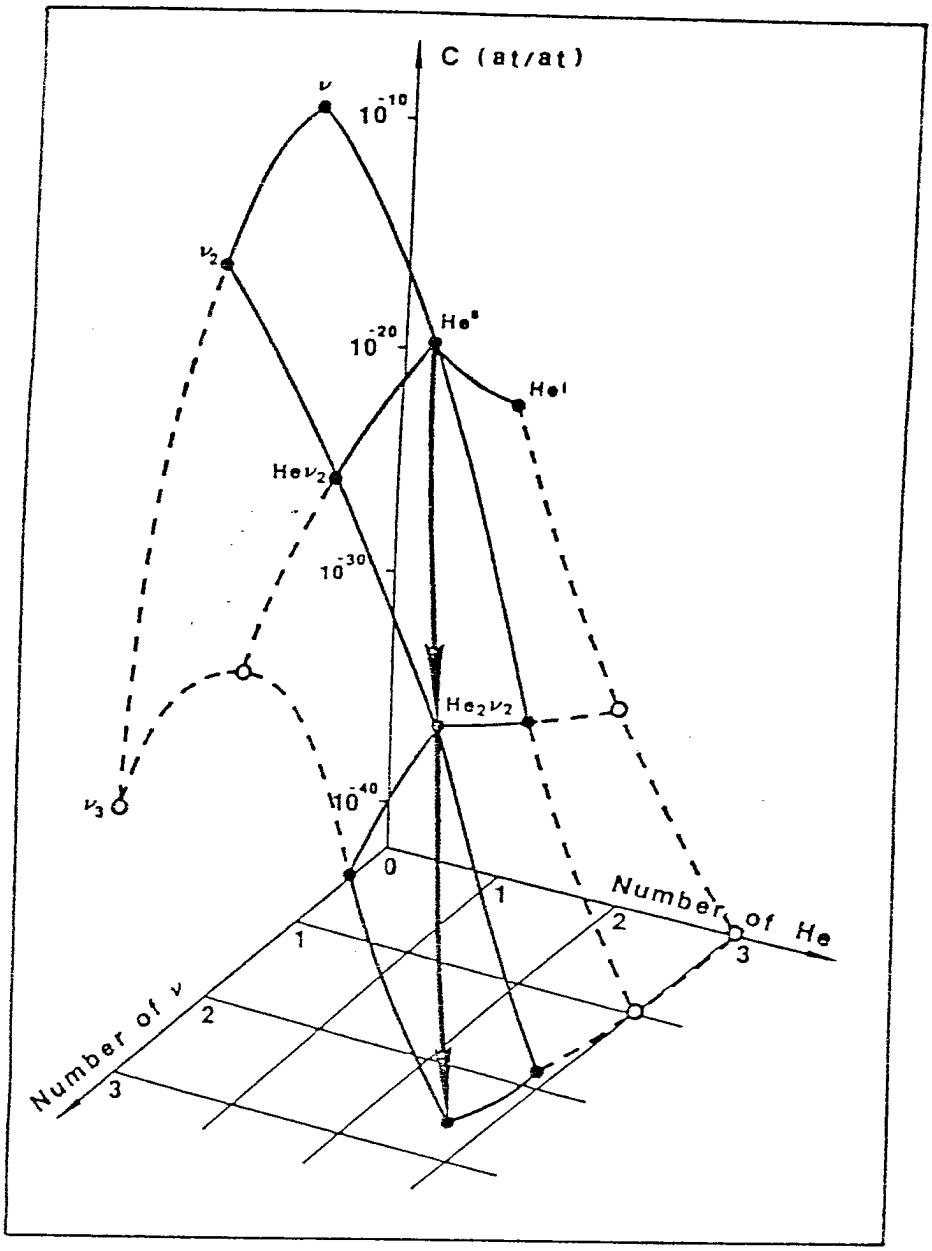

Fig. 1. Steady-state concentrations of HVCs in HFIR at 500°C.

single-helium cluster. Furthermore the choice of such a small system of equations simplifies the rate equations [Eqs. (12)-(16), Chapter IV] by reducing the number of double summation for each equation.

These fluxes for mobile species, combined with the nucleation current of stable HVCs, constitute the necessary input parameters to the continuum rate-theory model described in the following section.

3. FORMULATION OF THE FOKKER-PLANCK EQUATION FOR HVCs

The basic limitation for the rate-theory approach lies in the one-to-one relationship between the number of simultaneous differential equations to be solved and the number of species in a cluster. This limitation is made even more severe by the fact that we are looking at two species in a single cluster (helium atoms and vacancies). Therefore, the computations become prohibitively expensive for large defect clusters. This has prompted the development of approximate computational methods for the kinetics of defect clustering. Kiritani [14] has developed a scheme for the nucleation and growth of clusters in which clusters within a range of sizes are grouped together, and has applied the method to vacancy clustering after quenching. Hayns [15] has applied the Kiritani grouping scheme to study the nucleation and growth of interstitial loops during irradiation, and has shown that objections to the method by Koiwa [16] can be surmounted. Hayns [15] also reported calculations using the grouping scheme to study nucleation and growth of interstitial loops under fast reactor and simulation conditions.

A different approach for studying the nucleation and growth of defect clusters has considered solving continuum equations rather than rate equations. Sprague et al. [17] were able to describe vacancy clusters containing up to 3920 vacancies by descretizing a diffusion-type equation with variable diffusivity. Recently, Wolfer et al. [18] followed similar lines to demonstrate that the rate equations describing the clustering kinetics can be condensed into a Fokker-Planck continuum equation. The latter was interpreted as a diffusion equation with a drift term. They observed that void nucleation and growth can both be incorporated into such a unified formalism. No attempts were made to investigate the numerical solutions of these equations. Hall [19] investigated point-defect clustering considering a different form of the continuum description. Only the cluster concentrations were expanded in a Taylor series and the resulting set of rate equations were shown to be condensed into one partical differential equation. The majority of the approaches mentioned above have not been able to accurately describe the long term behavior of defect clusters, either due to the high computational penalties in rate theory methods, or because of the restrictive approximations in grouping methods. We developed a novel calculational method for the solution of the Fokker-Planck equation describing voids and interstitial loops [20]. The strength of that method lies in its hybrid nature. Small clusters were treated using separate rate equations including all possible details. On the other hand, a continuum approach was used for larger size clusters by descretizing a transformed Fokker-Planck equation. Defects containing up to millions of atoms were investigated using this hybrid approach. The numerical results of the

method compared well with experimental findings on heavy ion irradiated 316 stainless steel [20]. The newly developed method will now be extended to include helium bubble dynamics and kinetics. This will result in a two-dimensional array of coupled linear differential equations to be solved numerically.

3.1. Derivation of the Fokker-Planck Equation for HVC

In deriving descrete rate equations describing fundamental helium-vacancy clustering, we assume that vacancies, self-interstitials, interstitial helium atoms, divacancies, and divacancy single-helium atoms to be mobile. Seven rate equations, five to describe the time dependent concentrations of mobile species, one describing the matrix bubble concentration, and one describing critical bubble embryo concentrations, were solved. This provides defect fluxes as well as the concentration of critical HVCs. The stable or critical HVC concentration resulting from these discrete equations will now be considered as the nucleus for larger HVCs. These cavities will be examined using the following continuum approach, which will result in a Fokker-Planck equation describing the evolution of HVCs.

During irradiation, the vacancy-gas clusters follow the differential equation:

$$\frac{dC}{dt}_{v,h} = - C_{v,h}(k^{ic,ve} + k^{vc} + k^{gc} + k^{ge} + k^{gr})_{v,h}$$

$$+ C_{v+1,h}\, k^{ic+ve}_{v+1,h}$$

$$+ C_{v-1,h}\, k^{vc}_{v-1,h}$$

$$+ C_{v,h-1}\, k^{gc}_{v,h-1}$$

$$+ C_{v,h+1}\, k^{ge}_{v,h+1}$$

$$+ C_{v+1,h+1}\, k^{gr}_{v+1,h+1} \quad ,$$

where k^{xy} stands for the rate constant of process xy, and

ic = self-interstitial capture,

vc = vacancy capture,

gc = helium capture,

gr = helium replacement,

ge = helium emission

ve = vacancy emission,

and ic+ve is a sum of the rate constants for the two reactions. We have excluded the two reactions resulting from the capture of divancancies and divacancy single-helium clusters. Figure 2 will clarify this point. Expanding the last five terms of the equation in a Taylor series and truncating after the second derivative, we obtain,

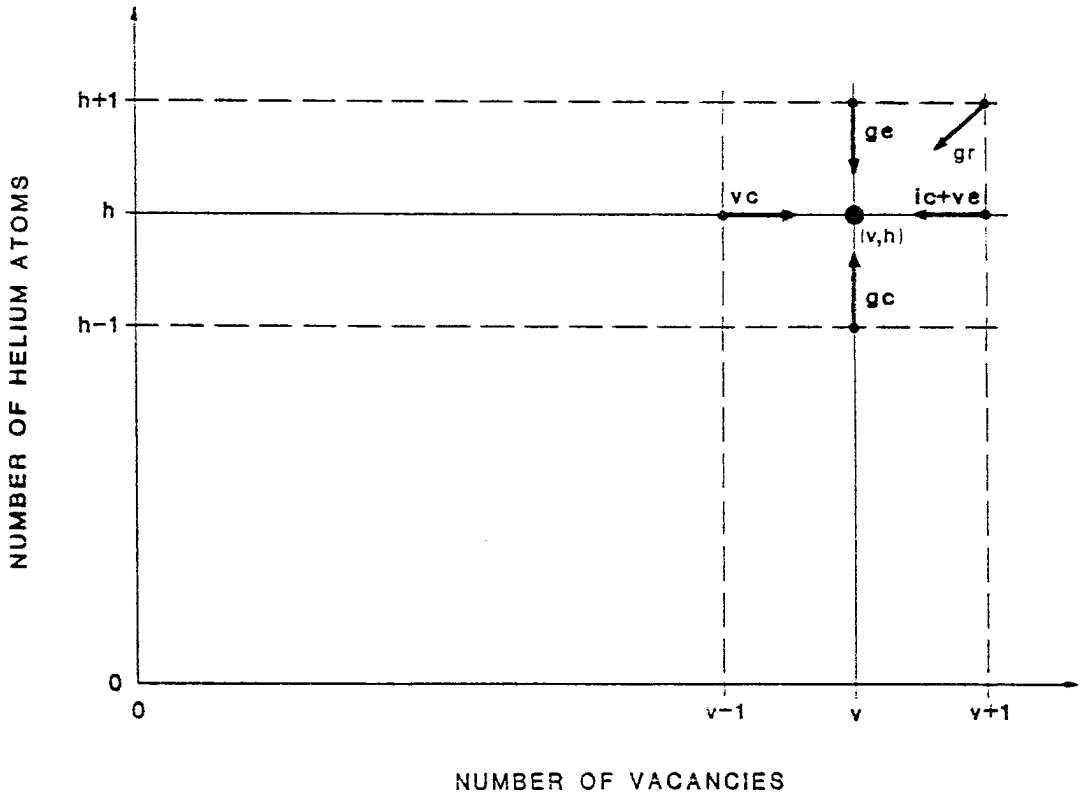

Fig. 2. Reactions leading to the formation of a v,h complex.

$$k^{ic+ve}(v+1,h)\ C_{v+1,h} \simeq k^{ic+ve}\ C + \frac{\partial}{\partial v}\,(k^{ic+ve}C)_{v,h} + \frac{1}{2}\,\frac{\partial^2}{\partial v^2}\,(k^{ic+ve}C)_{v,h}$$

$$k^{vc}(v-1,h)\ C_{v-1,h} \simeq k^{vc}C - \frac{\partial}{\partial v}\,(k^{vc}C)_{v,h} + \frac{1}{2}\,\frac{\partial^2}{\partial v^2}\,(k^{vc}C)_{v,h} \quad ,$$

$$k^{gc}(v,h-1)\ C_{v,h-1} \simeq k^{gc}C - \frac{\partial}{\partial h}\,(k^{gc}C)_{v,h} + \frac{1}{2}\,\frac{\partial^2}{\partial h^2}\,(k^{gc}C)_{v,h} \quad ,$$

$$k^{ge}(v,h+1)\ C_{v,h+1} \simeq k^{ge}C + \frac{\partial}{\partial h}\,(k^{ge}C)_{v,h} + \frac{1}{2}\,\frac{\partial^2}{\partial h^2}\,(k^{ge}C)_{v,h} \quad ,$$

$$k^{gr}(v+1,h+1)\ C_{v+1,h+1} \simeq k^{gr}C + \left(\frac{\partial}{\partial v} + \frac{\partial}{\partial h}\right)(k^{gr}C)_{v,h}$$

$$+ \frac{1}{2}\left(\frac{\partial^2}{\partial v^2} + \frac{\partial^2}{\partial h^2}\right)(k^{gr}C)_{v,h} + \frac{\partial^2}{\partial v \partial h}\,(k^{gr}C)_{v,h} \quad ,$$

where we have used [21]

$$f(x,y) = f(a,b) + \Delta x\ f'_x(a,b) + \Delta y\ f'_y(a,b)$$

$$+ \frac{1}{2!}\,\Delta x^2\ f''_{xx}(a,b) + 2\Delta x\ \Delta y\ f''_{xy}(a,b)$$

$$+ \frac{1}{2}\,\Delta y^2\ f''_{yy}(a,b) + \alpha_o\ \Delta\rho^3 \quad ,$$

where $\delta\rho = (\delta x)^2 + (\delta y)^2$, $\alpha_o = R/\delta\rho^3$, R = remainder. If we substitute back into the cluster equation we get

$$\frac{\partial C}{\partial t}_{vh} = \frac{\partial}{\partial v}\left(k^{ic+ve} + k^{gr} - k^{vc}\right)C_{vh}$$

$$+ \frac{\partial}{\partial h}\left(k^{ge} + k^{gr} - k^{gc}\right)C_{vh}$$

$$+ \frac{1}{2}\frac{\partial^2}{\partial v^2}\left(k^{ic+ve} + k^{gr} + k^{vc}\right)C_{vh}$$

$$+ \frac{1}{2}\frac{\partial^2}{\partial h^2}\left(k^{ge} + k^{gr} + k^{gc}\right)C_{vh} + \frac{\partial 2}{\partial v\,\partial h}\left(k^{gr}C_{vh}\right) \quad .$$

For the purpose of simplifying the analysis, we will introduce the following notations:

$$\kappa_v = k^{vc},$$
$$\kappa_h = k^{gc},$$
$$\lambda_v = k^{ic+ve} + k^{gr},$$
$$\lambda_h = k^{ge} + k^{gr}.$$

We now define the drift function as $F = \kappa - \lambda$ = point defect net bias flux and the diffusion function by $D = (\kappa + \lambda)/2$ = point defect average diffusion flux. Assuming k^{gr} to be small, the continuum equation can now be written as

$$\frac{dC}{\partial t} = -\frac{\partial}{\partial v}\left(F_v C\right) - \frac{\partial}{\partial h}\left(F_h C\right) + \frac{\partial^2}{\partial v^2}\left(D_v C\right) + \frac{\partial^2}{\partial h^2}\left(D_h C\right) \quad .$$

This is now the well known form of the Fokker-Planck equation that describes diffusion in a drift field [22]. If we denote the nucleation

current by $\overline{J}$, then $\overline{J} = FC - \overline{\nabla}(DC)$. Now the continuum equation can be expressed in the vector form: $\partial C/\partial t = - \overline{\nabla} \cdot \overline{J}$.

The Fokker-Planck equation has been the subject of investigation in various areas of physics [22-24], especially the physics of a non-equilibrium system of particles. However, even with the simplest initial and boundary conditions, this equation proved to be intractable for analytical solutions [22,23]. In order to utilize the Fokker-Planck equation to describe the microstructural behavior after large irradiation doses, we will therefore follow numerical methods outlined in the next chapter.

REFERENCES

[1] A. J. Markworth and E. M. Baroody, Met. Sci. J., 5 (1971) 55.

[2] A. J. Markworth, J. Mater. Sci., 7 (1972) 1225.

[3] M. R. Hayns and M. H. Wood, J. Nucl. Mater., 87 (1979) 97.

[4] L. K. Mansur, P. Okamoto, A. Taylor and Che-Yu-Ki, J. Nucl. Mater., 18 (1973) 509.

[5] P. J. Maziasz, "Effects of Helium Content on Microstructural Development in Type 316 Stainless Steel Under Neutron Irradiation," Ph.D. thesis, University of Tennessee, Knoxville (December 1984).

[6] P. Chou and N. M. Ghoniem, "On the Stochastic Theory of Point Defect Diffusion During Irradiation ...," J. Nucl. Mater. (in press).

[7] L. M. Brown, A. Kelly and R. M. Mayer, Philos. Mag., 19 (1969) 721.

[8] M. Kiritani, Proc. Conf. on Fundamental Aspects of Radiation Damage in Metals, M. T. Robinson and F. W. Young, Eds., CONF-751006-P2 (Nat. Tech. Info. Serv., Springfield, VA, 1975) p. 775.

[9] M. R. Hayns, J. Nucl. Mater., 56 (1975) 267.

[10] N. Q. Lam, ibid, p. 125.

[11] R. A. Johnson, ibid, 75 (1978) 77.

[12] B. O. Hall and D. I. Potter, in Proc. 9th Intl. Symp. on Effects of Radiation on Structural Materials, Am. Soc. Testing Mater., Richland, WA, July 11-13, 1978, ASTM-STP-683, p. 789.

[13] N. M. Ghoniem and D. D. Cho, Phys. Status Solidi A, 54 (1979) 171.

[14] M. Kiritani, J. Phys. Soc. Jpn., 35 (1973) 95.

[15] M. R. Hayns, J. Nucl. Mater., 59 (1976) 175.

[16] M. Koiwa, J. Phys. Soc. Jpn., 37 (1974) 175.

[17] J. A. Sprague, K. C. Russell and Y. H. Choi, in Fundamental Aspects of Radiation Damage in Metals (Proc. Conf., Springfield, VA, June 1975) CONF-751006-P2, p. 118.

[18] W. G. Wolfer, L. K. Mansur and J. A. Sprague, Radiation Effects in Breeder Reactor Structural Materials (Proc. Intl. Conf., Scottsdale, AZ, 1977) M. L. Bleiberg and J. W. Bennet, Eds., (AIME, NY, 1977) p. 841.

[19] B. O. Hall, J. Nucl. Mater., 85&86 (1979) 565.

[20] N. M. Ghoniem and S. Sharafat, ibid, 92 (1980) 121.

[21] N. Piskunov, Differential and Integral Calculus (MIR Publishers, Moscow, 1970) p. 292.

[22] R. I. Cukier, K. Lakatos-Lindenberg and K. E. Shub, J. Stat. Phys., 9 (2) (1973) 137.

[23] G. H. Weiss and M. Dishon, ibid, 13 (2) (1975) 145.

[24] S. Chandrasekhar, Rev. Mod. Phys., 15 (1943) 1.

CHAPTER VII

NUMERICAL MODEL

1. FINITE DIFFERENCE ANALYSIS OF THE FOKKER-PLANCK EQUATION

While separate rate equations are used for mobile defects such as single vacancies, self-interstials, and helium atoms, larger size clusters are simulated by condensing the set of rate equations into one generalized Fokker-Planck equation.

As shown in the previous chapter, the continuim equation that describes the nucleation and growth of helium-vacancy clusters (HVCs) can be expressed as a continuity equation in HVC space. This is given by:

$$\frac{\partial C_{v,h}}{\partial t} = - \vec{\nabla} \cdot \vec{J} \quad , \tag{1}$$

where $C_{v,h}$ = Concentration of HVCs containing v-number of vacancies and h-number of helium atoms, and $\vec{J}$ = the nucleation current.

Equation (1) is derived in the absence of sources and sinks in the vacancy-helium space. This is expected to occur if cavity coalescence does not exist. At temperatures of interest, and in fusion reactor applications, coalescence plays a minor role, and can therefore be ignored. J is denoted by:

$$J(v,h,t) = F(v,h,t)C(v,h,t) - \frac{\delta}{\delta v}\left[D(v,h,t)C(v,h,t)\right]$$

$$- \frac{\delta}{\delta h}\left[D(v,h,t)C(v,h,t)\right] \quad , \tag{2}$$

where v = vacancies and h = helium-atoms, F = DRIFT-function = point-defect net bias flux, and D = DIFFUSION-function = point-defect average diffusion flux. The derivation of the above form of the Fokker-Planck equation is discussed in Chapter VI.

The approach we use here to solve the Fokker-Planck equation is strictly numerical. We will first discretize the independent variable v (no. of vacancies) and h (no. of helium atoms), and then express all dependent variables in terms of the discrete points.

In order to simplify the description of our approach, we first start by a 1-D description of the Fokker-Planck equation. This is accomplished by assuming that the number of helium atoms is constant, and that discretization proceeds along the vacancy independent variable. We will later extend the technique to the 2-D problem.

The 1-D Fokker-Planck equation can now be given by:

$$\frac{\partial C}{\partial t} = - \frac{\partial J}{\partial v} \quad , \tag{3}$$

$$J_v(v,t) = F(v,t)C(v,t) - \frac{\partial}{\partial v} [D(v,t)C(v,t)] \quad . \tag{4}$$

The total concentration of HVCs per unit volume is given by:

$$C_{tot}(t) = \frac{1}{\Omega} \int_0^{\infty} C(v,t)dv \quad , \tag{5}$$

$$\simeq \frac{1}{\Omega} \sum_{v=1}^{MAX} C(v,t)\Delta v \quad ; \qquad \Delta v \geq 1 \quad . \tag{6}$$

Because v and t are independent variables, we can integrate Eq. (3) over a small interval Δv_i; for the ith mesh point,

$$\frac{\partial}{\partial t} \int_{v_{i-1/2}}^{v_{i+1/2}} C_i(t)dv = - \int_{v_{i-1/2}}^{v_{i+1/2}} \partial J_i \quad , \tag{7}$$

For simplicity, we use i+1/2 at $v_{i+1/2}$. Figure 1 illustrates the notation and coordinates of this problem. From Fig. 1, and using central differencing, we have:

$$\Delta v_i = v_{i+1/2} - v_{i-1/2} \quad , \tag{8}$$

and

$$v_{i+1/2} \equiv 1/2(v_{i+1} + v_i) \quad , \tag{9}$$

$$v_{i-1/2} \equiv 1/2(v_i + v_{i-1}) \quad , \tag{10}$$

thus

$$\Delta v_i = 1/2(v_{i+1} - v_{i-1}) \quad . \tag{11}$$

With this definition of Δv_i, the left-hand side of Eq. 7 becomes:

$$\frac{\partial}{\partial t} \int_{i-1/2}^{i+1/2} C_i dv \simeq \frac{\partial C_i}{\partial t} \Delta v_i \quad . \tag{12}$$

The right-hand side of Eq. 7 becomes:

$$\begin{aligned} - \int_{v_{i-1/2}}^{v_{i+1/2}} \partial J_i &= - J_{i+1/2} + J_{i-1/2} \quad , \\ &= J_{i-1/2} - J_{i+1/2} \quad , \\ &\equiv (J^v_{in} - J^v_{out})_i \quad , \end{aligned} \tag{13}$$

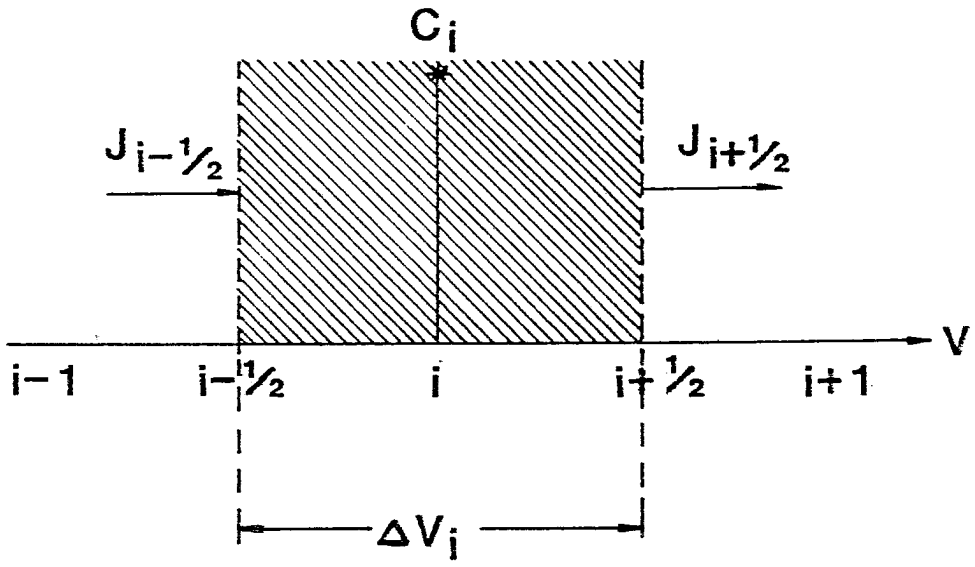

Fig. 1. Schematic of finite difference notations.

and

$$J_{i-1/2} = [FC]_{i-1/2} - \left[\frac{\partial DC}{\partial v}\right]_{i-1/2} \quad , \tag{14}$$

with

$$[FC]_{i-1/2} \simeq \frac{[FC]_i + [FC]_{i-1}}{2} \quad , \tag{15}$$

where Eq. 15 is obtained by a simple linear interpolation of the function [FC] between i-1 and i. For the midpoint value we are considering, central difference gives:

$$\left[\frac{\partial}{\partial v} DC\right]_{i-1/2} \simeq \frac{[DC]_i - [DC]_{i-1}}{\Delta v_{i-1/2}} + O[(\Delta v)^2] \quad , \tag{16}$$

with

$$\Delta v_{i-1/2} = v_i - v_{i-1} \quad . \tag{17}$$

Combining Eqs. (14), (15) and (16), we get:

$$J^v_{in} \equiv J_{i-1/2} \simeq \frac{[FC]_i + [FC]_{i-1}}{2} - \frac{[DC]_i - [DC]_{i-1}}{\Delta v_{i-1/2}} \quad , \tag{18}$$

where

$$\Delta v_{i-1/2} = v_i - v_{i-1} \quad . \tag{19}$$

So the continuim Fokker-Planck equation [Eq. (3)] is now represented by finite number of discrete equations of the form:

$$\frac{\partial C_i}{\partial t} = \frac{1}{\Delta v_i} \left\{ [J^v_{in} - J^v_{out}]_i \right\} \quad , \tag{20}$$

where

$$\Delta v_i \simeq \frac{1}{2} (v_{i+1} - v_{i-1}) \quad . \tag{21}$$

Thus, by simply extending the finite differencing scheme outlined above to both variables, we get

$$\frac{\partial C_{i,j}}{\partial t} = \frac{1}{\Delta v_{i,j}} [J^v_{in} - J^v_{out}]_{i,j} + \frac{1}{\Delta h_{i,j}} [J^h_{in} - J^h_{out}]_{i,j} \quad , \tag{22}$$

and

$$C(v,h,t) \simeq \sum_{i=1}^{I} \sum_{j=1}^{J} C_{i,j}(t) \, \Delta v_{i,j} \, \Delta h_{i,j} \quad , \tag{23}$$

where

$$\begin{aligned} \Delta v_{i,j} &= 1/2(v_{i+1} - v_{i-1})_j \quad , \\ \Delta h_{i,j} &= 1/2(h_{j+1} - h_{j-1})_i \quad , \\ v &= \text{no. of vacancies per HVC} \quad , \\ h &= \text{no. of helium atoms per HVC} \quad . \end{aligned} \tag{24}$$

I and J are maximum number of vacancy and helium intervals, respectively.

The resulting system of ODEs [Eq. (22)] is generally a stiff non-linear system of equations. Efficient multi-step implicit numerical integration methods are therefore necessary. For our purposes, we use the GEAR [4] numerical integration techniques, which have been widely used during the past decade.

To simplify the development of the numerical model, we will first investigate the 1-D Fokker-Planck equation [Eqs. (20) and (21)]. Thus we will assume for the time of growth no change in the number of helium atoms per HVC, and that the only means of growth or shrinkage of a HVC is through single-vacancy and self-interstitial interactions. This case may correspond to the development of a void size distribution with a fixed number of gas atoms.

2. DISCRETE SYSTEM OF EQUATIONS WITH FIXED BOUNDARY CONDITIONS

In developing a numerical method for the solution of the 1-D Fokker-Planck equation [Eqs. (20,21)] various cases were studied. Table I lists the cases examined that led to the method of dynamic mesh size incrementation.

As a first step in the numerical analysis of the discretized equations, we first investigate a system of equations with fixed boundary conditions.

As previously indicated, critical size HVCs can grow in an irradiation environment by acquiring a mobile single vacancy. During the initial stages of nucleation, the behavior of small HVCs is of prime importance. Therefore we will limit the vacancy phase space to its lower end and solve a system of equations describing the development of

TABLE I
CASES STUDIED

	System With Constant No. of Equations	System With Variable No. of Equations
Fixed boundary conditions (constant mesh sizes)	Zero-current boundary condition ($J_{in}=0$, $J_{out}=0$)	
	Non-zero current boundary condition ($J_{in}=0$, $J_{out}\neq 0$)	
Moving boundary conditions ($J_{in}=J_{out}=0$)	Uniform size mesh Variable size mesh	Uniform size mesh Variable size mesh

clusters containing up to only ~ 500 vacancies. The vacancy phase space is devided into 25 equal size mesh intervals, starting at a critical cluster size of 3 vacancies.

In this section, the number of equations, mesh size, and boundary conditions are all kept constant during numerical integration representing the evolution process.

2.1. Boundary Conditions

To simplify the development of numerical methods in solving the Fokker-Planck or growth equations, the following approach is followed: A set of detailed rate equations is solved for small clusters. This produces a self-interstitial flux, a single-helium atom flux, a single-vacancy flux, and a critical HVC nucleation current. Once quasi-steady-state flux rates are reached, mobile defect fluxes and the concentration of critical HVCs are taken as input parameters for the Fokker-Planck

equations. This separation of nucleation and growth is reasonable, since nucleation time scales are much shorter than growth time scales.

2.1.1. Zero-Current Boundary Conditions. In considering the nucleation and growth of HVCs in two stages, we are in effect setting the nucleation current (J_{in} for the lower boundary) equal to zero and monitor the growth of these clusters. If at the upper boundary (J_{out}), is also set equal to zero, the total number of HVCs will be conserved at all times. By setting J_{out} equal to zero we are allowing only shrinkage or growth but no annihilation of any HVCs. This conservation principle thus constitutes a check on our numerical solution to the Fokker-Planck or growth equation. The zero-current boundary condition is $J_{in/lower} = J_{out/upper} = 0$.

As a case study, we consider the High Flux Isotope Reactor (HFIR) irradiation conditions and stainless-steel material parameters. Figure 2 shows the behavior of the HVC size distribution at different irradiation times. At the onset of evolution (t_1 = 0.1 s), the distribution is shown to be dominated by small clusters. At $t_2 = 8.6 \times 10^3$ s we notice a decrease in the concentration of critical HVCs and a broadening of the distribution. Because the nucleation current J_{in} is set equal to zero, there is no supply of critical HVCs. As irradiation continues the distribution function broadens and the peak value decreases.

This behavior is expected from a Fokker-Planck equation in which the DRIFT term F forces the peak to move while the DIFFUSION term D causes a broadening of the distribution.

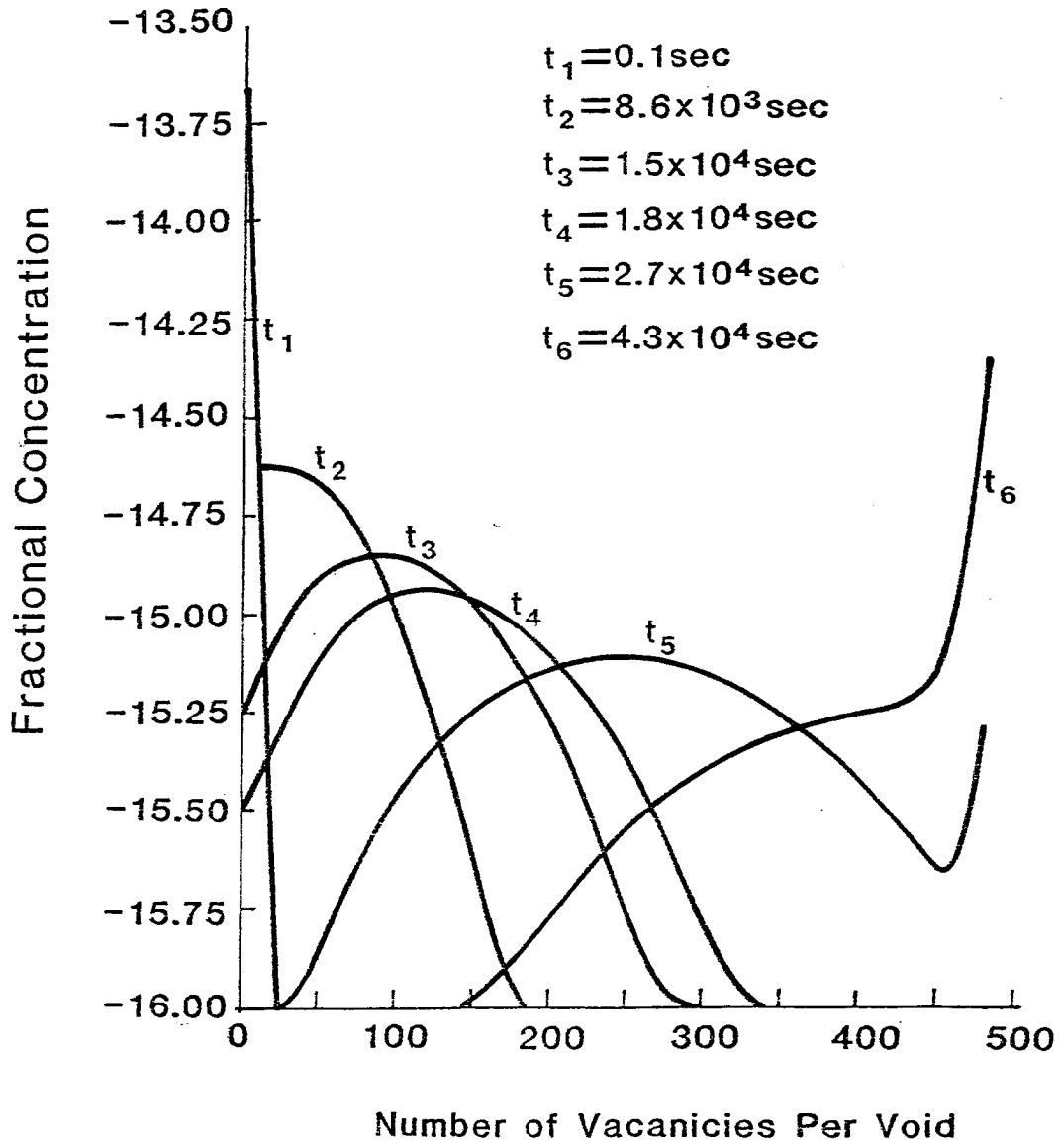

Fig. 2. Time evolution of small HVC with zero-current boundary condition.

Because we have set J_{out} equal to zero, there are no destruction mechanisms for the largest HVCs. The calculations indicate that the number density of large clusters increases steadily at the expense of smaller ones. Thus, once the peak has reached the maximum size considered, it stays at that position and its value steadily increases until about 10^5 seconds. Beyond this time, the distribution remains unchanged for any practical irradition time considered.

The conservation of the zeroth moment of the HVC distribution must now be checked. A simple trapezoidal rule, for estimating the area under the distribution function in Fig. 2, gives very satisfactory results. The largest error in the zeroth moment is found to be $\sim 10^{-10}$% which is close to the machine round-off error ($\sim 10^{-14}$ for the Cray).

2.1.2. Non-Zero-Current Boundary Condition. A variation on the previous boundary condition is to let $J_{out} \neq 0$ while keeping $J_{in} = 0$. Figure 3 depicts the results of this case. By comparison of Figs. 2 and 3, it is observed that the behavior of the HVC size distribution is almost identical until $t \approx 4.4 \times 10^4$ s. Beyond this time the peak of the distribution reaches the maximum HVC size considered. Because the system has a "leaky" boundary condition at the upper boundary of the phase space, the distribution gradually disappears. Accordingly, the zeroth moment is no longer conserved and at $t = 1.2 \times 10^5$ s an error of 100% is already reached. The behavior of the error in the zeroth moment is shown in Fig. 4.

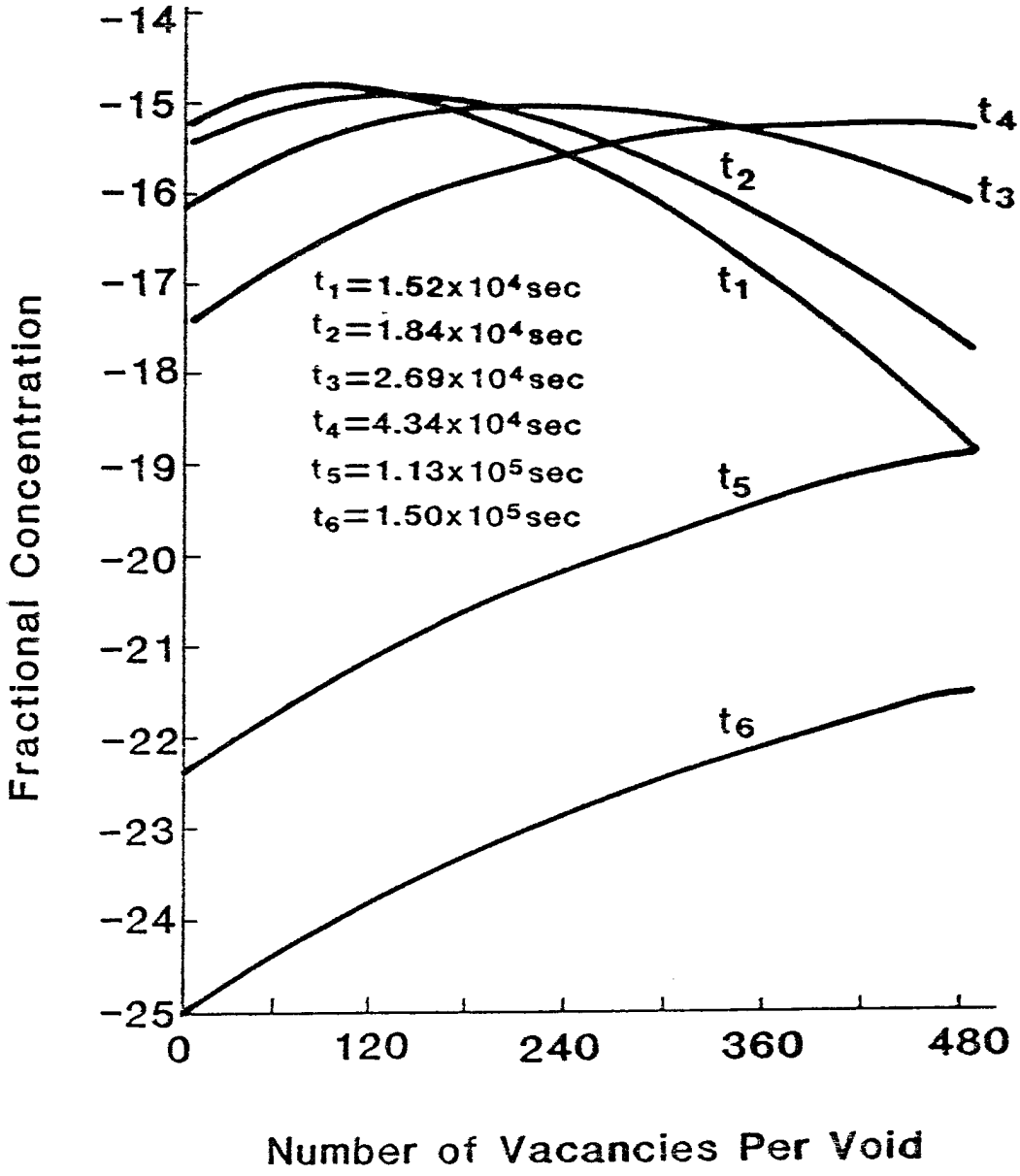

Fig. 3. Time evolution of small HVC with non-zero-current boundary condition.

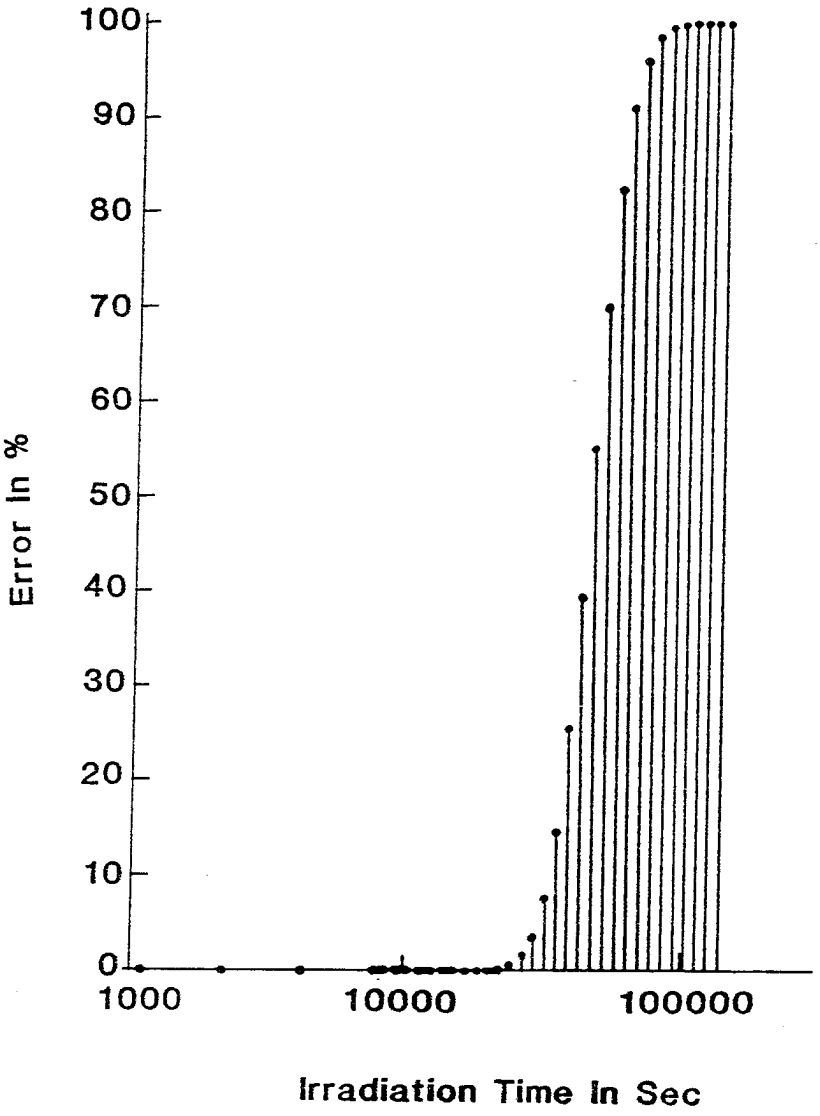

Fig. 4. Error in the zeroth moment for the non-zero-current boundary condition. [$J_{in}=0$, $J_{out}\neq 0$]

3. DISCRETE SYSTEM OF EQUATIONS WITH MOVING BOUNDARY CONDITIONS

By investigating a small and fixed system of Fokker-Planck equations, we established the general validity of the present numerical approach. Our goal is to follow the development of HVCs from subcritical to microscopically measurable sizes. To achieve this we have to expand our system of equations to include HVCs containing up to 10^7 vacancies (bubbles with a radius of a few hundred Angstroms).

Handling a system of non-linear first order ODEs which spans such a range in the vacancy phase space (from 1 to 10^7 vacancies) requires programming efficiency, flexibility, and economy. Therefore, the following considerations were followed in structuring the computer program:

1. Computing the minimum number of variables. Thus, time invariant quantities are computed once at the beginning. Time dependent equations contain the minimum number of time invariant arithmetic operations.

2. All variable input constants are incorporated in NAMELIST statements, so that any input data can easily be changed.

3. The numerical output is stored on user's files, such that plotting is easily implemented.

These guidelines are easily implemented. However, the major means to save computer time is to keep the number of ODEs to a minimum. In the following discussion, various approaches to insure programming economy will be outlined.

3.1. A Constant Number of Equations with Dynamically Increasing Mesh Sizes

As a start, the vacancy phase space between 1 and 10^7 may be divided into equally sized mesh points. The total number of equations are limited, for example, to 50; the mesh size would be 2 x 10^5 vacancies:

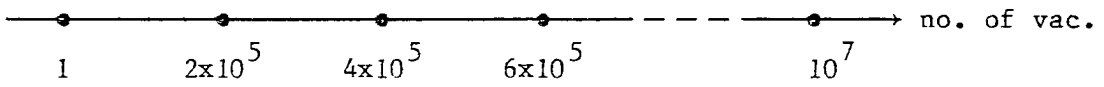

Each interval is represented by one discrete equation, which is coupled to its two neighboring equations. The coupling, which stems from the diffusion and drift expressions, is included in J_{in} and J_{out} of each equation.

At the onset of evolution, changes in the distribution function are very rapid. The distribution broadens while the peak moves rapidly to larger sizes.

The cluster distribution tends towards an equilibrium Gaussian-like distribution. Figure 5 shows the distribution function for sizes in the range of 3 to a few million vacancies at different times. As irradiation time increases from t_1 = 0.1 s to t_5 = 6.4 x 10^4, the distribution tends toward an equilibrium resembling a Gaussian. It is to be noted that as the distribution moves, the rate of change slows down. Therefore, it is crucial to monitor both fast and slow variations in the distribution function. This can be achieved by choosing a fine mesh size for small clusters and increasingly larger mesh size for larger clusters. Starting with a HVC size of 3 vacancies and then doubling the

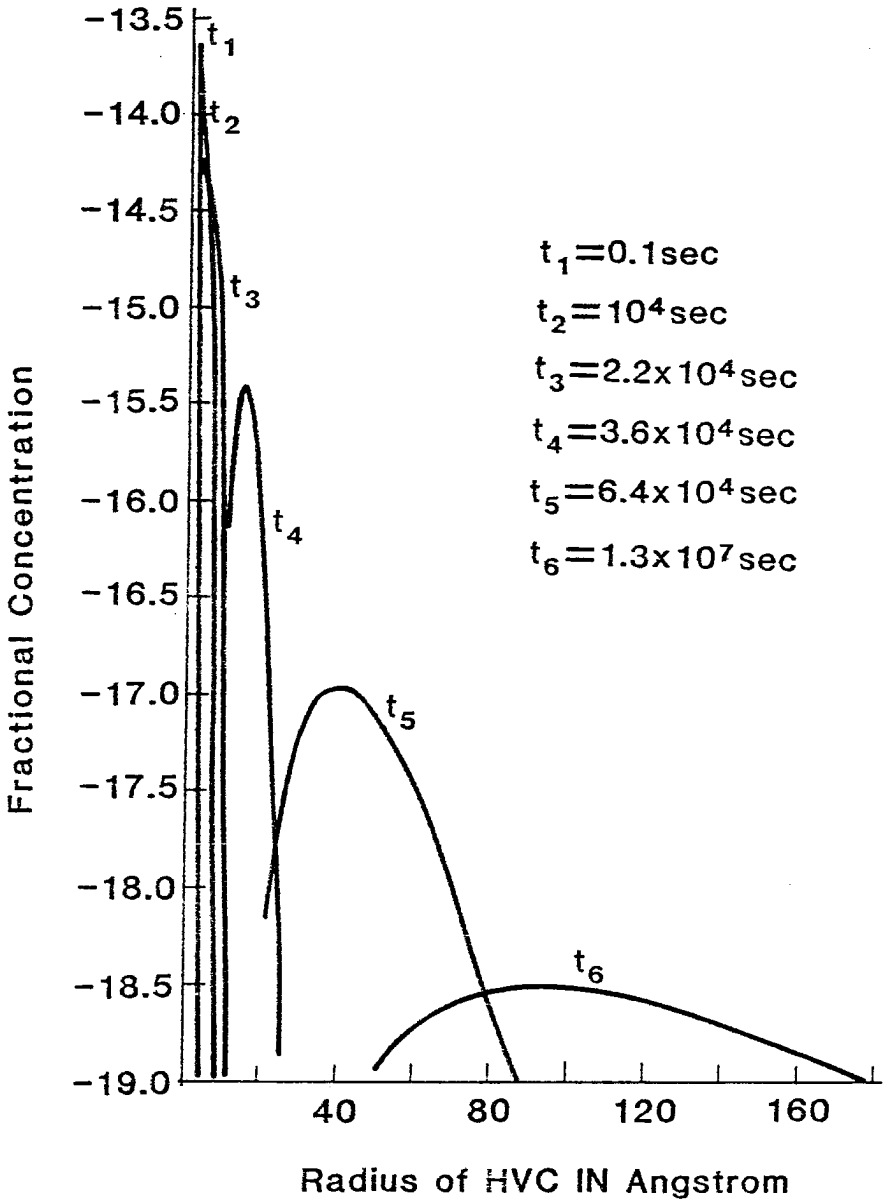

Fig. 5. HVC size distribution evolution as a function of irradiation time, for HFIR irradiation conditions at 500°C.

mesh size to 6 and then to 12 and so on, we can span the 10^7 range in about 25 equations.

In this case, the initially very sharp distribution is observed to flatten out with an accompanying motion of the peak value towards larger sizes. But once the peak value moves beyond ~ 100 vacancies per cluster, fluctuations are observed which eventually result in unacceptably negative distribution values.

Because of the highly economical nature of this approach, it will not be abandoned, but the following variation, is investigated.

3.2. Fixed Number of Equations With Variable Mesh Sizes

A variation of the above method is to allow the mesh size to remain constant over only a given range of values.

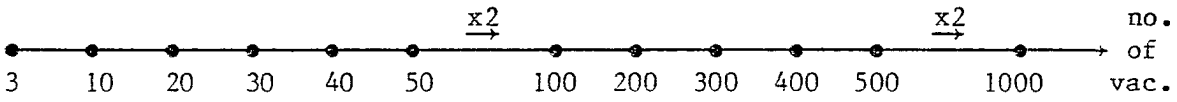

The choice shown spans the 10^7 vacancy range in about 35 equations. This system is designed to shed more light on the cause of instabilities in the previous method. In this case, the distribution function is observed to move toward larger sizes with numerical instabilities appearing at a much later time as compared to the previous method. Many variations on the choice of mesh sizes were examined. Because of numerical instabilities, this approach was found to be unsatisfactory when the number of equations was over 100.

The two previous investigations both point to a more stable system if the mesh sizes were kept constant. In order to solve the problem at a reasonable computing cost, the following scheme is developed.

3.3. Fixed Number of Equations with Dynamic Mesh Space Enlargement

In this approach, we first fix the number of equations to, say, 20. We then let these 20 equations span a cluster size range containing from 3 to 200 vacancies. The system of equations is then solved and the distribution function behavior is monitored. As expected, the peak moves away from the critical size (3 vacancies) towards larger cluster, while at the same time the distribution flattens.

The program is structured such that once the peak value of the distribution moves beyond, say, one-half of the range being monitered, the mesh spacing is doubled.

The cluster sizes under investigation range from 3 to 400. The concentration of the newly added sizes are initialized to some low floor value. Every other previous equation is dropped. Equations are renumbered and the system is solved as a new system with a given initial distribution function determined at the end of the previous calculation. Figures 6 and 7 schematically illustrate the process.

From $t = t_o$ the distribution moves toward its new shape at $t = t^*$ as shown in Fig. 6. Once the peak has moved, say, beyond 100 vacancies per cluster, the system is changed to Fig. 7. This expanding mesh space method is automatically controlled to continue as long as peak motion is detected. The frequency of expanding the mesh space is determined by the speed of the peak movement.

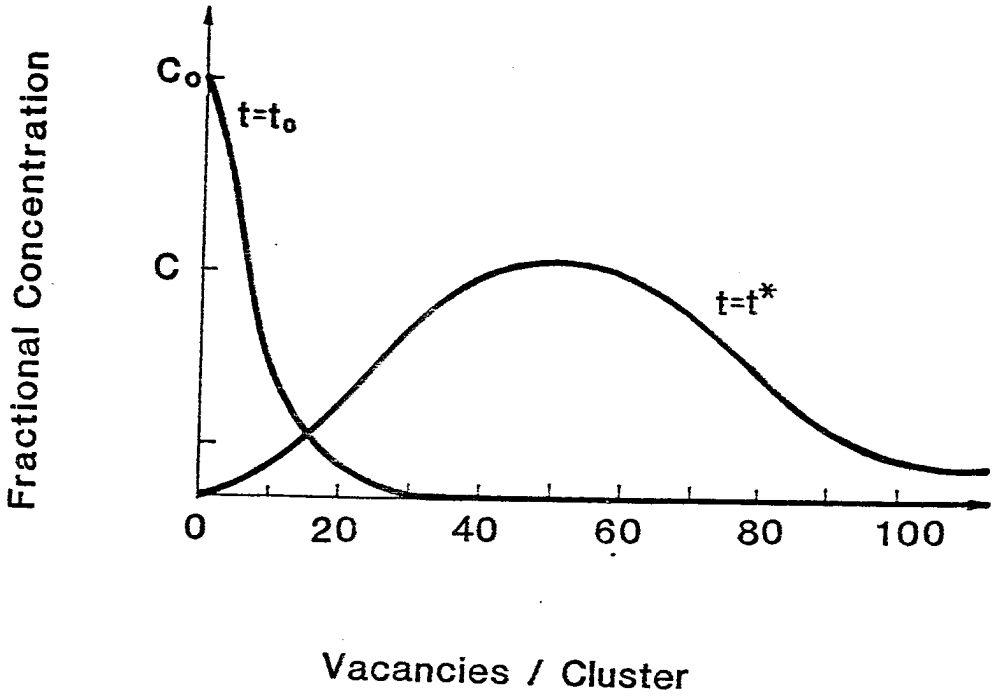

Fig. 6. Schematic of the distribution evolution.

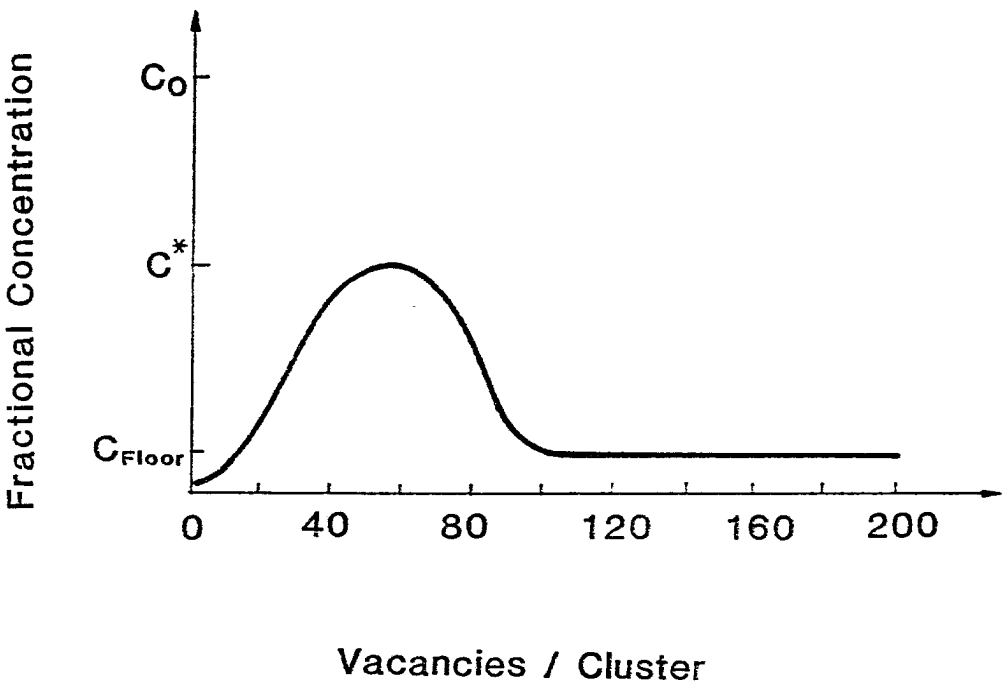

Fig. 7. Schematic of mesh size enlargement relative to a distribution evolution.

This method was found to be the most stable of all previous ones. Instabilities occur only towards the latter part of the calculations. However, the method is still not satisfactory, because the zeroth moment of the distribution function is not conserved. Many variations in mesh space expansions and t* were examined but conservation of the total number of clusters is found to be violated by more than 50% after only a few expansions.

3.4. Dynamic Size Incrementing Method

Each of the previous three methods has its shortcomings:

1. The increasing mesh size (Sect. 3.1) method is unstable.
2. The constant mesh size over a range (Sect. 3.2) is uneconomical.
3. The expanding mesh space (Sect. 3.3) violates the zeroth moment conservation principle.

Because the second method is stable and only uneconomical, we will investigate methods aimed at reducing computational times for that approach.

First the program is structured such that, once the peak of the distribution moves to larger sizes, a number of equations describing small sizes are removed from the system and another number is added to cover the evolution of large sizes.

At every output interval a check is run to determine the contribution of the smaller clusters (already surpassed by the peak) to the zeroth moment. Those equations contributing up to about 0.05% to the zeroth moment are removed from the system (see Fig. 8). This avoids using equations that do not significantly contribute to the system's behavior.

Equations are "dynamically" added to the distribution wavefront as it moves towards larger cluster sizes. For program efficiency, the addition of equations is only done every output interval to avoid constant peak monitoring at every interval timestep of the ODE solver (GEAR package [4]). Thus, a prediction of the distribution peak must be made at every output interval in order to decide whether an addition of equations is necessary and if so, at what mesh spacing and/or how many must be added.

By using the method of trajectories (described in Chapter V), it is possible to predict the temporal behavior of the average HVC size. The knowledge of the average cluster size at any time allows monitoring the movement of the distribution peak.

Thus, by simply adding enough equations to the wavefront of the distribution, such that the known average size is always somewhere close to the center of the system, the most significant system's range is always studied. Furthermore, the experience with constant mesh spacing indicates that 5 to 10 additional equal mesh spaces are adequate. The following is a summary of the method.

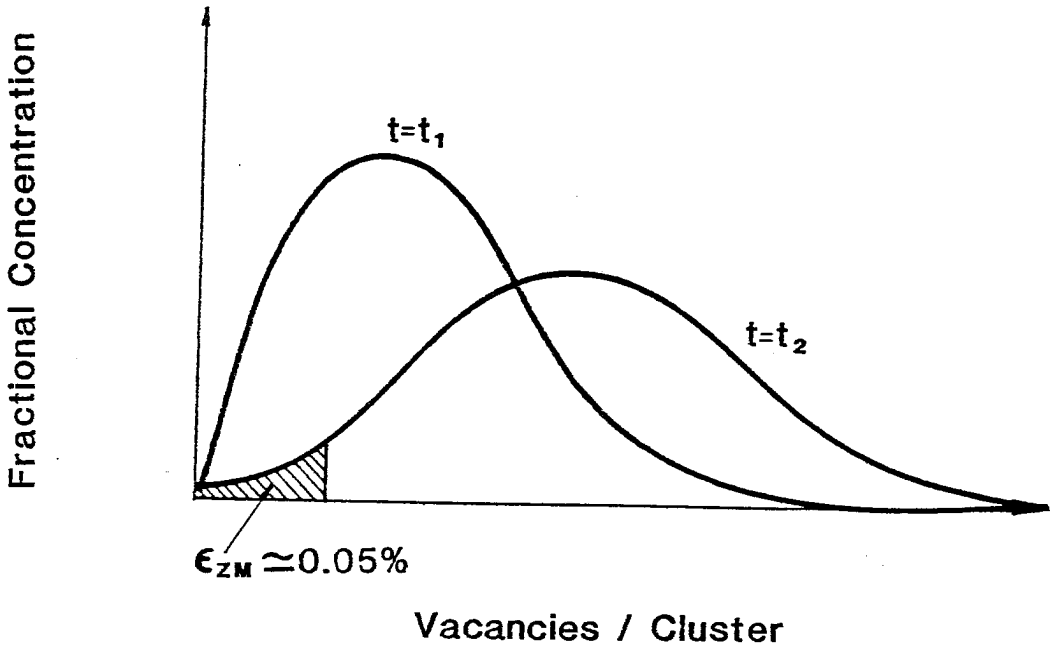

Fig. 8. Schematic of the distribution evolution showing the no. of equations dropped from the system. (ϵ_{zm}=contribution to the zeroth moment)

1. We start with a system of equally spaced mesh points spanning a small range from 3 to 600 vacancies per clusters. The boundary condition of J_{in} and J_{out} into and from the system is set equal to zero. The distribution starts to move towards larger sizes.

2. At each output interval (at the beginning, say, logarithmic up to 10^6 s of irradiation and from that time on, equally spaced at 10^5 s) the average HVC size is computed using the trajectory method.

3. At all times a check is made to ensure that the total discrete range in cluster size is at least five times larger than the average HVC size evaluated by the trajectory method.

4. If the peak position of the distribution becomes too close to the average HVC size, then 5 to 10 equations are added to the system. The mesh spacing of these new equations is chosen such that at the new output interval the total range covers 5 to 10 times the average size at the next output time.

5. At each output interval, a check is run on the small-size part of the distribution. The number of equations contributing less than 0.05% to that moment are removed from the system. According to removing or adding equations, the boundary conditions are also moved along with the system.

3.5. Example Using the Dynamic Incrementing Method

The following example is to show the application of the previous dynamic incrementing method to typical HFIR-irradiation conditions at a temperature of 500°C. Furthermore, we adopt a zero-current boundary condition (Sect. 2.1.1) to monitor the accuracy of our numerical model. This boundary condition is equivalent to having a zero nucleation current condition. Thus the total cluster concentration must remain constant at all times, or:

$$\int_0^\infty C(v,t)dv\Big|_{t=t_1} = \int_0^\infty C(v,t)dv\Big|_{t=t_2} \quad . \tag{25}$$

At time $t = t_o$ it is assumed that all clusters contain 3 vacancies and 3 helium atoms. The initial concentration of critical HVCs is evaluated under HFIR-irradiation conditions using a set of discrete rate equations. This set of rate equations is solved until quasi-steady-state conditions are established. This is true when: (1) the single vacancy concentration reaches its steady state and (2) the ratio of the vacancy flux to the self-interstitial flux ($D_v C_v / D_i C_i$) is larger than unity (D = diffusion coefficient). For typical HFIR-irradiation conditions at 500°C this condition is achieved within a few vacancy mean-lifetimes ($\tau_v \approx 1/\rho_d D_v$, where ρ_d = dislocation density) of about 50 seconds. The defect fluxes are assumed to remain at the quasi-steady-state values. Because the nucleation current of critical HVCs is set to zero, we expect the concentration of critical size clusters to decrease steadily as they grow into larger HVCs.

In Fig. 2 the time behavior of the HVC is shown. The critical HVC concentration starts to decrease monotonically until it completely

vanishes. Also, it is shown that the number density of a particular cluster size peaks at the expense of smaller clusters. It then decreases as the concentration of larger ones start to increase. In this fashion, the peak of the distribution of the HVC always moves to larger sizes as irradiation time increases. Simultaneously, the peak value decreases due to the broadening of the distribution. An indication of the problem's stiffness is the wide variation of time constants for different cluster sizes.

The figure also shows typical behavior of a Fokker-Planck equation composed of a DRIFT and DIFFUSION terms [Eqs. (1,2)]. The drift function represents growth of individual clusters due to an excess vacancy flux (bias). The diffusion-in-size describes random fluctuations about the average size, and it is this term that prevents all clusters from attaining the average cluster size. It acts as a diffusion effect in size space. Subject to diffusion and drift effects, the symmetrical part of the size distribution tends towards an equilibrium Gaussian-like distribution.

As shown above, our choice of boundary conditions, $J_{in} = J_{out} = 0$, allows us to monitor the zeroth moment of the concentrations:

$$M_0 \equiv \int_0^{\infty} C(v,t)dv \approx \sum_{i=1}^{I} C_i(t)\Delta v_i \quad . \tag{26}$$

The percent error in the zeroth moment is thus an indication of accuracy of our numerical analysis. Because of the nature of the dynamic system of equations (variable mesh size), we are not able to use Simpson's methods in estimating the integration of Eq. (26). The trapezoidal rule has been used instead. Figure 9 shows the results of monitoring the

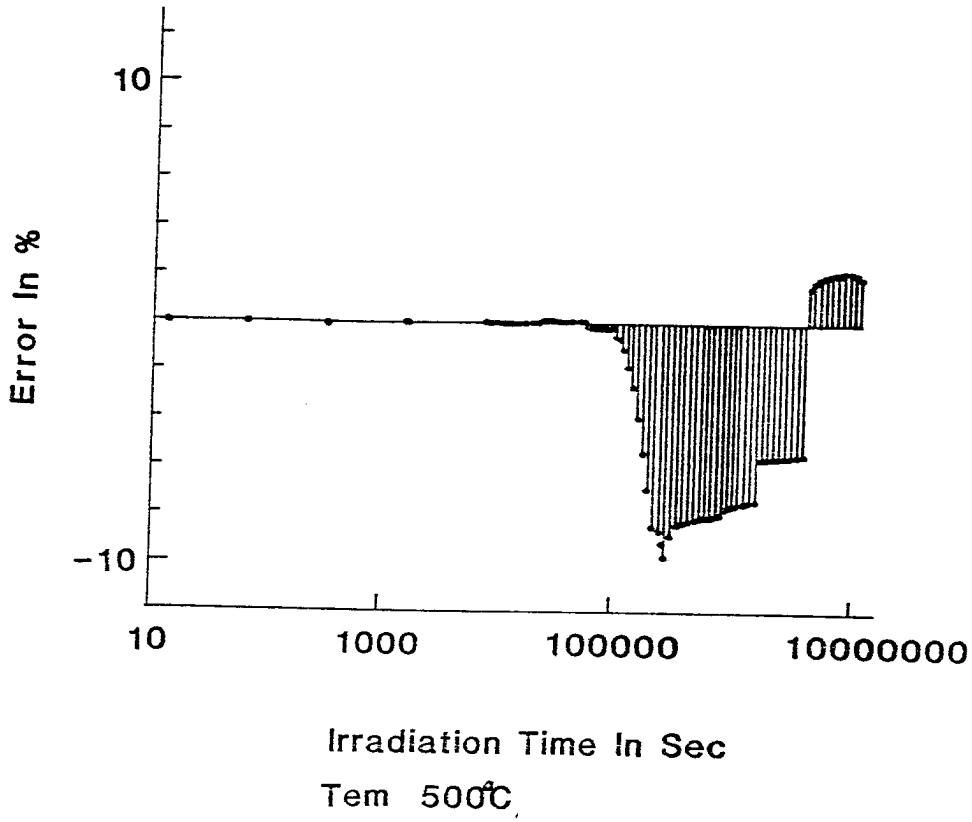

Fig. 9. Error in zeroth moment for the HVC distribution evolution depicted by Fig. 5.

zeroth moment. The error remains practically zero until the system of equations being solved is altered at 10^5 sec. As equations with larger and larger mesh sizes are added, the error starts to increase up to a maximum of ~ 10%. As the distribution tends toward the equilibrium shape, the error starts to decrease and settles around ~ 2%. Considering the vast variations in size space and in the magnitude of time constants, this level of error is felt to be reasonable.

The dynamic incrementing scheme has to be both flexible and economical. A typical run that (1) evaluates quasi-steady-state values of fluxes and critical HVCs; then (2) uses the method of trajectory to give values of the average cavity size, and (3) simulates the evolution of HVCs using not more than 50 discrete equations takes less than 0.1 CPU minutes on the Cray computer.

The program is quite flexible, and includes the following features:

- A choice of moving or fixed system of equations,
- Zero- or non-zero-current boundary conditions,
- Determination of initial mesh size,
- Control of the number of equations added at each necessary expansion time,
- Control of the peak position relative to the total range.

3.5.1. Instabilities of the 1-D Fokker-Planck Equation. In developing the above mentioned numerical schemes, inevitable numerical instabilities were found to develop. This is typical whenever a system of time-dependent ordinary differential equations are solved using the finite difference method. We will first discuss the following instability causing parameters.

1. Tolerances for convergence of solution,
2. Number of ODEs being solved,
3. Mesh spacing between grid points,
4. Relative size of the last grid spacing,
5. Absolute value of the solution's floor value,
6. Time steps between solver's interruptions,
7. "Dynamic" or "fixed" system of equations,
8. Relative peak-value position in the mesh grid,
9. Criteria for eliminating equations in a "dynamic" system,
10. Number of equations added to the ODEs in a "dynamic" system.

Our discussion of instabilities is then concluded with the description of a method developed to suppress numerical instabilities.

3.5.1.1. Tolerances for convergence of solution. The user of the GEAR package has a few options in setting the solution convergence tolerances (see Sect. 3.5.2). One can choose a relative (RTOL) or absolute (ATOL) error criterion for convergence. We adhere here to the relative tolerance method in which the user specifies the relative error criteria for each equation solved. As it turns out there is an optimum RTOL for

every problem solved. If the tolerance is chosen too loosely, instabilities occur very early. Reducing RTOL reduces the magnitude of numerical fluctuations. However, if RTOL is reduced to very low values ($\sim 10^{-10}$), one will inevitably pick up machine round-off errors which will render the solution unstable. For our application of the GEAR package, the optimum RTOL value was found to be around $\sim 10^{-7}$.

3.5.1.2. Number of ODEs. In developing the dynamic and fixed systems, we were inclined to reduce the number of equations in order to save CPU time during the development stages. We found for our particular problem that the minimum number of equations being solved should not fall beyond ten.

3.5.1.3. Mesh spacing between grid points. Because our goal is to span a mesh range from 1 to 10^7 vacancies, we first tried to increase the mesh spacing between two grid points in successive runs. If successful, the larger the mesh spacing the fewer the number of equations to be solved. It became apparent that with increasing mesh spacing instabilities are enhanced.

3.5.1.4. Relative size of the last grid spacing. In using a fixed system (see Sects. 3.2 and 3.3) with zero-current boundary conditions we are in effect imposing a reflective boundary condition at the upper end of the system. Thus the last mesh point experiences instabilities because of the stringent zero-current boundary condition. To avoid this, we chose a relatively large mesh spacing for the last equation

being included in our system. This suppresses the reflective instabilities at the upper bound of the system. A similar effect was later discovered to occur for the lower bound of the system. That problem is discussed in 3.5.1.9.

3.5.1.5. Absolute value of the solutions' floor value. To avoid unnecessary and excessive computations, a minimum value is imposed on the concentrations. This minimum value is called the floor value. The floor value reduces the number of iterations performed by the solver because the relative error criterion is a function of the absolute value of the solution. Thus, by choosing a large absolute value, for a floor value we reduce the computational time. However, the larger the floor value the more unstable the system becomes. Thus, it is desirable to find an optimum floor value which minimizes computational time but at the same time renders the system stable. That optimum value was found to be $\sim 10^{-20}$ for fractional concentrations. If the value was decreased any further, instabilities recurred because of the machine accuracy limit.

3.5.1.6. Time steps between solver's interruptions. In order to keep a check on the integration performed by the GEAR package, the user has the option to determine these checkpoints called TIME-OUTs. At every TIME-OUT the Gear package reinitializes the integration parameters and assumes it is starting a new problem with the previous TIME-OUT's solution as a new set of initial conditions. During an integration procedure between two consecutive TIME-OUTs, many integration parameters are

dynamically optimized in order to be able to deal with a stiff system and to reduce computational time.

Some of these parameters are the internal integration initial stepsize (HHO), maximum step size (HMAX), and maximum number of iteration steps between two TIME-OUTs.

By choosing a small delta TIME-OUT, these parameters are reinitialized more frequently and thus instabilities due to ever growing internal integration step sizes can be suppressed.

3.5.1.7. Dynamic or fixed system of equations. Developing a dynamic system of equations challenged the stability of our numerical results more than any other parameter choice. The following points (3.5.1.8 - 3.5.1.10) will elaborate on this.

3.5.1.8. Relative peak value position in the mesh grid. By this we mean the position of the peak of the cavity size distribution relative to the system's end points.

If, in describing the size distribution of a Gaussian-like shape, one chooses the system such that the Gaussian tails are not well represented (chopped off), end effects will render the system unstable. Therefore, in developing a "dynamically increasing system of equations," it was found that a sufficiently long distribution tail is desirable. Specifically the peak position had to be kept roughly at one-third of the total mesh size considered in order to keep the system stable.

3.5.1.9. Criteria for eliminating equations in a dynamic system. If the equations describing the system behavior behind the peak of the size distributions are dropped too soon, instabilities will immediately occur.

Another stability guideline was found to lie in the zeroth moment of the distribution. Because it is important to conserve the total number of cavities regardless of the size-distribution evolution, the eliminated equations should not cause an excess error in the zeroth moment of $\gtrsim$ 0.05%. This choice was found to result in a stable system with a maximum of ~ 50 equations representing the size distribution.

3.5.1.10. Number of equations added to the ODEs in a dynamic system. As the system of equations tracks and follows the size distribution dynamically, a number of equations have to be added to the wavefront of the size distribution. The concentration of these added sizes are initialized to the floor value of ~ 10^{-20} (at./at). If too many equations are added, the relative peak position slips back in the mesh grid and the system becomes unstable. If too few are added, the peak position moves forward too fast, and instabilities occur. Therefore, the approximate new peak position has to be known at the next TIME-OUT interruption. From this, the peak-movement velocity can be found and the optimum number of equations to be added can be determined. This procedure could be implemented with the help of the trajectories method we developed earlier (Chapter V). The optimum number of equations added was found to lie between five and ten.

While some of these instability causing parameters can be determined and set at the beginning of the integration, others will change during the course of the dynamically peak-tracing method. The number of equations is a function of the size-distribution evolution, so is the position of the peak value, the average mesh spacing, and the rate of adding and of dropping equations from the system. Even if one is most conservative and cautious with all other parameters, at some point along the size-distribution evolution, numerical instabilities will initiate and cause unacceptable fluctuations. Figure 10 shows such instabilities occuring at an irradiation time of approximately 10^7 s.

We developed the method described below to alleviate these instabilities which tend to occur during the latter stages of the calculations.

At every TIME-OUT the solution is checked for unacceptable fluctuations. In general these fluctuations extend over two to seven mesh grid points and if left as is, will eventually propagate to cover the whole system (see Fig. 10).

However, if at the onset of the fluctuations they are smoothed out and the new smooth system is resubmitted as a new initial condition, the fluctuations will not propagate any further and will be suppressed altogether.

The smoothing out was performed by fitting a second order polynomial over three times the range of the initial numerical fluctuation range. This included, on the average, fitting not less than six to nine mesh points to a polynomial. To ensure conservation, a check is run to

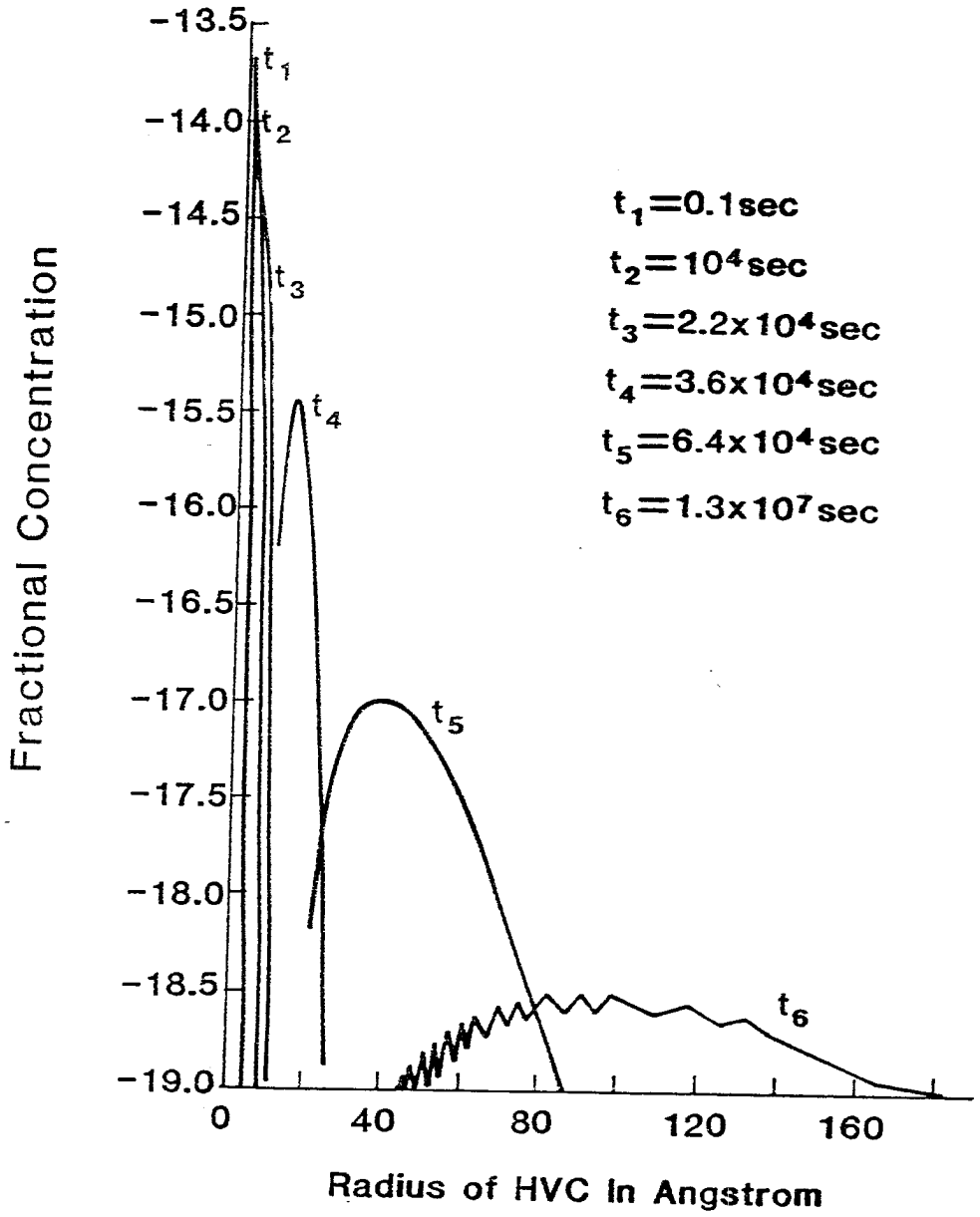

Fig. 10. HVC size distribution evolution as a function of irradiation time without suppression of numerical fluctuations.

monitor the effect of fitting on the zeroth moment. The smoothing had no effect on the conservation of the zeroth moment. With this scheme we were able to rid the system of numerical instabilities while ensuring conservation of the cavity number density. Figure 5 shows the results of the size-distribution evolution using the smoothing routine in our code, and Fig. 9 shows the behavior of the corresponding zeroth moment. We feel that an error of ~ 2% to 3% in the zeroth moment is acceptable (see Fig. 9) considering the range of void sizes covered with not more than 0.1 s of CRAY/CPU time used.

3.5.2. Numerical Aspects. As discussed above, the present numerical model is not free from numerical instabilities inherent to any system of ODSs.

The set of discretized Fokker-Planck equations (Eq. 20) is solved using a new version of the original GEAR package [4], which is designed for stiff non-linear ordinary differential equations. The following is a brief description of the methods used by the LSODE version of the GEAR package in error control of the solver. The user supplies values for ATOL (absolute tolerance), RTOL (relative tolerances), and ITOL (integer value) determining which one of the error criteria is to be used by the solver. For a more detailed description, please see Ref. [4].

The problem we are solving is of the form:

$$\frac{d\underline{Y}}{dt} = f(\underline{Y}t) \quad , \tag{27}$$

The error of the problem is evaluated by:

$$\text{rms-norm of } \left[\frac{e(i)}{ewt(i)}\right] \quad .LE. \quad 1 \quad , \tag{33}$$

$$ewt(i) = RTOL(i)*abs[Y(i)]+ATOL(i) \quad , \tag{34}$$

$$\text{rms-norm}(Y) = \frac{\sum_{i=1}^{neq} [Y(i)]^2}{neq} \quad , \tag{35}$$

where ewt = vector of weights which must always be positive, and neq = no. of equations solved.

By increasing ATOL and/or RTOL the vector of weights [ewt(i)] increases, thus the rms-norm of e(i)/ewt(i) decreases more rapidly and the above inequality is satisfied more readily. The opposite is also true. If pure absolute error control is used, the Y(i) with the largest error will determine convergence of the solver because then we have

$$\left\{\frac{\sum\left[\frac{e(i)}{ewt(i)}\right]^2}{neq}\right\}^{1/2} = \left\{\frac{\sum[e(i)]^2}{atol^2} * \frac{1}{neq^2}\right\}^{1/2} \quad , \tag{36}$$

and

$$\frac{1}{(ATOL)(neq)}\left(\sum_{i=1}^{neq}[e(i)]^2\right)^{1/2} \simeq \frac{e(i)max/neq}{ATOL} \quad . \tag{37}$$

By using purely relative error control this problem is relieved but the solver will converge very slowly. To control the convergence, it is best to use the combination of ATOL and RTOL option.

3.6. Integral Formulation of the Two-Dimensional Finite Difference Solution of the Fokker-Planck Equation

3.6.1. The 2-D Fokker-Planck Equation. The previous section outlined the finite difference scheme we developed to solve the 1-D Fokker-Planck (void growth) equation. This allowed us to investigate and consequently demonstrate the validity of our numerical approach. We can now apply the above method to the 2-D Fokker-Planck equation with confidence. In the next sections we demonstrate the expanded finite difference scheme.

The Fokker-Planck Equation, in absence of external sources or losses, is:

$$\frac{\partial C}{\partial t} = - \vec{\nabla} \cdot \vec{J} \quad , \tag{38}$$

Our analysis looks at HVCs and assumes only two constituents: vacancies and helium atoms. Precipitates or other impurities are excluded in our description of bubble evolution. Thus the current $\vec{J}$ consists of two components:

$$\vec{J} = \vec{e}_h J^h + \vec{e}_v J^v \quad , \tag{39}$$

where: $\vec{e}_{h,v}$ = unit vector in helium, vacancy direction in a helium-vacancy-phase-space, respectively.

$J^{h,v}$ = the scalar values of helium and vacancy currents, respectively.

With this current the 2-D or 2-component Fokker-Planck equation describing the growth evolution of HVCs is given by:

$$\frac{\partial C_{v,h}}{\partial t} = - \frac{\partial J^v}{\partial v} - \frac{\partial J^h}{\partial h} \quad , \tag{40}$$

where: $C_{v,h}$ = the concentration of HVCs containing v (no. of vacancies) and h (no. of helium atoms).

The helium current J^h is given by:

$$J^h \equiv [J(h,t)]_v = \left\{F(h,t)C(h,t) - \frac{\partial}{\partial h}\,[D(h,t)C(h,t)]\right\}_v \quad ,(41)$$

and the vacancy current J^v:

$$J^v = [J(v,t)]_h = \left\{F(v,t)C(v,t) - \frac{\partial}{\partial v}\,[D(v,t)C(v,t)]\right\}_h \quad ,(42)$$

where F = DRIFT-function = point defect net bias and D = DIFFUSION-function = point defect diffusion flux.

In short form notation, Eqs. (41) and (42) can be written as:

$$J^h = [F^h C]_v - \left[\frac{\partial D^h C}{\partial h}\right]_v \quad ,$$

$$J^v = [F^v C]_h - \left[\frac{\partial D^v C}{\partial v}\right]_h \quad . \tag{43}$$

Because v,h and t are independent variables we can integrate Eq. (40) over a small element $\Delta h\ \Delta v$ for the (i,j)th meshpoint:

$$\int_{h_{i,j-1/2}}^{h_{i,j-1/2}} \int_{v_{i-1/2,j}}^{v_{i+1/2,j}} \partial v \, \partial h \, \frac{\partial C_{i,j}}{\partial t}$$

$$= - \int_{h_{i,j-1/2}}^{h_{i,j+1/2}} \int_{v_{i-1/2,j}}^{v_{i-1/2,j}} \partial v \, \partial h \left(\frac{\partial J_{i,j}}{\partial h} + \frac{\partial J_{i,j}}{\partial v} \right) \quad . \quad (44)$$

Figure 11 illustrates the notation and coordinates of this (i,j)th element. From this figure and using central differencing, we have for the vacancy direction:

$$\left[\Delta v_i \right]_j = \left[v_{i+1/2} - v_{i-1/2} \right]_j \quad , \quad (45)$$

and

$$\left[v_{i+1/2} \right]_j \equiv \left[\frac{1}{2} \left(v_{i+1} + v_i \right) \right]_j \quad ,$$

$$\left[v_{i-1/2} \right]_j \equiv \left[\frac{1}{2} \left(v_i + v_{i-1} \right) \right]_j \quad . \quad (46)$$

Equations (45) and (46) give:

$$\left[\Delta v_i \right]_j = \left[\frac{1}{2} \left(v_{i+1} - v_{i-1} \right) \right]_j \quad , \quad (47)$$

Similarly in the helium direction we get:

$$\left[\Delta h_j \right]_i = \left[\frac{1}{2} \left(h_{j+1} - h_{j-1} \right) \right]_i \quad . \quad (48)$$

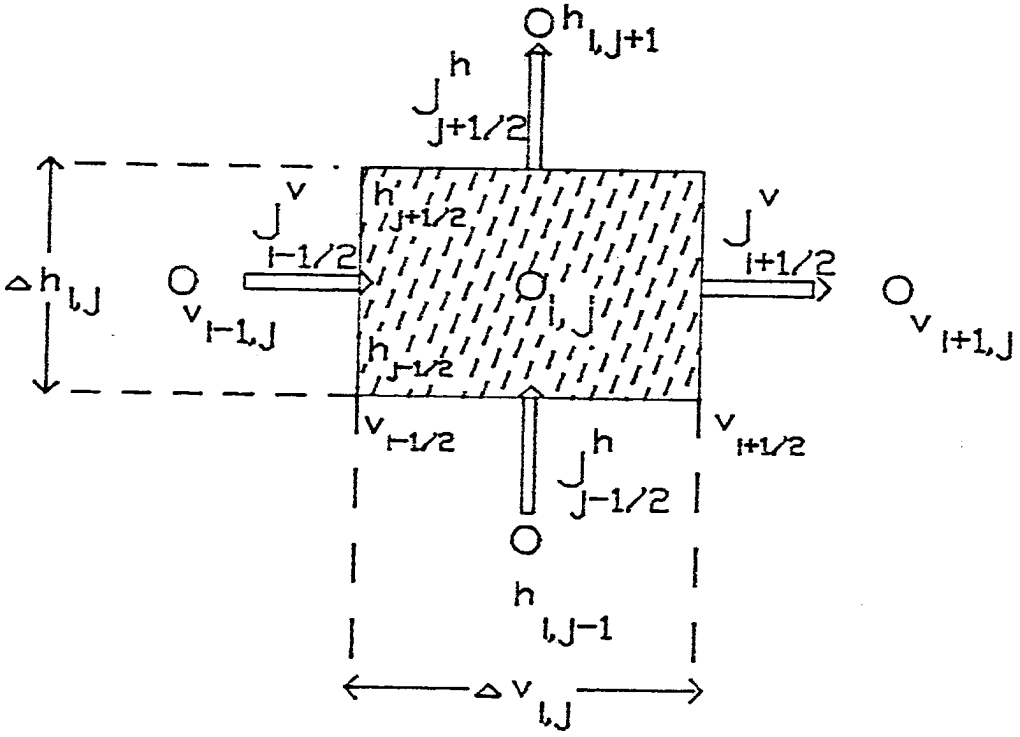

Fig. 11. Notation and coordinates of the i,jth element in a helium-vacancy phase space.

With these definitions of $\Delta v_{i,j}$ and $\Delta h_{i,j}$ the left-hand side of Eq. (44) becomes:

$$\frac{\partial}{\partial t} \int_{h_{i,j-1/2}}^{h_{i,j+1/2}} \int_{v_{i-1/2,j}}^{v_{i+1/2,j}} C_{i,j} \, \partial v \, \partial h \simeq \Delta h_{i,j} \, \Delta v_{i,j} \frac{\partial C_{i,j}}{\partial t} \quad , (49)$$

and the right-hand side of Eq. (44) becomes:

$$- \int_{h_{i,j-1/2}}^{h_{i,j+1/2}} \int_{v_{i-1/2,j}}^{v_{i+1/2,j}} \partial v \, \partial h \left[\frac{\partial J^h_{i,j}}{\partial h} + \frac{\partial J^v_{i,j}}{\partial v}\right] =$$

$$- \Delta v_{i,j} \int_{h_{i,j-1/2}}^{h_{i,j+1/2}} \partial J^h_{i,j} - \Delta h_{i,j} \int_{v_{i-1/2,j}}^{v_{i+1/2,j}} \partial J^v_{i,j} \quad , \quad (50)$$

with

$$- \int_{h_{i,j-1/2}}^{h_{i,j+1/2}} \partial J^h_{i,j} \simeq \left[-J^h_{j+1/2} + J^h_{j-1/2}\right]_i$$

$$= \left[J^h_{j-1/2} - J^h_{j+1/2}\right]_i \quad . \quad (51)$$

Defining

$$J^h_{\text{lower}} \equiv \left[J^h_{j-1/2}\right]_i$$

$$J^h_{\text{upper}} \equiv \left[J^h_{j+1/2}\right]_i \quad , \quad (52)$$

Eq. (51) becomes:

$$-\int_{h_{i,j-1/2}}^{h_{i,j+1/2}} \partial J^h_{i,j} \simeq \left[J^h_{low} - J^h_{upp}\right]_i \quad . \tag{53}$$

Similarly, for the vacancy integral of the right-hand side of Eq. (50) we get:

$$\int_{v_{i-1/2,j}}^{v_{i+1/2,j}} \partial J^v_{i,j} \simeq \left[J^v_{low} - J^v_{upp}\right]_j \quad , \tag{54}$$

where:

$$J^v_{low} \equiv \left[J^v_{i-1/2}\right]_j \quad ,$$

$$J^v_{upp} \equiv \left[J^v_{i+1/2}\right]_j \quad . \tag{55}$$

The expressions for J^h_{low}, J^h_{upp} and J^v_{low}, J^v_{upp} are derived by finite differencing equations (41) and (42).

$$J^h_{low} \equiv \left[J^h_{j-1/2}\right]_i$$

$$= \left[(F^h C)_{j-1/2}\right]_i - \left[\left(\frac{\partial D^h C}{\partial h}\right)_{j-1/2}\right]_i \quad . \tag{56}$$

Using a simple linear interpolation of the function $(F^h C)_{j-1/2}$ between j-1 and j we obtain:

$$\left[(F^h C)_{j-1/2}\right]_i \simeq \left[\frac{(F^h C)_j + (F^h C)_{j-1}}{2}\right]_i \quad . \tag{57}$$

And for the midpoint value considered, central differencing gives

$$\left[\left(\frac{\partial}{\partial h} D^h C\right)_{j-1/2}\right]_i \simeq \left[\frac{(D^h C)_j - (D^h C)_{j-1}}{\Delta h_{j-1/2}}\right]_i + O\left[(\Delta h)^2\right] \quad , \tag{58}$$

with $\Delta h_{j-1/2} = h_j - h_{j-1}$.

Combining Eqs. (56), (57) and (58), we get:

$$J^h_{low} \simeq \left[\frac{(F^h C)_j + (F^h C)_{j-1}}{2}\right]_i - \left[\frac{(D^h C)_j - (D^h C)_{j-1}}{\Delta h_{j-1/2}}\right]_i \quad . \tag{59}$$

Finite differencing J^h_{upp}, J^v_{low}, and J^v_{upp} we get:

$$J^h_{upp} \simeq \left[\frac{(F^h C)_{j+1} + (F^h C)_j}{2}\right]_i - \left[\frac{(D^h C)_{j+1} - (D^h C)_j}{\Delta h_{j+1/2}}\right]_i \quad , \tag{60}$$

where $\Delta h_{j+1/2} = h_{j+1} - h_j$,

and

$$J^v_{low} \simeq \left\{\frac{1}{2}\left[(F^vC)_i + (F^vC)_{i-1}\right]\right\}_j - \left\{\frac{1}{\Delta v_{i-1/2}}\left[(D^vC)_i - (D^vC)_{i-1}\right]\right\}_j \quad , \tag{61}$$

and

$$J^v_{upp} \simeq \left\{\frac{1}{2}\left[F^vC)_{i+1} + (F^vC)_i\right]\right\}_j - \left\{\frac{1}{\Delta v_{i+1/2}}\left[(D^vC)_{i+1} - (D^vC)_i\right]\right\}_j \quad , \tag{62}$$

where

$$\Delta v_{i-1/2} = v_i - v_{i-1} \quad ,$$

$$\Delta v_{i+1/2} = v_{i+1} - v_i \quad . \tag{63}$$

The Fokker-Planck equation (40) is now represented by a finite number of discrete equations of the form:

$$\frac{\partial C_{i,j}}{\partial t} = \frac{1}{[\Delta hj]_i}\left\{[J^h_{low} - J^h_{upp}]_i\right\} + \frac{1}{[\Delta v_i]_j}\left\{[J^v_{low} - J^v_{upp}]_j\right\} \quad , \tag{64}$$

where $[\Delta v_i]_j$, $[\Delta h_j]_i$, J^h_{low}, J^h_{upp}, J^v_{low}, and J^v_{upp} are given by Eqs. (47), (48), (59), (60), (61), and (62), respectively.

3.6.2. Integral Finite-Difference Formulation of Boundary and Interior Elements in a Helium-Vacancy Phase Space. One of the biggest advantages of Eq. (64) is the convenience with which the conservation principle can be enforced through the boundary conditions.

During irradiation the bubble size and helium-content distribution follows a certain path in a helium-vacancy phase space (see Fig. 12) depending on irradiation parameters.

The deviation of bubble sizes from this path (called trajectories) tends to be a Gaussian. Thus a solution space or "cage" can be constructed around the trajectory beyond which the contribution to the bubble distribution is negligible (see Fig. 13). The trajectory represents the average size and helium content of the HVCs.

Upon discretization of the Fokker-Planck equation (64), the continuum variables are replaced by discrete units of vacancies and helium atom. Thus the helium-vacancy phase space is also discretized (Fig. 14).

The discretization leads to six different types of mesh elements:

1. Upper Corner element
2. Upper Bound element
3. Interior element
4. Lower Corner element
5. Lower Boundary element
6. Outer Boundary element

Each element in this helium-vacancy phase space is represented by one discrete equation (64), which consists of four currents. Because there

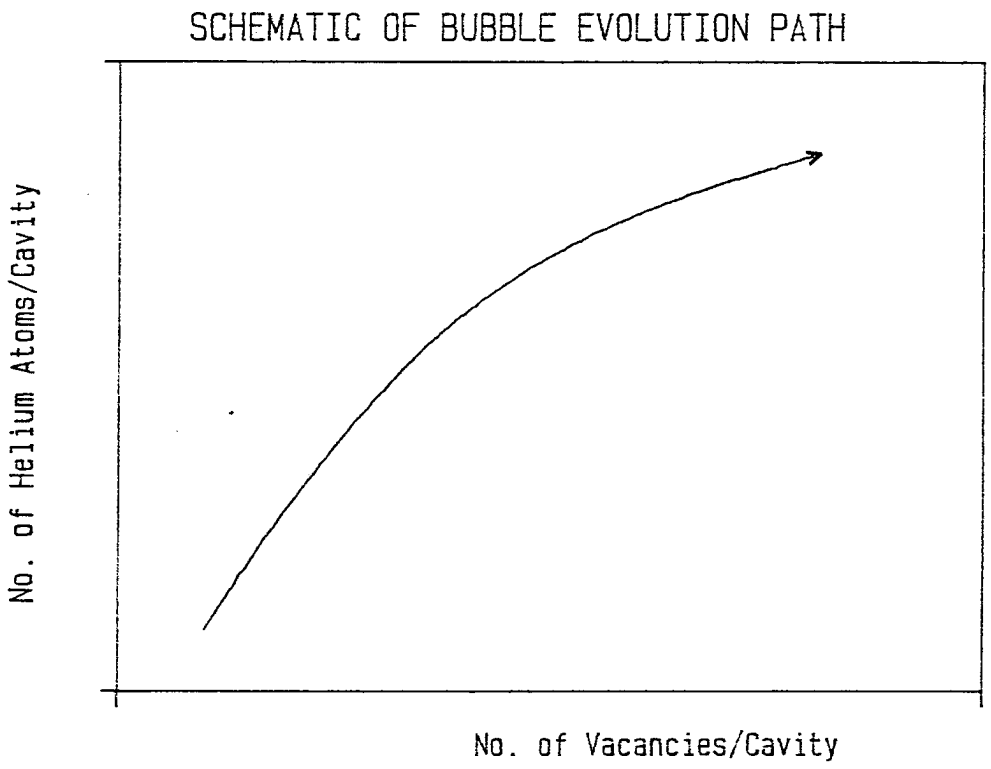

Fig. 12. Schematic of the evolution path of the bubbles in a helium-vacancy phase space.

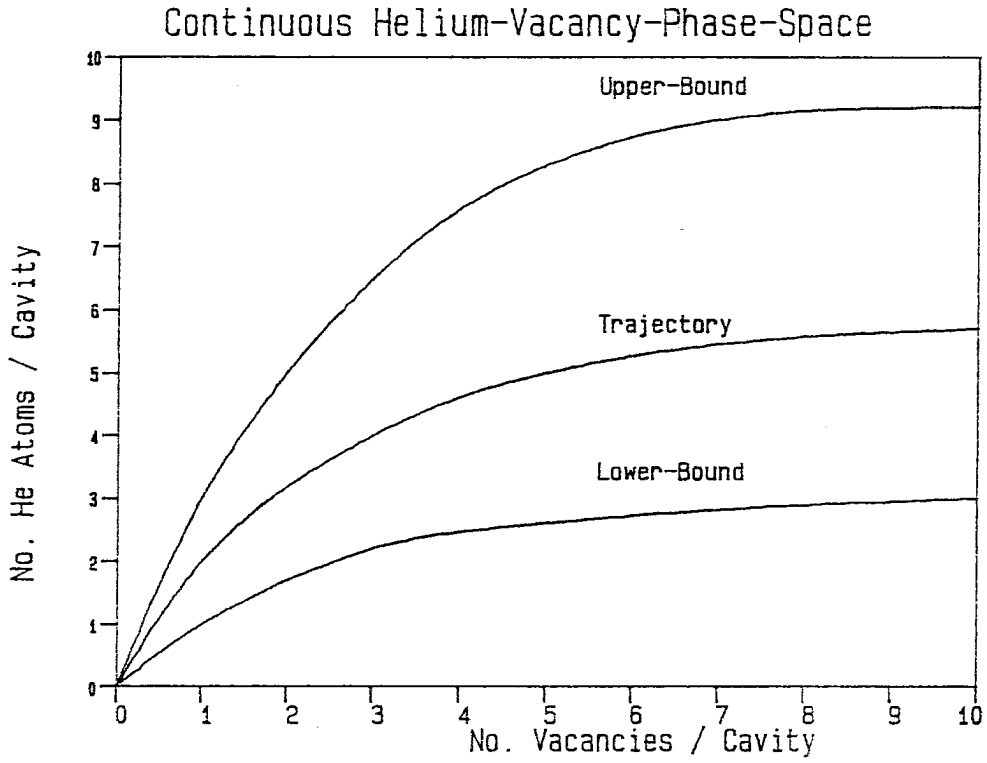

Fig. 13. Solution space of bubble-size and helium-content distribution around the trajectory.

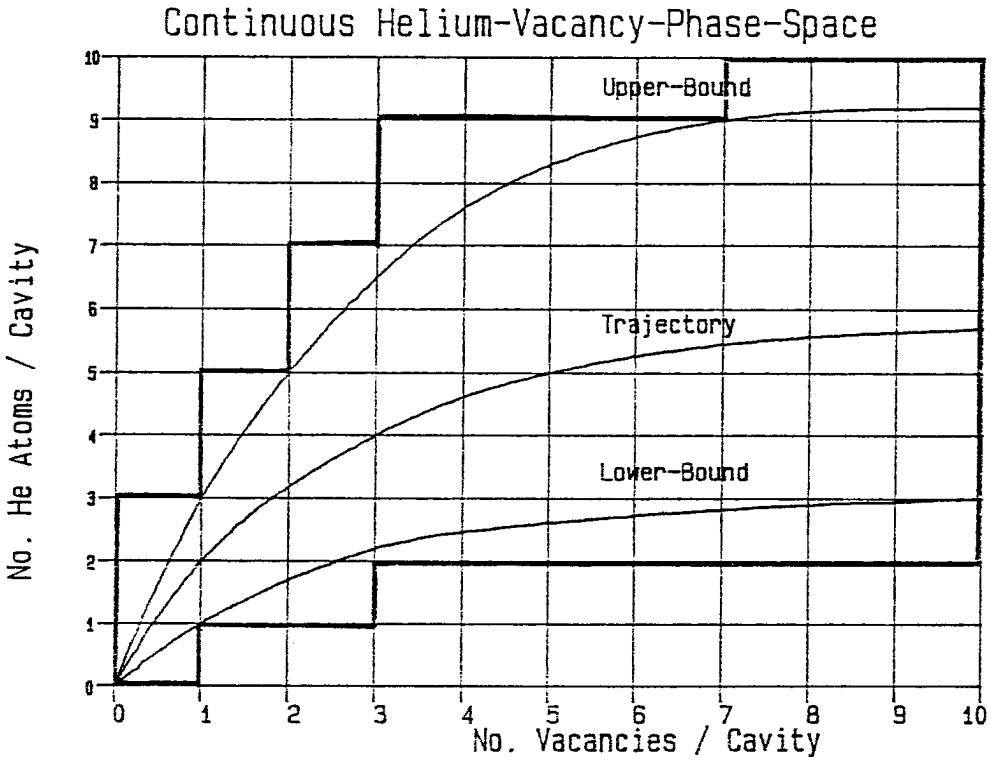

Fig. 14. Discretized solution space around the trajectory in a helium-vacancy phase space.

is no current across any of the boundaries along the solution space, the six elements experience different combinations of current components in the v- and h-direction.

Figure 15 illustrates the current-conditions for the six possible discretized mesh elements.

Enforcing the current conditions on all mesh elements of our discretized Fokker-Planck system of equations ensures conservation of defect concentrations. Since nothing can leak through the boundaries of the solution space (see Fig. 14), the total number density must be conserved at all times:

$$M_0 = \int_v \int_h \partial v \; \partial h \; C(v,h,t_0) = \int_v \int_h \partial v \; \partial h \; C(v,h,t_1) \quad . \tag{65}$$

In other words, the zeroth moment M_0 must be conserved.

3.6.3. Finite Differencing the Transition Elements Between Small and Large Mesh Grids. By using a Fokker-Planck analysis, we have replaced a series of coupled rate equations (ordinary differential equations) by a partial differential equation, in which the particle numbers in clusters are considered continuous variables.

The principal advantage of the chemical rate equations lies in providing insight into atomistic details, while the Fokker-Planck equation provides insight into the main kinetic features of the microstructural evolution. This prompted us to develop a hybrid [5] (combined) approach in which rate equations are used for small cluster sizes whereas the Fokker-Planck approach is applied to large cluster sizes. This

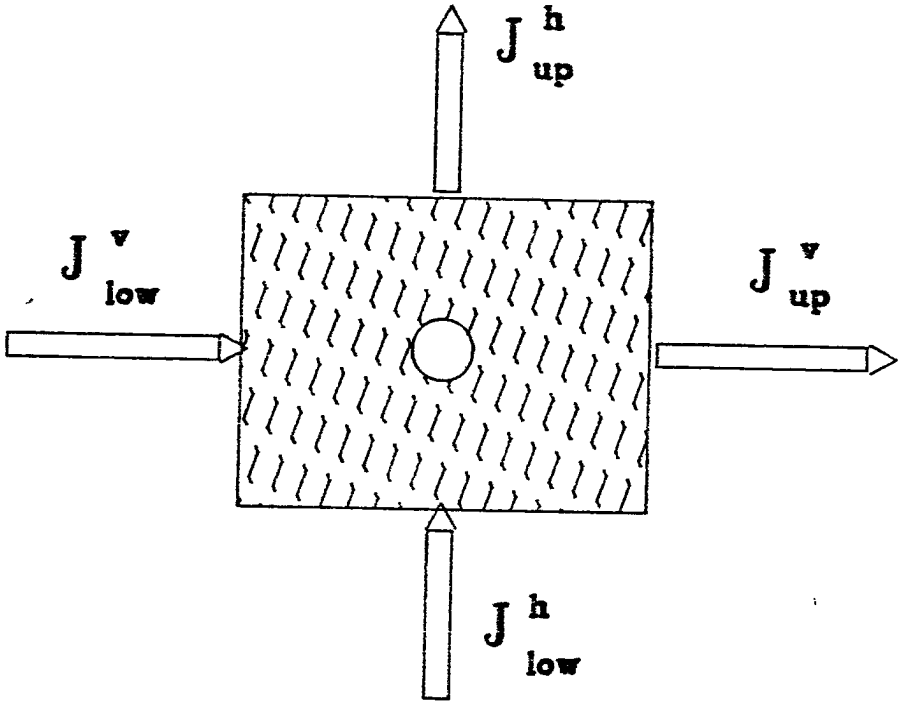

Fig. 15. Schematic of current flow to and from a finite difference element.

approach is based on the division of bubble evolution into characteristic periods of nucleation and growth. Nucleation is analysed with the rate equations while growth is represented by the Fokker-Planck equations.

Bubble evolution is caused by the interaction of three species: single vacancies, self-interstitials, and single-helium atoms. Because more than one specie is involved, the classical nucleation theory approach in determining nucleation periods and the onset of growth periods cannot be utilized. Besides the multi-component character of bubble evolution, its sensitivity to many parameters makes the division between the characteristic periods even more difficult.

Our hybrid approach allows for an analysis of bubble evolution without being forced to distinguish between nucleation and growth periods. This is simply done by choosing a very fine mesh spacing for the Fokker-Planck equations at the boundary of the hybrid rate equation/Fokker-Planck equation system. In fact by reducing the mesh spacing to unity in the Fokker-Planck equations we should recover the system of single-step rate equations. In our original documentation [5] of this hybrid method we have shown this to be satisfied. Here we allowed for a smooth transition between the rate equations and the continuum Fokker-Planck equation by using a dynamically expanding mesh spacing (see Sect. 3).

We want to utilize the same principle in describing the helium content evolution in bubbles. For this purpose we derive a set of finite-difference equations for transition elements. By transition elements we are referring to mesh elements that interlink two different sized mesh grids (see Fig. 16). Our transition elements consist of two kinds: quadrilateral and triangular.

First, we will derive the finite-difference formula for the quadrilateral transition element; second we will derive it for the triangular transition element.

3.6.3.1. Quadrilateral transition element. To derive the finite-difference formula for the quadrilateral transition element we start with the Fokker-Planck equation:

$$\frac{\partial C}{\partial t} = - \vec{\nabla} \cdot \vec{J} \quad , \tag{66}$$

with

$$\vec{J} = \vec{e}_h J^h + \vec{e}_v J^v \quad , \tag{67}$$

where J^h, J^v are given by Eqs. (41), (42), and (43) and $\vec{e}_h$ and $\vec{e}_v$ are unit vectors in the vacancy and helium directions, respectively.

We integrate Eq. (66) over the area of an expansion element as shown in Fig. 17.

$$\int_v \int_h \frac{\partial C}{\partial t} \, dh \, dv = - \int_v \int_h (\vec{\nabla} \cdot \vec{J}) \, dv \, dh \quad . \tag{68}$$

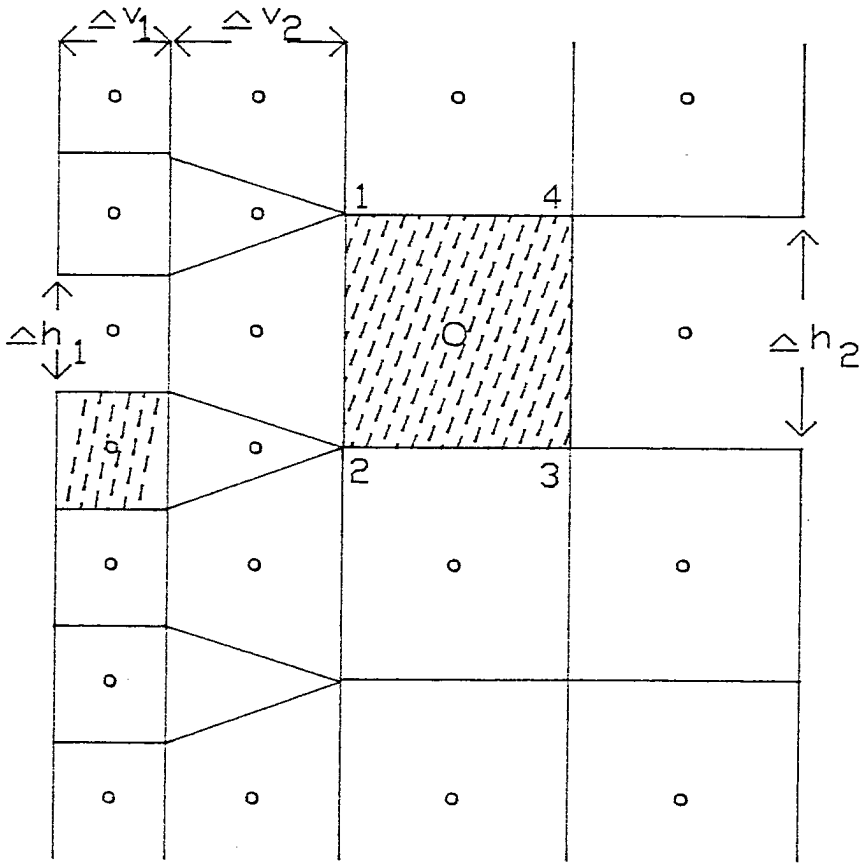

Fig. 16. Helium-vacancy phase space showing two mesh grids of different sizes, joined by a transition element mesh band.

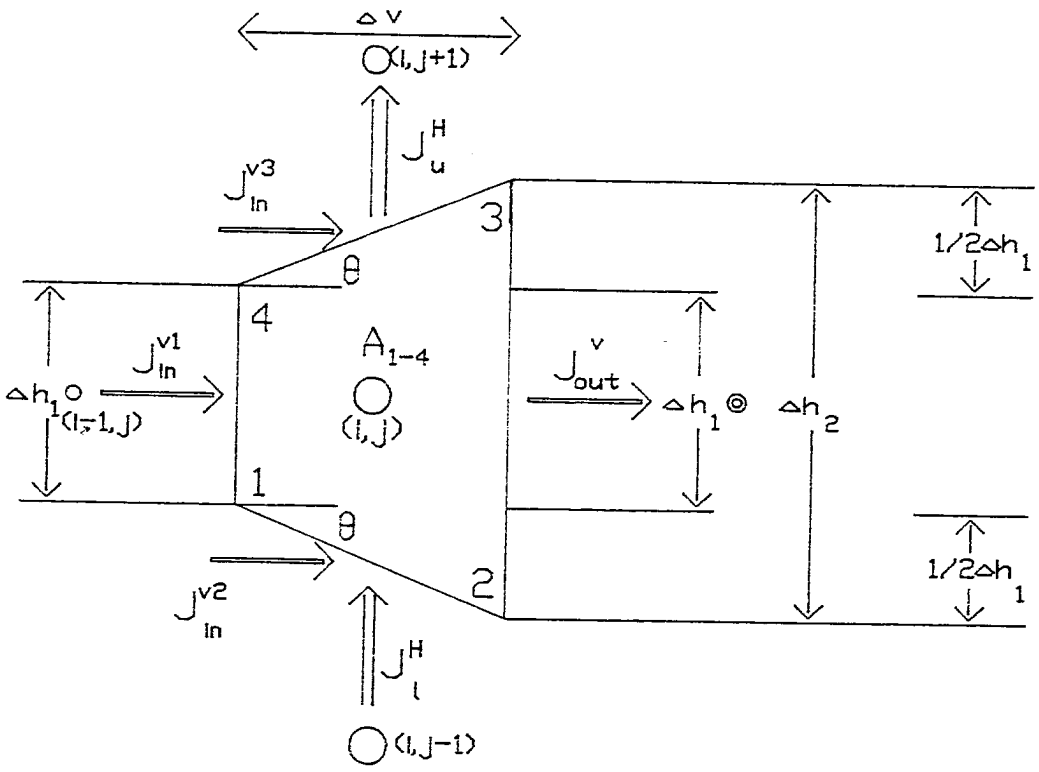

Fig. 17. Notations of the quadrilateral transition element.

Using Gauss' divergence theorem we replace the volume integral by a surface integral. The right-hand side of Eq. (68) becomes

$$\int_v \int_h (\vec{\nabla} \cdot \vec{J})\, dv\, dh = \oint_s \vec{J} \cdot \vec{ds} \quad . \tag{69}$$

Equation (66) thus becomes:

$$\int_v \int_h \frac{\partial C}{\partial t}\, dv\, dh = - \oint_s \vec{J} \cdot \vec{ds} \quad . \tag{70}$$

Using the notations of Fig. 17, Eq. (66) can be written as:

$$\left(\frac{\partial C_{i,j}}{\partial t}\right) A_{1-4} = -\left(\int_1^2 \vec{J} \cdot \vec{ds} + \int_2^3 \vec{J} \cdot \vec{ds} + \int_3^4 \vec{J} \cdot \vec{ds} + \int_4^1 \vec{J} \cdot \vec{ds}\right) \quad . \tag{71}$$

The line integrals of $\vec{J}$ are:

$$\int_1^2 \vec{J} \cdot \vec{ds} \simeq J_{\ell}^{H} \overline{R}_1 \cos\theta + J_{in}^{v2} \overline{R}_1 \sin\theta \quad ,$$

$$\int_2^3 \vec{J} \cdot \vec{ds} \simeq - J_{out}^{v} \overline{R}_{23} \quad ,$$

$$\int_3^4 \vec{J} \cdot \vec{ds} \simeq - J_{u}^{H} \overline{R}_4 \cos\theta + J_{in}^{v3} \overline{R}_{34} \sin\theta \quad ,$$

$$\int_4^1 \vec{J} \cdot \vec{ds} \simeq J_{in}^{v1} \overline{R}_{41} \quad , \tag{72}$$

where we have defined any current leaving the element as a negative and any current entering the element as positive, and $\overline{R}$ denotes the arc length. Furthermore:

$$\begin{aligned}
\overline{\overline{R}}_{12} \cos\theta &= \Delta V \quad , \\
\overline{R}_{34} \cos\theta &= \Delta V \quad , \\
\overline{R}_{12} \sin\theta &= \frac{1}{2}\Delta h_1 \quad , \\
\overline{R}_{34} \sin\theta &= \frac{1}{2}\Delta h_1 \quad , \\
\overline{R}_{23} &= \Delta h_2 = 2\,\Delta h_1 \quad , \\
\overline{R}_{41} &= \Delta h_1 \quad , \\
\Delta V &= V_{i+1,j} - V_{i,j} \quad , \\
\Delta h_1 &= h_{i,j+1} - h_{i,j} \quad .
\end{aligned} \tag{73}$$

Combining Eqs. (72), (71), and (73) we get:

$$\left(\frac{\partial C_{i,j}}{\partial t}\right)A_{1-4} = \left[J^{H}_{\ell}(\Delta V) + J^{v2}_{in}\left(\frac{1}{2}\Delta h_1\right) - J^{v}_{out}(2\,\Delta h_1) - J^{H}_{u}(\Delta V)\right.$$

$$\left. + J^{v3}_{in}\left(\frac{1}{2}\Delta h_1\right) + J^{v1}_{in}(\Delta h_1)\right] \quad , \tag{74}$$

and for the area A_{1-4} we have:

$$A_{1-4} = \frac{3}{2}\Delta h_i\,\Delta V \quad . \tag{75}$$

Equations (75) and (74) give:

$$\frac{\partial C_{i,j}}{\partial t} \simeq -\frac{2}{3\ \Delta h_1}\left(J_{\ell}^{H}\Big|_{i,j-1} - J_{u}^{H}\Big|_{i,j+1}\right)$$

$$-\frac{2}{3\ \Delta V}\left[\left(J_{i}^{v} + \frac{J_{in}^{v2}}{2} + \frac{J_{in}^{3}}{2}\right) - 2\ J_{out}^{v}\right]_{i,j} \quad . \qquad (76)$$

The currents are defined as follows:

$$\left[J_{\ell}^{H}\right] \simeq \frac{\left[F^{h}C\right]_{i,j} + \left[F^{h}C\right]_{i,j-1}}{2} - \frac{\left[D^{h}C\right]_{i,j} - \left[D^{h}C\right]_{i,j-1}}{\left(j_{i,j} - h_{i,j-1}\right)} \quad ,(77)$$

$$\left[J_{u}^{H}\right] \simeq \frac{\left[F^{h}C\right]_{i,j+1} + \left[F^{h}C\right]_{i,j}}{2} - \frac{\left[D^{h}C\right]_{i,j+1} - \left[D^{h}C\right]_{i,j}}{\left(h_{i,j+1} - h_{i,j}\right)} \quad .(78)$$

The vacancy currents:

$$\left[J_{out}^{v}\right] \simeq \frac{\left[F^{V}C\right]_{i+1,j} + \left[F^{V}C\right]_{i,j}}{2} - \frac{\left[D^{V}C\right]_{i+1,j} - \left[D^{V}C\right]_{i,j}}{\left(V_{i+1,j} - V_{i,j}\right)} \quad ,(79)$$

$$\left[J_{in}^{v}\right]_{i,j} \simeq \frac{\left[F^{V}C\right]_{i,j} + \left[F^{V}C\right]_{i-1,j}}{2} - \frac{\left[D^{V}C\right]_{i,j} - \left[D^{V}C\right]_{i-1,j}}{\left(V_{i,j} - V_{i-1,j}\right)} \quad .(80)$$

3.6.3.2. Triangular transition element. In order to write the expressions for J_{in}^{v2} and J_{in}^{v3} we first have to derive the finite-difference formula for the triangular transition element depicted in Fig. 18. Figure 18 shows the notation for this element. Using the same approach as for the quadrilateral transition element we have

$$\left(\frac{\partial C_{i,j}}{\partial t}\right)A_{1-3} = -\left[J_{\ell}^{H}(\Delta v) - J_{out}^{v\ell}\left(\frac{1}{2}\Delta h_1\right) - J_{out}^{vu}\left(\frac{1}{2}\Delta h_1\right) - J_{u}^{H}(\Delta V) + J_{in}^{v}(\Delta h_1)\right] \quad , \tag{81}$$

and for the area A_{1-3} we have,

$$A_{1-3} = \frac{1}{2}\Delta V\ \Delta h_1 \quad . \tag{82}$$

Combining Eqs. (81) and (82) we have

$$\frac{\partial C_{i,j}}{\partial t} = -\frac{2}{\Delta h_1}\left(J_{\ell}^{H} - J_{u}^{H}\right) - \frac{2}{\Delta V}\left[J_{in}^{v} - \frac{1}{2}\left(J_{out}^{v\ell} + J_{out}^{vu}\right)\right] \quad , \tag{83}$$

where Δh_1, ΔV, J_{ℓ}^{H}, J_{u}^{H} are the same as described by Eqs. (73), (77), and (78) respectively, and J_{in}^{v} is the same as J_{in}^{v1} given by Eq. (80).

Furthermore $J_{out}^{v\ell} = J_{in}^{v2}$ and $J_{out}^{vu} = J_{in}^{v3}$. The difficulty in deriving the expressions for $J_{out}^{v\ell}$ and J_{out}^{vu} of the triangular transition element lies in the absence of an (i+1,j) element. To evaluate $J_{out}^{v\ell}$ and J_{out}^{vu} we will have to approximate the triangular element by two rectangular elements as depicted in Fig. 19.

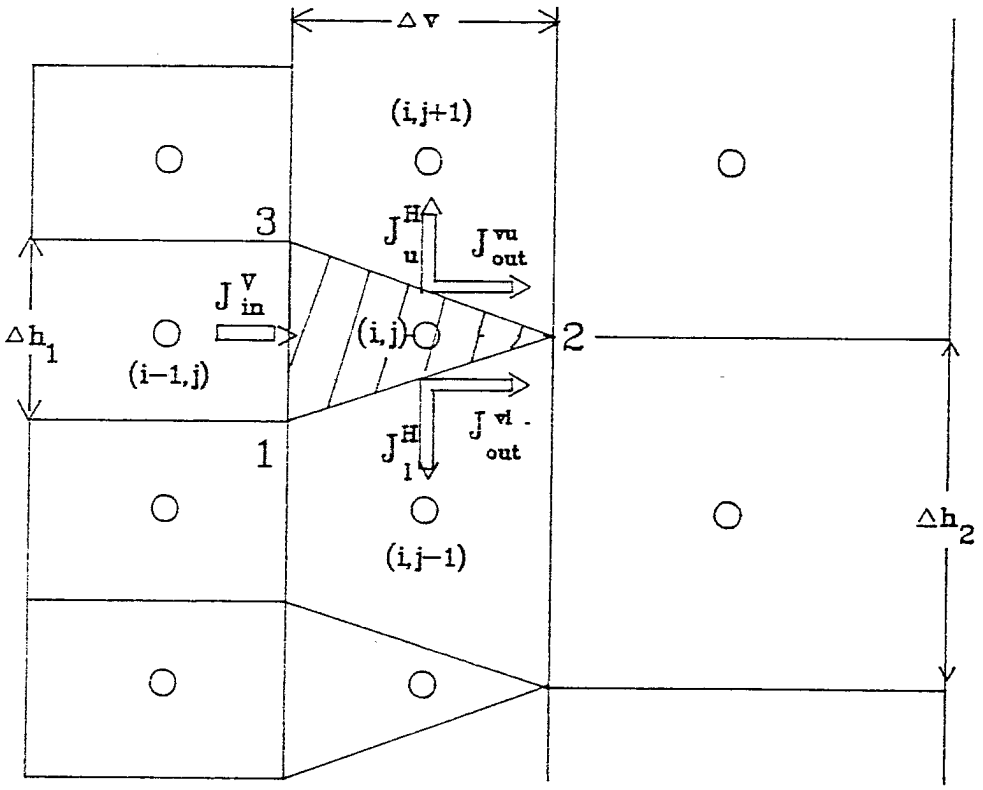

Fig. 18. Notations of the triangular transition element.

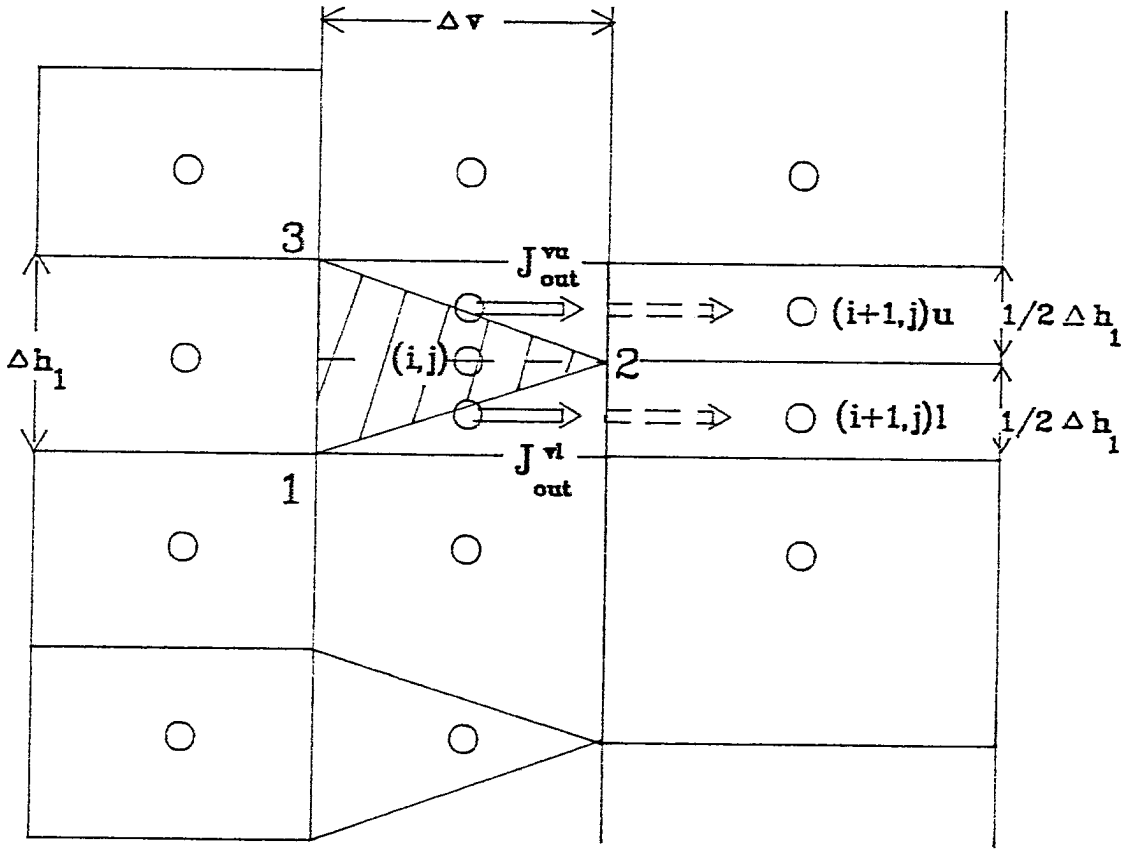

Fig. 19. Notations for the approximation of the triangular element by two rectangular elements.

The concentrations at the center of the lower and upper rectangular elements is approximated by a second order polynomial fit between (i,j) and (i+1,j) and (i-1,j) points. Once determined we can readily derive the formulations for $J^{v\ell}_{out}$ and J^{vu}_{out}.

$$\left[J^{v\ell}_{out}\right]_{i,j} \simeq \frac{\left[F^{v}C\right]_{(i+1,j)\ell} + \left[F^{v}C\right]_{(i,j)\ell}}{2} - \frac{\left[D^{v}C\right]_{(i+1,j)\ell} - \left[D^{v}C\right]_{(i,j)\ell}}{\left(v_{i+1,j} - v_{i,j}\right)} \quad , \tag{84}$$

and

$$\left[J^{vu}_{out}\right]_{i,j} \simeq \frac{\left[F^{v}C\right]_{(i+1,j)u} + \left[F^{v}C\right]_{(i,j)u}}{2} - \frac{\left[D^{v}C\right]_{(i+1,j)u} - \left[D^{v}C\right]_{(i,j)u}}{\left(v_{i+1,j} - v_{i,j}\right)} \quad . \tag{85}$$

Because J^{uv}_{out} is equal to J^{v3}_{in} and $J^{v\ell}_{out}$ is equal to J^{v2}_{in} in the trapizoidal transition element, we now have all necessary equations to describe the transition band finite-difference formulas.

4.1. Model Application to Stainless Steel Irradiated Under HFIR Conditions

An important aspect of the present work is its ability to analyse the behavior of very large clusters of vacancies and helium atoms. The majority of previous theoretical treatments has been confined to small clusters of helium and vacancies or did not properly include helium in the evolution analysis [6]. For example Wehner and Wolfer [6] used the

path integral approach to study cavity evolution. A drawback of this method is neglecting the influence of helium on the evolution process. Their analysis has been only one dimensional.

The present model is applied to stainless steel irradiated in typical HFIR conditions at 450°C. We have restricted ourselves to studying this case because of lack of experimental data regarding helium-filled cavity evolution.

Recently, Maziasz [7] investigated the sensitivity of microstructural evolution to increased helium content during neutron irradiation. In particular, he used EBR-II- and HFIR-irradiated samples to study cavity evolution. The increased helium generation in HFIR makes its data a useful test of the present theory. HFIR conditions have been previously identified to result in spontaneous nucleation.

In his experiments, Maziasz [7] found that the low fluence swelling peaks at 425° to 450°C, as cavities grow among a constant background of finely dispersed bubbles present at ~ 9 to ~ 14 dpa. This results in a bi-modal cavity distribution, characteristic only to this temperature range.

4.4.1. Results of Discrete Rate Equations. Before cavities can reach the growth stage, we have to establish the quasi-steady-state concentration of critical HVCs. As explained in Chapter V, this is accomplished by solving a set of detailed rate equations describing the kinetics of interaction between helium and displacement damage.

The typical displacement damage rate for HFIR irradiation conditions is 1.11×10^{-6} dpa/s, and the helium production rate is 6.35×10^{-11} at./s. While the re-solution parameter b has been set equal to 1, and the dislocation bias factor to Z_i=1.08, the remainder of material parameters are the standard values for 316 stainless steel and are given in Table II.

Figure 20 shows the conentrations of single vacancies C_v, self-interstitials C_i, interstitial helium atoms C_{He}, as well as critical HVCs. Although the time structure of C_v and C_i is little affected by the presence of helium, the absolute magnitude of the vacancy concentration in this case is less than the corresponding case [5,13] without the interaction with helium gas. During the early stages of irradiation, helium is generated as an interstitial helium atom, but is soon trapped when vacancies become available. This mechanism keeps the concentration of untrapped helium atoms low. This trapping eventually leads to the formation of bubbles from substitutional helium. The bubble concentration has been reported to be $\sim 2 \times 10^{-8}$ at./at. for HFIR irradiation experiments performed at 467°C [14]. Our simple set of rate equations predicts a critical HVC concentration of $\sim 8 \times 10^{-9}$ at./at. (Fig. 20).

TABLE II
STANDARD MATERIAL PARAMETERS FOR 316 STAINLESS STEEL

Notation	Parameter	Value	Units	Ref.
a	Lattice parameter	3.63	Å	8
k	Boltzmann's constant	8.617×10^{-5}	eV/K	
ρ	Dislocation density	3×10^{10}	cm/cm^3	
E_i^m	Migration energy of single interstitials	0.2	eV	9
E_g^m	Migration energy of interstitial helium	0.1	eV	
E_v^m	Migration energy of single vacancy	1.4	eV	9
E_v^F	Formation energy of a vacancy	1.6	eV	9
E_i^F	Formation energy of an interstitial	4.08	eV	3
γ_b	Surface energy	6.24×10^{14}	eV/cm^2	3
ν_i	Interstitial vibration frequency	5×10^{13}	s^{-1}	10
ν_g	Helium vibration frequency	5×10^{13}	s^{-1}	11
ν_v	Vacancy vibration frequency	5×10^{12}	s^{-1}	10
B	Van der Waals' constant	1.75×10^{-23}		11
b	Re-solution parameter	1		
Z_i	Bias factor of interstitials	1.08		
Ω	Atomic volume	1.1958×10^{-23}	cm^3	12

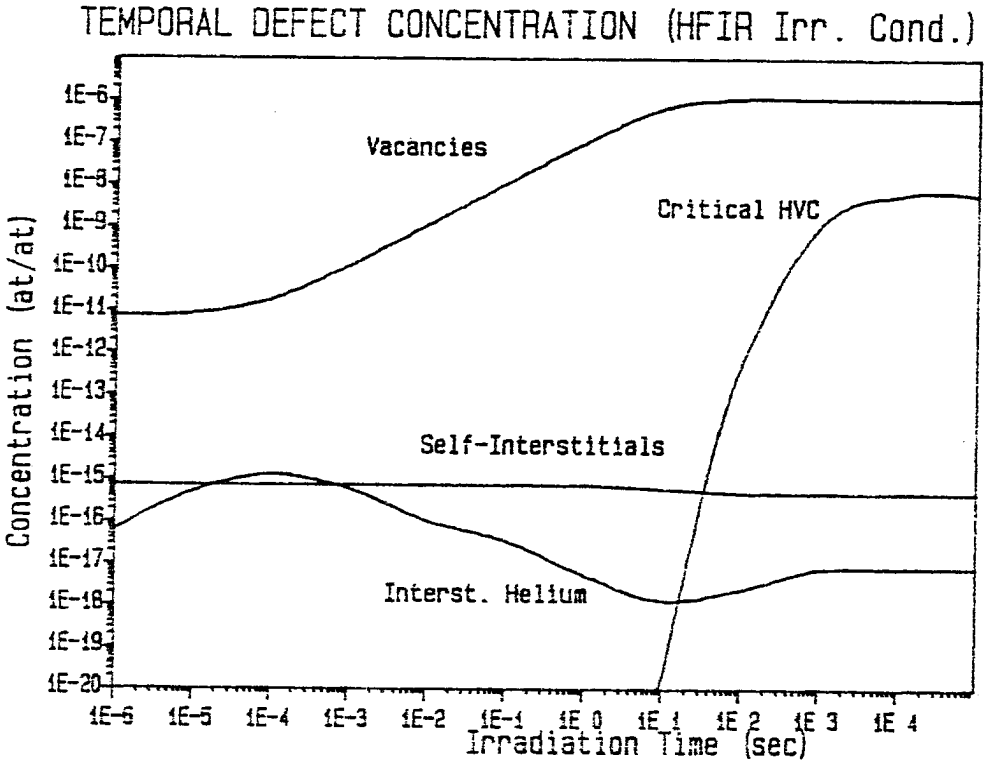

Fig. 20. Irradiation produced defects and critical HVC concentration as a function of time for HFIR irradiation conditions at 450°C.

Having established the quasi-steady-state concentrations of critical HVCs and mobile defects, we use the trajectory analysis (Chapter V, Sects. 3.1 - 3.6) to establish the most probable helium-vacancy combinations for growing cavities. Using the parameters of Table II and the results of the detailed rate equation analysis, Fig. 21(a) shows the trajectory of these calculations. Using Van der Waal's equation of state for comparison, we have also shown the trajectory of cavities in mechanical equilibrium with the surrounding lattice. In equilibrium cavities, the pressure is equal to the surface tension stress. It is shown [Fig. 21(a)] that the amount of helium is smaller than that needed for mechanical equilibrium for cavities with less that ~ 1000 vacancies. The opposite trend takes place for larger cavities. When the rate of radiation re-solution is set to ~ 1 times the atomic displacement rate, a different trajectory is obtained in the helium-vacancy phase space [Fig. 21(b)]. Note however that the scales of Figs. 21(a) and (b) are logarithmic, and that large cavities become underpressurized because of the effect of re-solution. In our applications we have used a re-solution rate that is equal to the atomic displacement rate. Therefore we will follow the trajectory outlined in Fig. 21(b).

At this point, we can compare the prediction of the trajectory analysis to that of the experimental findings of Masziasz [7]. When plotted as a function of irradiation time, the cavity diameter along the trajecttory of Fig. 21(b) can be compared to measured bubble diameters. Figure 22 shows our analytical results and the available experimental data points. Although only a few data points are available, it can be

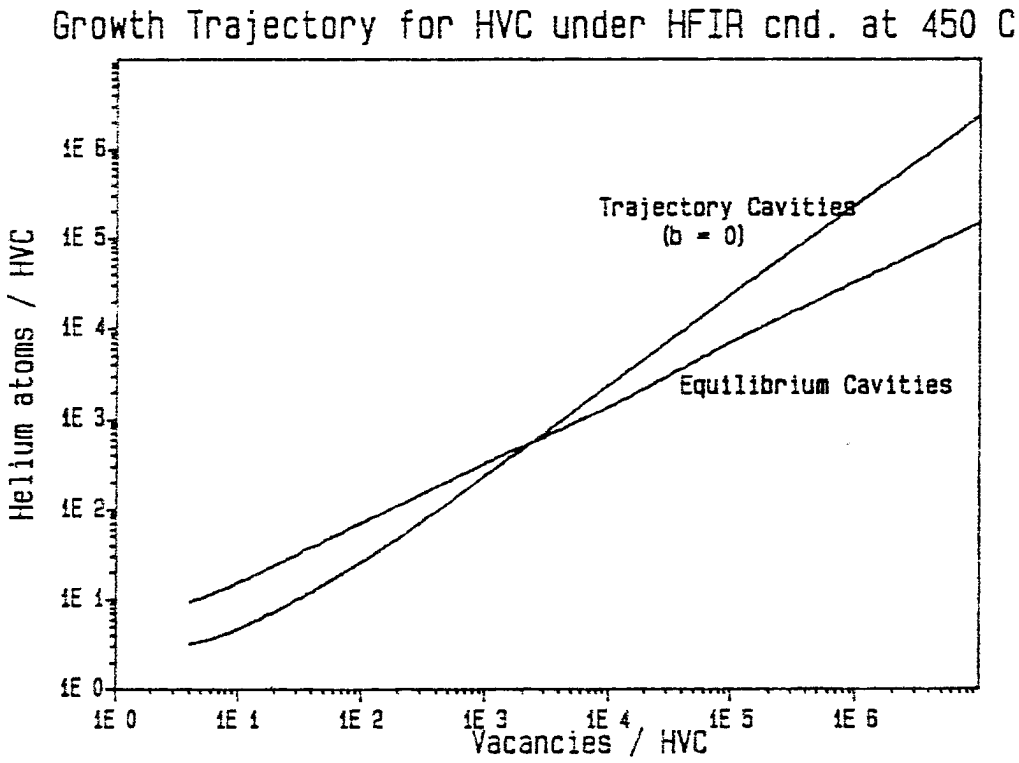

Fig. 21(a). Growth trajectory for HVCs under HFIR irradiation conditions at 450°C. (b=0, re-solution parameter)

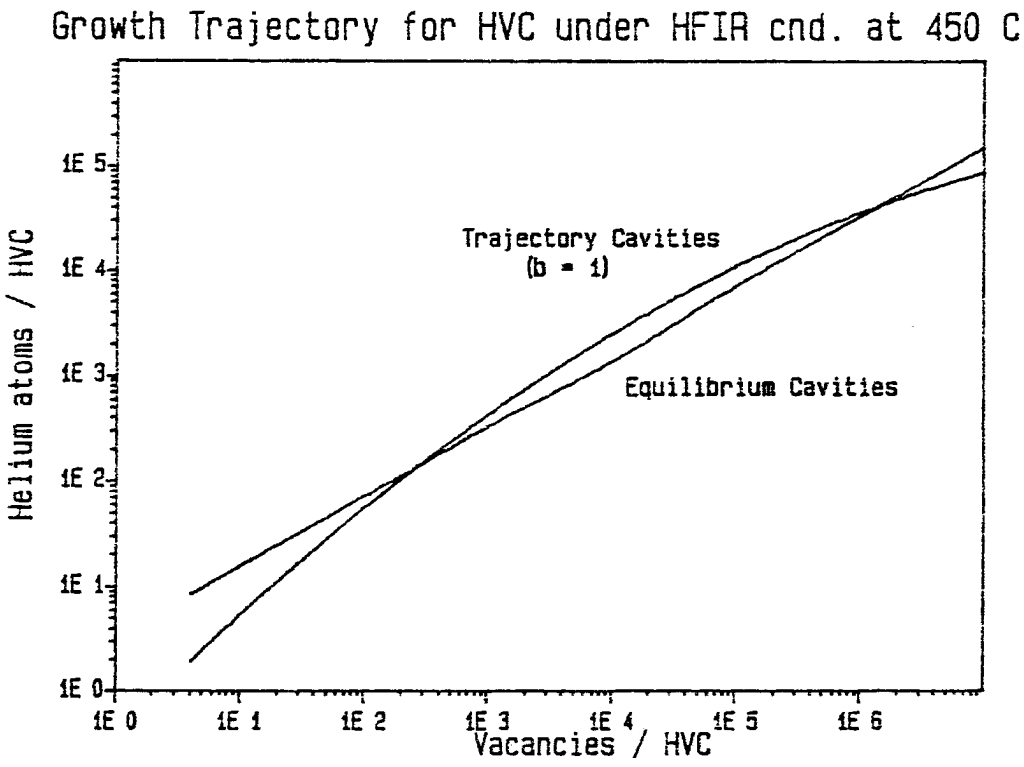

Fig. 21(b). Growth trajectory for HVCs under HFIR irradiation conditions at 450°C. (b=1, re-solution parameter)

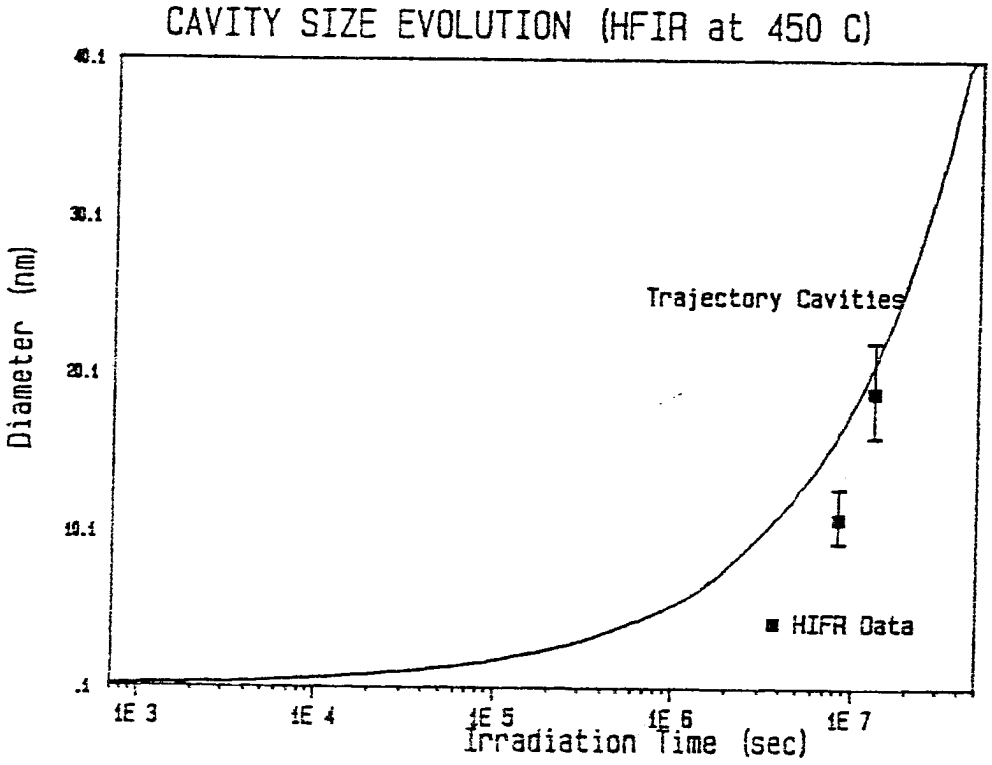

Fig. 22. Time evolution of cavity size under HFIR irradiation conditions at 450°C. (Data points after Maziasz [56].)

seen from Fig. 22 that the average trajectory analysis comes close to experimental findings. This experimental and analytical agreement is of significance to the remainder of our model. The present Fokker-Planck model follows the evolution of cavities from the critical HVC size of three vacancies and three helium atoms to large bubbles containing millions of helium-vacancy combinations.

Figure 22 shows the ranges in a helium-vacancy phase space that need to be considered. We need to consider cavities containing up to 10^7 vacancies and 10^5 helium atoms. Since the trajectory traces the path of the average helium-vacancy combination, we can assume that HVCs located far from the trajectory are nonexistent. This concept is used to develop a regime in helium-vacancy phase space where the analysis can be carried out and can be realistically compared with experiments. By using an estimated diffusional spread around the trajectory (Chapter V, Sect. 3.6), we determine the outer boundaries of the solution domain. Figure 23 shows the diffusional spread around the trajectory. This is estimated as five times the standard deviation, containing more than 99% of the distribution.

We will solve the Fokker-Planck equation describing the growth of HVCs for the region between the upper and lower boundaries of Fig. 23. The results of the Fokker-Planck analysis should be insensitive to the choice of trajectory boundaries. In the following we will investigate the results of the evolution analysis and analyze the effects of the size of the solution domain.

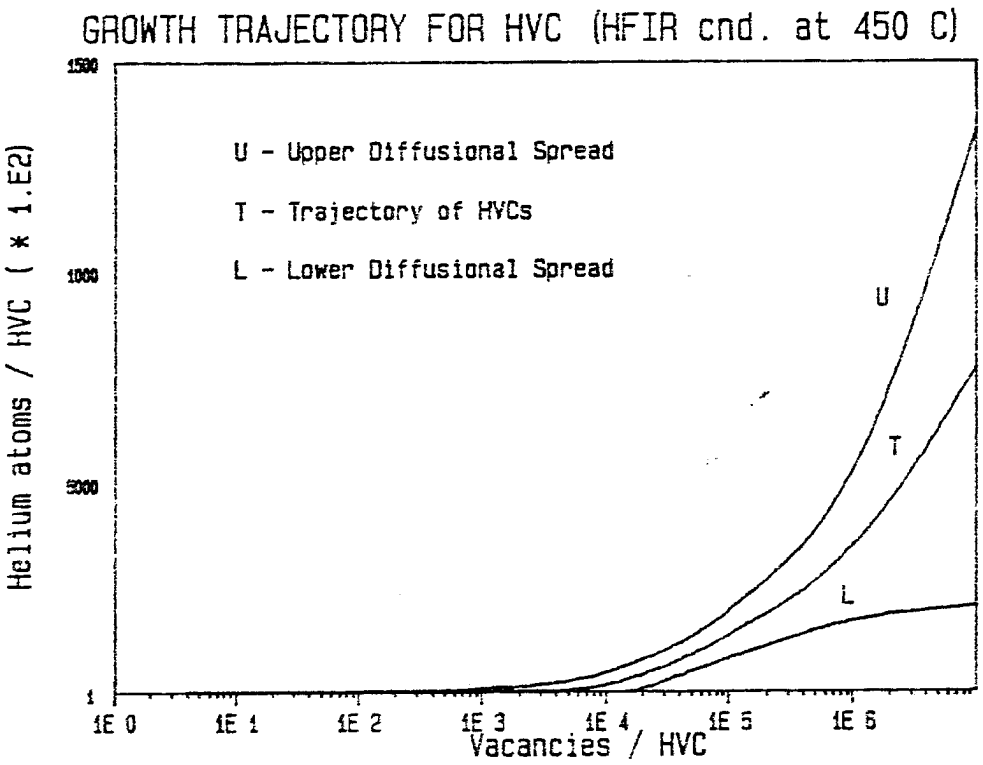

Fig. 23. Growth trajectory for HVC for HFIR irradiation conditions at 450°C with 5 times the standard deviation diffusional spreads.

4.4.2. Results of the Fokker-Planck Equation. In applying the Fokker-Planck equation to the domain outlined in Fig. 23, one is faced with the question of mesh spacing. As mentioned in Sect. 3.4, a dynamic mesh-space incrementation method is developed to minimize computation time and errors while assuming numerical stability. At the onset of computations only ~ 20 equations are solved describing HVCs containing up to 300 vacancies and 200 helium atoms. Using the dynamic meshspace method, that system of ~ 20 equations is eventually increased to ~ 110 equations describing HVCs containing between 5×10^5 and 2×10^6 vacancies and 10^4 to 10^5 helium atoms. This method is computationally very efficient. To investigate the present case up to ~ 15 dpa, the total CPU time needed was ~ 4.5 minutes on the E-Cray machine for solving the discrete rate equations, the trajectory analysis, and the Fokker-Planck equation.

The cavity evolution model assumes a separation between critical HVC nucleation and cavity growth regimes. Thus, we assume that the total concentration of critical HVCs does not increase once the growth state has set in. Therefore, the total cavity concentration at any time during cavity evolution must be conserved. Because of the dynamic mesh-space incrementation method, we frequently eliminate equations from the system and add some at the same time. To ensure conservation of the zeroth moment, this parameter is monitored throughout the computations. Figure 24 depicts the error in the total cavity concentration from the onset of irradiation to ~ 15 dpa. Considering the range of cavities being monitored by our model (from 3 to 2×10^6 vacancies) and not utilizing more than 110 equations at any time, the small error accumulated is reasonable.

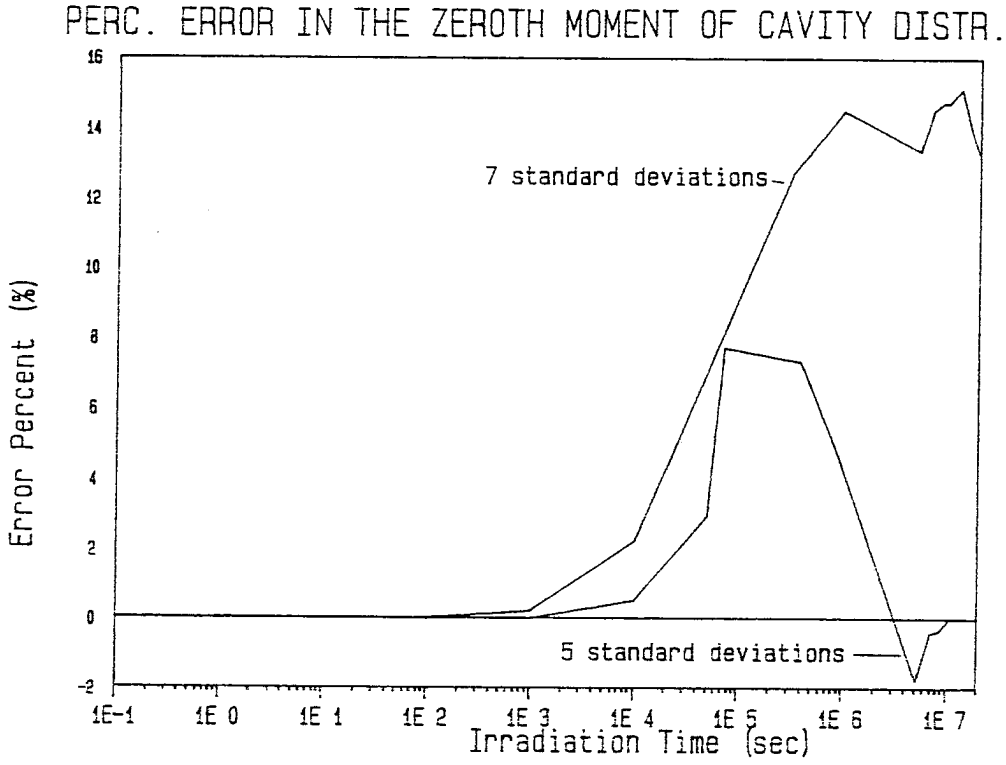

Fig. 24. Percent error in the zeroth moment as a function of irradiation time. (F = no. of standard deviations)

An important question that needs attention is the influence of the extent of the solution domain on the results. In Fig. 24, we show that if the boundary is determined as seven times the standard deviation away from the trajectory, the accumulated error is only few percent up to $\sim 10^6$ seconds. At later times, roundoff errors seem to start accumulating because of the larger extent of the solution domain.

Aside from the increase in concentration error, increasing the solution domain of HVCs in helium-vacancy phase space does not change the results of the cavity evolution analysis. The reliability of the model is therefore established with a solution domain determined by five standard deviations away from the trajectory. The following results are for the choice of HVC size region as depicted by Fig. 23, where we have used five times the diffusional spread around the trajectory.

At the onset of cavity growth, all cavities are of the same size. They contain three vacancies and three helium atoms. As irradiation proceeds, these critical HVCs diffuse in the helium-vacancy phase space and the once-peaked distribution broadens. Figure 25(a) and (b) show the results of such a cavity distribution at $\sim$ 14 dpa after irradiation has set in. (For HFIR conditions this corresponds to $\sim 1.3 \times 10^7$ s of irradiation.) In Fig. 25 (a) and (b), the concentration of cavities is shown as a function of helium and vacancy content. While the distribution is narrow for small clusters, it broadens as the peak traces out a path close to the trajectory prediction. Although all previous analytical attempts have only been able to predict the trajectory path of HVCs [15], our model is the first one that establishes the time-dependent distribution of HVCs in the helium-vacancy phase space.

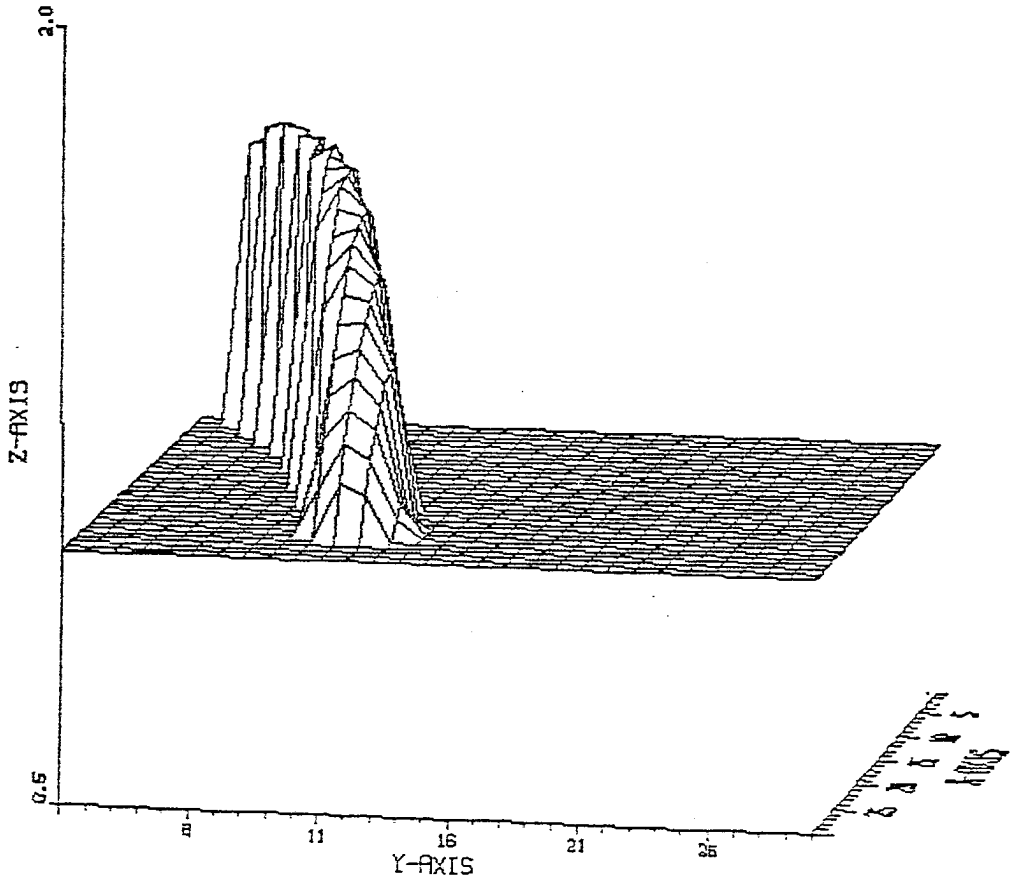

Fig. 25(a). Cavity concentration at 14 dpa as a function of no. of vacancies (size) and helium content for HFIR irradiation conditions at 450°C. (Entire helium content distribution is shown.)

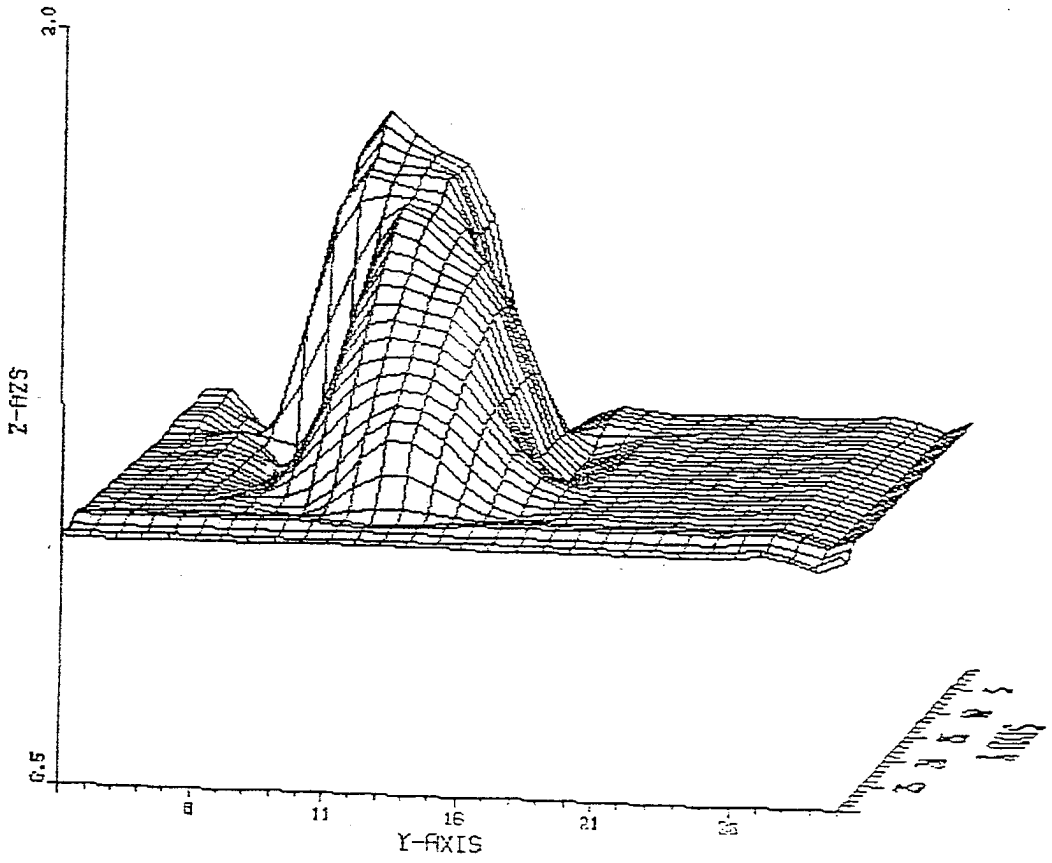

Fig. 25(b). Cavity concentration at 14 dpa as a function of no. of vacancies (size) and helium content for HFIR irradiation conditions at 450°C. (Partial helium content distribution is shown.)

To demonstrate some aspect of cavity evolution, we will first investigate the cavity size distribution for average helium contents at various displacement damage levels. Figure 26 shows the helium content as a function of irradiation time. During the early stages of irradiation (~ 0.1 dpa), the average helium content of HVCs is only ~ 170 helium atoms, while at ~ 14 dpa it increases to ~ 3×10^4 atoms. Figure 26 also shows the size distribution at various dpa levels. The distribution of average size cavities as a function of helium content at various irradiation times is shown in Fig. 27. We see that at the onset of irradiation (~ 0.1 dpa), there is a large concentration of small HVCs (~ 2 nm/diam), all containing between 100 to 200 helium atoms. As irradiation proceeds, the HVCs grow in size and one can find 5 nm HVCs containing from a few hundred to several thousand helium atoms. This evolution process is followed up to ~ 14 dpa. At that time, the average HVC has a diameter of ~ 20 nm and may contain from 2.5×10^4 to 3.5×10^4 helium atoms. Because the distribution spreads, while the zeroth moment is conserved, the peak of the concentrations decreases (Figs. 26 - 28). Unfortunately there are no experimental data for the helium content distribution of cavities as a function of irradiation time and cavity size. The data available are only with respect to the size distribution. Most of the experimental data report the percent of the distribution as a function of size at various dpa's. Figure 28 shows the results of calculated size distributions. While at ~ 0.1 dpa, the distribution consists only of small cavities (< 2 nm/diam), the distribution has broadened to sizes of ~ 20 nm cavities.

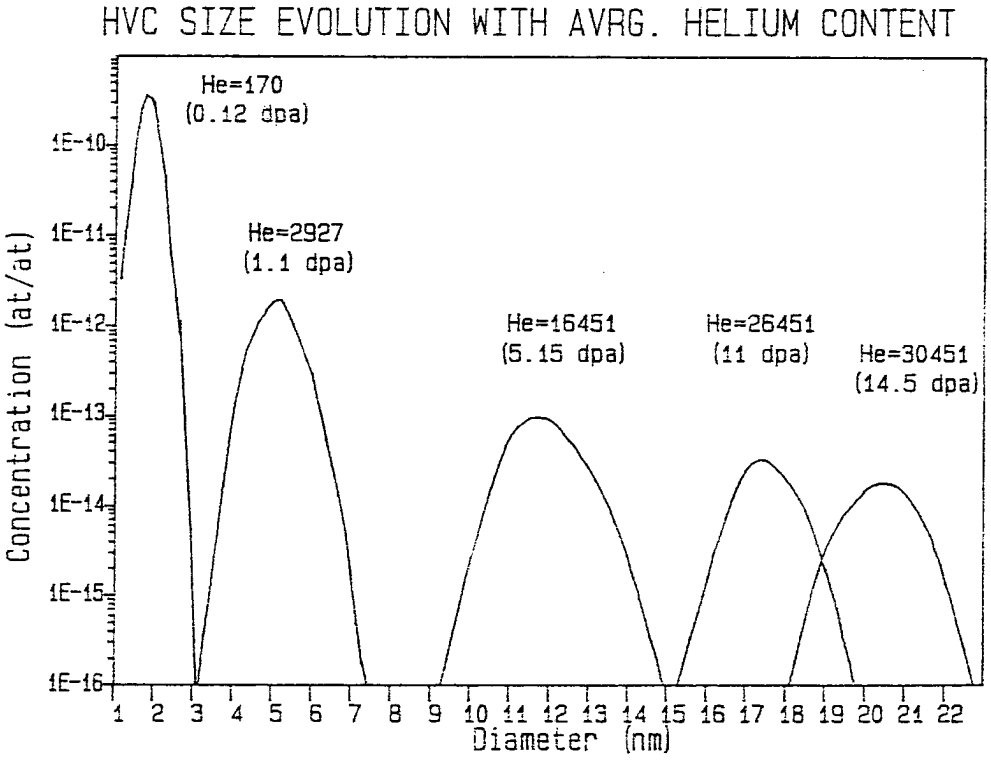

Fig. 26. Cavity size evolution at average helium content for HFIR irradiation conditions at 450°C at different dpa's.

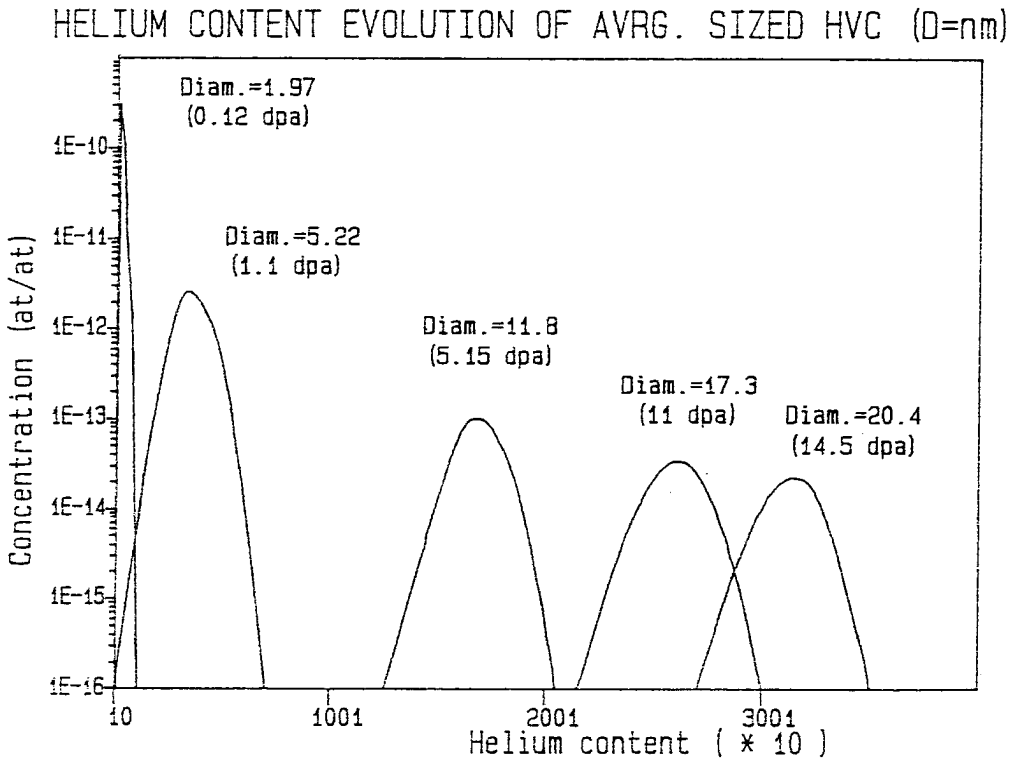

Fig. 27. Distribution of average size cavities as a function of helium content for HFIR irradiation conditions at 450°C.

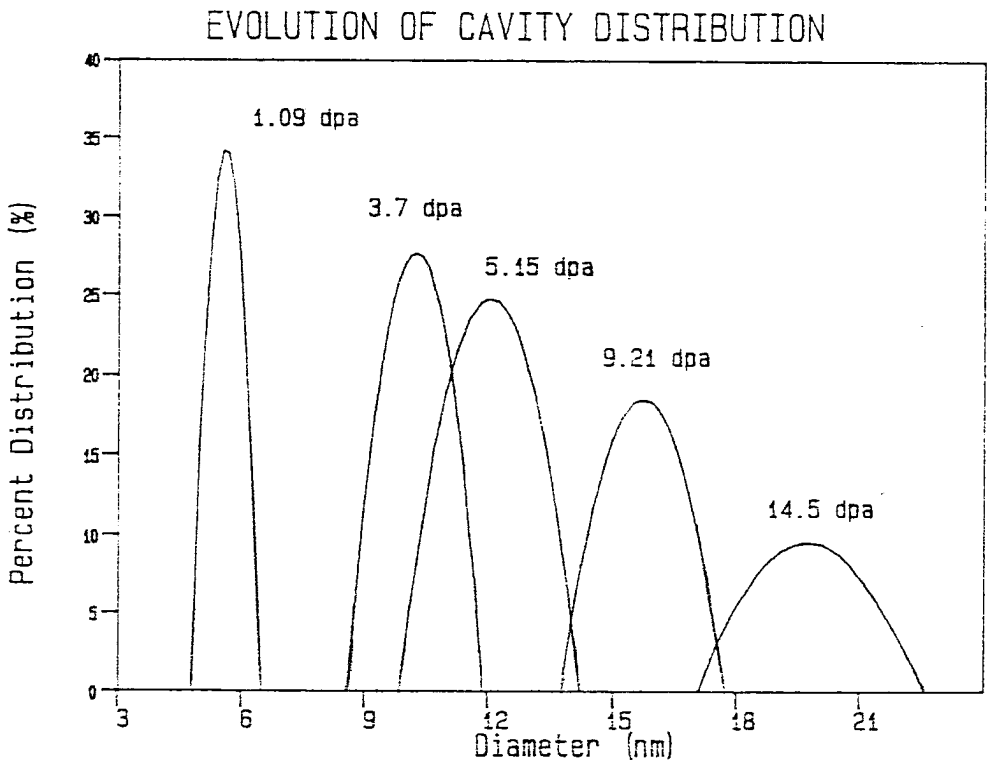

Fig. 28. Evolution of % cavity distribution as a function of cavity diam at various irradiation times.

To compare our computer model to experimental findings, we have to convert the numerical concentration results into distribution percentages. In this regard, a simple transformation relating the number of vacancies to the radius of a cavity is used:

$$v\Omega = (4/3)\pi r^3 \quad , \tag{86}$$

where v = no. of vacancies,

Ω = atomic vol,

r = radius of cavity containing v vacancies.

At any time, the total cavity concentration is given by

$$C_{tot} = \int_v \int_h C(v,h)dvdh \quad , \tag{87}$$

$$\approx \sum_v \sum_h C(v,h)\Delta v \Delta h \quad , \tag{88}$$

where Δv = meshsize in the vacancy direction and Δh = meshsize in the helium direction. In terms of size, the total cavity concentration is given by

$$C_{tot} = \int_r C(r)dr \quad , \tag{89}$$

$$\approx \sum_r C(r)\ \Delta r \quad . \tag{90}$$

At a particular radius r_o, corresponding to a number of vacancies v_o we have from Eqs. (87) and (89)

$$C(r_o)dr = [\sum C(v_o,h)\ \Delta h]dv \quad , \tag{91}$$

or

$$C(r_o) = [\sum_h C(v_o,h)\ \Delta h](\frac{dv}{dr}) \quad . \tag{92}$$

Equation (86) yields

$$\frac{dv}{dv} = \frac{4\pi}{\Omega} r^2 \quad . \tag{93}$$

We have shown experimental [7] data at 9.2 dpa of the size distribution in detail in Fig. 29. The results of the computer model using Eqs. (92) and (93) are shown on the same figure as a smooth curve. The model predicts a narrower size distribution, with the peak shifted by a few nano-meters towards larger cavities. In Fig. 30 we compare our results to the experimental findings [17] of Maziasz at 14.3 dpa. Again, the model predicts a narrower distribution but the experimental peak position is roughly coincident with the model at ~ 20 nm. Equation (92) combined with Eq. (93) transforms the vacancy-helium atom dependent distribution function into one that is dependent only on the radius. It is this size-dependent cavity concentration which can be expressed as a percent of total cavity concentration and compared to experimental data.

It is encouraging to observe that the computed size distribution is narrower than that experimentally observed. The broadening in our model is solely due to the dependence of the emission/absorption probabilities on the cavity size. We have not accounted for other stochastic effects

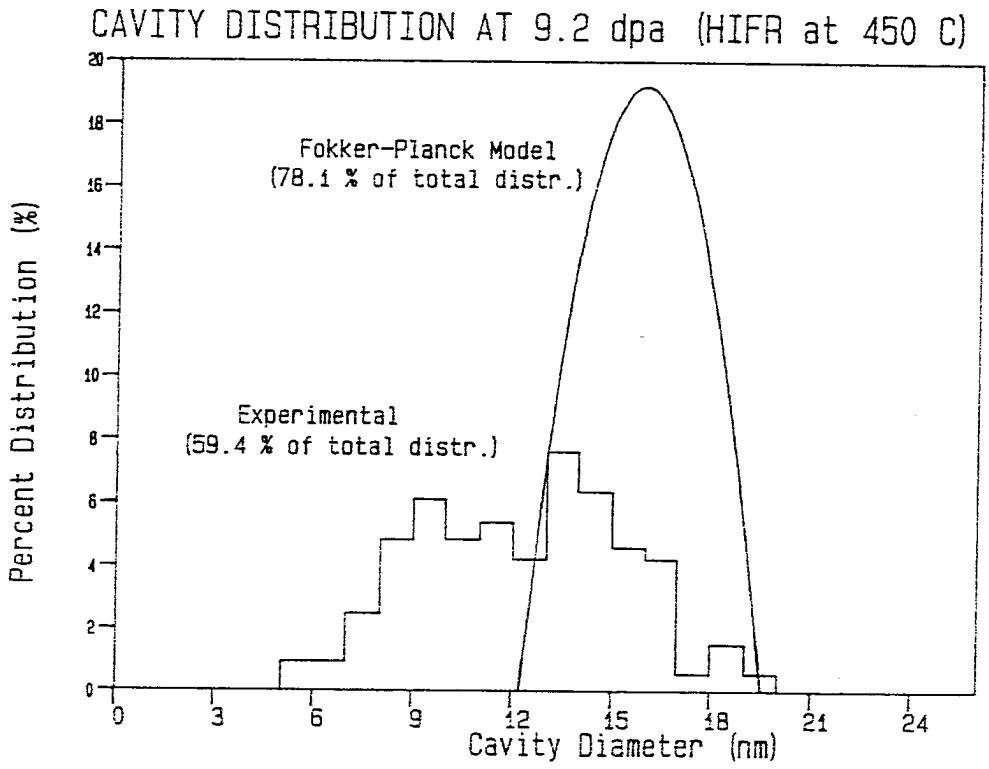

Fig. 29. Comparison of analytical and experimental cavity size distribution at 9.2 dpa for HFIR irradiation conditions at 450°C. (Experimental data after Maziasz [16].)

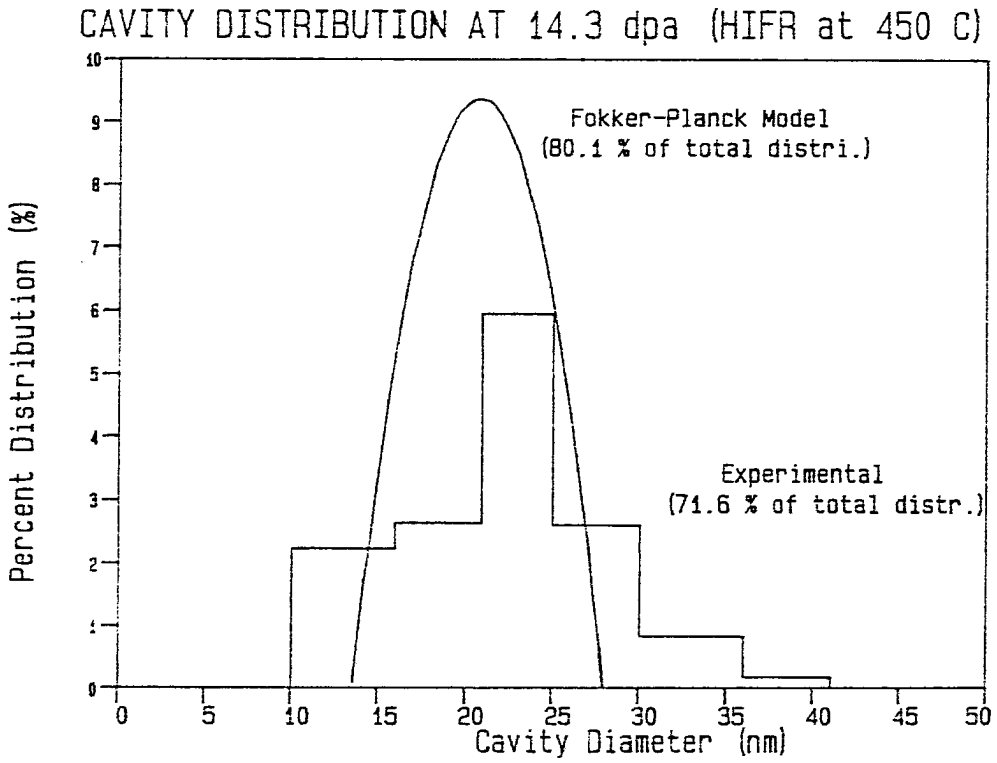

Fig. 30. Comparison of analytical and experimental cavity size distribution at 14.3 dpa for HFIR irradiation conditions at 450°C. (Experimental data after Maziasz [16].)

on these probabilities, which are reflected in the function D. If other stochastic effects are considered (e.g., spatial distribution of cavities and stochastic nature of point-defect production [17]), the computed distribution may broaden even further.

As pointed out earlier, Maziasz also examined the fine bubble concentration persistent at ~ 450°C up to ~ 14 dpa. Those fine bubbles constitute a large portion of the total distribution. At 9.2 dpa, 43% of the total cavity concentration is in the form of bubbles ranging between 1 and 3 nm/diam (Fig. 31a). This fraction slightly reduces to ~ 31% at ~ 14.3 dpa, while the sizes of these fine bubbles stay around 2 nm/diam (Fig. 31b). At both dpa's the sum of the fine bubbles with their coarse counterparts adds up to ~ 100% of the total distribution.

In our model, we monitored the behavior of all sizes and found that various HVCs did not grow beyond a certain size and helium content. The continuum rate equations (Fokker-Planck) describing the helium-vacancy phase space are coupled via reaction rates. These reaction rates are a function of helium content and size of the HVC being investigated. The code is written in such a fashion that, when the concentration of a certain HVC reaches a low value (floor value), the equation describing that cluster is eliminated from the system in order to avoid numerical instabilities (see Sect. 3.5.1). Thus in effect, this method eliminates unstable HVCs from the system of equations being monitored. Therefore, a HVC containing, for example, 5×10^4 vacancies may be stable with respect to vacancy emission if it contains 7×10^3 helium atoms (Fig. 23). That same size HVC is unstable with regard to vacancy emission if it contains far less than 7×10^3 helium atoms, i.e., 500 helium

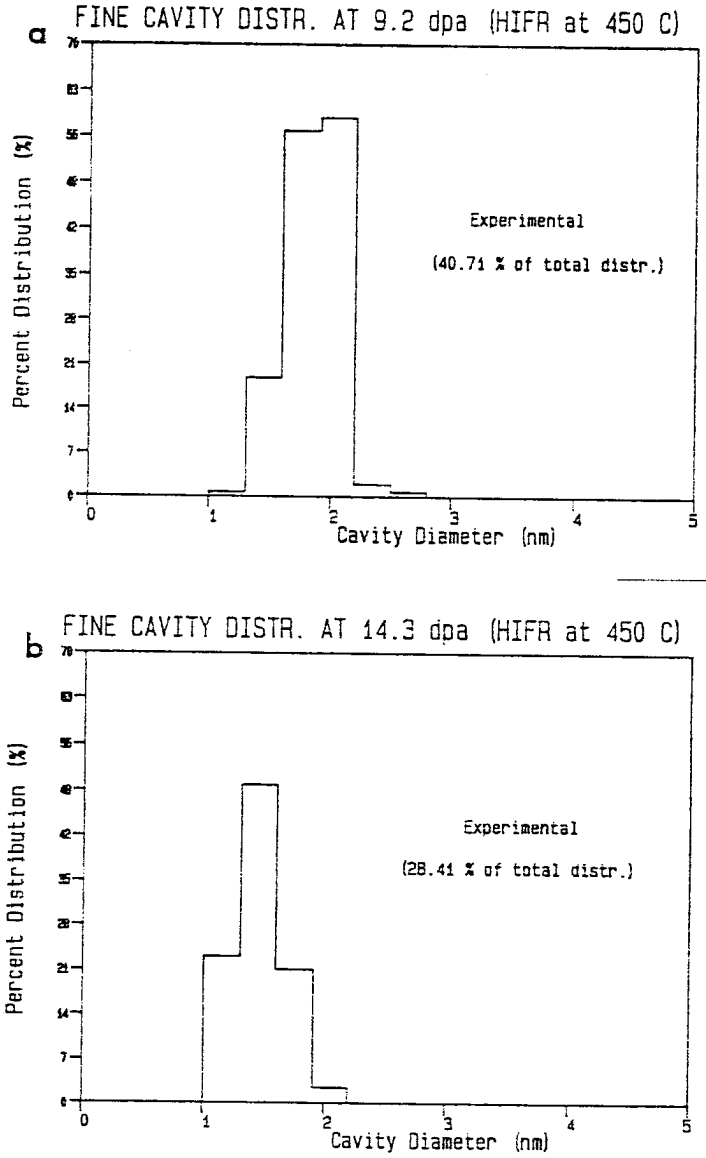

Fig. 31. Experimental bi-modal cavity size distribution for HFIR irradiation conditions at 450°C for (a) 9.2 dpa and (b) 14.3 dpa (after Maziasz [16]).

atoms. Therefore a HVC containing 5×10^4 vacancies will emit vacancies until it reaches the size at which 500 helium atoms will prevent any further reduction in size [$\sim 10^4$ vacancies (Fig. 21)]. A similar scenario may happen with respect to helium emission from a cluster. In this fashion we have monitored HVCs that have been isolated from the growing system of HVCs. These HVCs are therefore the most stable clusters that will no longer undergo any transformation in the helium or vacancy direction. This process of isolation eventually comes to an end as the cavity sizes increase. In our case, no more HVC isolations occur above a mean diameter of 10 nm. This is due to the fact that for larger HVCs ($\geq$ 10 nm), the distribution is very broad in vacancy and helium content (Figs. 26 and 27). By monitoring the zeroth moment of the cavity distribution, we determined the percentage of isolated HVCs as a function of irradiation time and cavity size. Our stationary background HVCs constitute about 20% of the total HVC distribution at 9.2 dpa which remains constant from here on. These "stationary" HVCs are the reason for not having 100% of the cavity distribution present in Figs. 29 and 30. With regard to the size distribution of the calculated background HVCs (bi-modal), we found a broader and less peaked distribution compared to the experimental findings.

Besides these differences, it is interesting to note that our model not only predicts the correct size evolution of HVCs for HFIR irradiation conditions, but it also indicates the development of a bi-modal distribution.

REFERENCES

[1] R. Chandrasekhar, Rev. Mod. Phys., 15 (1943) 1.

[2] G. H. Weiss and M. Dishon, J. Stat. Phys., 13 (1975) 145.

[3] R. I. Cuker, K. Lakatos-Lindenberg and K. E. Shuler, ibid, 9 (1973) 2.

[4] A. C. Hindmarsh, June 17, 1980 Version of LSODE, Lawrence Livermore Lab. Report UCID-3001 (1974).

[5] N. M. Ghoniem and S. Sharafat, University of California Los Angeles Report UCLA-ENG-7962 (1979).

[6] M. F. Wehner and W. G. Wolfer, "Vacancy Cluster Evolution in Metals Under Irradiation," U.S. Department of Energy Report DOE-ER-0046-19 (Sept. 1984) 75.

[7] P. Mazsiasz, "Effects of Helium Gontent on Microstructural Development in Type-316 Stainless Steel Under Neutron Irradiation," Ph.D. thesis, University of Tennessee, Knoxville, (December 1984).

[8] M. I, Baskes, J. Nucl. Mater., 83 (1979) 139.

[9] G. Farrell and W. A. Grant, Radiat. Eff., 3 (1970) 249.

[10] J. E. Inglesfield and J. B. Pendry, Philos. Mag. 34 (2) (1976) 205.

[11] D. L. Johnson and J. R. Cost, in Proc. Conf. on Defects and Defect Clusters in B.C.C. Metals and Their Alloys, National Bureau of Standards, Gaithersburg, MD, August 1973, p. 279.

[12] D. B. Poker and J. M. Williams, Appl. Phys Lett., 40 (1982) 851.

[13] N. M. Ghoniem and D. D. Cho, University of California Los Angeles Report UCLA-ENG-7845 (August 1978).

[14] P. Maziasz, J. Nucl. Mater., 103&104 (1981) 987.

[15] W. Jäger, R. Manzke, H. Trinkaus, G. Crecelius and R. Zeller, ibid, 111&112 (1982) 674.

[16] P. Maziasz, private discussions.

[17] P. Chou and N. M. Goniem, "On the Stochastic Theory of Point Defect Diffusion During Radiation ...," J. Nucl. Mater. (in press).

CHAPTER VIII

SUMMARY AND CONCLUSIONS

The effects of helium on bulk material properties such as tensile strength, creep rupture, fatigue, etc., were outlined in Chapter II of this thesis. In a fusion environment, helium production rates will be in a regime that can cause any one or all of these properties to degrade in metallic alloys (see Tables I and II, Chapter III). In order to minimize the effects of helium on alloy property degredation, the formation and growth of helium bubbles during irradiation would have to be suppressed. Until prototypical fusion test reactors are available, this can only be accomplished through experimental alloy tailoring, supported by detailed theoretical understanding of helium bubble evolution.

This thesis provides a tool aimed at understanding the formation and the development of helium bubbles from atomistic to macroscopic sizes.

First the atomistic behavior of helium as a single impurity atom inside the host lattice has been reviewed. Atomistic calculation results have been compared with experimental findings aimed at determining the energetics of helium atoms at various lattice sites (Chapter II). These findings have been used to investigate the interaction of helium with other defects produced during irradiation. Using a model based on rate theory equations, it has been possible to identify the effects of these interactions on the helium migration mechanisms (Chapter IV).

The developed model enables us to reproduce experimental findings regarding the effective diffusion energy of helium measured under specific irradiation conditions. Furthermore, without resorting to extrapolation techniques, it is possible now to estimate effective diffusion coefficients under conditions that are experimentally difficult to measure. Under fusion reactor irradiation conditions, the model gives the following approximate values for helium-effective migration energies in nickel:

$$E_{He}^{eff} \approx 0.83 \text{ eV for } T \geq 800^0K,$$

$$E_{He}^{eff} \approx 1.4 \text{ eV for } 400 \leq T \leq 800^0K,$$

$$E_{He}^{eff} \approx 0.65 \text{ eV for } T \leq 400^0K.$$

Our analytical and numerical approaches to this problem constitute a pioneering effort in this field, since all mechanisms influencing helium transport have been included. These features consist of the temperature effects on HVC stability, the competition between self-interstitials and helium atoms to react with vacancies, and the displacement collision cascade re-solution of helium atoms from HVCs.

The inclusion of <u>all</u> mechanisms in our model allowed us to determine and identify the domain of each detrapping mechanism as a function of irradiation conditions and material parameters. Thus we determined that for fusion reactor irradition conditions, thermal

detrapping is the main mechanism responsible for the effective helium migration energy above 800°K. Below 400°K, helium re-solution due to PKAs keeps the effective helium migration energy low ($E_{He}^{eff} \approx 0.65$ eV). For temperatures between 400° and 800°K, the competition between self-interstitials and helium atoms for free vacancies affects the effective helium migration energy the most.

The next step in understanding the evolution of helium bubble evolution deals with the stability of HVCs. It is the size and the helium content of the critical (stable) HVC that determine the final bubble size distribution.

To determine the helium-to-vacancy ratio of critical HVCs, we followed the nodal line analysis first applied to HVCs by Russell et al. (Chapter V). We expanded their model by including the self-interstitial helium replacement reaction and the PKA helium re-solution mechanisms. Our approach allowed us to map the nucleation regimes for spontaneous and stochastic regions as a function of irradiation conditions and material parameters.

In the spontaneous nucleation mode, very small nucleation barriers exist and nucleation of stable HVCs proceeds homogeneously in the matrix. This occurs under irradiation conditions of high helium generation rates, low temperatures, and low sink density.

The second mode, that is stochastic nucleation, proceeds with substantial nucleation barriers, which must be overcome by subcritical HVCs in order to reach stable configurations. This case is best achieved at high temperatures, high dislocation sink density, and low helium generation rates.

Thus we are able to explain the differences in basic experimental findings concerning cavities in HFIR and EBR-II irradiation samples. The high helium generation rate of HFIR renders a spontaneous nucleation mode which leads to the formation of 20 to 50 times more numerous, and 10 times smaller, bubbles than found in EBR-II-irradiated steel samples.

In setting up our nodal line method for HVC stability analysis, we added one other feature not present in Russell's approach. While he used estimates of free energy of formation of HVCs, we used numerical equations of state for dense gases in cavities to estimate the binding energies of the last helium and the last vacancy to a HVC.

When applied to very small HVCs, our approach to calculating the helium-vacancy binding energies compared supprisingly well with atomistic calculations performed by Wilson, Baskes, and Johnson. Thus we no longer needed to use estimates of free energies or extrapolation of atomistic values to establish the nodal line analysis for HVC stability.

After determining the irradiation conditions under which stable HVCs nucleate, we next focused our attention on establishing the evolution path of bubbles in a helium-vacancy phase space. The goal has been to predict the average HVC size and helium-vacancy ratio as a function of time and irradiation conditions. For this, we used the method of growth trajectories recently used by Trinkaus (Chapter V). He formulated an analytical model which can be solved for a narrow range of conditions. We employed a similar approach and developed a simple numerical model that compared well with Trinkaus's analytical solution. However, our numerical model is no longer limited to a

specific case but can be applied to a variety of realistic irradiation conditions.

We have established the growth trajectories for accelerator, HFIR, and EBR-II irradiation conditions and compared these with growth trajectories for equilibrium helium bubbles. Furthermore, we have been able to show the effects of using the ideal gas law versus the Van der Waal equation of state on the development of the growth trajectories (Chapters V and VII). As expected, the choice of gas law only affects the early stages of HVC trajectories, while for larger HVCs the answers converge to similar values.

The growth trajectory of HVCs in a helium-vacancy phase space not only traces the loci of the average HVC size and helium-vacancy ratio, but it can also be used to determine a finite solution space for numerical analysis. Here, we have used a multiple of the diffusion spreads in the helium and vacancy direction for loci along the growth trajectory to establish the size of the solution domain for Fokker-Planck analysis. By envoking a zero-current boundary condition on this prescribed contour, we have been able to minimize the solution space in the helium-vacancy phase space.

This brings us to the final stage of bubble evolution: the growth of HVCs to macroscopic sizes. To model bubble growth, we have derived the Fokker-Planck equation for HVCs. This has been established by expanding a generalized rate equation for HVCs using a Taylor series expansion technique. Collecting terms resulted in a continuum rate equation in which the coefficients of the drift term represents the first moment and the coefficients of the diffusion term the second

moment of the fluctuation probability in point-defect absorption rates. We have developed a novel calculational method for the solution of this 2-D Fokker-Planck equation. First, we solve a set of eleven discrete rate equations describing the time-dependent concentrations of five fundamental mobile species and the concentration of critical HVC embryos. The five mobile species being monitored are single vacancies, self-interstitial atoms, interstitial helium atoms, divacancies, and divacancy single-helium clusters.

The quasi-steady-state solution to these equations provides five defect fluxes as well as the critical HVC concentration, which will now be considered as the nucleus for growing HVCs.

At this stage, the Fokker-Planck equation is solved numerically. In order to maximize programming efficiency and to minimize computational time, a dynamic incrementing mesh spacing method has been developed. In this method, only equations are solved that lie in the vicinity of the moving peak of the HVC size distribution (Chapter VII).

The application of these hybrid discrete and continuum rate theory equations are demonstrated in Chapter VII. We have chosen typical HFIR irradiation conditions in order to be able to compare our results to experimental findings. Good agreement between our predicted size distributions and those measured by Maziasz has been found. In addition, our calculations allow the estimation of the helium content distribution which cannot be experimentally determined at the present time. Our calculations can thus be considered as pioneering in establishing a 2-D distribution of HVCs. Other stochastic sources for the spread in the size distribution due to cascades have been recently

discussed by Kitajima. Those can easily be included in the analysis, with the effect of spreading the distribution function further. Therefore better agreement with experiments is expected.

Thus we have followed the bubble evolution from an atomistic level of helium-defect complexes over the stable nucleation regime of HVCs to macroscopically verifiable helium bubbles. Although other microstructural evolution processes such as grain boundaries, precipitates, and dislocation line densities have been grossly modeled, this work is a first attempt in developing a unified bubble evolution model that is not subject to non-physical simplifying assumptions.